INFORMATION TO USERS

This manuscript has been reproduced from the microfilm master. UMI films the text directly from the original or copy submitted. Thus, some thesis and dissertation copies are in typewriter face, while others may be from any type of computer printer.

The quality of this reproduction is dependent upon the quality of the copy submitted. Broken or indistinct print, colored or poor quality illustrations and photographs, print bleedthrough, substandard margins, and improper alignment can adversely affect reproduction.

In the unlikely event that the author did not send UMI a complete manuscript and there are missing pages, these will be noted. Also, if unauthorized copyright material had to be removed, a note will indicate the deletion.

Oversize materials (e.g., maps, drawings, charts) are reproduced by sectioning the original, beginning at the upper left-hand corner and continuing from left to right in equal sections with small overlaps. Each original is also photographed in one exposure and is included in reduced form at the back of the book.

Photographs included in the original manuscript have been reproduced xerographically in this copy. Higher quality 6" x 9" black and white photographic prints are available for any photographs or illustrations appearing in this copy for an additional charge. Contact UMI directly to order.

UMI

A Bell & Howell Information Company
300 North Zeeb Road, Ann Arbor MI 48106-1346 USA
313/761-4700 800/521-0600

Grating Light Reflection Spectroscopy

by

Brian Benjamin Anderson

A dissertation submitted in partial fulfillment of the
requirements for the degree of

Doctor of Philosophy

University of Washington

1996

Approved by ______________________________
(Chairman of Supervisory Committee)

____

Program Authorized
to Offer Degree Chemistry

Date August 21, 1996

UMI
300 North Zeeb Road
Ann Arbor, MI 48103

Doctoral Dissertation

In presenting this dissertation in partial fulfillment of the requirements for the Doctoral degree at the University of Washington, I agree that the library shall make its copies freely available for inspection. I further agree that extensive copying of this dissertation is allowable only for scholarly purposes, consistent with "fair use" as prescribed in the U.S. Copyright Law. Requests for copying or reproduction of this dissertation may be referred to University Microfilms, 1490 Eisenhower Place, P. O. Box 975, Ann Arbor, Michigan 48106, to whom the author has granted "the right to reproduce and sell (a) copies of the manuscript in microform and/or (b) printed copies of the manuscript made from microform."

Signature__________

Date 8-21-96

University of Washington

Abstract

Grating Light Reflection Spectroscopy

by

Brian B. Anderson

Chairman of the Supervisory Committee: Professor Bruce R. Kowalski
Department of Chemistry

A new optical technique for analytical sensing, termed Grating Light Reflection Spectroscopy (GLRS), is described and evaluated in this dissertation. GLRS relies on the existence of thresholds in diffracted transmitted light for the interrogation of the dielectric properties of the sample in contact with a transmission diffraction grating. These thresholds are created when a particular diffracted transmitted order is transformed from a traveling wave into an evanescent one. This occurs at a specific wavelength that is dependent upon the angle of incidence, grating period, and complex dielectric function of the sample. The existence of transmission thresholds produces singularities in reflected light that occur at the threshold wavelength due to the redistribution of optical energy from the threshold order to all diffracted orders. GLRS theory, developed by Dr. Anatol Brodsky, predicts that application of GLRS will yield measurements that are sensitive to optical properties such as refractive index and absorbance and in addition will allow for the deconvolution of refractive index and absorbance effects as well as surface and bulk effects.

A binary metal/dielectric diffraction grating having submicron periodicity was fabricated and used in the characterization of GLRS. The GLRS singularity in reflected light is visible as a sharp change in reflection coefficient at the threshold wavelength. An evaluation scheme was devised to test the sensor response to model sample matrices and evaluate the correlation of that response with each major theoretically predicted response. Experimental evidence directly supports predictions regarding the response of GLRS to changes in the complex dielectric function of the sample. Calibration of GLRS response yielded sensitivity to refractive index changes on the order of 2×10^{-6} and an absorbance dynamic range to 250 A. U. In addition, the sensor was exposed to mixtures, simulated fouling layers and a sample set of model scattering systems. The experimental results prove theoretical claims that the sensor is relatively insensitive to surface fouling and it is shown

that GLRS may provide substantial information regarding the characteristics of colloids and suspensions including the particle shape and density distribution.

Table of Contents

Chapter 1:

Chapter 2:

Chapter 3:

Chapter 4:

Chapter 5:

Chapter 7:

Appendix:

Acknowledgments

First I would like to thank my advisors: Dr. Lloyd Burgess and Prof. Bruce Kowalski for valued input into this work as well as guidance throughout my graduate career. In addition, I would like to thank my supervisory committee members for their perseverance and valued input into this work: Professors Robert Synovec, William Reinhardt, Anatol Brodsky, and Martin Afromowitz. Thanks also to the reading committee for the prompt reading of this dissertation and return of comments. Specifically, I would like to acknowledge the extraordinary collaborative relationship I have been a part of in working with Anatol Brodsky and Lloyd Burgess. Anatol has been a source of encouragement and philosophical musings as well as, more importantly, the driving force behind the theoretical development of GLRS. I appreciate the attention paid to my work and the persistent inquiries of "Anything new?". Lloyd is due a tremendous amount of credit for his perseverance and patience with the beginning of this project. Thanks also to Lloyd for his constant interest in the future of this project as well as for his advice on improving the experimental design and for keeping the big picture in mind.

I would also like to thank the past and current members of the Burgess research group for insight and advice: Dr. Leslie Moore, Dr. Dianna Blair, Dr. Ke Hong, Dr. Zhiao Lin, Dr. John Hinshaw, and Dr. Kevin Kuhn. A special thanks to Dave Kuhns for sanity checks and for assembling almost every spectrometer that is currently in use in the lab. Also, Sean Smith deserves credit for taking on the challenge of interferometric GLRS characterization.

Thank you to the Chemometrics group for profitable discussions regarding data analysis. Thanks to Ed, John, and Brian in the machine shop for "rapid" prototyping. Prof. Bruce Darling provided the grating fabrication facilities and Scott Karlsen and Chuck Jung provided the initial technical assistance that resulted in the gratings used in this work. All of the CPAC sponsors who took an interest in this work and provided funding as well as much needed industrial perspective are appreciated. Thank you also to Dr. Patrick Jones for helpful discussions regarding the theoretical basis for GLRS and the patent process. In addition, thank you to Security Pacific Bank for the fellowship that funded half of my time at the University of Washington.

Dr. Walter Emken deserves much credit for encouraging me to go to graduate school and for being a mentor to me, both professionally and personally. I would like to thank my family and friends for also encouraging me to pursue a graduate degree in chemistry. Thank you to Bob Weller for much needed motivation during the final days of the preparation of this dissertation. Most of all, I would like to thank my wife, Gretchen, for undying love, support, and sacrifice during this endeavor.

List of Figures

List of Tables

Chapter 1

Introduction and Rationale

1.1 Introduction

The rationale behind the investigation of Grating Light Reflection Spectroscopy in this dissertation is the need for robust, non-invasive optical methods that may be used in a wide variety of process and laboratory environments. The field of analytical chemistry has long relied on optical techniques for the determination of the nature and concentration of specific analytes in analytical samples as well properties such as diffusion and dynamic effects in an analytical matrix. The application of optical techniques in analytical science requires understanding of both fundamental optical effects as well as the interaction of light with the analyte and sample. A considerable effort has been expended in the application of optical devices in industrial process analysis, where both sampling and optical effects tend to be convoluted with other physical parameters such as temperature, flow characteristics, sample rheology, and inhomogeneities on both micro- and macroscopic scales.

Process and real-time chemical analysis in the ideal would provide chemically relevant information from a process or analyte matrix with minimum perturbation of the sample. Sample dilution, pre-preparation, filtering, and chemical modification to impart selectivity are sample treatment procedures that require invasive sampling or sophisticated sample treatment loops. Established technologies such as fiber optic transmission and reflectance probes and transmission windows allow for the interrogation of a process *in situ*, but the usefulness of such probes depends upon the transmission characteristics of the process, and are again convoluted with other physical perturbations.

Optical chemical sensors to a large part rely on the well-characterized transduction of optical interactions to provide chemical speciation and/or concentration information regarding the analyte. In general, accepted theories exist for most optical phenomena that the analytical chemist then applies to a specific problem, generating data that can be used for calibration or speciation. In this dissertation, a general theory is developed and outlined regarding the optical interaction of light with a binary transmission diffraction grating in contact with a sample. A unique aspect of this work is that the optical theory is new and has been applied directly to analytical matrices with direct relevance to real-time and process analysis.

1.2 History of Diffraction Grating use in Analytical Sensor Technology

The investigation of optical diffraction is a wide and diverse field of study with extensive reviews and scientific papers appearing in the literature addressing fundamental theory and applications. The development of novel optical sensors has to some extent employed diffraction effects for coupling, transduction, and modulation of optical energy. Significant investigations into the theory and applicability of gratings as integrated optic coupling elements have yielded novel sensors in a limited area of research, namely biochemical sensor development, where the optimization of experimental parameters has focused on the monomode waveguiding layer sensitivity to surface properties. Lukosz and Tiefenthaler[1,2] demonstrated the utility of embossed grating couplers on thin TiO_2/SiO_2 spin-coated waveguides by measuring changes in an adsorbed or bound protein layer thickness of .04 nm and refractive index changes of 2.0×10^{-5}. In order to characterize and stabilize the surface sensitivity of the waveguide/grating coupler sensor, Spohn and Siefert[3] investigated the input coupler response to pH, salt concentration and diffusion effects in a flow-injection apparatus.

In complementary experiments, Nellen and Lukosz[4] and Lukosz, et al.[5] described input and output grating couplers, respectively, and the reciprocity between laser coupling directly into a waveguide mode from either the grating itself or the end of the substrate. Each configuration relied on the passivation of the waveguiding layer in regions not containing the grating, and each demonstrated similar surface sensitivity. The exceptional surface sensitivity of these couplers has been theoretically described by Tiefenthaler and Lukosz[6] and the effects of surface adsorption and surface refractive index demonstrated to correlate with experimental investigations. Each embodiment of the grating coupler sensor presented here relies on the change in effective index of the waveguiding layer, which is a

---

[1] Lukosz, W. ; Tiefenthaler, K. *Sensors and Actuators*, **1988**, *15*, 273-284.

[2] Lukosz, W. ; Tiefenthaler, K. *Sensors and Actuators*, **1988**, *15*, 285-295.

[3] Spohn, P.K.; Siefert, M. *Sensors and Actuators*, **1988**, *15*, 309-324.

[4] Nellen, Ph. M.; Lukosz, W. *Sensors and Actuators B*, **1990**, *1*, 592-596.

[5] Lukosz, W.; Nellen, Ph. M.; Stamm, Ch.; Weiss, P. *Sensors and Actuators B*, **1990**, *1*, 585-588.

function of the cover solution index and surface coverage of specific binding analytes, and thus represent a suite of differential refractometer-based instruments. Several other investigators have extended the grating coupler research to include comparisons of grating coupler, surface plasmon resonance spectroscopy (SPRS), and differential interferometry responses to identical immunosensing applications[7] and applications of novel grating coupler configurations[8]. Burgess and Kuhn[9] demonstrated the development of a multimode, grating coupled, ion-diffused thin-film waveguide where the waveguiding layer was exposed to the cover solution and served as a thin film attenuated total reflection (ATR) element operating in the visible region of the spectrum. The refractive index, absorbance, and surface active responses of the sensor were deconvoluted via multivariate statistics applied to the multi-mode output of the sensor, demonstrating the utility of a grating tapped waveguide for non-invasive absorbance spectroscopy. The use of diffraction gratings with other waveguiding optics as sensors has been demonstrated in the wealth of literature describing Bragg gratings incorporated into optical fibers. However, the focus of this dissertation is the investigation of a planar technique, and thus optical waveguide sensors in the cylindrical geometry are outside of the scope of this work.

Diffraction gratings have also been employed as chemical sensors in the absence of waveguiding layers or other coupling phenomena. Rytov and Fabelinskii[10] investigated the idea of using a phase transmission grating as a total internal reflection diffraction grating (TIRDG). Sainov and Tontchev have demonstrated the utility of a TIRDG for the interrogation of optical absorbance[11]. The metal diffraction grating in this case was fabricated on a prism with a period considerably larger than the wavelength of light (Helium Neon laser at 633 nm) and relied on the total internal reflection of the incident beam. Essentially, the effect was described as a phase shift of the incident light resulting in an intensity variation that is correlated back to refractive index and absorbance by calibration. Sainov[12] has also described the application of a TIRDG as a differential laser micro-refractometer containing 2 sample cells and a reference cell. In addition, S. Sainov[13]

---

[6] Tiefenthaler, K.; Lukosz, W. *J. Optical Society of America B*, **1989**, 6 (2), 209-220.

[7] Huber, W.; Barner, R.; Fattinger, Ch.; Hubsher, J.; Koller, H.; Muller, F.; Schlatter, D. *Sensors and Actuators B*, **1992**, *6*, 122-126.

[8] Brandenburg, A.; Gombert, A. *Sensors and Actuators B*, 1993, *17*, 35-40.

[9] Kuhn, K. J.; Burgess, L. W. *Analytical Chemistry*, **1993**, *65* (10), 1390-1398.

[10] Rytov, S.; Fabelynskii, I. *Zh. Eskp. Teor Fiz., SSSR*, **1950**, *20* , 340.

[11] Sainov, S.; Tontchev, D. *Optics and Lasers in Engineering*, **1989**, *10*, 17-26.

[12] Sainov, S. *Applied Optics*, **1992**, *31* (31), 6589-6591.

[13] Sainov, S.; *Sensors and Actuators A*, **1994**, *45*, 1-6.

has extended the theory of TIRDG sensing in the Fraunhofer approximation to obtain satisfactory experimental agreement with respect to the response of the TIRDG to refractive index changes and absorbing liquids.

1.3 Rationale for the Investigation of GLRS

Currently, several reflection based technologies exist for optical investigation of highly absorbing or heterogeneous matrices. Bulk ATR elements working in the infrared portion of the spectrum are routinely used as sensing elements in process analysis. ATR is a reflection method which is based on the transfer of energy across the interface boundary via an evanescent wave which decays into the sample medium with a very short penetration depth (on the order of the wavelength of incident light). ATR is useful for systems that are homogenous and do not form surface fouling layers as the destruction of the sample interface by scattering or a fouling layer presents a significant sampling problem. In addition, the refractive indices of the sample and crystal determine the penetration depth of the evanescent wave in ATR spectroscopy and any changes in the ATR crystal due to temperature shifts or changes in sample bulk composition will yield a modulated absorbance pathlength, making quantitation difficult. This convolution of the refractive index and absorbance characteristics of the ATR response is difficult to correct for in most process analysis systems.

In addition, surface plasmon resonance (SPR) is a technique that is gaining wide popularity for biosensing and bioassays. SPR relies on a resonance condition that exists for coupling optical energy into a charge density wave along the surface of a thin metal/dielectric interface. The SPR coupling condition is very dependent upon the refractive index of the thin interface layer, thus making SPR an attractive platform for the study of surface loading and monolayer antibody-antigen binding. The dependence upon the refractive indices of the interface layers and the special attention needed in fabricating precise metal layers of gold or silver on a dielectric make SPR unattractive for process analysis as robustness and insensitivity to surface layers are needed.

Most optical techniques under development in the literature do not specifically address the pitfalls associated with using reflection methods in systems where convolutions exist. There is a need for a sensor that yields analytical information from systems where refractive index and absorbance are changing simultaneously. In addition, the surface sensitivity associated with most, if not all, current reflection methods point to the need for the development of new spectroscopies that can surmount surface fouling problems. Also, the interrogation of heterogeneous matrices is a ubiquitous problem in process analysis. The use of commercial laser light scattering in process analysis is rife with data interpretation problems due to the convolution of different scattering regimes. In general, the results that are generated by a process analyzer are more dependent upon initial assumptions about the sample than the properties of the sample itself. Thus, there is a need for a robust, reliable, and non-invasive sensor platform that responds in such a way as to minimize the effects of various convolutions that render many reflection techniques difficult or impossible to implement.

1.4 Research Goals and Dissertation Overview

A new optical scattering theory has been developed by Dr. Anatol M. Brodsky which describes optical scattering from a binary metal-dielectric transmission diffraction grating near diffraction thresholds that exist in transmitted light. These transmitted thresholds are connected via the grating with the phases and intensities of reflected diffracted light. Thus, changes in transmitted light modulate the reflected light around these thresholds, enabling GLRS to be used as a reflection-based optical sensor. The scattering parameters that determine the positions of the thresholds are the grating physical parameters and the dielectric function of the medium in contact with the grating. The theoretical development was conducted in conjunction with the experiments presented in this work while the experiments were guided by theoretical considerations.

GLRS is an optical technique that may have applications in process analysis based solely on theoretical predictions of enhanced sensitivity to bulk dielectric changes in sample and deconvolution of competing optical effects that render other reflection methods unusable. The goals of the research are to understand the physical parameters that define the diffraction thresholds, test the theoretical predictions with respect to model chemical and physical systems, and expose the GLRS sensor to systems that preclude the use to transmission methods was well as other reflection techniques.

Significant differences exist between GLRS and SPR, ATR and grating coupler sensors. It is useful to contrast the physical sensing mechanisms of each of these methods in order to understand the uniqueness of GLRS in its current embodiment. ATR relies on the total internal reflection of incident light, and thus requires a prism or grating to coupling light into the optical element above the critical angle. Also, ATR requires that the sample refractive index be lower than the index of the crystal. Thus, there are materials constraints associated with the sample matrix and the ATR element that must be satisfied before ATR may be implemented. Similarly, SPR requires the use of carefully controlled thicknesses and morphology of specific metal layers that meet the SPR coupling criteria. GLRS, however, requires only that a periodic structure exist in the permittivity across an interface. This modulation may be due to alternating metal and dielectric strips, it may be a phase grating, a volume grating, or a free-space grating formed by the interference of two laser beams. The lack of materials constraints in GLRS make it particularly suitable for process analysis in that the grating materials may be chosen for optimal response to a particular sample stream. Furthermore, the planar geometry of the substrate effectively cancels the effects of the substrate on threshold positions and, as will be seen in chapter 6, the GLRS sensor allows for the deconvolution of bulk and surface effects such that the bulk dielectric properties of a matrix may be measured in the presence of an optical fouling layer that would wash out a bulk signal in ATR or SPR.

Optical waveguide phenomena as analytical sensing mechanisms do not function well in the visible region of the spectrum due to high Rayleigh scattering losses in the supporting medium. In addition, sensitivity to analytes that have visible absorption is low unless a high number of reflections are present to increase the pathlength to a viable level. In the work by Kuhn and Burgess discussed above, sufficient sensitivity to a visible absorber was achieved via an ATR element with approximately 3,000 reflections/cm. This necessitated a very thin film ATR element which created difficulties in coupling the incident radiation. The losses associated with the waveguide were overcome by the use of a laser to achieve a high photon density in the waveguide itself allowing for significant loss due to scattering. Most ATR implementations are in the infrared region of the spectrum where the Rayleigh losses are lower and the analyte molar extinction coefficients are higher. In contrast, GLRS functions well in the visible using standard white light illumination and may be extended into the ultraviolet or the infrared simply by changing the grating period or the incident angle. Additionally, as GLRS is a single-hit reflection method, the losses due to Rayleigh scattering are insignificant.

The sensitivity of the GLRS platform to analytes of interest is achieved without a waveguiding medium or other supported surface wave which may be attenuated. ATR and SPR are by nature attenuation schemes, where the loss of incident light by evanescent absorbance or by SPR resonance yields an analytical signal. GLRS is not an attenuation technique, but relies on the loss of coherence between the scattered and incident waves to generate a singularity in reflected light that may result in intensity enhancement or attenuation due to redistribution of optical energy at the grating. The absorbance response is simply a smoothing of the singularity caused by the absorbance characteristics of the sample which reduce the coherence of the forward scattered light relative to the incident beam due to losses in the transmitted, not reflected, beam.

Unlike other reflection methods, GLRS responds orthogonally to refractive index and absorbance, opening the possibility of simultaneous determination of absorbance and refractive index of a given sample. Figure 1.1 displays a representative derivative plot of the GLRS response to changes in ethanol (refractive index modulation) and methylene blue concentration (absorbance modulation). Note that changes in the position of the peak are related to ethanol concentration, and changes in peak height are related to methylene blue concentration. This is the type of data generated by GLRS experiments, where a peak in the derivative has magnitude and position components that allow for the separation of the real and imaginary parts of the dielectric function. As GLRS does not analyze the transmitted light intensity, a wide dynamic range in absorbance is expected from theory, and this shown in the experiments presented in this dissertation. In addition, the refractive index of highly absorbing systems may be measured with accuracy to <0.0001 refractive index units.

The orthogonal response of GLRS to real and imaginary parts of the dielectric function in combination with the reflection-based nature of the sensor allow for interrogation of scattering systems where particle size, distribution, and concentration in a matrix affect the real and imaginary parts effective dielectric function for particles with no inherent absorbance at the incident frequency. As will be seen in chapter 6, GLRS represents a method for particle sizing and distribution analysis that does not require sample dilution or transmission through the sample.

In short, GLRS has been developed experimentally based on theoretical predictions of a universal sensing platform that responds to changes in bulk dielectric properties of the sample. The evaluation of the GLRS sensor response to a range of model chemical and physical systems is the prime objective of this dissertation. The validity of the theory[14] and applications of the technique[15,16] have been demonstrated and accepted in the scientific

---

[14] Anderson, B. B.; Brodsky, A. M.; Burgess, L. W. *Physical Review E*, **1996**, *54* (1).

[15] Anderson, B. B.; Brodsky, A. M.; Burgess, L. W. *Analytical Chemistry*, **1996**, *68* (7), 1081-1088

[16] Anderson, B. B.; Brodsky, A. M.; Burgess, L. W. *Langmuir*, submitted.

literature and also by the issuance of a United States Patent[17]. A discussion of the results will yield a course for the future implementation of GLRS as a generic platform for process analysis.

This dissertation is organized as follows. Chapter 2 will outline the basic GLRS theory as it relates to characterization of the optical phenomena and utilization of GLRS as a process analytical sensor platform. Chapter 3 will detail the fabrication of the diffraction gratings used in these studies and chapter 4 will explain the experimental instrumentation and procedures for GLRS characterization to model physical and chemical systems. Chapter 5 will discuss the results of the initial characterization of GLRS. Chapter 6 will deal with what will be termed "process relevant" samples, where the GLRS response to surface fouling and scattering samples will be probed. Finally, chapter 7 will contain a summary of the main conclusions of this particular research with implications for future work.

---

[17] Anderson, B. B.; Brodsky, A. M.; Burgess, L. W. **March 26, 1996**, U.S. Patent Number 5,502,560.

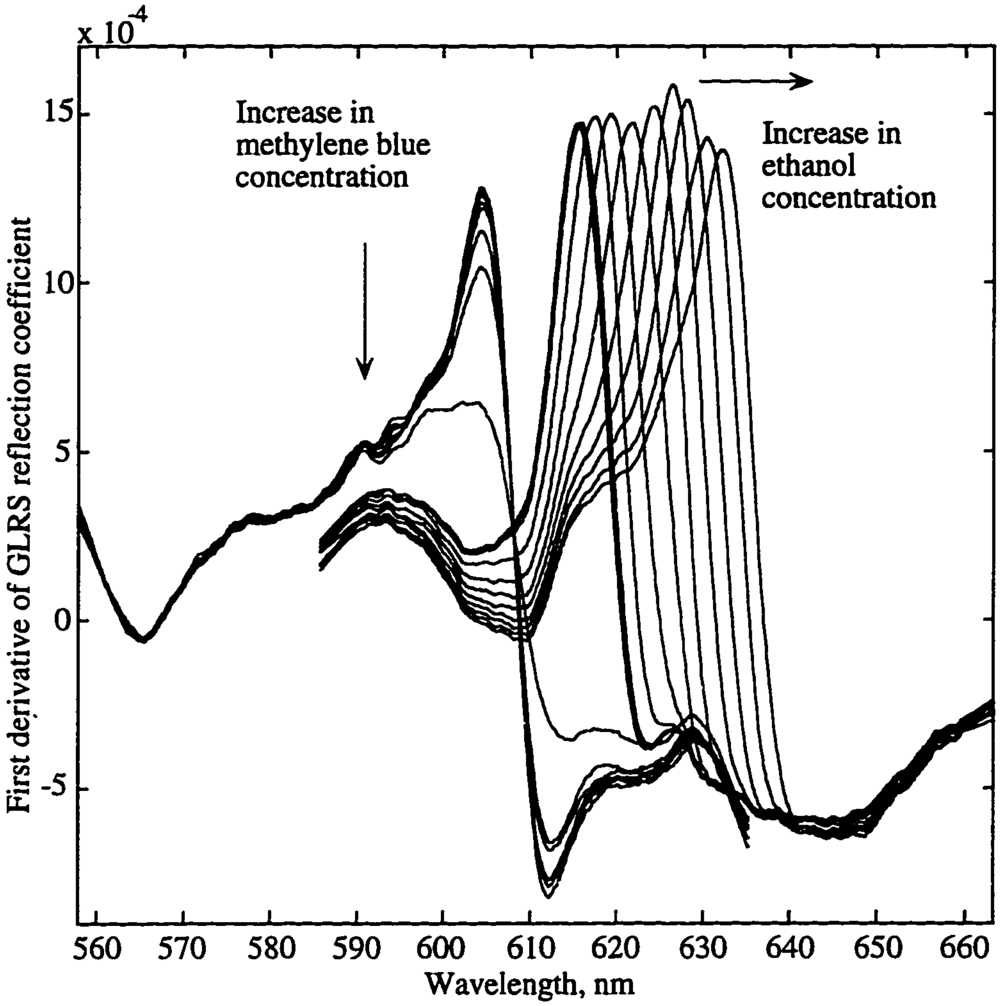

Figure 1.1 Representative GLRS response to model refractive index and absorbance test systems.

Chapter 2

Theory

2.1 Introduction

Optical diffraction by a periodic structure is a complicated wave scattering process that has wide application in physics, engineering, and chemistry. Many detailed papers regarding the analysis of diffraction efficiency and spatial distribution of diffracted beams from a diffraction grating have appeared in the literature. The vast number and the nature of these papers depend upon the scientific or engineering discipline focus and are therefore too numerous to discuss here. Rigorous solutions to the diffraction problem and applications of diffraction gratings have been discussed in a number of reviews and papers[1,2,3]. The formulations of the diffraction problems are dependent upon the assumptions made and the nature of the physical system to be described mathematically. As holographic techniques allow for the fabrication of gratings having volume and surface periodicity in a variety of materials, the application of gratings has extended to chemical sensing in the fields of immunosensing and sample optical properties analysis (refractive index and absorbance). These applications are based on waveguide and diffraction efficiency phenomena as discussed in the previous chapter.

For the application of transmission gratings as sensors, simple models have been developed that appear to provide analytical answers for the case of total internal reflection[4] of the incident beam where the sensor is used to measure relative refractive index in a cover solution in contact with the grating. Previous sensor application of gratings with periodicities on the order of the incident light wavelength have been restricted to waveguide couplers.

Existing light scattering theories attempt to describe the diffraction patterns and intensities in regions where the mathematics are well-behaved. Significant aberrations exist

---

[1] Gaylord, T.; *Proceedings of the IEE*, **1985**, *73* (5), 894-937.

[2] Dushkina, N.; Sainov, S. *J. Modern Optics*, **1992**, *39*.(1), 173-187.

[3] Gupta, M. C.; Peng, S. T. *Applied Optics*, **1993**, *32* (16), 2911-2917.

[4] Sainov, S.; Chernov, B.; Dushkina, N. *Optics and Lasers in Engineering*, **1993**, *18*, 293-305.

where the mathematics produce singular behavior as a result of thresholds in scattered light intensity and phase and previously described theories provide no insight into the exploitation of these thresholds in analytical science. The connection between transmitted and reflected diffraction orders around such thresholds is the basis for the technique discussed in this dissertation. The GLRS theory can be developed as a specific realization of the general threshold theory of multichannel wave scattering[5] and has been developed in conjunction with the experiments presented in this research. However, in this chapter, the general threshold theory of light scattering from a binary diffraction grating is described as it relates to the utilization of the grating for analytical sensing. The full derivation of the reflection coefficients and the related expressions appear in the appendix and in a related article[6]. For the purposes of this dissertation, only the expressions relevant to application of GLRS experimentally are discussed with implications for sensing and predicted responses detailed.

The following description provides a framework with which one may understand the physical processes occurring at the grating. The oversimplification in describing the diffraction effects is a result of the lack of an adequate physical picture for wave phenomena interactions on the scale of the wavelength of light. Geometrical optics may apply in the form of a ray trace on a macro scale, but in terms of momentum conservation, time inversion symmetry, and redistribution of optical energy at the grating, wave mechanics must be applied and Maxwell's equations must be solved with appropriate boundary conditions. However, it is more informative to describe the physical basis for GLRS and describe the general results of GLRS theory as they pertain to applying GLRS as an analytical chemical sensor.

2.2 Theoretical Considerations in the Application of GLRS

2.2.1 Optical Diffraction

Optical diffraction occurs when an incident light beam strikes a structure with a periodic variation in permittivity. Diffraction is the name given to the process where light waves constructively and destructively interfere at the region of periodicity, producing phase and intensity shifts upon reflection and transmission relative to the incident beam.

---

[5] Newton, R. *Scattering Theory of Waves and Particles*, McGraw-Hill; New York, 1966, Chapter 17.

[6] Anderson, B. B.; Brodsky, A. M.; Burgess, L. W. *Physical Review E*, **1996**, *54* (1).

The existence of regions of light and dark in the far field is a result of interference effects at the grating surface (near-field). For a binary metal/dielectric diffraction grating, with some finite transmission coefficient, reflected and transmitted diffraction orders exist that are dependent upon the bulk properties of the internal and external media in contact with the grating region.

Figure 2.1 displays schematically diffraction from a transmission grating where the sample medium is in contact with the grating structure and the thickness of diffraction grating and interface region is assumed to be much smaller than the wavelength of light. The grating is formed on a dielectric substrate from a thin metal layer (resulting in alternating metal and dielectric strips) and is assumed to be strictly periodic with one period present and grating lines oriented normal to the incidence plane.

2.2.2 Dielectric Function and Complex Refractive Index

In figure 2.1, the external medium, substrate, and sample matrix are characterized by frequency dependent dielectric functions $\varepsilon^{(o)}(\omega)$, $\varepsilon^{(1)}(\omega)$, and $\varepsilon^{(2)}(\omega)$ respectively. The superscripts on the wavevector or dielectric function symbols in the following equations refer to the medium , as designated above by (0), (1), (2). Subscripts in the equations refer to the Cartesian coordinate component, with 1 being the normal to the incident plane.

The dielectric function is a complex quantity related to the optical properties more easily measured experimentally: index of refraction and absorbance. The complex index of refraction, n_c, is defined by:

$$n_c = n - i \cdot k \tag{2.1a}$$

where the subscript c denotes complex quantity and k is the extinction coefficient. The real part of the refractive index, n, is inversely proportional to a light wave's phase velocity in a medium. Thus, a lower refractive index results in a higher velocity of propagation. The imaginary part of the refractive index, k, is related to the loss in a medium, where the wave amplitude decays exponentially as the product kx, where x is the distance traveled by the wave in the medium.

The dielectric function, or permittivity, is simply the square of the index of refraction:

$$\varepsilon = n_c^2 \qquad (2.1b)$$

The complex dielectric may be separated into real and imaginary components:

$$\varepsilon = n^2 - 2i(nk) + k^2,$$

therefore

$$\begin{aligned} \mathrm{Re}(\varepsilon) &= n^2 + k^2, \text{ and} \\ \mathrm{Im}(\varepsilon) &= 2nk. \end{aligned} \qquad (2.2)$$

In addition, the imaginary part of the dielectric may be related to the optical absorbance by:

$$\mathrm{Im}(\varepsilon) = \frac{c}{\omega} \cdot 2.303\sqrt{\mathrm{Re}(\varepsilon)} \cdot A \qquad (2.3)$$

where A is the one centimeter path transmission absorbance, c is the speed of light in vacuum, and ω is the frequency of light. For small absorbances, $k << n$, k may be neglected when calculating the index of refraction.

The real and imaginary components of the complex index of refraction are interrelated by the Kramers-Kronig relations[7] where the dispersion relationship between refractive index and wavelength (frequency) is influenced by the optical absorption spectrum. Normal material dispersion is the slight monotonic decrease in refractive index of an optical medium with wavelength of light. The term anomalous dispersion is used to describe deviations from normal material dispersion around a strong absorption band, where the index of refraction is lower than the normal value on the short wavelength side of the band and higher on the long wavelength side of the absorption band. At the absorption peak, the index of refraction is exactly the normal value as the index progresses smoothly from low to high values relative to the normal value as shown in figure 2.2.

---

[7] Pankove, J. *Optical Processes in Semiconductors*, Dover, New York, 1971, Chapter 4.

2.2.3 Polarization

An electromagnetic wave is comprised of electric and magnetic field components that have vector quantities normal to the direction of propagation. The term polarization refers to the orientation of the magnetic or electric vector of a propagating electromagnetic wave. In optics, the orientation of the electric vector determines the plane of polarization. When a beam strikes an interface, the electric vector may be decomposed into components perpendicular and parallel to the plane of incidence, which is the plane defined by the incident, reflected and transmitted beams. For a plane electromagnetic wave with the electric vector oriented such that it lies parallel to the plane of incidence, this is said to be p-polarized light, or transverse magnetic (TM), as the magnetic vector is transverse to the plane of incidence. Likewise, a wave with electric vector oriented perpendicular to the plane of incidence is said to be s-polarized, or transverse electric (TE), as the electric vector is oriented transverse to the plane of incidence.

There are many conventions and notation systems that describe the state of polarization of a beam, namely Stokes parameters, Jones calculus, etc. For the purposes of this dissertation, the polarization of the incident light is assumed to be s or p. The experiments reflect this in that all experiments were performed using plane polarized white light in either the s- or p-polarization state.

2.2.5 Thresholds in Diffracted Light

As a beam of light is incident upon the grating through the substrate, it refracts through the substrate and strikes the grating in contact with the sample matrix. The emergence of reflected and transmitted beams are a result of diffraction from the grating structure at the substrate/sample interface. For specific experimental conditions there exists a threshold where a transmitted diffraction order is transformed from a traveling wave in the sample medium to an evanescent wave. An expression that describes the position of this threshold is derived based on where the normal component of a scattered wave vector in the sample medium is equal to zero:

$$\delta_{m_{cr}} = \mathrm{Re}\left(\varepsilon^{(2)}(\omega)\right) - \left(\sin\theta + \frac{m_{cr}\lambda}{a}\right)^2 = 0 \qquad \lambda = \frac{2\pi c}{\omega} \tag{2.4}$$

where $\text{Re}\left(\varepsilon^{(2)}(\omega)\right)$ is the real part of the frequency dependent dielectric function (related to refractive index), θ is the incident angle, a is the grating period where the grating lines are perpendicular to the plane of incidence, λ is the free-space wavelength of light, and m_{tr} is the transmitted diffraction order undergoing the transformation.

When (2.4) is equal to zero, the critical order is defined at a particular frequency, for a constant θ and grating period, that corresponds to a specific value of $\text{Re}\left(\varepsilon^{(2)}(\omega)\right)$. As the normal component of the wavevector of the threshold order is equal to zero when (2.4) is zero, the direction of propagation for that frequency is along the interface. There is a possibility that surface waves will be excited along the interface, and the metal dielectric combination is chosen such that the probability of surface wave generation is minimized.

The threshold behavior occurs when there is a passing off of any diffracted order between reflection and transmission or when the propagation constant transitions from a real to imaginary value. GLRS takes advantage of the dependence of the threshold position on the dielectric function of the matrix in contact with the grating. Figure 2.3 displays the wavelength dependence of $\delta_{m_{tr}}$ on $\text{Re}\left(\varepsilon^{(2)}(\omega)\right)$ for a constant angle of incidence and grating period and the zero crossing of each curve is defined as the threshold wavelength.

2.2.6 Singularities in Reflected Light

The presence of the threshold in transmitted diffracted light allows for the utilization of the reflected light as an analytical signal. When the critical, or threshold, order is present, at the threshold wavelength there are features in the reflected diffraction orders that are directly related to the dielectric function of the sample medium. The power that was propagating in the narrow frequency interval is no longer allowed to propagate in either direction normal to the interface, and as no surface wave is present, the optical energy is redistributed to all other diffraction orders based on energy and momentum conservation laws at the grating/sample interface. At the threshold frequency (wavelength), the reflected orders exhibit singular behavior, with a drastic change in reflected intensity and phase

When the absorbance characteristics of the medium in contact with the grating are such that $\text{Im}\left(\varepsilon^{(2)}(\omega)\right) < \text{Re}\left(\varepsilon^{(2)}(\omega)\right)$ these specific singularities in the behavior of reflected light at $\delta_{m_{tr}}=0$ are observed. The positions of such singularities, $\delta_{m_{tr}}=0$, as well as the functional dependence on $\delta_{m_{tr}}$ in the interval where $\delta_{m_{tr}}$ is small, when $\left|\delta_{m_{tr}}\right| << 1$, are dependent only on the bulk properties of the matrix at distances from the sample-grating interface on the order of a few wavelengths.

The physical origin of such singularities can be interpreted as follows. The intensity $I(\bar{r}, m)$ of the light corresponding to the mth diffraction order in medium (2) is proportional to:

$$I(\bar{r},m) \sim \left(\bar{E}^{(2)}(\bar{r},m)\cdot\bar{E}^{(2)*}(\bar{r},m)\right) \qquad \text{for } r_1 > 0 \tag{2.5}$$

where $\bar{r}$ is the direction of propagation vector, $\bar{E}^{(2)}(\bar{r},m)$ is the complex amplitude of the mth diffracted transmitted beam, and the asterisk denotes the complex conjugate of the quantity $\bar{E}^{(2)}(\bar{r},m)$. According to the solutions for Maxwell's equations for propagation through a medium, the intensity of the critical order is proportional to:

$$I(\bar{r},m)_{cr} \sim \left(e^{i\sqrt{\delta_m}\cdot r_1}\cdot e^{-i\sqrt{\delta_m}\cdot r_1}\right) \sim \text{ constant for } \delta_{m_{cr}} \geq 0 \tag{2.6a}$$

and

$$I(\bar{r},m)_{cr} \sim \left(e^{i\sqrt{|\delta_m|}\cdot r_1}\cdot e^{-i\sqrt{|\delta_m|}\cdot r_1}\right) \sim e^{-2\sqrt{|\delta_m|}\cdot r_1} \text{ for } \delta_{m_{cr}} < 0 \tag{2.6b}$$

where r_1 is the distance from the interface normal to the interface. According to (2.6a) and (2.6b), the dependence of transmitted light on the distance from the surface has been drastically changed near the point $\delta_{m_{cr}}=0$. At $\delta_{m_{cr}}=0$, the intensity of the critical, or threshold, order remains constant at infinite distance but begins to diminish with further decline of $\delta_{m_{cr}}$. In real systems this distance becomes finite even for $\delta_{m_{cr}}=0$ since the imaginary part of the dielectric constant is always nonzero ($\mathrm{Im}\,\varepsilon^{(2)}(\omega)>0$), though negligible in transparent media. Due to this finite penetration depth of the optical energy in the critical order around the threshold, the singular behavior in reflected light intensity and phase is determined at $\delta_{m_{cr}}=0$ by the bulk complex dielectric properties of the sample matrix.

2.2.7 GLRS Reflection Coefficients

When a plane wave strikes a boundary between two materials having different indices of refraction, a portion of the optical energy is transmitted and a portion is reflected based on the angle of incidence, wavelength, refractive index contrast between materials, and polarization of the beam relative to the incidence plane. For a non-periodic structure, the reflection and transmission characteristics of the boundary can be described by Fresnel coefficients of transmission and reflection[8]. These may be expressed in terms of incident angle, refraction angle, and refractive index directly for transmission (see figure 2.4):

$$t_p^F = \frac{2n^{(1)}\cos\theta_i}{n^{(2)}\cos\theta_i + n^{(1)}\cos\theta_t},$$

$$t_s^F = \frac{2n^{(1)}\cos\theta_i}{n^{(1)}\cos\theta_i + n^{(2)}\cos\theta_t}, \tag{2.7a}$$

and reflection:

$$r_p^F = \frac{n^{(2)}\cos\theta_i - n^{(1)}\cos\theta_t}{n^{(2)}\cos\theta_i + n^{(1)}\cos\theta_t},$$

$$r_s^F = \frac{n^{(1)}\cos\theta_i - n^{(2)}\cos\theta_t}{n^{(1)}\cos\theta_i + n^{(2)}\cos\theta_t}, \tag{2.7b}$$

where the F in the superscript denotes Fresnel coefficients, subscripts s and p denote polarization state of the incident beam, and $n^{(1,2)}$ are the indices of refraction of the respective media where (1) is the incident medium and (2) is the transmission medium. The subscripts i and t in the angle designation refer to the incident angle and angle of propagation for the transmitted beam with respect to a plane normal to the interface.

Note that the wavelength dependence of the reflection coefficient is inherent in the material dispersion characteristics for both media. As normal dispersion dominates for most optical materials in the visible region of the spectrum, one would expect no sharp features in the reflection spectrum of such a two-layer system. However, when the reflection coefficients are calculated for the same system with a grating present in the interface region, there is a sharp dependence of the reflection coefficient on wavelength. Using the threshold approximation rather than perturbation theory to calculate the reflected light's behavior at the threshold yields expressions that may be used analytically. This

---

[8] Born, M.; Wolf, E. *Principles of Optics*, 5th ed., Pergamon Press, Oxford, 1975, 40-41.

singular behavior can be described by the following expressions for reflection coefficients $R^{(s,p)}(m)$, for s- and p- polarized light, TE and TM respectively:

$$\begin{aligned} R^{(s,p)}(m) &\cong C_1^{(s,p)}(m) + C_2^{(s,p)}(m)\sqrt{\frac{1}{2}\left(\sqrt{\delta_m^2 + \left(\operatorname{Im}\varepsilon^{(2)}\right)^2} - \delta_m\right)} + \\ &\quad C_3^{(s,p)}(m)\sqrt{\frac{1}{2}\left(\sqrt{\delta_m^2 + \left(\operatorname{Im}\varepsilon^{(2)}\right)^2} + \delta_m\right)} \\ &\underset{\text{as } \operatorname{Im}\varepsilon^{(2)} \to 0}{=} C_1^{(s,p)}(m) + \begin{cases} C_2^{(s,p)}(m)\sqrt{|\delta_m|} & \text{for } \delta_m \le 0 \\ C_3^{(s,p)}(m)\sqrt{|\delta_m|} & \text{for } \delta_m > 0 \end{cases} \end{aligned} \tag{2.8}$$

where coefficients $C_{1,2,3}^{(s,p)}(m)$ are proportional to Fresnel's reflection and transmission coefficients. These expressions are correct for the parameter interval where δ_m lies near zero. Near the thresholds, the real coefficients $C_{1,2,3}^{(s,p)}(m)$ are essentially constant. For $m \neq 0$, these coefficients are proportional to the difference in dielectric constant between the grating lines and the substrate material. Depending on the signs of the coefficients $C_{1,2,3}^{(s,p)}(m)$ one of the behaviors of the reflection coefficients presented in figure 2.5 will be present. Notice that the GLRS reflection coefficients contain components related to the real and imaginary parts of the dielectric of the sample in contact with the matrix.

According to (2.8), the singularity should be present in all reflected diffracted orders and in all polarizations of reflected light. This allows for the optical interrogation of a sample by the collection of the broad band specular reflection from the grating/sample interface and analysis of the intensity distribution via a standard dispersive or non-dispersive spectrometer. Experimentally it is difficult to measure the reflection coefficients directly and therefore it is more useful to calculate a relative reflection coefficient:

$$R_{rel}^{(s,p)} = \frac{R^{(s,p)}}{\tilde{R}^{(s,p)}} \tag{2.9}$$

where $\tilde{R}^{(s,p)}$ is a representative spectrum of the source intensity distribution. Furthermore, the relative reflection coefficient is difficult to use to obtain analytical information and it is more useful to calculate a derivative of the relative reflection coefficient where the dependence of the derivative of the relative reflection coefficient on δ_{m_α} is given by:

$$\frac{dR^{(s,p)}}{d\delta_m} = \frac{1}{4\sqrt{\delta_m^2 + \mathrm{Im}\,\varepsilon^{(2)}}}\left(C_3^{(s,p)}\sqrt{\sqrt{\delta_m^2 + \mathrm{Im}\,\varepsilon^{(2)}} + \delta_m^2} - C_2^{(s,p)}\sqrt{\sqrt{\delta_m^2 + \mathrm{Im}\,\varepsilon^{(2)}} - \delta_m^2}\right) \tag{2.10}$$

for $\delta_m \sim 0$

This derivative contains a peak at the threshold wavelength where shifts in the peak position are related to real refractive index of the sample and the height of the peak is related to the absorbance characteristics of the sample according to figure 2.6.

2.3 Predicted GLRS Experimental Response

2.3.1 Predicted Real Refractive Index Response

When the derivative of the relative reflection coefficient is calculated for a specific set of experimental parameters, the peak in the spectrum will yield directly sample refractive index according to (2.4). A change to higher refractive index in the sample will yield a shift to higher wavelength for constant grating period and incident angle. The sensitivity of the peak wavelength shift to changes in refractive index may be calculated directly from (2.4) by taking the derivative when (2.4) is equal to zero:

$$\frac{dn^{(2)}}{d\lambda} = \frac{m}{a} \tag{2.11}$$

This value is 0.0012 index units/nm for m=+1 and a = 829 nm, which are the experimental parameters representative of the experiments performed in this work. It is clear that to increase sensitivity using a dispersive instrument the lowest transmitted diffraction order and the largest grating period must be utilized for a given instrumental resolution. This is correct for all diffraction orders except for m = 0 as total internal reflection of the incident beam is not possible due to the planar nature of the substrate. For a refractive index range of 1.000 to 2.000 which covers gaseous and most liquid systems, the singularity wavelength shift would be from 353 nm to 1183 nm for a 35° incident angle and grating period of 829 nm. This wide dynamic range is attainable with no moving parts and the range may be shifted by simply changing the grating period or incident angle.

The predicted sensitivity takes into account only the wavelength shift of the singularity and neglects the information content away from the singularity that is related to the Fresnel reflection and transmission coefficients. As the position of the threshold is polarization independent, the singularity should be present in all incident polarizations where the shape of the reflection coefficient is dependent upon polarization but not the position in wavelength space. As will be discussed in the results portion of this dissertation, statistical methods may be used to increase the sensitivity of the technique by taking into account all variance in the signal that is correlated to sample properties and building a calibration model based on that variance.

In addition, as the singularity position allows for the calculation of refractive index at the wavelength of the singularity, the material dispersion curve of a sample may be measured by scanning the incident angle to produce singularities at various wavelengths and using those threshold positions to calculate the index at each wavelength.

2.3.2 Predicted Absorbance Response

The GLRS sensor is predicted to have absorbance sensitivity based on the dependence of the reflection coefficients $R^{(s,p)}(m)$ on the imaginary part of the dielectric function $\mathrm{Im}\,\varepsilon^{(2)}(\omega)$. The reflection coefficients $R^{(s,p)}(m)$ are relatively independent of the sample absorbance characteristics in regions away from the threshold region if

$$\mathrm{Im}\,\varepsilon^{(2)}(\omega) << \mathrm{Re}\,\varepsilon^{(2)}(\omega) \qquad (2.12).$$

However, in the vicinity of the thresholds, where $\delta_{m_\sigma} \sim 0$, the influence of $\mathrm{Im}\,\varepsilon^{(2)}(\omega)$ is substantial and determines the smoothing of the singular behavior of $R^{(s,p)}(m)$ where two terms on the right hand side of (2.8) cancel each other. In particular, at the exact value δ_{m_σ} =0, the reflection coefficient is independent of the real part of the dielectric and a square root dependence of the reflection coefficient on $\mathrm{Im}\,\varepsilon^{(2)}(\omega)$ exists:

$$R^{(s,p)}(m) = C_1^{(s,p)}(m) + \sqrt{2}\left(C_2^{(s,p)}(m) + C_3^{(s,p)}(m)\right) \cdot \sqrt{\left|\mathrm{Im}\,\varepsilon^{(2)}\right|} \qquad (2.13)$$

As mentioned above, the derivative of the reflection coefficient is used to experimentally determine the relative contributions of the real and imaginary parts of the dielectric. Thus, the peak at $\delta_{m_\sigma} = 0$ will have a height dependence on the imaginary part of the dielectric where larger values of $\operatorname{Im} \varepsilon^{(2)}(\omega)$, which correspond to higher absorbance values, yield a decline in the derivative peak height.

The sensitivity of the relative reflection coefficients to absorbance is related to the relative real dielectric difference between the substrate and sample matrix and as the index is closely matched the sensitivity to absorbance will increase. The dynamic range is predicted to be large in comparison to transmission based measurements of absorbance. These parameters have been explored empirically but not theoretically in any rigorous manner as the general nature of the reflection coefficient derivation leaves much numerical modeling to be done that is outside the scope of this dissertation.

2.3.3 Sensitivity to Surface Fouling and Surface Active Species

An important consequence of applying threshold theory in the analysis of singular behavior in reflected light is that the positions of singularities $\delta_{m_\sigma}=0$ and the functional dependence of the reflection coefficients on δ_{m_σ} are dependent only on the bulk properties of the solution at distances from the solution-grating interface on the order of a few wavelengths. This may be understood in that the threshold approximation does not solve for the electric field amplitudes or propagation in the grating region at the threshold, but only connects bulk values of the wave vectors in terms of a scattering matrix in regions away from the interface, yielding singular behavior that is independent of the grating/sample interface region. This means that this position, as well as the reflection coefficient's and phase shift's behavior in the vicinity of this position, in contrast to other properties of reflected light, will remain stable and unaffected by changing surface properties at relatively large distances less than $\frac{\lambda}{\operatorname{Im} \varepsilon^{(2)}}$. The overall reflectivity and behavior of reflected light will be affected in regions away from $\delta_{m_\sigma}=0$, and this allows for the deconvolution of bulk and surface effects.

2.3.4 Substrate Temperature Effects

The planar nature of the GLRS substrate system removes the contribution of the substrate dielectric from the threshold position. This is due to the fact that the components of the wave vectors parallel to the interface are conserved upon refraction, diffraction at the grating, and subsequent propagation back through the substrate. This is why the angle of incidence used in the threshold equation is that of the air/substrate interface and not the substrate/grating interface. As the substrate optical parameters do not appear in (2.4), it is reasonable to assume that physical changes in the substrate such as temperature and thickness (expansion) as well as isotropic changes in refractive index due to temperature should not affect the position of the threshold and therefore the position of the singularity in reflected light.

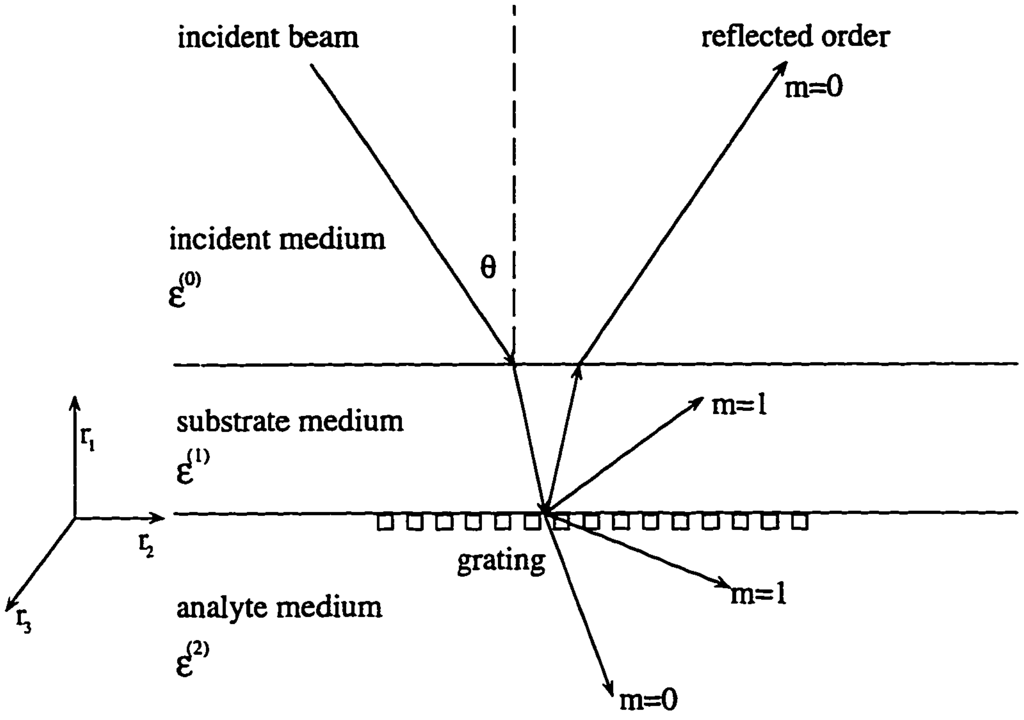

Figure 2.1 GLRS schematic.

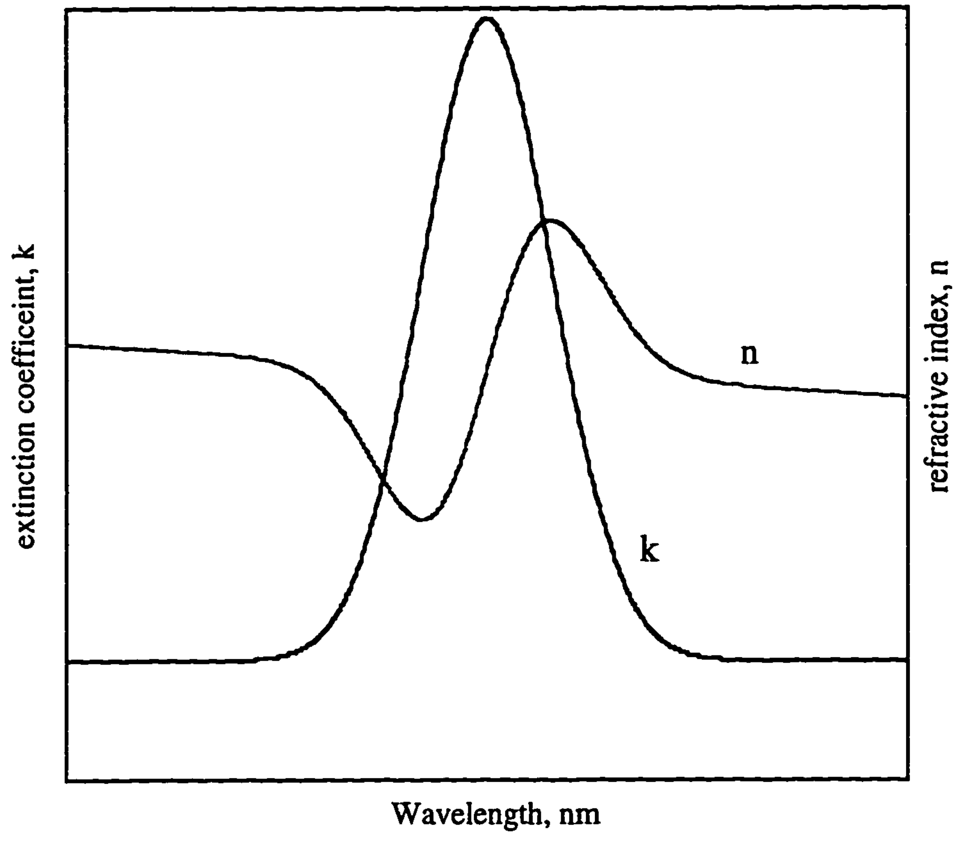

Figure 2.2 Representration of Kramers' Kronig relations between the real and imaginary parts of the refractive index, n and k. Values are scaled similarly in order to show the relationship qualitatively.

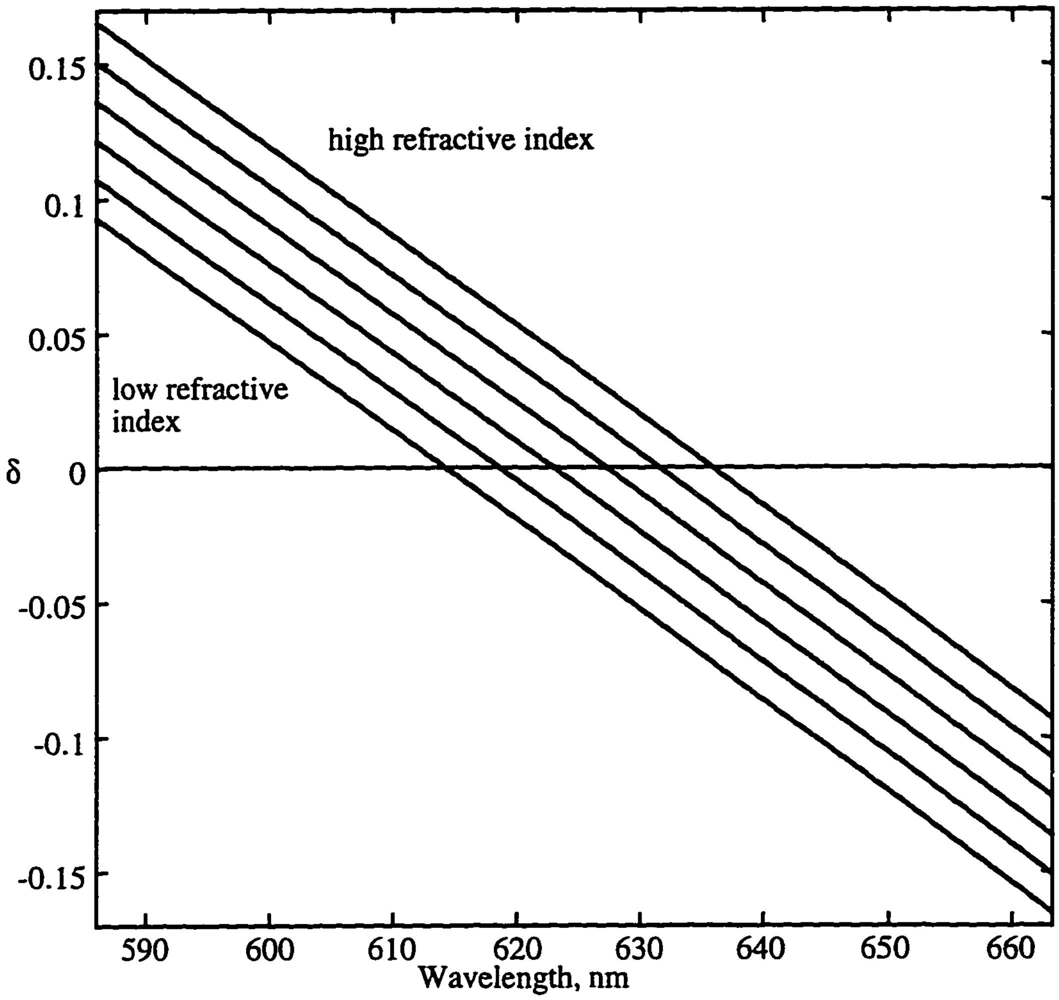

Figure 2.3 GLRS dependence of δ on ethanol concentration. Zero crossing is wavelength of threshold, where (2.4) is equal to zero.

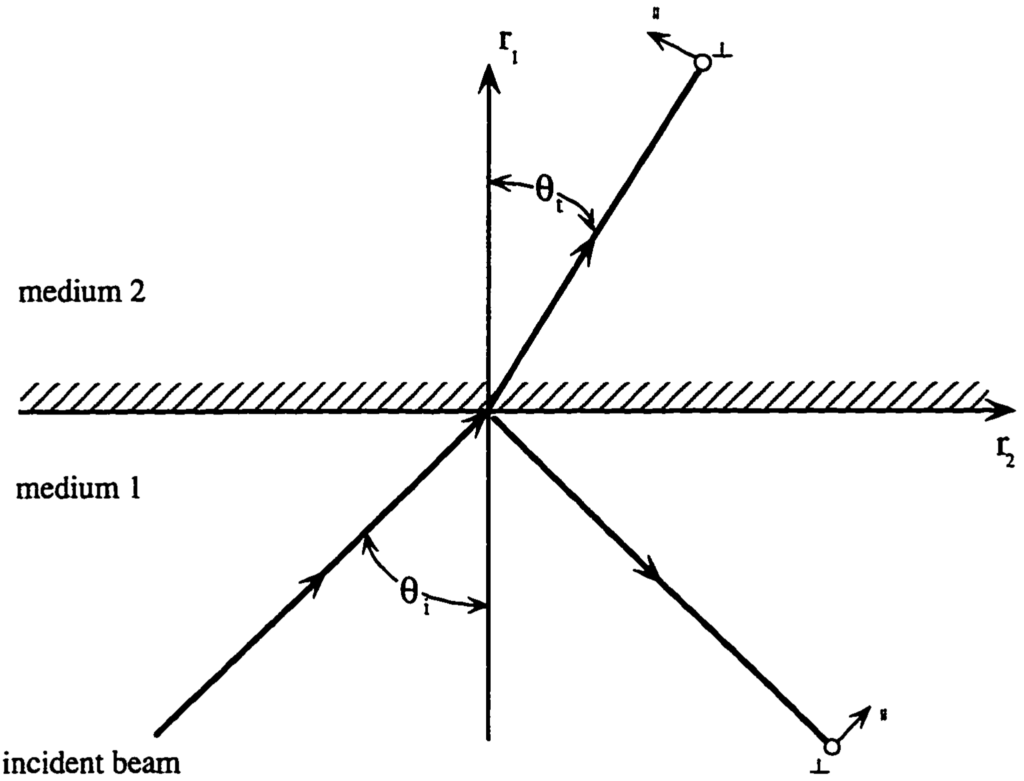

Figure 2.4 Schematic of reflection from a plane interface, where perpendicular and parallel components of the electric vector are shown relative to the incident plane. The angles of incidence and transmission are related by Snell's law:

$$n_1\sin(\theta_i) = n_2\sin(\theta_t)$$

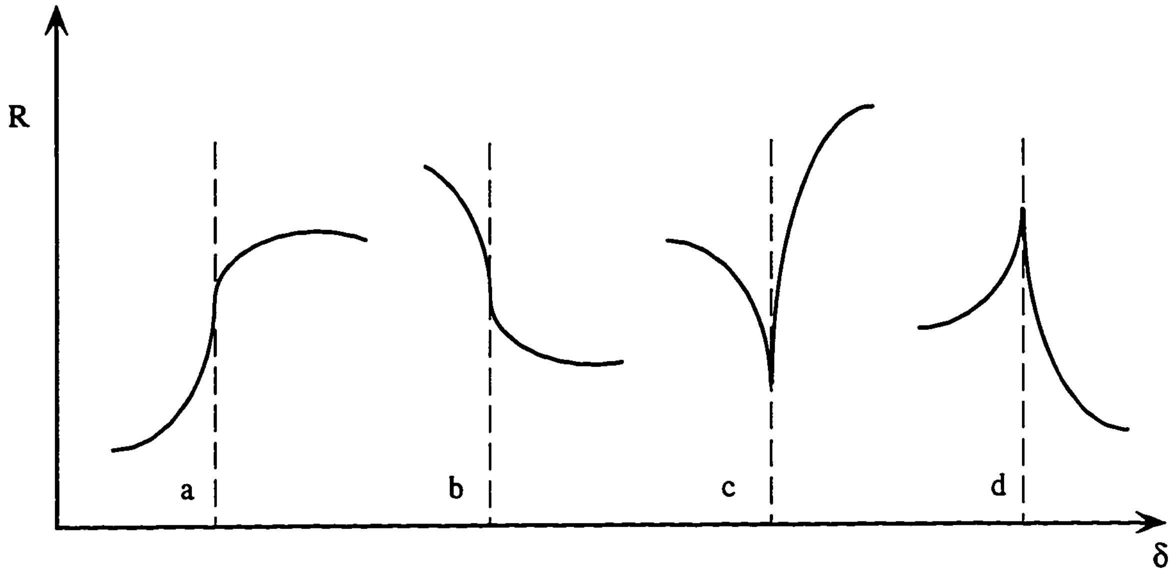

Figure 2.5 General types of behavior of solutions to equation (2.8) for the case of Im(ε(2))=0. The position of the threshold at $\delta = 0$ for each curve is denoted by the dashed line. In the case of Im(ε(2))≠0 the behavior near the singularities according to (2.8) would be rounded. a) $C_2 - C_3$, b) $-C_2 + C_3$, c) $C_2 + C_3$, d) $-C_2 - C_3$.

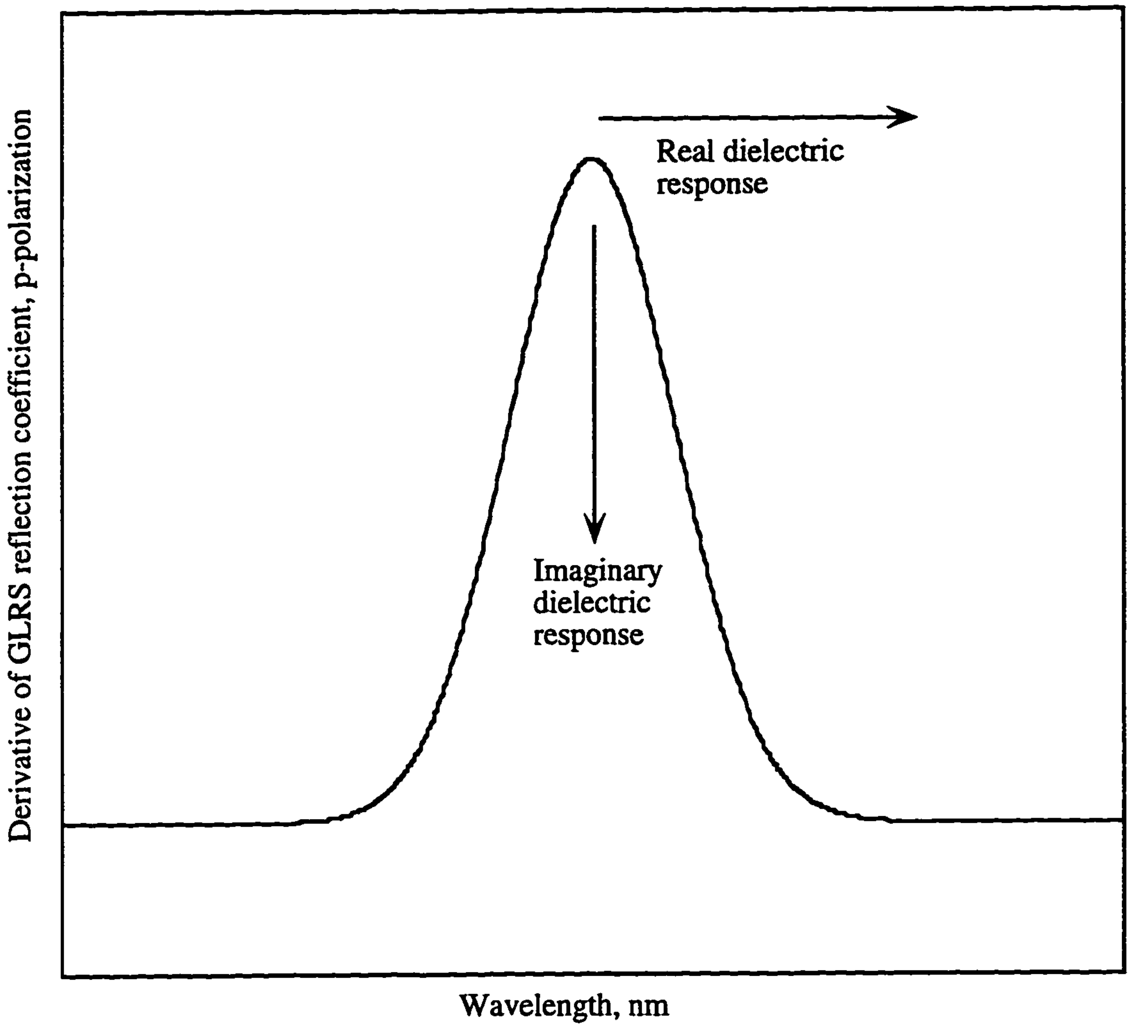

Figure 2.6 Predicted orthogonal response of GLRS derivative peak to changes in dielectric properties of a sample in contact with the grating.

Chapter 3

Diffraction Grating Fabrication and Characterization

3.1 Introduction

The GLRS technique is reliant upon a strictly periodic grating that is formed on a planar substrate. In the course of fabricating waveguide grating couplers, the procedures to fabricate gratings were developed and optimized based on procedures in the literature[1] and internal documents[2]. Significant effort was expended to fabricate reproducible gratings in glass and chrome. Due to the nature of the facilities used in the Electrical Engineering Department at the University of Washington, the procedure needed to be optimized to some extent for the conditions on the day of the experiment. The optical system underwent extensive re-engineering in order to reduce aberrations in the gratings, and a cleaning procedure that worked one day did not work the next. Thus, the actual fabrication procedure presented here is the best case scenario that produced the gratings used in this work, and subsequent fabrication of gratings in the future will be highly dependent upon facilities and chemical agents employed.

3.2 Optical System

All optics were mounted on an air-floated vibration isolation table (Newport, Inc.) using a rail and post system. The optical system used to fabricate diffraction gratings is shown schematically in figure 3.1. An argon ion laser (Spectra Physics) was used for photoresist exposure operating at 458 nm and in the TEM_{00} mode. An internal etalon allowed for selection of the appropriate wavelength and single mode operation which is essential for holographic applications. The incident beam was spatial filtered using a Newport, Inc. spatial filter assembly with a 40x objective lens and 5 micron pinhole

---

[1] Mai, X.; Moshrefzadeh, R.; Gibson, U.; Stegeman, G.; Seaton, C. *Applied Optics,* **1995**, *24* (19), 3155-3161.

[2] Karlsen, S. *Procedure for Fabrication of Diffraction Gratings*, Dept. of Electrical Engineering Class Report, 1992.

aperture. This expanded beam was collimated via a 200 mm focal length singlet lens (Melles Griot) and reduced using an iris aperture to a spot size of 1 cm. The beam was incident on a sample holder/mirror assembly to form a single wavefront division Lloyd's mirror configuration where the first surface mirror (Melles Griot) was mounted to a sliding mount that held the mirror in a 90° orientation relative to the substrate. The substrate holder was mounted onto a translation/rotation stage assembly that allowed translational adjustment in the yz plane (light is incident along x axis) and angular resolution of .083°.

3.3 Fabrication Procedure

3/16 inch thick by one inch diameter fused silica disks were chosen as substrates for their mechanical durability and good adhesion properties with a chromium metal layer. Initially, target chrome layers of 1000 angstrom thickness were sputter coated in house using a DC planar magnetron (Denton Vacuum). However, uniformity and reproducibility were poor due to the small target size and the need to rotate the samples through the target region. Thus, a fabrication facility was located (Nanofilm, Inc.) that cleaned and coated each substrate with a standard photolithographic chromium mask layer of 1000 angstrom thickness that was optimized chemically for relatively fast etching with a commercial etchant (Microchrome CEP-200). The cleaned and coated substrates were placed onto a vacuum chuck spin coating stage in a class 100 clean room. A positive photoresist solution was prepared using a 1:2 dilution of Shipley 1400-17 photoresist with Shipley Type A thinner. The resist was applied via a filter syringe, spin-coated at 5000 rpm for 30 seconds, and baked in a vacuum oven at 90° C for 15 minutes to drive off excess solvent.

The substrates were then transported in a light tight box to the exposure laboratory. Each substrate was mounted onto the holder such that the photoresist is exposed in a semicircle pattern in the center of the substrate. The angle was chosen based on the period desired and is dependent upon the refractive index of the photoresist and the wavelength of incident light for a given target period. Table 3.1 summarizes the dependence of grating period on incident angle for the experimental conditions during fabrication. Using the regression between incident angle and period, the incident angle α was set at 16° to yield a nominal 830 nm grating period. The laser power was measured prior to the exposure and adjusted so that the 1 cm diameter beam yielded a power of 1.00 milliwatts on a silicon diode photodetector power meter (Newport, Inc.). Each substrate was then exposed for 18 seconds and replaced into the box for transport back to the clean room.

After exposure, each substrate was developed in a bath of Shipley Microposit Developer for 10 seconds, rinsed in deionized water, dried on the spinner, and then wet chemically etched. The development was stopped when the entire grating region produced uniform relatively intense diffraction that peaked when the optimum development time had been reached. The etching was monitored by viewing the back of the substrate as the semicircle pattern appeared; etching was stopped when the diffraction efficiency was visually determined to be at its peak. The substrate was rinsed again with deionized water, placed on the spinner, and rinsed with acetone to remove the unexposed resist. Optimal etching time was determined to be 56 seconds for this particular fabrication run.

3.4 Grating Characterization

The interference pattern produced in the photoresist upon exposure is a sinusoid traversing the entire resist thickness to the substrate/resist interface. According to published methods[3] on in-situ monitoring of photoresist development in grating fabrication the development process produces a rectified sinusoid in the resist as the developer removes resist to the substrate (see figure 3.2). This pattern is transferred to the chrome layer as the etching process is isotropic and exposed chrome strips will be etched first, followed by the areas masked by the photoresist strips due to undercutting and removal of resist by the aqueous etchant solution. It is possible to remove the chrome entirely if the etching process is allowed to progress, and the degree of undercutting of the resist will affect the duty cycle of the grating.

The characterization of the grating proceeded based on the grating period determination only. As GLRS threshold positions are not dependent upon grating duty cycle and periodic line shape, the accurate determination of the period was the primary focus. The grating substrate was mounted onto a rotation stage with 0.083° angular resolution where the incident angles are determined such that the first and second order diffraction angles are identical to the corresponding incident angles. The diffraction peaks were found to be well-defined, with little divergence, indicating that the grating was strictly periodic with one period present. According to the classical grating equation relating incident and diffracted angles this condition allows for the determination of the grating period:

---

[3] Nakano, Y.; Tada, K. *Optics Letters*, **1988**, *13* (1), 7-9.

$$\sin\theta = \sin\phi + \frac{m\lambda}{a} \tag{3.1}$$

for $\theta = \phi$:

$$a = \frac{m\lambda}{2\sin\theta} \tag{3.2}$$

where m is the diffraction order, a is the period, θ and ϕ are the incident and diffracted angles, respectively, and λ is the free space wavelength of incident light. A helium neon laser (λ=632.991 nm) was used to determine the grating period for substrates 1and 4, which were used for all experiments, and the period was found to be 829.1 ± 1.1 nm and 829.4 ± 0.76 nm respectively. These values were used for all subsequent prediction calculations.

The grating periodicity, modulation depth, and duty cycle may be described by a series of Fourier coefficients (see appendix). In order to take full advantage of a numerical model to rigorously calculate the reflection coefficients, the Fourier coefficients must be known, and these may be derived from scattering angle and intensity data and also by microscopic imaging analysis. Figure 3.3 displays an atomic force microscope (AFM) TIFF image of a 830 nm period chrome grating on a glass microscope slide that was produced in the first run of successful gratings and is representative of the diffraction gratings produced for this study as it was produced under nominally the same conditions. The AFM image shows that the grating is periodic in one direction and that the modulation depth and duty cycle are clearly seen. AFM images were not obtained for the gratings used in experiments presented in this dissertation as the gratings would need to be destroyed to perform the analysis. Due to the unavailability of the fabrication facilities after the final fabrication run, destructive evaluation of the gratings was removed as an option. In view of this discussion, a full numerical analysis of a model grating system should be the first step in devising schemes for grating fabrication where the gratings are optimized for application in GLRS.

Table 3.1 Dependence of grating period *a* on incident angle for a laser wavelength of 458 nm and a photoresist refractive index of 1.668 [see footnote 2].

Incident angle, degrees	Grating period, nanometers
1	13,118.5
2	6,560.3
3	4,374.6
4	3,282.1
5	2,226.9
6	2,190.3
7	1,878.7
8	1,645.1
10	1,318.5
13	1,017.8
16	830.6
20	669.4
23	586.0
27	504.3
30	457.9

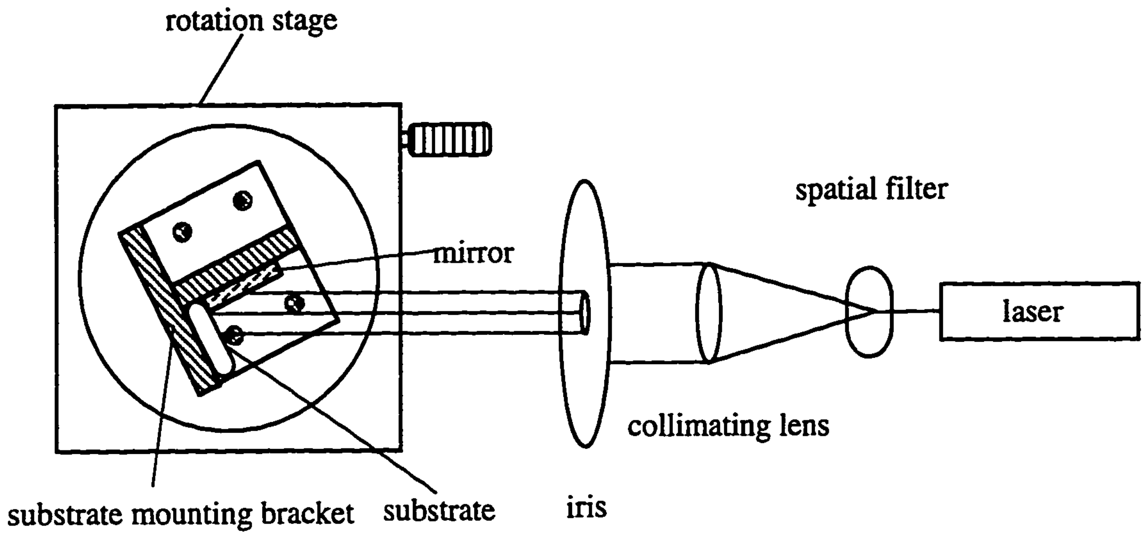

Figure 3.1 Optical schematic for the fabrication of diffraction gratings on fused silica substrates. The incident angle is between the normal to the substrate and the collimated beam.

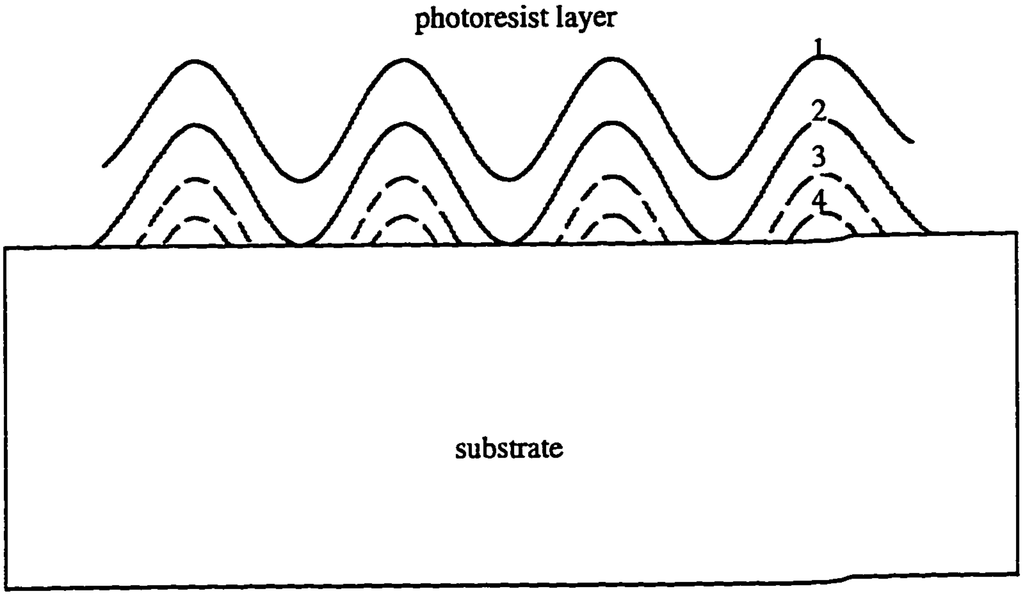

Figure 3.2 Stages in the development of photoresist layer for grating fabrication. 1) onset of development, the resist is removed in a sinusoid pattern, 2-3) subsequent stages of development where the rectified sinusoid is formed, 4) final development stage, where the duty cycle is approximately 50%.

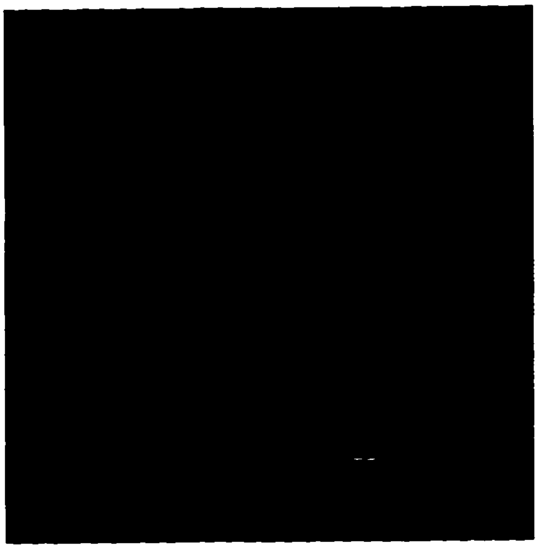

Figure 3.3 TIFF image of a ~830 nm period chrome grating holographically fabricated via Lloyd's mirror configuration on glass. The image was acquired using an atomic force microscope and the light bands correspond to chrome lines. Inclusions in the image are due to less than perfect cleaning procedures before fabrication.

Chapter 4

Experimental: GLRS Characterization

4.1 Introduction

The development of new optical theory requires the experimenter to fully characterize the physics of the phenomenon and then utilize the information to refine and develop further theory. In the discipline of analytical chemistry, the value of a technique is not in its inherent physical significance but in the ability to use the technique to gather analytical information in a way that is unique or solves a pressing problem. The GLRS technique provides a means for measuring the bulk dielectric properties of a sample in contact with the grating using reflected light. The experiments performed here utilize collimated white light illumination of the grating from the backside of the substrate, isolating the optical train from the sample matrix. As such, design considerations for sampling and analytical optical evaluation outweighed the desire to model the phenomenon and thus the experiments progressed in a direction that looked to the utility of the technique for process analysis. In the beginning of the project, the focus was on the characterization of the stability of the optical design and the exposure of the technique to neat solution samples of varying refractive index and absorbance characteristics. In addition, the exploration of the experimental parameter space as well as environmental perturbations was carried out in order to more fully understand the capabilities of the sensing mechanism and the optical embodiment presented here.

4.2 Instrumentation

4.2.1 Input Optical System

All optics were mounted via post and rail system on an air floated optical bench (Newport, Inc.). The optical system is shown schematically in figure 4.1. An R.Wolf 32 V. tungsten halogen medical diagnostic lamp was coupled via a non-coherent optical fiber bundle and condenser lens system into the 220 micrometer core fiber to increase coupling efficiency and reduce intensity fluctuations due to source filament vibration. The diverging output of the fiber was collimated via an achromat lens assembly in order to remove chromatic aberrations arising from material dispersion in the lens. The purpose for coupling the incident light to the collimation system via a fiber is that the degree of collimation of the incident beam affects the sharpness of the singularity. The degree of collimation is inversely related to the size of the spot from which the beam diverges before entering the lens. Therefore, the use of a fiber end as the input image allows for the beam to achieve a high degree of collimation relative to imaging a source filament.

The incident beam size was minimized to a 2 mm spot using an iris aperture to reduce off-axis light incident on the grating. This collimated beam was polarized s or p (TE or TM) using a Glan-Taylor polarizing cube with an extinction ratio of $1{:}10^5$. This polarizer was fixed into a post-mounted rotation stage that allowed for 2° incremental changes in polarization angle. The incident s- and p-polarization states were determined by setting the rotation stage at an incident angle that corresponds to the Brewster, or polarizing, angle for an air/silica interface, in this case approximately 56°, where the reflected intensity is polarized upon reflection to the s-polarization state. The polarizer was rotated to the minimum in reflected intensity from the air-substrate interface, thus achieving p-polarization. The entire collimation and polarization assembly was mounted on a translation stage to allow for alignment of the incident beam with the center of the grating region.

4.2.2 Collection of Zeroth Order Diffraction

The reference beam was collected via a ball lens coupled fiber optic at the output of the collimator, removing a portion of the poorly collimated light at the limit of the clear aperture of the lens but not affecting the light incident on the sensor. The reference beam served not only as an overall intensity reference but also as a representation of the source intensity distribution and instrument function.

The grating/substrate interface specular reflection (zeroth order diffraction peak) was collected as the sample beam. The incident angle and substrate thickness allowed for spatial separation of the first surface and grating/substrate interface reflections, thus removing the influence of the first surface reflection overlap. These two collection fibers were coupled into a McPherson 218 monochromator (retrofitted with imaging optics) with a 300 groove/mm holographic grating via singlet aperture matching optics and adjustable slit as a stacked pair. These dispersed images were vertically resolved onto a Santa Barbara Instruments Group (SGIB) ST-6 CCD (750 pixels wide) camera placed in the image plane of the monochromator, producing two discrete spectra simultaneously with a magnification factor of approximately 8x. In addition, a Princeton Instruments LN/CCD (575 pixels wide) camera was used for additional experiments along with a 600 groove/mm ruled grating blazed at 300 nm when the SBIG CCD array was no longer available. Each detection system was controlled by a 486 PC using supplied spectroscopy software. Data were collected as 10-20 scan averages and stored in ASCII format for further data processing.

The resolution of the spectrometer was 1.9 nm for an entrance slit width of 500 microns. The reciprocal linear dispersion (RLD) was dependent upon the grating used in the spectrometer, but the wavelength registration along the pixel axis remained at ~.100 nm/pixel for each system due to the differences in RLD for each grating and differences in pixel sizes for each detector. The wavelength range of the spectrometer could be selected via a scanning dial and the wavelength reproducibility of the system is dependent upon the accuracy with which the selection dial could be reset. It was found that with care a wavelength reproducibility of 0.1 nm could be achieved.

4.2.3 Collection of First Order Diffraction

The coupling optics were identical to the optics described above for the collection of the first order reflection where the grating acted as the dispersing element. The $m = -1$ reflected diffraction order was imaged on a 512 element fiber-optic window photodiode array (EG&G Reticon). The image was spectrally calibrated via bandpass filters and exhibited a linear dependence of wavelength on diode number, with approximately 120 nm imaged on the array. The beam diameter was approximately 2 mm, and the diffracted light was focused on the detector with a 63 mm focal length achromatic lens. The array images were collected on a PC-XT as 5 scan averages and stored as ASCII data files for data processing.

4.2.4 Substrate Mounting System

4.2.4.1 Staging

The substrate was mounted in a vertical format on a dual axis rotation stage (figure 4.2). The incident angle was selected via a high resolution rotation stage (Newport, Inc.) with 0.083° absolute accuracy. To allow for the measurement of relative angular displacement, the stage was fitted with a micrometer and vernier with .0125° accuracy. A second rotation stage with .5° accuracy was fitted orthogonal to this rotation axis and allowed for adjustment of the azimuthal angle (the angle between the direction of grating periodicity and the incident plane). This azimuthal angle was adjusted to 0° and locked for all experiments by aligning all reflected diffracted orders along the incident plane prior to each experiment. The sample holder assembly was fitted to the dual axis rotation stage via a bracket assembly such that the axis of rotation was located at the grating/sample interface. This minimized translational adjustments when the incident angle was adjusted.

4.2.4.2 Static Cell

A sandwich type cell was fabricated using aluminum for the face plate and back plate as shown in figure 4.3. A circular substrate material was chosen for this work because the stresses induced by sandwiching the substrate into a holder are more evenly distributed along the edges than for a rectangular substrate. A bevel was formed in the front of the face plate along with a counterbore in the back of the plate to accept the diameter of the substrate and an O-ring to relieve stress on the substrate. The back plate contained two counterbores: one to accept the grating side of the substrate and the other to allow for a Teflon sample cell to be placed in contact with the grating (see figure 4.4) and sealed with a Parafilm Gasket. The Teflon was chosen for chemical inertness and non-wetting properties in aqueous systems and a top channel facilitated easy introduction and removal of sample. The volume of the Teflon cell was approximately 2 mL. The two halves of the substrate holder were pressure fitted via four 1/4-28 Allen head bolts that were tightened symmetrically to reduce lateral stresses in the substrate.

4.2.4.3 Flow Cell

In initial experiments it was necessary to use a flow cell assembly to add and remove sample form the cell. Figure 4.5 details schematically the flow cell assembly. The same beveled front plate was used as above. A back plate fashioned out of PEEK (polyetheretherketone) with a 1 inch by 3/16 inch counterbore to accept the grating substrate and gasket and two 1/8" though holes to accept sample inlet and outlet 1/8" o.d. Teflon tubing. The gasket was fashioned out of optically clear silicone (Petrarch Systems) and contained a 3/4" by 1/4" oval flow cell. The gasket was aligned such that the sample flowed in from the bottom and out through the top of the cell in order to increase flushing efficiency and remove entrained air bubbles. The sandwich cell was again pressure fitted with the front O-ring and Allen head bolts and mounted to the stage. Sample was introduced to the cell via a peristaltic pump under computer control to allow for reproducible flushing.

4.2.5 Temperature Programming

A thermoelectric temperature control unit was fabricated at the electronics shop. The control device allowed for setpoint control and readout to .1° C. Temperature feedback was facilitated through the use of an RTD transducer that was placed within 1 cm of the controlled device. The capacitors and voltage ramp settings inside the electronics box were optimized for use with the following system. A peltier thermoelectric device (Melcor, 1.7 V) was mounted between the face plate of the flow cell and the dielectric side of the grating substrate according to figure 4.6. The thermoelectric cooler (TEC) was a center hole type with a clear aperture of 14 mm. The face plate was constructed of aluminum with a 14 mm clear aperture bevel in order to allow for optimal thermal coupling to the TEC device. A flow cell gasket was fashioned as above out of optically clear silicone and placed in contact with the grating side of the substrate. Contained in this gasket was an RTD temperature transducer for TEC setpoint control and the range for temperature control was 17°C to 45°C (see figure 4.6). The RTD was thermally coupled to the grating side of the substrate via thermal grease and was not in contact with sample in the flow cell. Sample was introduced into the cell via a peristaltic pump using Teflon 0.5 mm i.d. tubing through the back of the flow cell back plate, thus placing the sample in contact with the grating.

4.3 Experimental Procedure

For all experiments presented in this section, the SBIG CCD camera was used to collect the spectral data using a 2 s. integration time and collecting 20 scans of the dual channel spectral image. In addition, as the p-polarization produced the highest intensity reflection off of the grating due to the low intensity first surface reflection, this polarization was used for all experiments except the polarization modulation and s-polarization ethanol solution experiments. In addition, the azimuthal angle was set to 0° for all experiments.

4.3.1 Dependence of the GLRS Thresholds on Incident Polarization State

GLRS is a reflection method and thus is polarization dependent. The cleaned substrate (#4) was placed in the static cell with deionized water in the cell with the incident angle set to 36.17° and the initial polarization state set to p. The polarization state was then incremented toward the s state in 10° increments using the Glan-Taylor polarizer rotation stage. In addition, the s+45° polarization angle was used to test the midpoint polarization angle.

4.3.2 Dependence of the GLRS Thresholds on Incident Angle

In order to test the incident angle dependence of the GLRS signal, data were acquired at incremental incident angles using the high resolution vernier to determine the relative angular displacement. The substrate (#4) was mounted in the sample holder and the initial incident angle set at 36.08. As the coupling angle was changed, the specular reflection collection optics were moved in order to collect the specular reflection. Two individual experiments were run with deionized water in the cell, the first with monochromator dial set to 800 and the incident angles chosen from 36.08° to 33.53° in .319° increments. Then the monochromator dial was then set at 765, with incident angles ranging from 36.25° to 38.42° in approximately .5° increments, the angles being chosen for placement of the singularity in wavelength space. Table 4.1 details the incident angles used in this experiment.

4.3.3 Refractive Index Response

The ethanol:water system was used to characterize the GLRS sensor response to changes in the real dielectric value of the matrix in contact with the grating. This system was chosen because of the chemical similarity between ethanol and water and the wide refractive index range that may be attained due to the high miscibility of ethanol in water. The refractive index will be the quantity measured and compared experimentally as the reference method measures refractive index via the critical angle method.

Deionized water was obtained via a laboratory purification system and used to prepare subsequent sample solutions. A total of nine ethanol solutions were prepared volumetrically in deionized water from absolute ethanol (McCormick, lot #CO35l2) in concentrations ranging from 1% to 40% in 5% EtOH increments. An Abbe refractometer (Bausch and Lomb) coupled to a temperature controlled bath was used to measure reference refractive index values for all solutions. The error in measurement of index by this means is ±0.0001 index units. The sodium D-line refractive indices were measured and normal dispersion values $\left(\frac{dn}{d\lambda}\right)$ calculated for the solutions at 4 different temperatures: 25°C, 30°C, 35°C, and 40°C. Figure 4.7 displays the dependence of the refractive index on ethanol concentration at 25° C. The dispersions were calculated using the compensator prism settings. An equation was derived from linear regressions of the wavelength, temperature, and ethanol concentration dependent refractive indices that was used to generate reference values of refractive index for comparison with GLRS determined bulk index values for the solutions:

$$
\begin{aligned}
& n(\lambda,T,C) = 1.33203 + \left(5.47\times10^{-4}\cdot C\right) + \frac{dn}{d\lambda} + \frac{dn}{dT} \\
& \frac{dn}{d\lambda} = \left[-3.73\times10^{-5} - 1.815\times10^{-8}\cdot C\right]\cdot\left[\lambda - 589.3\right] \qquad (4.1) \\
& \frac{dn}{dT} = \left[-1.11\times10^{-4} - 4.14\times10^{-6}\cdot C\right]\cdot\left[T - 25\right]
\end{aligned}
$$

where λ is in nanometers, C is in %EtOH by volume, and T is in degrees Celsius.

The cleaned substrate (#4) was mounted in the substrate/Teflon sample holder static cell assembly, and the incident angle set to 36.17° using the rough vernier. The polarization was initially set to p-polarization. Sample was introduced into the Teflon sample holder via a clean disposable glass pipette. The reproducibility of the sensor and optical system was tested using 3 replicate runs of 4 ethanol solutions in 10% ethanol increments run in random order. Between samples the cell was rinsed and aspirated with copious amounts of deionized water and then rinsed twice with sample. 20 scans of the array taken for each sample at a 2 second integration time, as well as a 20 scan dark current measurement that was subtracted manually at the data analysis stage. Identical experimental technique was used to run the nine ethanol test samples as well as two water samples, again run in random order. The polarizer was then rotated to achieve s-polarization and the ethanol samples run again in random order.

The collection of the zeroth order reflected diffraction peak facilitated easy implementation of GLRS with standard spectroscopic systems. The collection of the first order diffraction proceeded under similar experimental conditions but with a different substrate and will be presented as comparison data in the results section in order to show the similarity and symmetry between diffraction orders collected.

4.3.4 Absorbance Response

Methylene blue was chosen as a model absorbance system because the predicted wide dynamic range and difficulty in measuring systems with low absorbance using the current GLRS system required highly absorbing systems to test GLRS. Methylene blue has high solubility in water relative to other dye systems and therefore allows for concentrated dye solutions to be prepared. Methylene blue (Aldrich, 86, 124-3) was recrystallized from 1:1 EtOH:water and six solutions were prepared from the dried crystals. The concentrations of the methylene blue solutions are given in table 4.2. As methylene blue is a cation in its basic form and glass and fused silica act as cation exchange surfaces, a 0.1 M nitric acid rinse solution was prepared from 69%-71% nitric acid (Baker Analyzed, lot # D01047) in deionized water. This served to reduce the cation affinity of the glass surface and regenerate a fresh surface after each sample. The solutions were stored in Nalgene bottles for approximately 1-3 days before use, and each sample was transferred to the sample cell using a clean, disposable Pasteur pipette.

It was necessary to understand the nature of the absorbance characteristics of the dye system at high concentration as the linear relationship of absorbance with concentration breaks down at high concentration. The absorbances of the least concentrated five methylene blue samples were measured on a Hewlett Packard 8540A UV/Vis diode array spectrometer in a thin cell fashioned from two fused silica plates and a thin Teflon spacer.

The thin cell thickness was calculated by comparing the absorbance of the 9.992×10^{-6} M solution thin cell absorbance with the corresponding 1 cm path absorbance. The thin cell was measured to be 290 microns thick. The sixth solution, .005 M, was placed between two silica plates with no spacer as the optical density did not allow for transmission measurements using the 290 micron cell. The molar extinction coefficients were calculated for each solution as a function of wavelength according to Beer's Law:

$$\varepsilon_m = \frac{A}{bc} \tag{4.2}$$

where A is the absorbance corresponding to the pathlength b, and c is the concentration of dye in moles per liter.

These molar extinction coefficients are shown in figure 4.8 for all dye solutions. Notice that the extinction coefficient is dependent upon concentration as seen by the absorbance maximum shifts from around 660 nm to 610 nm. This is due to a monomer-dimer equilibrium that is perturbed at higher concentrations for methylene blue[1,2]. The relative stability of the extinction coefficient with concentration at around 610 nm allowed for the pathlength to be approximated for the .005 M solution from the extinction coefficients calculated from the five other absorbance measurements. Knowing these pathlength allows for the equivalent 1 cm. pathlength absorbances for each solution. The absorbance maxima positions and amplitudes for equivalent 1 cm path measurements are tabulated in table 4.2. The change in absorbance characteristics with concentration will allow for the anomalous dispersion properties of the dye system to be probed, yielding information about non-linearities in absorbance.

The cleaned substrate (#4) was mounted in the substrate holder/static sample cell assembly. Three angles of incidence were chosen in order to test the GLRS absorbance response in different regions of anomalous dispersion. The azimuthal angle was set to 0° and the incident polarization set to p-polarization. The system was initially set to an incident angle of 37.11° to produce a singularity around 605 nm. This would correspond to a region on the absorbance peak at high concentration. The monochromator dial was set to 765, and all other spectrometer parameters identical to the ethanol experiments.

Sample was introduced into the Teflon sample holder via a clean disposable glass pipette. The cell was cleaned with deionized water, and then rinsed with .1 M nitric acid, rinsed again with water, and then the first sample (water) was run. Subsequent samples

---

[1] Rabinowitch, E.; Epstein, L. F. *J. American Chemical Society*, **1941**, *63*, 69.

were run, again with nitric acid rinse, water rinse, and 2 volumes of sample rinse before final addition of sample. The second angle of incidence was chosen to be 34.98° with the monochromator at 800, yielding a singularity at 630 nm, corresponding to a mid point between absorbance peaks. Finally the incident angle was set at 30.620° with the monochromator set at 850, yielding a singularity around 683 nm, a region on the high wavelength side of both absorbance peaks. The methylene blue samples were run in random order at the three different angles of incidence and three spectrometer settings.

4.3.5 Simultaneous Refractive Index and Absorbance Response

A sample set comprising a range of methylene blue and ethanol concentrations was prepared volumetrically from the solutions used in the absorbance experiments and fresh ethanol solutions in order to test the orthogonality of the real and imaginary dielectric responses. The sample set is detailed in table 4.3. The cleaned substrate (#1) was placed into the sample cell (static, Teflon) and the incident angle set at 36.83° to produce a singularity around 605 nm for deionized water. The polarization state was set to p and the set of 20 samples run in random order with nitric acid rinses and 2 volume flushes between samples.

4.3.6 Dependence of the GLRS Thresholds on Temperature

The cleaned substrate (#1) was mounted in the temperature controlled sandwich flow cell and the incident angle set to 36.5° where the polarization was set to p-polarization. Deionized water was pumped into the cell and then stopped. The temperature of the TEC was initially set to 25°C. The temperature transducer was in contact with the grating side of the substrate but not with the liquid in the cell, and the cell was allowed to stabilize for 5 minutes although the TEC reached the setpoint in about 15 seconds. The temperature was set from 20° C to 40° C in 2.5° increments and then ramped back down to 25° C using the same increments to test for hysteresis in the system. 20 scans of the array were taken for each subsequent temperature setting, with stabilization achieved between each run.

---

[2] Lewis, G. N. et. al *J. American Chemical Society*, **1943**, *65*, 1150.

4.4 Data Analysis

4.4.1 Univariate Data Analysis

Each sample generated two 20x750 matrices of sample and reference data that were averaged to obtain 1x750 vectors of sample and corresponding reference spectra which were then dark corrected. The high frequency components of the signals which were unrelated to sample variations required the application of an 11 point 0th order Savitsky-Golay smoothing filter to each reference spectrum while the sample spectra were unaltered except for dark correction. Relative reflection spectra were calculated for each run by calculating the ratio of each sample spectrum to its corresponding reference spectrum.

Due to the intensity variations in the angle and polarization measurements associated with translation of the coupling optics and polarization state, each sample scan was normalized to a ccd pixel well away from modulation, where the intensity should be very similar from run to run. The ratio of each sample spectrum to its corresponding reference spectrum was calculated to obtain the relative reflection coefficient for each sample. The derivatives were calculated using a 71 point Savitsky-Golay first derivative filter, with the peak maxima located for comparison with theoretical predictions corrected for temperature and dispersion. The peak positions, grating period, and angle of incidence were used with equation (2.4) to generate a predicted absolute index at the wavelength of the singularity. Reference refractive index values were obtained from Abbe′ refractometer measurements and used for statistical comparison with the refractive index values from GLRS experimental data. This type of analysis was used to generate bias and prediction statistics for the univariate data analysis techniques: the bias calculated as the mean of the residuals for each experiment and the precision calculated as the rms error with the bias subtracted for refractive indices predicted from equation (2.4). In addition, the peak height variations were calculated for the absorbance sample set in order to compare with theory.

The data analysis techniques described above rely on the use of a smoothing derivative filter in the case of the univariate data analysis, as a derivative is calculated from experimental data for comparison with theory. As comparison with theory was the prime objective, a large smoothing filter was justified in calculating each derivative, as the general shape of the sample and reference data allowed for the removal of high frequency components without significant distortion of the lineshape.

In order to understand the distortion of the data that occurs under data processing variations, a test set of a single water run was analyzed using different filter lengths. Figure 4.9 shows the effect of first derivative filter length on derivative peak height and position. A 71 point first derivative filter was chosen because it represented a balance between distortion of the peak position and the suppression of harmonics in the derivative. These harmonics are the result of utilizing a small filter size relative to the size of the features in the data, which are in this case fairly large. The full width at half maximum (FWHM), on average, for the derivative peaks for all experiments excepting the temperature experiments, was approximately 7 nm. A 7 nm wide feature in the data would correspond to a width of 68 pixels. Thus, a 71 point derivative filter would not significantly distort the feature.

4.4.2 Multivariate Analysis: Partial Least Squares Calibration

The GLRS reflection coefficients are in a format that allows for multivariate statistical analysis. Information contained in the wavelengths away from the threshold wavelength is related to the reflectivity of the sample grating interface and thus may be used in addition to modulations due to GLRS thresholds to predict sample concentration and other properties with appropriate data analysis. In general, the systems studied using GLRS generate data that is indicative of a single component changing. However, the information content is multivariate in that the single component variance produces position and “intensity” variations that may be modeled using multivariate statistics.

A technique known as Partial Least Squares (PLS) calibration allows for the calibration of non-linear systems with respect to single analyte parameters by attempting to describe the variance in n-dimensional space that is correlated with an input matrix of reference values. From this decomposition, a regression vector is constructed that is multiplied by each input sample vector to generate a prediction. This prediction is checked via a leave one out cross validation procedure such that the model is constructed on the entire sample set with error statistics generated that describe the prediction error as a root mean square error of cross validation (RMSECV) statistic. This statistic gives a measure of the strength of the model in that it may be compared with the error associated with the method used to generate reference values. This technique was used in order to test the feasibility of applying multivariate statistics for calibration of the GLRS response to refractive index and absorbance.

Table 4.1 Incident angles used in GLRS angle variation experiments.

Incident angle, degrees
38.42
37.98
37.55
37.11
36.68
36.25
36.09
35.76
35.44
35.12
34.80
34.48
34.16
33.85
33.53

Table 4.2 Methylene blue in water, calculated equivalent 1 centimeter pathlength absorbances at each maxima.

Sample number	Methylene blue concentration moles/L	Absorbance maximum #1, nm	Absorbance at maximum #1, A.U.	Absorbance maximum #2, nm	Absorbance at maximum #2, A.U.
1	5.127×10^{-3}	599.2	244.14	661.7	106.35
2	1.022×10^{-3}	605.2	43.83	661.2	28.30
3	4.996×10^{-4}	606.7	24.30	661.3	17.42
4	1.000×10^{-4}	610.3	4.620	661.3	5.422
5	4.996×10^{-5}	610.7	2.464	661.8	3.300
6	1.000×10^{-5}	615.3	.459	662.3	.8345

Table 4.3 Ethanol and methylene blue mixtures sample set.

Sample number	Ethanol concentration, % vol/vol	Methylene blue concentration, moles/L
1	0	0
2	0	8.493×10^{-5}
3	0	4.246×10^{-4}
4	0	8.687×10^{-4}
5	0	4.358×10^{-3}
6	5	0
7	5	8.493×10^{-5}
8	5	4.246×10^{-4}
9	5	8.687×10^{-4}
10	5	4.358×10^{-3}
11	10	0
12	10	8.493×10^{-5}
13	10	4.246×10^{-4}
14	10	8.687×10^{-4}
15	10	4.358×10^{-3}
16	15	0
17	15	8.493×10^{-5}
18	15	4.246×10^{-4}
19	15	8.687×10^{-4}
20	15	4.358×10^{-3}

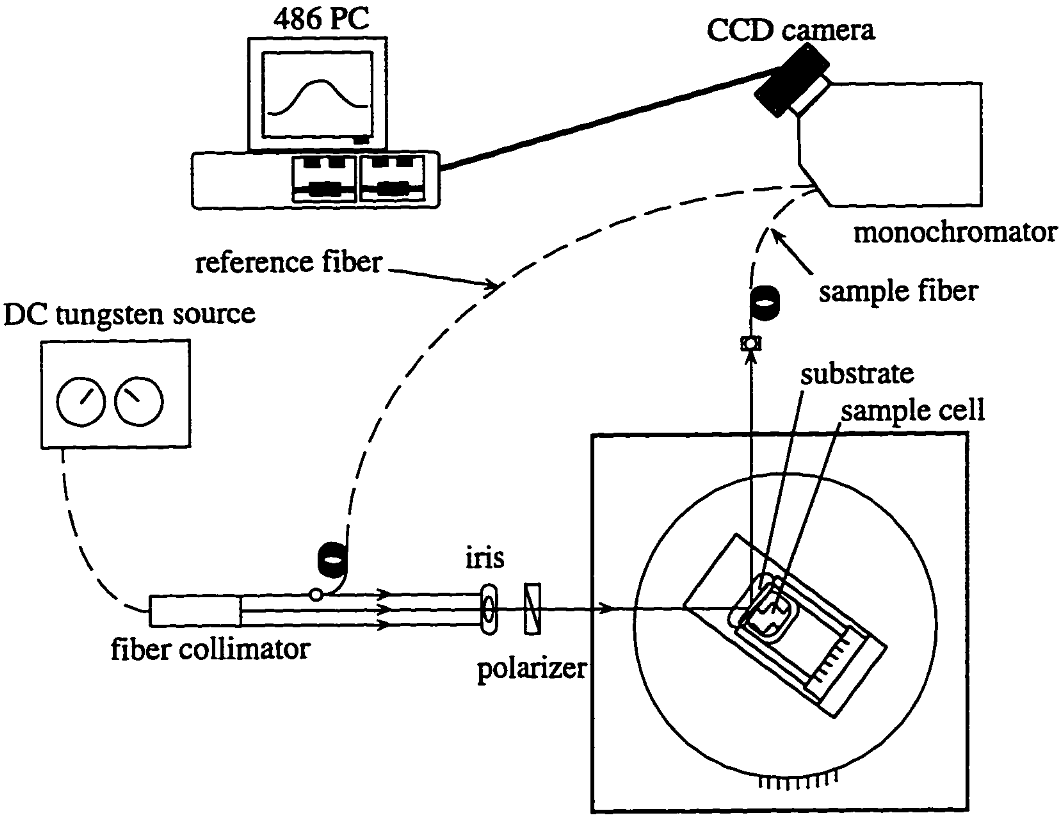

Figure 4.1 Experimental schematic for collection of the zeroth order GLRS diffracted reflection.

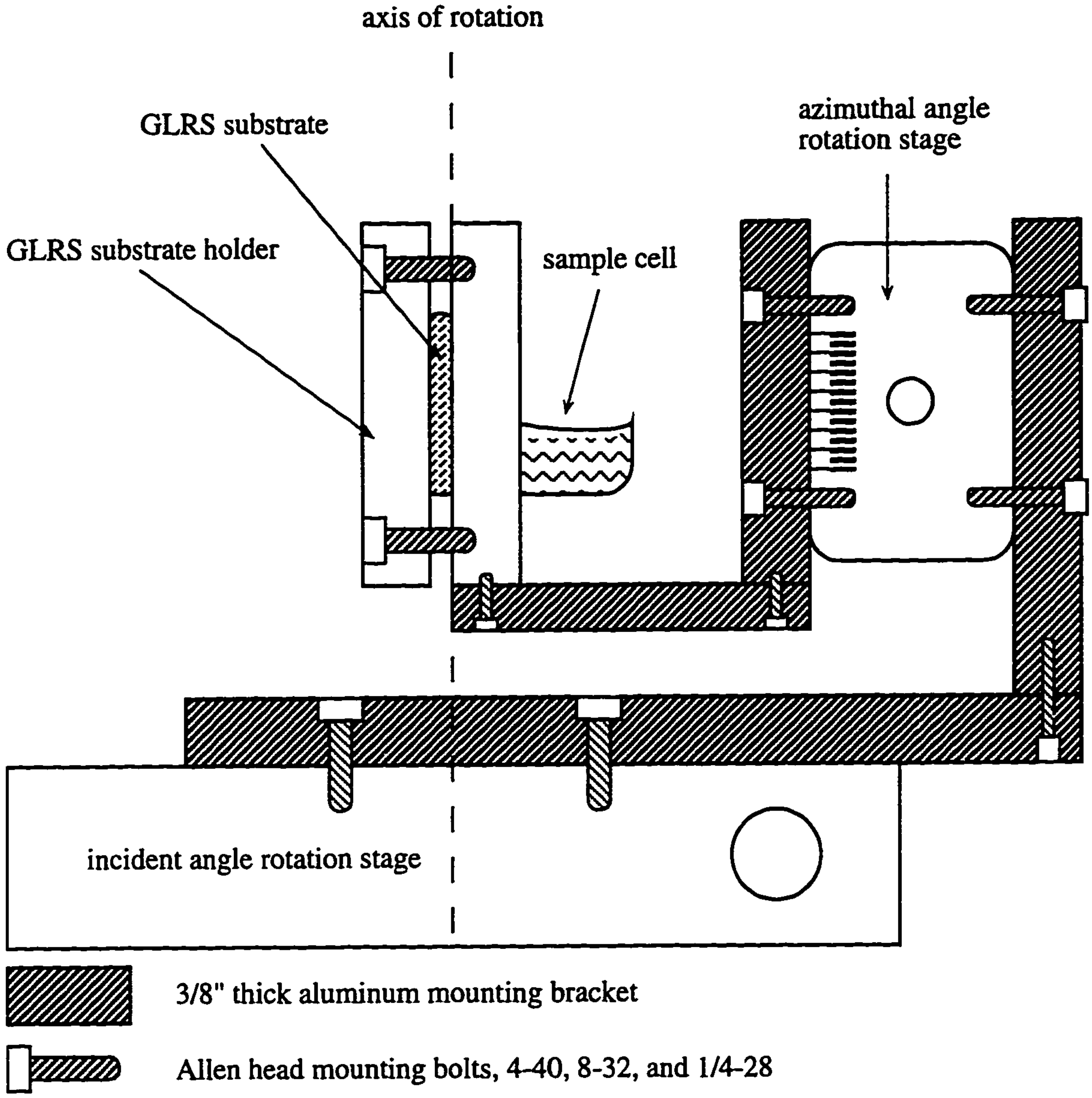

Figure 4.2 GLRS substrate holder staging system which allows for selection of the incident and azimuthal angles. The bracket is constructed such that the grating face of the substrate is positoned along the axis of rotation for the entire assembly. This ensures that minimal translation occurs as the substrate incident angle is adjusted.

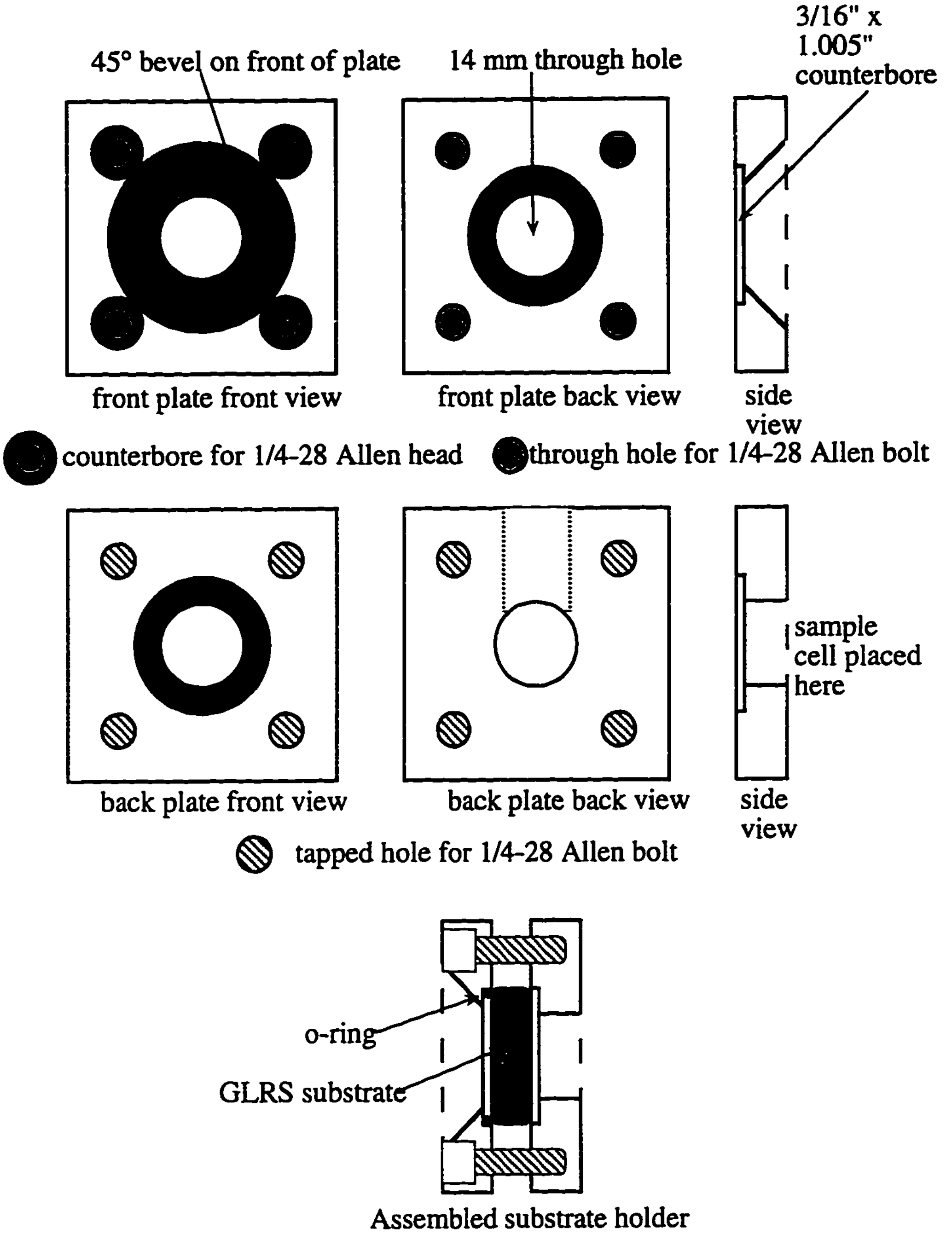

Figure 4.3 The GLRS substrate holder is a sandwich type cell with a bevel on the front plate to allow for optical interrogation of the grating at high incident angles. The sample cell is placed against the backside of the grating substrate in contact with the grating.

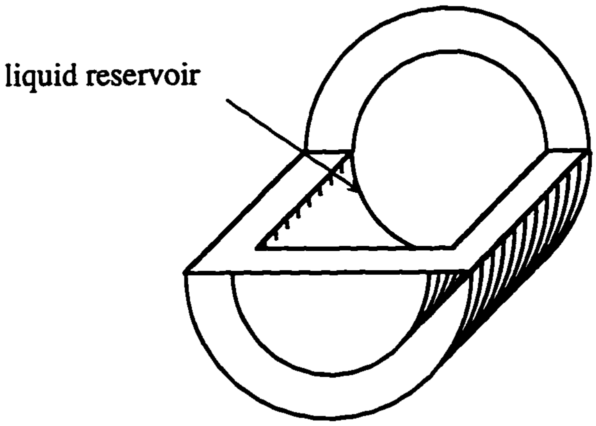

perspective view of Teflon sample cell

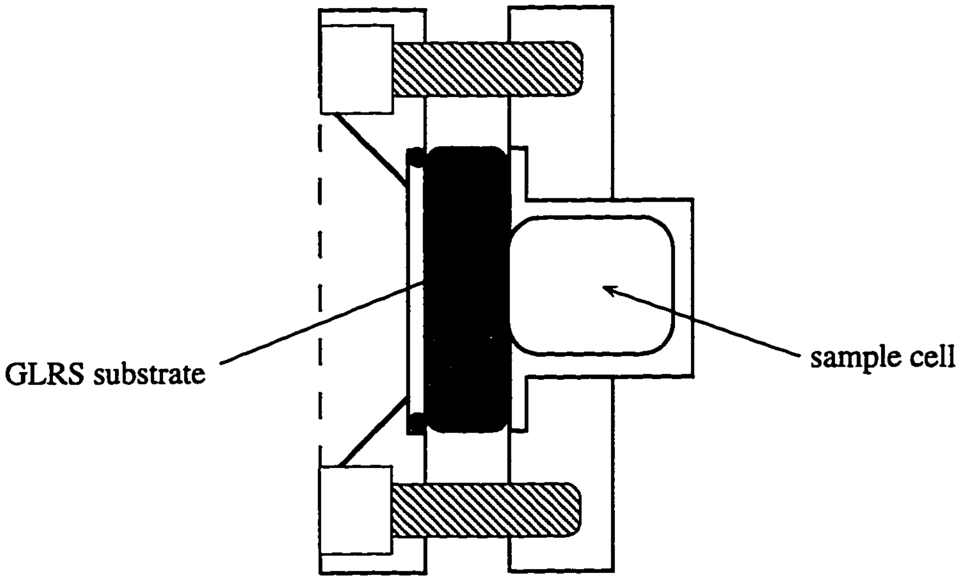

top view of sample cell installed into substrate holder

Figure 4.4 Teflon sample cell

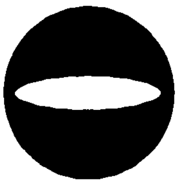

optical silicone gasket with flow channel

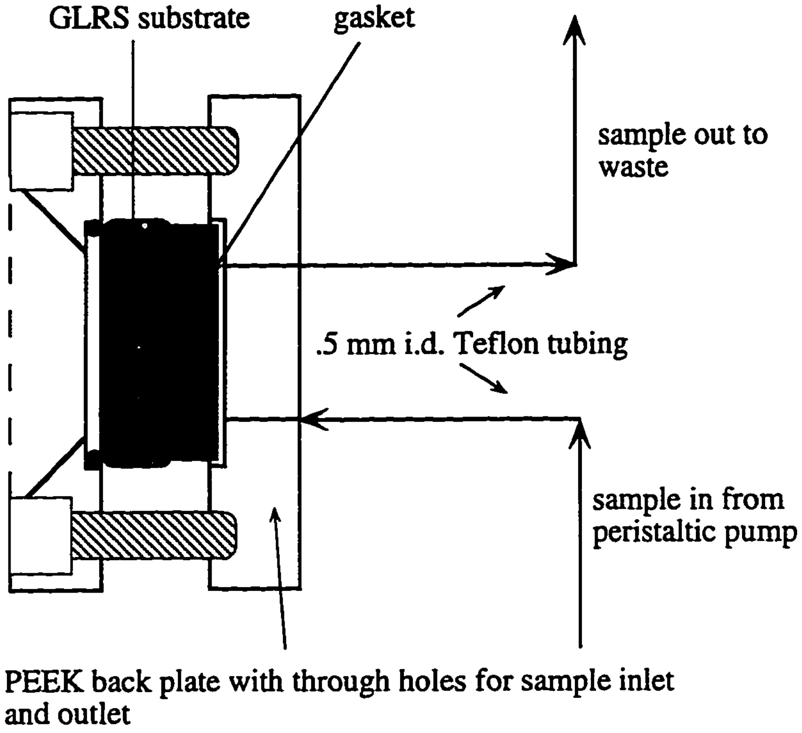

Figure 4.5 GLRS flow cell schematic with silicone rubber flow channel gasket and PEEK back plate. Sample is pumped in via peristaltic pump.

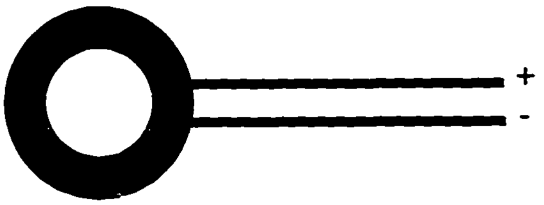

Thermoelectric (Peltier) cooler with a 14 mm center hole

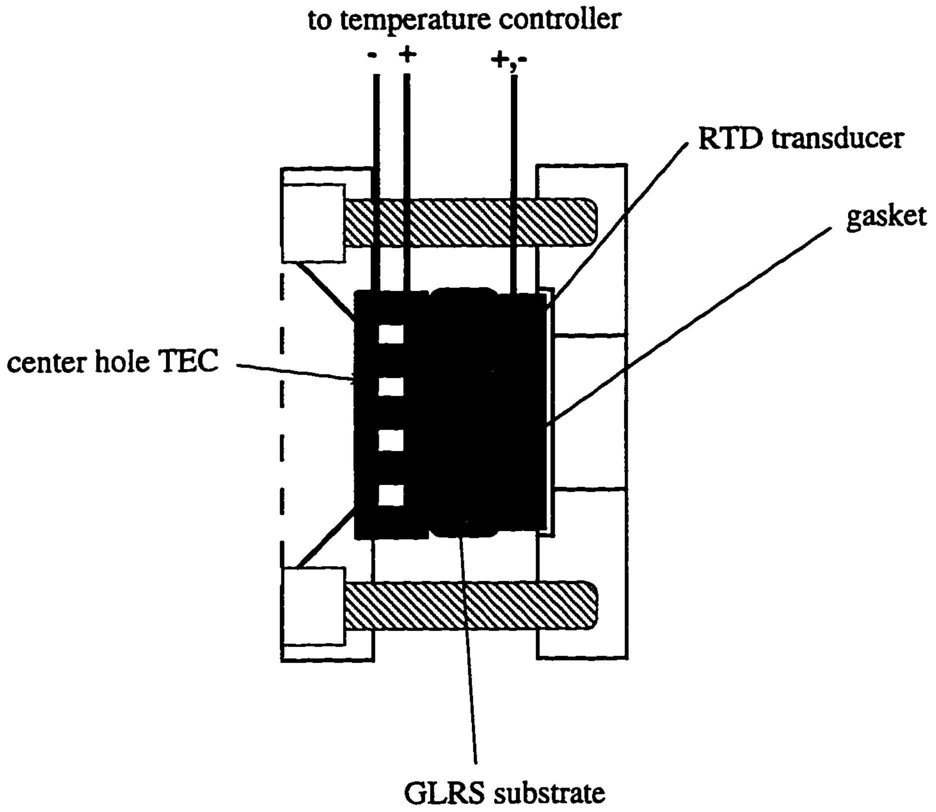

Figure 4.6 Schematic of the TEC temperature controller and resistive transducer (RTD) integrated into the GLRS flow cell. Sample was heated through the GLRS substrate and temperature was controlled via the RTD in contact with the grating side of the substrate.

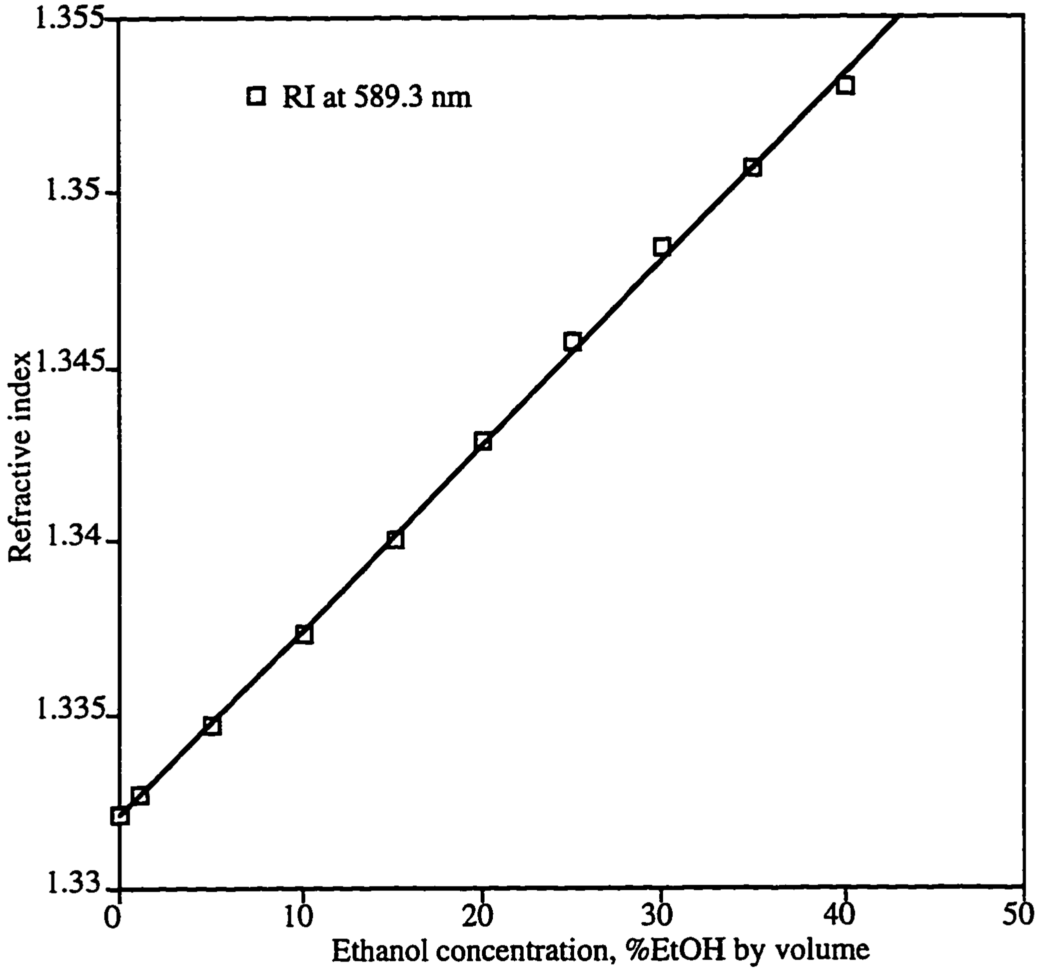

Figure 4.7 Sodium D-line refractive indices for the set of ethanol solutions. The regression equation is $y = 0.0005312*x + 1.33213$ with a correlation coefficient of 0.9992.

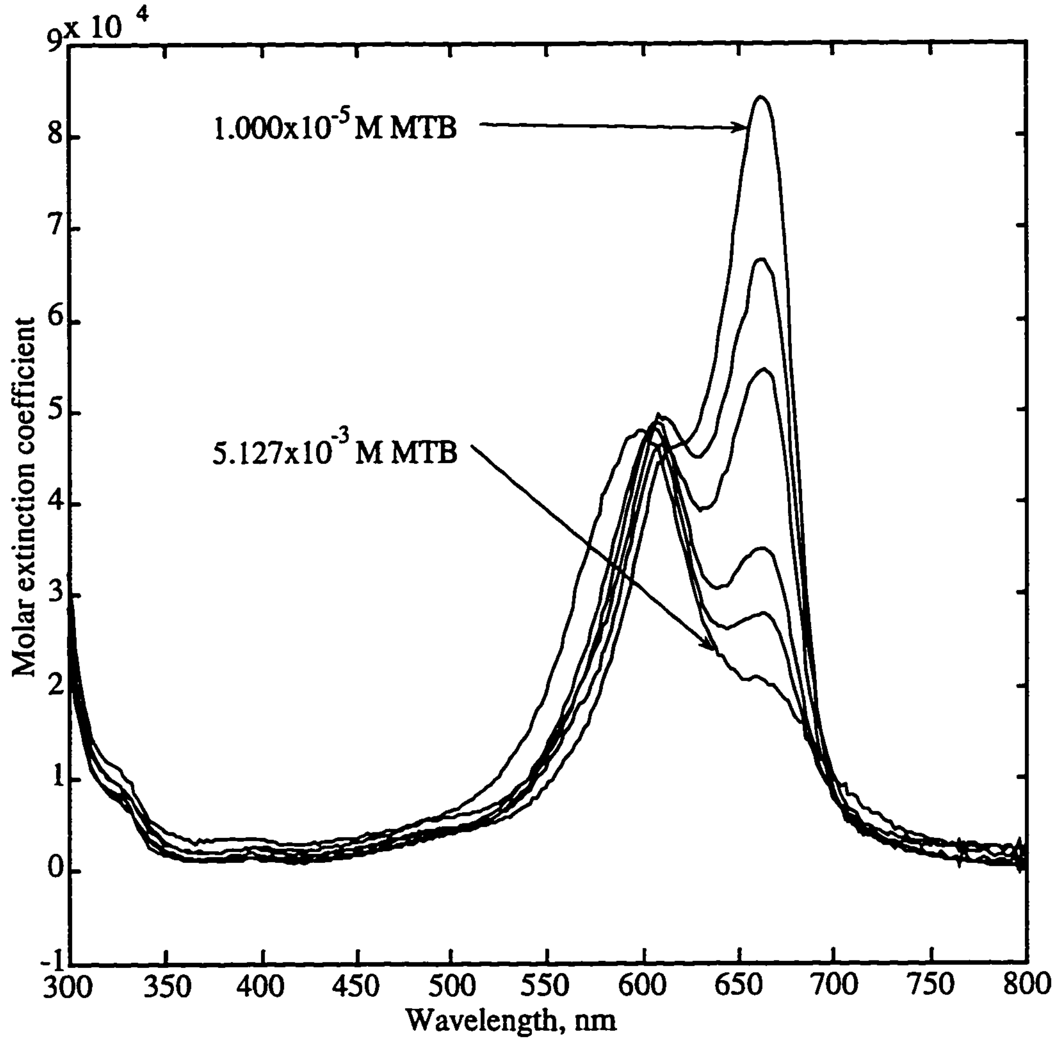

Figure 4.8 Molar extinction coefficients for the series of methylene blue sample solutions. Notice the decrease in molar extinction coefficient with concentration around 660 nm.

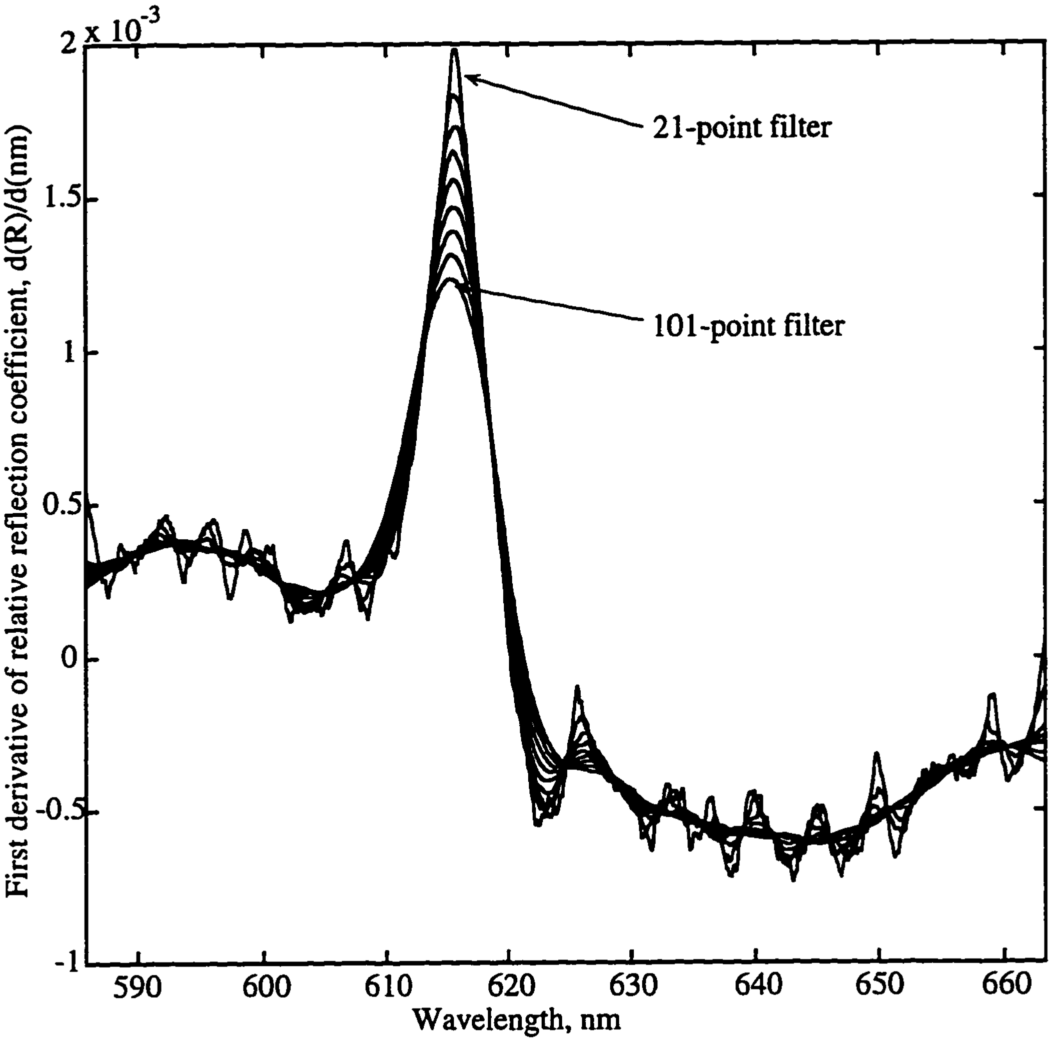

Figure 4.9 Effects of Savitsky-Golay first derivative filter length on peak position and height. Harmonics are suppressed as the filter length increases.

Chapter 5

Results and Discussion: GLRS Characterization

5.1 Forms of Reflection Coefficients and Derivatives

5.1.1 Sharpness of the GLRS Singularity and Experimental Considerations

The experimental design progressed from an initial instrument with a desire to eliminate non-correlated experimental variance and utilize a simultaneously obtained reference spectrum for calculations. The use of optical fibers and a dual channel spectrometer facilitated easy collection of the sample and reference beams but added some complications in the forms of structure on the array and variance that needed to be understood and/or corrected. In addition, the experimental design was optimized in order to identify and reduce sources of variance that were not correlated with chemical or physical changes in the sample throughout the course of the work until a final design yielded consistent results. The experimental design detailed in the previous chapter was the final design and represents the optimized instrumentation that was used for all experiments.

A number of experimental parameters affect the data collected and how it is processed. The sharpness of the reflection singularity is predicted by theory to be infinite as it is a singularity in the mathematical sense. The sharpness that is attainable experimentally is reliant upon the nature of the optical and spectroscopic systems. A low degree of collimation will smooth the singularity based upon the range of angles launched at the grating. A finite range of incident angles reduces the absorbance sensitivity of the singularity as the smoothing will result in a peak height decline that is unrelated to absorbance properties. Likewise, a smoothed singularity will result in broader derivative peaks, thereby reducing the sensitivity of the measured singularity to changes in bulk refractive index. Thus, it is desirable to achieve the highest degree of collimation possible, and this was achieved using the fiber as an approximate point source and an achromat lens to reduce chromatic aberrations.

Another experimental parameter that affects the sharpness of the singularity is the resolution of the spectrometer used in the data collection. The spectrometer used in these experiments was fitted with an aperture matching optical assembly to match the numerical aperture of a standard glass on glass optical fiber to that of the 1/3 meter monochromator. A 300 groove/mm grating coupled with a CCD array set the resolution limit at 0.1 nm. However, the insertion loss of the fibers and the grating sensor reduced the intensity of collected light such that a wide slit was needed to achieve a useable signal to noise on the detector, which is not a good low-light detection system by design. Thus, within the bandwidth of the instrument, a resolution of approximately 2 nm was achieved which represented a balance between collection efficiency and signal to noise. Higher resolution could be achieved at a loss of signal to noise ratio, which would widen the derivative peak width by requiring a larger derivative filter to achieve an acceptable level of smoothing.

As will be seen in the raw and reference ratioed data, a significant amount of high frequency structure is present, and this structure requires the use of a smoothing filter to achieve a reproducible derivative. This structure may have a number of sources that are directly related to experimental factors and not the inherent GLRS response function. First, the optical fibers used in the work were highly multimode. The launch conditions were chosen to maximize throughput, and the internal propagation modes resulted in output structure that consisted of finely spaced concentric rings of high and low intensity. As the spectrometer was used in an imaging format, the structure at the output of the fiber was reproduced at the detector array. This was verified by the induction of mode shifting microbends in the fiber which resulted in shifts of the fine structure superimposed on the source intensity profile on the array. Also, the monochromator coupling optics were comprised of singlet lenses which did not adequately focus the entire white light spectrum to a single spot in the slit plane of the monochromator, resulting in a concentric ring chromatic aberration. These structural components contribute to the degree of mathematical smoothing that was required for the GLRS sample, reference, and derivative data.

5.1.2 Dependence of GLRS Thresholds on Incident Polarization State

The GLRS characterization proceeded with the polarization variance data collected in the middle of the experimental sequence, however, presenting it here first allows for general discussion of the forms of the reflection coefficients and the qualitative correlation of these forms with theory. Any reflection-based spectroscopic method will be highly dependent upon polarization of incident light relative the incident and the interface plane. GLRS reflection coefficients contain a polarization dependence while the position of the threshold is predicted to be incident polarization state insensitive. For these experiments, and subsequent characterization experiments, the first diffracted transmitted order is chosen to undergo the threshold transformation according to (2.4). Zeroth order grating reflection intensities for the series of polarization angles are presented in figure 5.1 for water in the cell. Figure 5.2 displays the dependence of the integrated zeroth order reflected intensity on polarization angle. The overall intensity of the zeroth order reflection progresses smoothly from a low value for the incident s-polarization and a high value for the incident p-polarization. This may be understood in terms of the reflection intensity expected from the first surface reflection. Figure 5.3 shows the normalized external reflection intensity vs. angle of incidence for an air-fused silica interface. The p-polarization undergoes a zero intensity reflection at the Brewster angle, or polarizing angle, and then progresses smoothly to the 100% intensity value for 90° incident angle. At the incident angle used in this experiment, The s-polarized reflection intensity is roughly double that of the p-polarization. Thus, more intensity is striking the grating after the initial first surface reflection for the p-polarization allowing for a stronger reflection off of the grating. This, however, does not account fully for the factor of eight difference between s- and p-polarization GLRS zeroth order reflections. The connection between the diffraction orders and the coupled reflectivity of the chrome and glass materials accounts for the high reflectivity of the grating relative to the glass-sample interface. The intensity difference between GLRS reflections for different polarizations is due to the coupled effects of Fresnel reflections and the grating where the C_i coefficients in (2.8) contain polarization and Fresnel information as well as some dependence upon the grating parameters.

The form of the reflection coefficient is calculated using a reference reflection or intensity distribution. Figure 5.4 displays the reference spectra recorded simultaneously with the sample spectra. The shape of the reference spectra is due to the spectrometer instrument function and the fiber optic collection fiber. The reference spectra were ratioed to the corresponding grating zeroth orders reflections in order to obtain the corresponding relative reflection coefficients as displayed in figure 5.5. The polarization dependence of the reflection coefficient is seen in these curves, but the nature of the dependence is difficult to see due to scaling. Thus, the data were normalized to the intensity at diode 650 for each scan, corresponding to a wavelength away from the GLRS singularity. These normalized curves are presented in figure 5.6. The reflection coefficient dependence on polarization angle is clearly seen as the curves progress through a series of forms that appear to be weighted sums of the pure polarization reflections. Thus, like Fresnel reflection, the

GLRS reflection coefficient appears to be a two component form that may be deconvoluted into its constituent lineshapes that are reflections of the pure s- or p-polarized incident light.

In order to characterize the differences in polarization dependent GLRS threshold positions, the first derivatives of the respective curves were calculated and are shown in figure 5.7 for the non-normalized reflection coefficients and in figure 5.8 for the normalized reflection coefficients. Notice the degree of difference between derivatives of the normalized and non-normalized reflection coefficients. The data are presented here in order to show the effect of data processing on the derivative magnitude in that the normalization procedure scales the derivative magnitudes for the range of polarizations. This is important to consider when calculating the derivative peak magnitude dependence on absorbance in that any calibration has to take into account polarization shifts and normalization procedures.

The shape of the derivatives is expected from theory in that a peak exists at the wavelength of the threshold. Figure 5.9 displays the positions of the GLRS threshold peaks (positive or negative going) as a function of polarization angle. At s+20° there is no peak in the derivative spectrum and this accounts for the anomalous peak position at s+20° in figure 5.9. The significance of the peak position trend is that as the polarization angle is scanned through to the p-polarization, the wavelength of the threshold shifts approximately 0.5 nm. It is most likely that the incident angle was disturbed as the polarization angle was scanned due to displacement of the beam during rotation of the cube polarizer. Also, the pickup optics needed to be adjusted slightly to capture the sample beam after adjusting the polarizer, which indicates that the incident coupling angle was disturbed. Thus, it is reasonable to assume that the monotonic increase in threshold wavelength is due to a monotonic decrease in coupling angle and not an inherent dependence of the threshold position on polarization angle.

The complimentary nature of the s- and p-polarization derivatives is a result of a sign change in the coefficients in (2.8). The midpoint in polarization angle (s+45°) derivative contains a singularity peak that is indicative of a dominant p-polarization component. At the midpoint in polarization angle, the grating scattering parameters that are dependent upon the threshold are not equally canceled but are weighted to the p-polarization. Thus, the coefficients C_i in (2.8) are not compensated equally for orthogonal polarizations, and may change relative magnitude with modulated incident polarization state. The s+20° derivative curve appears to contain s- and p-polarization components that are equally compensated. This has implications for the characterization of materials in contact with the grating that modulate the polarization of the transmitted and evanescent fields on either side of the threshold. For a mixed incident polarization state, chiral molecules in contact with the grating may be distinguished based on a derivative modulation from the null response at the s+20° polarization angle.

These are qualitative arguments based on a general understanding of the reflection and diffraction phenomena. Rigorous solution of the GLRS scattering parameters will provide a basis for quantitatively understanding the dependence of the thresholds on polarization state and give insight into developing new experimental procedures to take advantage of the differences in responses based on polarization of incident light.

5.1.3 Angular Dependence of Reflection Coefficients and Derivatives

An understanding of the physical parameters of the grating function need to be established in the absence of changes in the sample chemistry. In light of this consideration, experiments were performed with water in the cell without sample regeneration while the incident angle was varied manually. In addition, it was necessary to establish the forms of the reflection coefficients and the errors in prediction due to mechanical alteration of the coupling conditions. Figure 5.10 (a and b) displays the normalized reflection coefficients for the two experiments performed. An additional angle of incidence was chosen to yield a singularity at approximately 700 nm in order to investigate the shape of the reflection coefficient well away from a singularity modulation, and this is denoted in figure 10b. Differences in overall magnitude of the reflection coefficients in figures 5.10a and 5.10b are a result of the first surface reflectivity differences and the changes in the monochromator efficiency as the wavelength range was adjusted mechanically between experiments. However, the forms agree with theoretical expectations in that point of highest slope in each curve corresponds to the position of the threshold for each set of experimental conditions.

Figure 5.11 displays the derivatives of the normalized reflection coefficients for the range of incidence angles. Notice that on the low wavelength side of the threshold, the slope of the reflection coefficient has a higher value than on the high wavelength side of the thresholds. In addition, the peak magnitudes track similarly to the baseline variance, where the local minima and maxima in the derivative away from the threshold affect the peak height of the singularity when it is present at the threshold wavelength. This baseline trend has been termed the underlying grating function, and is influenced by the grating parameters and the surface characteristics of the interface region. Figure 5.12 displays the peak height versus wavelength for each peak in the derivative plots. It is clear that the peak height trend with angle of incidence may be modeled as a baseline or blank in absorbance measurements for prediction of imaginary part of the dielectric function of the sample as this trend is expected to be stable unless an absorber is present in the solution.

5.1.3.1 Calculation of the Dispersion of Water Using GLRS

The changes in derivative peak positions correspond with the changes in real part of the dielectric as it depends on wavelength. As the incident angle is varied, the threshold appears at a different wavelength according to (2.4). There is a slight change induced in the threshold wavelength due to dispersion as the refractive index is dependent upon the wavelength of light. Hence, it is possible to measure the refractive index as a function of wavelength by simply varying the incident angle. Figure 5.13 is a comparison of the experimental and theoretical singularity wavelengths as functions of incident angle. As expected, a nominal linear relationship exists between incident angle and threshold wavelength for the narrow range of angles used in the experiments. Deviation from the theoretical curve is due to the fact that dispersion was not taken into account in the modeling. The peak positions were used with equation (2.4) to predict refractive index of water at the various threshold wavelengths, and these results are plotted in figure 5.14. The reference refractive index values were calculated using equation (4.1). The discontinuity in the reference data at an incident angle of 36.3° is due to the difference in ambient temperatures between runs, as the experiments were performed on two different days. The GLRS predicted dispersion displays what appears to be significant deviation from the reference data, and this may be explained as follows. First, the reference data are obtained by solving for refractive index based on dispersion, temperature, and chemical composition relationships that were determined empirically where normal dispersion was assumed. The refractive indices determined by GLRS are the result of manual adjustment of the coupling angles where the errors are associated with the translation stage vernier due to lash and hysteresis. Also, as the GLRS sample cell was not thermostated, local temperature variations in the cell may account for the deviations.

The root mean square error calculated using the GLRS and reference refractive indices was found to be .0007 refractive index units. The error associated with the Abbe refractometer is ±.0001 index units, and uncertainties in the angle determinations add to the existing Abbe error. In addition, the slope of the dispersion curves are different. This is demonstrated by the solid line in figure 5.14 which corresponds to a linear least squares fit of the GLRS determined refractive index values to threshold wavelength. This may be due to the fact that the calculation of dispersion using the Abbe refractometer relies on lookup tables and a single compensator prism setting to determine dispersion across several hundred nanometers, whereas the GLRS method measures the dispersion at discreet points. In short, the error associated with these measurements is on the order of the error associated with the Abbe refractometer, and is therefore not unreasonable. Improvements could be made in dispersion measurements by using more precise rotation staging and by using a temperature controlled sample cell, which will be discussed later.

5.2 GLRS Refractive Index Response

As discussed above, the GLRS threshold positions may be used to calculate the refractive index of a sample in contact with the grating. The accuracy with which the positions are found and the stability of the optical system determine the accuracy of the refractive index measurement. Thus, ethanol:water solutions were utilized in these studies to explore the changes in the GLRS refection coefficients' form due to variations in refractive index in the sample in the absence of mechanical adjustments of the optical train. This represents a first step in the characterization of GLRS to chemically relevant perturbations. First, however, the forms of the reflection coefficients will be presented and compared.

5.2.1 Comparison of the GLRS Threshold Positions with Theory

5.2.1.1 Zeroth Order Reflection

Figures 5.15 and 5.16 display the GLRS reflection coefficients for the ethanol series for incident p- and s-polarization states respectively. Notice that the forms of the reflection coefficients are consistent with the previous polarization state dependence where the relative values of the C_i coefficients in (2.8) determine the shapes of the reflection coefficients away from the thresholds. The s-polarization plot demonstrates the similarity of the threshold in transmitted light with a standard critical angle measurement, where a flat baseline abruptly changes as the incident angle progresses through the critical angle for total internal reflection. The thresholds in the p-polarization plot generate reflection coefficient plots that are considerably more complex, where the incident light contains electric field components that are perpendicular to the interface. However, the similarity in both polarization responses is seen in that the dominant feature progresses to a larger wavelength for a higher concentration of ethanol, which corresponds to a higher refractive index of the sample, as expected from theory. Note that the overall reflectivity changes as a function of sample refractive index, but the general shape of the feature does not change, as is expected for a pure refractive index response.

Figures 5.17 and 5.18 display the derivatives of the reflection coefficients for the ethanol runs; p- and s-polarization states, respectively. The shapes of the derivatives agree qualitatively with the derivatives obtained in the polarization angle and incident angle experiments. The symmetry between the two polarization responses is clearly seen as the s-polarization yields negative going peaks, and the p-polarization yields positive going peaks. The peak positions correspond to the threshold wavelengths for the various sample refractive indices, and the peak positions track to higher wavelengths for increasing sample refractive index. The peak magnitudes (maxima and minima) reveal that the underlying grating function exists, as seen in the incident angle variation data, and is similar for both polarizations, and further supports the claim that a water baseline peak magnitude may be used as a blank value for absorbance determinations, as will be discussed later.

The correlation of the refractive index response with theoretical predictions was carried out by modeling equation (2.4) using the wavelength dependent refractive index, angle of incidence, grating period, and grating diffraction order for each sample. Thus, a δ_m value was assigned to each point of the wavelength axis. Theory predicts that the derivative peaks (positive and negative for p- and s-polarizations respectively) will occur at $\delta_m = 0$. It was necessary to perform this modeling in order to confirm that the threshold was occurring at the prescribed location and that the experimental derivative peaks were indeed corresponding to their theoretical singularities. Figure 5.19 (a and b) displays the resulting dependence of the reflection coefficients and derivative peak positions on δ_m. As expected, the derivative peaks line up at the zero crossing of the delta function. Deviations from the peak occurring at zero are the result of errors in the incident angle determination and in the calculation of the dispersion of each sample. This analysis verifies that the GLRS theory correlates very well with experimental evidence and that the choice of the positions and magnitudes of the derivative peaks is valid for prediction of refractive index and absorbance.

5.2.1.2 Comparison of First and Zeroth Order Reflections

The GLRS thresholds that occur in transmitted diffracted light are connected with all diffraction orders in that singularities exist in each reflection order. To test this, the first order diffraction intensity was collected in conjunction with the zeroth order reflection in response to a series of ethanol solutions of varying concentration. It was not experimentally feasible to obtain a first order reference reflection that can be used generate a first order reflection coefficient. Thus, in order to compare reflection intensity variations between orders in response to ethanol concentration changes, sample reflected intensities were referenced to corresponding water reflections in order to generate difference plots for comparison. In this way, the responses of the various diffraction orders may be compared and similarities between polarizations may be exhibited. Figures 5.20 (a and b) display the difference spectra for the first order diffraction responses; p- and s-polarizations, respectively. Notice that there is simultaneous attenuation and enhancement in reflected intensity that is dependent upon wavelength, refractive index, and polarization state. This is significant in that other reflection methods rely on attenuation of incident light as the chemical to optical transduction mechanism.

For comparison, similar difference spectra for the zeroth reflected order are plotted in figures 5.20 (c and d). The forms of the difference spectra are very similar, and in addition, interesting symmetries exist between orthogonal polarizations and diffraction orders. The series of zeroth order s- polarization difference spectra follows a similar trend in intensity variation as the first order p-polarization spectra. Likewise, the zeroth order p-polarization difference spectra look qualitatively similar to the series of first order s-polarization difference spectra. It may be inferred from these data that that first order reflection contains complimentary information to the zeroth order. The grating connects the reflected diffraction orders to the transmitted orders via the singularity, and these connections are clearly seen in these symmetries. If a suitable first order reference reflection is captured, the simultaneous collection of the first and zeroth order reflection may allow for rejection of common mode noise. In addition, the collection of two diffraction orders simultaneously allows for the reduction in unknown variables in the solutions to the reflection coefficient matrix problem, thus opening an avenue for rigorous mathematical modeling of the experimental curves. These data support the general nature of the GLRS threshold theory in that the singularities exist in all diffracted orders, where the existence of the first order singularity is inferred by the similarities between the responses of the zeroth and first order reflected diffraction orders.

5.2.2 Refractive Index Calibration Results

The above discussion has described the experimental verification of the GLRS theory. This theory may be used directly to predict refractive index of a sample, as demonstrated in the angle variation experiments. The analytical performance of the GLRS sensing platform in real world applications depends upon the calibration of the sensor for a given set of experimental conditions. This set of conditions includes factors that affect reproducibility, absolute accuracy, and precision. These figures of merit contribute to the error associated with a certain measurement, giving a reasonable estimate of the predictive power of the instrument. In light of this, several methods were used to generate prediction statistics that are estimates of error, both bias and precision. The direct comparison of the positions of the thresholds for a given set of experimental parameters with theory (equation (2.4)) yields a measure of absolute accuracy when compared with a reference set of values. Likewise, an independent univariate calibration model may be constructed based on a linear least squares fit of the positions with GLRS predicted refractive indices. This will give a measure of the precision of the system as it relates to the use of the linear GLRS model in equation (2.4). Finally, the application of multivariate statistics to the GLRS data will allow for a model to be constructed that takes into account variance away from the thresholds. In each calibration case, the errors are reported as root mean square (rms) values, and where bias is present, precision is calculated by removing the bias component and producing another rms statistic.

5.2.2.1 Univariate Analysis

In order to establish the reproducibility of the GLRS derivative peak positions and magnitudes, four samples of different ethanol concentrations were run in triplicate. Peak positions and maxima were found for the replicate sample runs and are tabulated in table 5.1. The means and standard deviations of these replicate runs are given in table 5.2. A measure of the overall precision of the technique is obtained by taking the mean standard deviation along each axis, yielding a wavelength position precision of .10 nm and a relative peak height precision of 7.6×10^{-6}. The wavelength precision is a result of the wavelength registration along the ccd array, which is .1 nm/pixel. The peak height reproducibility is a function of the derivative filter used and the fluctuations in overall intensity and pixel to pixel shot noise on the array. The filter length used to calculate the derivatives represents a balance between precision and sensitivity. By increasing the filter length, significant averaging occurs that results in a more reproducible peak height at the expense of reducing the sensitivity of the derivative to changes in reflection coefficient slope at the threshold. However, the average peak height precision corresponds to a relative standard deviation of .18%, which is indicative of a stable experimental system.

The full set of ethanol solutions was used as a calibration set for refractive index. The derivative peak positions for each threshold for each polarization state are given in table 5.3 along with the predicted refractive index using GLRS (equation (2.4)). The difference in peak positions between polarizations may be due to the fact that the experiments were performed on different days with ambient temperatures (27° C and 28° C). These differences in temperature along with the change in the optics due to rotation of the polarizer may account for the differences in predicted refractive index based on GLRS peak positions. The refractive index values obtained with GLRS were compared with reference values calculated as before in the measurement of the dispersion of water using GLRS angle variation. Figure 5.21 displays the reference and GLRS predicted refractive indices vs. threshold wavelengths for the p-polarization. Notice the offset between the reference values and the GLRS predicted values. This amounts to an rms bias in refractive index prediction of 0.0012 index units when compared to the reference values. This bias is due to the error in incident angle determination that was described earlier, where a precision of 0.0083° yields a refractive index error of 0.0012. Accordingly, the rms precision for prediction is 0.00023 index units. Figure 5.22 displays the analogous data for the s-polarization, where the reference and GLRS predicted values are plotted against threshold wavelength. The rms bias calculated for the s-polarization is 0.00072 index units where the rms precision is 0.00031 index units. These numbers are consistent with what is expected from the errors associated with the reference methods of measuring the temperature and concentration dependent refractive index and dispersion of each sample. The rms precisions are more representative of the error associated with these measurements than the bias as the bias may be corrected for in the calibration model. As demonstrated, the errors calculated for a bias corrected calibration are on the order of the errors described for wavelength stability and reference refractive index calculation.

Included in figures 5.21 and 5.22 are the linear least squares fits of the threshold wavelength with each set of refractive index data, where the lines represent the best fits. These best fit lines represent the ability of GLRS to predict refractive index based on the linear model equation (2.4). The correlation coefficients for the GLRS fits are considerably higher than for the fit of the reference data, indicating that the reference data contains more variance than the GLRS predicted data. This is verified by the rms error values for the linear least squares fits, which are 0.000058 and 0.000076 index units for the p- and s-polarization runs, respectively. These precision estimates are due to the use of the theoretical expression (2.4) to calculate refractive index where the errors inherent in the expression are from the determination of the wavelength positions, incident angle, and grating period. For a static system, one would expect the grating period determination to be the limiting factor and thus yield an error on the order of 5 significant figures. The calibration errors reported in this section are summarized in table 5.4.

5.2.2.2 Multivariate Calibration: Partial Least Squares Calibration

The data generated by the GLRS sensor in this format is first order in that a full vector of data is obtained for each sample. The multivariate nature of the response is such that a calibration may be attempted based on a response matrix and a set of reference values that are independent of the GLRS method. In the previous calibrations, the reference values were obtained by solving a function that describes the refractive index as a function of wavelength, ethanol concentration, and temperature for the wavelength of the singularity. Thus, error was introduced into the reference values by the utilization of GLRS-obtained wavelengths. In order to build a model based on two independent sets of data that contain the least amount of initial error, reference values of refractive index measured at 589.3 nm were used (table 5.5). This reduces the error in the reference values to the Abbe limit of ±0.0001 index units as no interpolation is needed, dispersion is not corrected for, and the reference values are independent of GLRS wavelengths. The reflection coefficients were used as a sample matrix, where the nth row in the reflection coefficient matrix corresponds to the nth value in the reference vector. The dark-corrected reflection coefficients were chosen as a sample matrix over the raw data because the reflection coefficients contained features that are more readily modeled by a linear multivariate technique.

Individual partial least squares (PLS) calibration models were constructed for each incident polarization state. The root mean error of cross-validation statistic (RMSECV) is calculated by the model based on a leave one out prediction scheme, as described in the previous chapter. table 5.6 summarizes the RMSECV values for the different numbers of latent variables used in constructing the PLS model on the GLRS ratio data. This multivariate calibration of refractive index for ethanol in water yields significantly better prediction errors than the determination of refractive index using peak positions and equation (2.4). For the case where three PLS factors are used in the model, the error in both the s- and p-polarization experiments is comparable with the measurement error associated with using the Abbe refractometer as a reference method. The use of the full data set in calibration, as opposed to a single number obtained from the data, allows the calibration procedure to take into account the reflection differences due to refractive index away from the thresholds.

Because there are nine ethanol solutions, with data taken in a static format, the maximum number of PLS factors that can be used to model the data is nine as there is no continuous time axis with which to remove non-correlated time dependent drift. Using eight PLS factors to model the p-polarization response data results in an RMSECV of 1.8×10^{-6} index units. Likewise, using nine factors for the s-polarization data yields an RMSECV of 2.7×10^{-6} index units. Although these represent the true minima in the latent variable vs. RMSECV curves, the large number of latent variables used indicate that the models are not compact, hence the variance that is correlated with refractive index variations is not linear. However, both the fact that the third factor reaches the error limit imposed by the reference method and a two orders of magnitude decrease in the prediction error over the range of model sizes indicates that the GLRS technique is directly amenable to multivariate statistical analysis and calibration.

The error limit reached by PLS is lower than the error (precision) obtained by calibrating the GLRS predicted refractive index with the threshold wavelength position using a linear least squares model. Also, the RMSECV is lower for the p-polarized than for the s-polarized experiments. This may be due to the lineshapes of the p-polarized reflection coefficients. The extra structure inherent in the p-polarized reflection coefficients contributes to a better calibration in the multivariate sense due to the added amount of variance that is correlated with concentration changes.

The analytical performance of the GLRS sensor demonstrated in this section points to the need for more precise and accurate reference methods for calibration and comparison.

The largest errors were obtained in the comparison of the GLRS response with reference methods that are less precise but have acceptable accuracy. In spite of this, the GLRS sensor performs as well as any other white light refractometer found in the literature, and approaches the accuracy and precision obtained by differential laser refractometers. In addition, this analysis points out the fact that GLRS may be used as an absolute refractometer, where the position of the threshold in wavelength space is used to obtain refractive index directly. Other differential refractometers rely on displacement of a laser beam, calibration of a diode array to angular displacement, and transmission through the sample. GLRS allows for the determination of refractive index using existing white light spectroscopic instruments and fiber coupling in a reflection format where the optics are isolated from the sample. These points make GLRS an attractive candidate for application in process analysis of bulk refractive index.

5.3 Absorbance Response

5.3.1 Forms of the Reflection Coefficients and Derivatives

Methylene blue was chosen as a model absorbance system because of its unique concentration dependent absorbance characteristics. The absorbance response is predicted to be a smoothing of the threshold, where the position of the threshold is determined by the real part of the dielectric function of the sample (refractive index). The forms of the coefficients are expected to follow the general trend seen with the other model responses. Figures 5.23 (a and b), 5.24 (a and b), and 5.25 (a and b) display the GLRS reflection coefficients and derivatives for three angles of incidence, 30.62°, 34.98°, and 37.11°, respectively, in response to samples of varying methylene blue concentration. At the three angles of incidence, the thresholds occur at different positions according to the real part of the dielectric of the samples. In each case, the peak corresponds to the zero crossing of the threshold function (equation (2.4)), which is determined by the refractive index of each sample. The 1 cm pathlength equivalent absorbances for these samples are high, (see table 4.3) and this shows that the ability to measure the real part of the dielectric in the presence of high absorbance is a unique aspect of the GLRS sensing mechanism. A discussion regarding anomalous dispersion will follow where the relationship between the real and imaginary parts of the dielectric (refractive index and absorbance, respectively) will be dealt with in more depth.

The forms of the reflection coefficients and derivatives agree with theory in that the dominant modulation due to absorbance is a decline in the slope of the singularity in reflected light. This is essentially a smoothing of the threshold due to coherence loss from absorption around the transmitted threshold frequency. For each incident angle in each derivative plot, higher absorbance values result in a larger peak height deviation from the water derivative peak height value. The forms of the derivatives undergo what seems to be a transformation as the threshold wavelength moves to lower values to higher incident angles. At a threshold wavelength of 605 nm, it appears that the shapes of the reflection coefficients and derivatives have shifted from what corresponds to a positive and negative combination of C_i values in (2.8) to values that are both negative according to figure 2.5. The resulting derivative retains a symmetry around an isosbestic point at 608 nm, with absorbance response on either side of the threshold that is unique compared with the other angles of incidence experiments. If the threshold did indeed occur at 608 nm, then the error in determining the angle would have been four times the error associated with determining the angles of incidences in the previous experiments. Thus, it is unlikely that the threshold occurs at 608 nm due to the care that was taken in determining the incident angles. However, the difference in responses points to a difference in reflection coefficient form that is related to angle of incidence and/or refractive index, and the peak is still taken as the wavelength of the threshold corresponding to that particular system.

Table 5.7 summarizes the imaginary dielectric values at each threshold wavelength for each sample of methylene blue calculated from the thin cell transmission absorbance measurements. For each of the angles of incidence the amplitude change from a water derivative peak magnitude was calculated and plotted in figure 5.26 against the values in table 5.7. The magnitude of each peak height modulation is dependent upon the imaginary portion of the dielectric function at the threshold wavelength. The singularity at 683 nm represents a region in the absorbance spectrum where the extinction coefficient becomes smaller with concentration, yielding a smaller peak height decline relative to the singularity at 605 nm, which corresponds to a wavelength region where the imaginary portion of the dielectric (absorbance) is linear with concentration.

A least squares fit of the peak amplitude decline to the imaginary dielectric values calculated from the transmission absorbance measurements at 605 nm yields a power relationship given by the equation $\Delta(\text{amplitude}) = 0.00280 \times (\text{Im}(\varepsilon^{(2)}))^{.529}$. The peak decline for the threshold at 605 nm follows the expected trend of a square root dependence that would be observed in the derivative of the reflection coefficients in equation (2.8). However, the peak modulations at 630 nm and 683 nm do not follow a square root dependence on Im(ε). There are a number of competing mechanisms that may affect the peak height which include the contribution of anomalous dispersion and the nature of the tautomeric reaction in which the peak in the absorbance spectrum at 660 nm introduces a concentration dependent non-linearity into the response that compensates for the non-linear response of the GLRS derivative. Thus, qualitative agreement with theory is obtained for the threshold at 605 nm, while the higher wavelength thresholds produce results that are difficult to correlate with theory.

5.3.2 Anomalous Dispersion Effects

The real part of the dielectric is affected by the imaginary part due to the Kramers-Kronig relations for high absorbances as discussed in Chapter 2. As seen in the reflection coefficient derivatives for the three angles of incidence, a real refractive index change is occurring at the two lower angles of incidence due to the high concentrations of dye affecting the bulk index. This real index change is seen as a shift in the position of the singularity for high concentration of dye and this results from the Kramers-Kronig relations between the real and imaginary parts of the refractive index which predict large index shifts at wavelengths corresponding to shoulders of the absorption band for the highest concentration of dye.

Figure 5.27 displays the dependence of the peak position on methylene blue concentration for the three angles of incidence. The peak shift (and thus the index shift) is largest where the singularity occurs at the high wavelength shoulder of the absorbance band, and this is borne out experimentally as the singularity occurring at 683 nm produces the largest index shift with dye concentration. The threshold position at 605 nm yields a very small shift in index, consistent with the Kramers-Kronig relations, where 605 nm represents a position very close to the absorbance maximum at higher concentrations and thus the zero crossing in index shift. At 630 nm, it is expected that an intermediate shift in position and height would occur, and this is what is borne out experimentally as the singularity is in a position where the absorbance maximum moves from the high wavelength side of the singularity at low concentrations to the low wavelength side at higher concentrations. This data demonstrates the ability of GLRS to deconvolute the coupled effects of refractive index and absorbance for a single component system.

5.3.3 Calibration Results

5.3.3.1 Univariate Analysis

The errors in prediction of absorbance form these data may be summarized as follows. In terms of experimental error and prediction of absorbance from the peak amplitude modulations at 605 nm, the reproducibility in determining the peak amplitude was 0.0000076 units from the replicate ethanol measurements, and this corresponds to an error in absorbance of 0.077 A.U. Thus, three times the experimental error results in a limit of detection for absorbance of .232 A.U. In addition, the dynamic range extends to approximately 250 A.U. based on the absorbance characteristics of the methylene blue system at high concentrations and the fit to the GLRS peak decline data at 605 nm. The dynamic range is not linear, however, and an increase in sensitivity is observed for higher absorbances due to the square root nature of the dependence. This indicates that the GLRS sensor in its current state is uniquely suited to highly absorbing systems which are not amenable to ATR spectroscopy due to changing composition resulting in refractive index variations.

5.3.3.2 Multivariate Calibration: Partial Least Squares Calibration.

The first order response of the GLRS sensor indicates that a reasonable calibration may be constructed using a PLS algorithm and generating an RMSECV statistic in terms of methylene blue concentration. This was attempted for the methylene blue responses at the three different angles of incidence, where the reference vector used consisted of concentrations of methylene blue as prepared. The determination of the lowest RMSECV was dependent upon the shape of the data as input sample matrices were chosen as reflection coefficient or derivative matrices. It is not clear which curve type produces a better prediction as the errors are on the same order of magnitude for each corresponding derivative:reflection coefficient matrix pair. A comparison was made of the resulting RMSECV values and is given in table 5.8. In general, the minima in the RMSECV versus latent variable curves occur between 4 and 5 PLS latent variables. As there are six absorbance samples, this number of factors indicates that the system first order response to absorbance appears to be non-linear in a statistical sense. This may be explained by the fact that the GLRS absorbance response is localized to around the threshold wavelengths, and the amount of variance that is correlated with analyte concentration contained in the wavelength space is dependent upon concentration of analyte.

For the two lower angles of incidence, where a qualitative disagreement with theory was seen based on the peak magnitudes and calculated imaginary dielectric, lower RMSECV values were obtained in general, indicating that the system has a lower degree of non-linearity. The RMSECV values for the threshold position at 605 nm are an order of magnitude larger than those obtained at the two other incident angles. This is indicative of the inability of PLS to handle non-linearities, where the GLRS response that is most correlated with the non-linear theoretical response is modeled to a higher degree of error using PLS. In addition, the lineshapes of the reflection coefficients for the 37.11° incident angle are considerably different than the lineshapes of the other curves. As the lineshape affects the shape of the derivative it may also contribute to the efficiency of a given statistical model to predict concentration.

At the two lower angles of incidence, the error in the prediction concentration of methylene blue is on the order of the lowest concentration for each sample matrix input, reflection coefficient or derivative. Considering the difficulties encountered in working with methylene blue, where a significant amount of cation exchange occurred between the volumetric glassware and solution, it is reasonable to assume that the concentrations reported as prepared are different than the concentrations seen by the GLRS sensor. The use of methylene blue as a model system allowed the characterization of high concentrations of absorbing material at the expense of precision in the determination of the concentration of analyte in each sample.

5.4 Refractive Index and Absorbance: Mixture Results

An important aspect of this research is the orthogonality of GLRS responses to refractive index and absorbance. The methylene blue:ethanol system was chosen as a model mixture system primarily due to the fact that methylene blue solutions were spectroscopically characterized and the concentration dependence of the absorbance spectrum is understood. It is expected that the ethanol additions to the methylene blue solutions will affect the tautomerization reaction between free and dimer forms of

---

methylene blue[1]. Thus, the effects predicted by anomalous dispersion will be convoluted by the added chemical effect. However, this perturbation of the absorbance due to concentration of ethanol is predicted to be small compared with the perturbation due to methylene blue concentration as the concentration of ethanol is sufficiently small.

Errors in the concentrations of both methylene blue and ethanol are predicted to be higher than those for the bulk preparations in the previous sections due to dilution and the small volumes prepared (15 mL volumetric glassware was used). These errors will affect the prediction of refractive index and absorbance as well as correlation of the response with theory. In addition, due to the high concentrations of methylene blue, reference values used in the predictions and theory comparisons were calculated from the concentrations of reagents and thus represent estimates of the true concentrations. A result of these considerations is that the primary objective of these experiments is the comparison GLRS responses to real and imaginary dielectric changes in a mixture system.

5.4.1 Univariate Analysis

5.4.1.1 Refractive Index Response

The truncated derivatives of the reflection coefficients are given in figure 5.28 for the entire sample set of mixtures. The data set may be broken up into series of ethanol solutions with changing absorbance characteristics as the absorbance response is clearly orthogonal to the refractive index response. At 0% ethanol, the derivative peaks occur at a wavelength of approximately 607 nm and successive increases in ethanol concentration shift the series of peaks over to the singularity wavelengths that correspond to the real dielectric functions of the absorbance modulation series. Figure 5.29 is a plot of the peak maxima vs. peak position for the derivative data, and it is clear that as the ethanol concentration increases, the position shifts internal to each series increase due to increasing anomalous dispersion effects. This is due to the fact that as the singularity shifts to higher wavelength, the threshold is moving off of the absorbance peak to the high wavelength side, producing shifts to higher bulk index. This is more clearly demonstrated in a plot comparing the reference values of refractive index with the GLRS predicted values in figure 5.30. For lower absorbances the predicted values agree well with the reference values, but at higher concentrations of methylene blue and ethanol, the deviations become substantial.

---

[1] Lin, J.; Brown, C. W. *Spectroscopy,* **1995,** *10* (5), 48-51.

5.4.1.2 Absorbance Response

Figure 5.28 shows nature of the absorbance response of GLRS for the mixture system. The peak height decline is demonstrated for increases in absorbance for each ethanol series as the wavelength dependence of the peak height follows the underlying grating function. In order to compare this response with theory, the derivative peak height variance from the derivative peak height for water versus methylene blue concentration is plotted in figure 5.31. At threshold wavelengths around 607 nm, the peak magnitude decline with methylene blue concentration is largest. This indicates that the threshold wavelength around 607 nm corresponds to the an absorbance region close to the absorbance maximum for methylene blue. As the threshold wavelengths shift to higher wavelengths due to increasing ethanol concentration, the peak height deviation becomes smaller, indicating that the thresholds are occurring away from absorbance maximum. At these ethanol concentration, the absorbance spectrum is predicted to contain two peaks, and the shifts in bulk refractive index result in a shift of the threshold to the valley between peaks. Although this was not confirmed experimentally by a reference method, it is a logical explanation based on the literature and the results presented here.

In order to establish the dependence of the peak height on absorbance, the peak magnitudes were regressed with the methylene blue concentrations. Best fits were achieved for a power relationship between peak height variance and concentration, as expected from theory, and are plotted in figure 5.31 with regression equations and correlation coefficients tabulated in the figure. An exponent range of .37 to .47 indicates qualitative agreement with the theoretical square root dependence of peak height on absorbance. The exponent deviation is most likely a result of dilution induced errors in concentration values and the effect of the ethanol on the equilibrium between methylene blue forms.

5.4.2 Multivariate Analysis: Partial Least Squares Calibration

The degree to which PLS can predict concentration of each analyte in a two component system is related to the orthogonality of response to each analyte. As the derivative peak response to refractive index and absorbance has been shown to be roughly orthogonal, is expected that a PLS calibration of each analyte in the presence of the other would yield satisfactory RMSECV values. This PLS calibration was attempted for two types of sample inputs: a matrix of reflection coefficients and a matrix of the derivatives of the reflection coefficients. As no independent reference method was used for these samples, the as prepared concentrations were used as the reference vector inputs. Table 5.9 details the RMSECV values versus latent variables used in building each model. The RMSECV values are shown graphically in figure 5.32 (a and b) for the EtOH and methylene blue concentration predictions. The variance correlated with changes in EtOH concentration was more easily modeled by PLS as the local minima were reached for models which used between 4 and 6 factors. The derivative spectra generated lower RMSECV values than the reflection coefficient calibrations due to enhanced modeling efficiency resulting from the lineshape of the derivatives. The RMSECV minimum of.440% EtOH for a 5 factor model, which corresponds to a 0.00023 error in refractive index, is representative of the error inherent in the volumetric glassware used and the precision associated with determining peak position. However the PLS modeling procedure was able to predict ethanol concentration to a reasonable error in the presence of a significant absorbance modulation.

Similarly, the PLS modeling procedure was able to predict methylene blue concentration in the presence of ethanol. The methylene blue prediction models required more PLS latent variables (see figure 5.32b) than the ethanol prediction model due the fact that the variance associated with absorbance changes is localized to the threshold region where, in contrast, the refractive index variance is distributed across the wavelength space. However, the errors reported here are lower than the errors for the single component RMSECV methylene blue PLS calibration performed earlier on the reflection coefficients containing the threshold at 605 nm. Due to dilutions of the original methylene blue samples, the sample set concentration range was effectively shifted to a region in the dynamic range that more uniformly spanned the response space which in turn yielded better prediction across the range. In addition, the two lowest concentration methylene blue samples were not used in this calibration, reducing error associated with GLRS insensitivity to low relative absorbance. The errors reported here are similar in magnitude to the single component methylene blue PLS calibrations and give a representation of the power of GLRS to predict concentration of methylene blue in the presence of a refractive index modulating interference.

5.5 GLRS Temperature Response

GLRS threshold theory predicts that substrate temperature variations will not affect the positions of the thresholds. To test this, the sample in contact with the grating was heated through the substrate while data was taken in a static format after some time constant to allow for stabilization. The nature of the temperature programming also allowed for the effects of hysteresis in the sample cell and temperature control electronics to be investigated. The truncated GLRS reflection coefficient derivatives are given figure 5.33 for response to changes in system temperature. The peak position shifted to a lower wavelength for an increase in system temperature. As the temperature was ramped back down to 25°C the peak shifted to higher wavelengths with some apparent hysteresis, which is on the order of 0.1-0.2 nm.

The GLRS peak positions were used to calculate the predicted refractive index at each wavelength for each temperature and the resulting refractive index predictions are given in figure 5.34 along with a linear regression of the data. The correlation coefficient of .987 is due to the small relative wavelength shift as the wavelength accuracy of .1 nm over 2 nm range results in a relative accuracy of 5%. However, the data does allow for comparison of the slope of the regression, which is the temperature dependent dispersion of sample, with the literature value for water. The literature value[2] for the temperature dispersion of water is $\frac{\partial n}{\partial T} = -1.17\times10^{-4}/°C$ and the dispersion obtained from the regression is $\frac{\partial n}{\partial T} = -1.49\times10^{-4}/°C$. This GLRS experimental dispersion agrees well with the literature value considering that the literature value is calculated for a static wavelength and the GLRS value has contained in it a normal dispersion component due to the wavelength shift of the GLRS threshold position.

These data suggest a strong correlation with GLRS theory in that changes in substrate temperature have minimal to no effect on the measurement of refractive index of the sample. For changing substrate temperatures bias would be introduced into ATR and SPR measurements as the response function is dependent upon the relative refractive indices of the sample and substrate material. The planar nature of the substrate allows for the cancellation of substrate effects, even in instances where the sample is heated through the substrate, as demonstrated here.

---

[2] Weast, R. C. Ed.*CRC Handbook of Chemistry and Physics*, 70th ed.; CRC Press: Boca Raton, FL, 1989, E-384.

Table 5.1 GLRS derivative peak positions and magnitudes for triplicate runs of four ethanol solutions.

Ethanol Concentration in water, %vol./vol.	GLRS derivative peak position, nanometers	GLRS peak magnitude, relative
10	619.349	0.0044128
10	619.246	0.0044212
10	619.246	0.0044347
20	624.202	0.0045363
20	624.202	0.0045340
20	624.408	0.0045410
30	628.126	0.0046560
30	628.022	0.0046500
30	628.023	0.0046530
40	632.049	0.0041695
40	632.049	0.0041622
40	632.360	0.0041877

Table 5.2 Means and standard deviation values for replicate runs of ethanol:water solutions.

Ethanol Concentration, %vol./vol.	Mean Peak Position, nanometers	Standard deviation of peak position, nanometers	Mean Peak magnitude, relative	Standard deviation of peak magnitude, relative
10	619.28	0.059	0.00442	0.000011
20	624.27	0.12	0.004537	0.0000036
30	628.06	0.060	0.004653	0.0000030
40	632.15	0.18	0.00417	0.000013
Mean Standard Deviation		0.10		0.0000076

Table 5.3 GLRS threshold positions for each polarization and GLRS predicted refractive indices using equation (2.4).

Ethanol concentration, % vol./vol	GLRS first derivative peak position, λ_{cr}, p-polarization	GLRS first derivative peak position, λ_{cr}, s-polarization	GLRS predicted refractive index at λ_{cr}, p-polarization	GLRS predicted refractive index at λ_{cr}, s-polarization
0.00	615.48	614.59	1.3322	1.3311
0.00	615.46	614.57	1.3322	1.3311
1.00	615.79	615.14	1.3326	1.3318
5.00	617.28	617.06	1.3344	1.3341
10.00	619.26	619.14	1.3368	1.3366
15.00	621.64	621.31	1.3396	1.3392
20.00	624.14	623.75	1.3427	1.3422
25.00	626.28	626.16	1.3452	1.3451
30.00	628.11	628.48	1.3474	1.3479
35.00	630.31	630.37	1.3501	1.3502
40.00	632.16	632.18	1.3523	1.3524

Table 5.4 Summary of calibration errors for the GLRS sensor response to refractive index variations.

Calibration model	Bias, RMS index units	Precision, RMS index units
p-polarization, comparison with reference values	0.0012	0.00024
s-polarization, comparison with reference values	0.00072	0.00031
p-polarization, linear least squares fit to wavelength data	-	0.000058
p-polarization, linear least squares fit to wavelength data	-	0.000076

Table 5.5 Reference values of refractive index used in the multivariate calibration of the GLRS sensor to refractive index.

Ethanol concentration, % vol./vol	Refractive index at 589.3 nm, 27° C
0.00	1.3321
1.00	1.3327
5.00	1.3347
10.00	1.3373
15.00	1.3400
20.00	1.3429
25.00	1.3457
30.00	1.3484
35.00	1.3507
40.00	1.3530

Table 5.6 RMSECV values for Partial Least Squares calibration of GLRS refractive index response.

Number of PLS Latent Variables	RMSECV, p-polarization, refractive index units	RMSECV, s-polarization, refractive index units
1	0.0004471	0.0002576
2	0.0003861	0.0001583
3	0.0001278	0.0000785
4	0.0000763	0.0000488
5	0.0000627	0.0000305
6	0.0000413	0.0000240
7	0.0000175	0.0000238
8	0.0000018	0.0000238
9	0.0000032	0.0000027
10	0.0000039	0.0000054

Table 5.7 Imaginary part of the dielectric function at specific threshold wavelengths, $\mathrm{Im}(\varepsilon) = \lambda\sqrt{\mathrm{Re}(\varepsilon)} \cdot A_{1\,\mathrm{cm.}}$, where $A_{1\,\mathrm{cm.}}$ is the one centimeter pathlength absorbance of methylene blue at λ.

Methylene Blue Concentration, M	Im(ε) at 605 nm	Im(ε) at 630 nm	Im(ε) at 683 nm
0.00000999	0.0000742	0.0000935	0.0000970
0.00004996	0.0004263	0.0004335	0.0004005
0.00009992	0.0008055	0.0007583	0.0006632
0.0004996	0.004361	0.003173	0.002210
0.001022	0.008892	0.005904	0.003853
0.005127	0.04435	0.02810	0.01770

Table 5.8 PLS calibration of GLRS absorbance response to methylene blue solutions at three angles of incidence using GLRS ratio and derivative data as sample input matrices. Local minima are given in boldface type.

PLS factor	RMSECV, M MTB: 30.62° incident angle, reflection coefficient calibration	RMSECV, M MTB 30.62° incident angle, derivative calibration	RMSECV, M MTB: 34.98° incident angle, reflection coefficient calibration	RMSECV, M MTB: 34.98° incident angle, derivative calibration	RMSECV, M MTB: 37.11° incident angle, reflection coefficient calibration	RMSECV, M MTB: 37.11° incident angle, derivative calibration
1	0.0001538	0.0003360	0.0002278	0.0002095	0.0013576	0.0008180
2	0.0001560	0.0001835	0.0001116	0.0001455	0.0005360	0.0008162
3	0.0000925	0.0001166	**0.0000533**	0.0001147	**0.0005311**	0.0007863
4	**0.0000641**	0.0001141	0.0000577	0.0000595	0.0005385	0.0007812
5	0.0000648	**0.0000866**	0.0000544	**0.0000580**	0.0005384	**0.0007775**
6	0.0000649	0.0000876	0.0000543	0.0000660	0.0005385	0.0007775
7	0.0000647	0.0000877	0.0000543	0.0000660	0.0005385	0.0007783
8	0.0000374	0.0000926	0.0000551	0.0000655	0.0005448	0.0007767
9	0.0000383	0.0000921	0.0000557	0.0000706	0.0005471	0.0007829
10	0.0000395	0.0000932	0.0000560	0.0000691	0.0005329	0.0007877

Table 5.9 GLRS ethanol:methylene blue mixture calibration results using individual PLS calibration models to predict one analyte in the presence of the other. RMSECV values are given for both reflection coefficient and derivative matrices input as the response matrices in the PLS model. Local minima are given in boldface type.

PLS factor	RMSECV, % EtOH, reflection coefficient calibration	RMSECV, % EtOH, derivative calibration	RMSECV, M MTB, reflection coefficient calibration	RMSECV, M MTB, derivative calibration
1	1.276	1.556	0.001314	0.001291
2	0.966	1.479	0.000720	0.001196
3	1.040	1.139	0.000722	0.000728
4	0.689	0.951	0.000275	0.000346
5	0.733	**0.440**	0.000202	0.000259
6	0.516	0.466	0.000145	0.000173
7	0.471	0.432	0.000111	0.000158
8	**0.435**	0.580	0.000115	0.000108
9	0.486	0.517	0.000062	0.000059
10	0.476	0.477	**0.000058**	**0.000048**
11	0.476	0.554	0.000058	0.000068
12	0.476	0.531	0.000058	0.000064
13	0.476	0.527	0.000058	0.000064
14	0.476	0.529	0.000058	0.000063
15	0.476	0.527	0.000058	0.000063
16	0.476	0.527	0.000058	0.000063
17	0.476	0.527	0.000058	0.000063
18	0.476	0.526	0.000058	0.000062
19	0.476	0.526	0.000058	0.000062
20	0.476	0.526	0.000058	0.000062

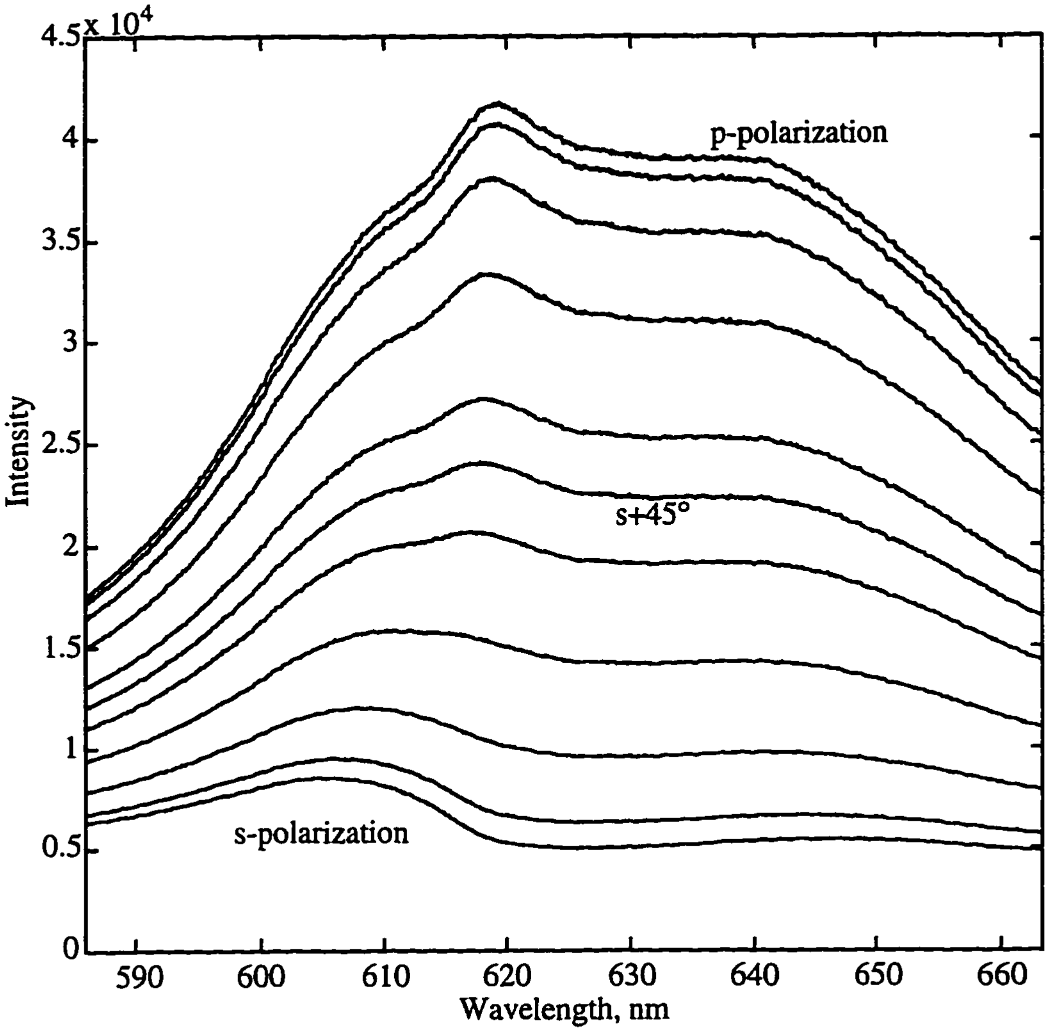

Figure 5.1 GLRS reflection intensity, zeroth order reflection, polarization variation experiment.

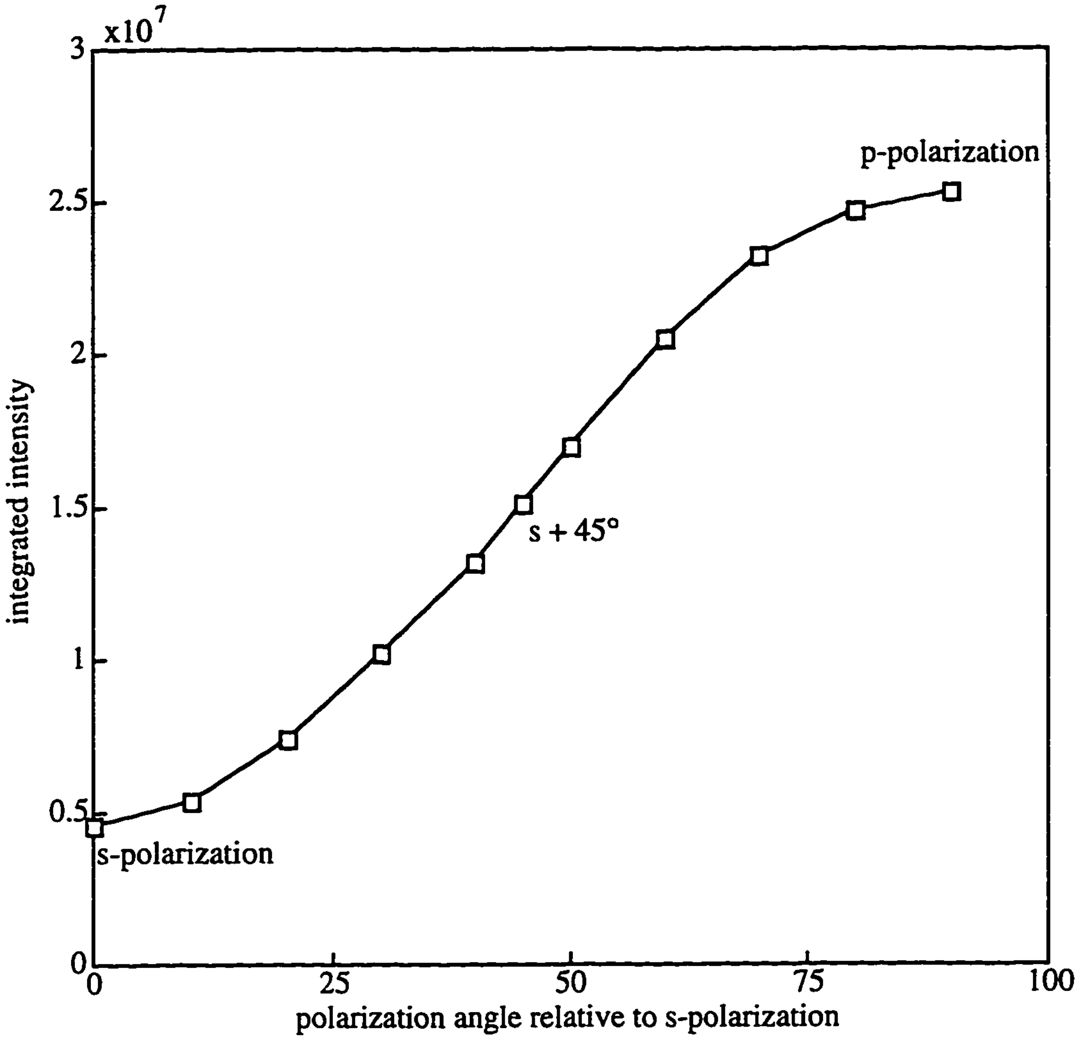

Figure 5.2 Dependence of the integrated intensity of the zeroth order reflection on polarization angle.

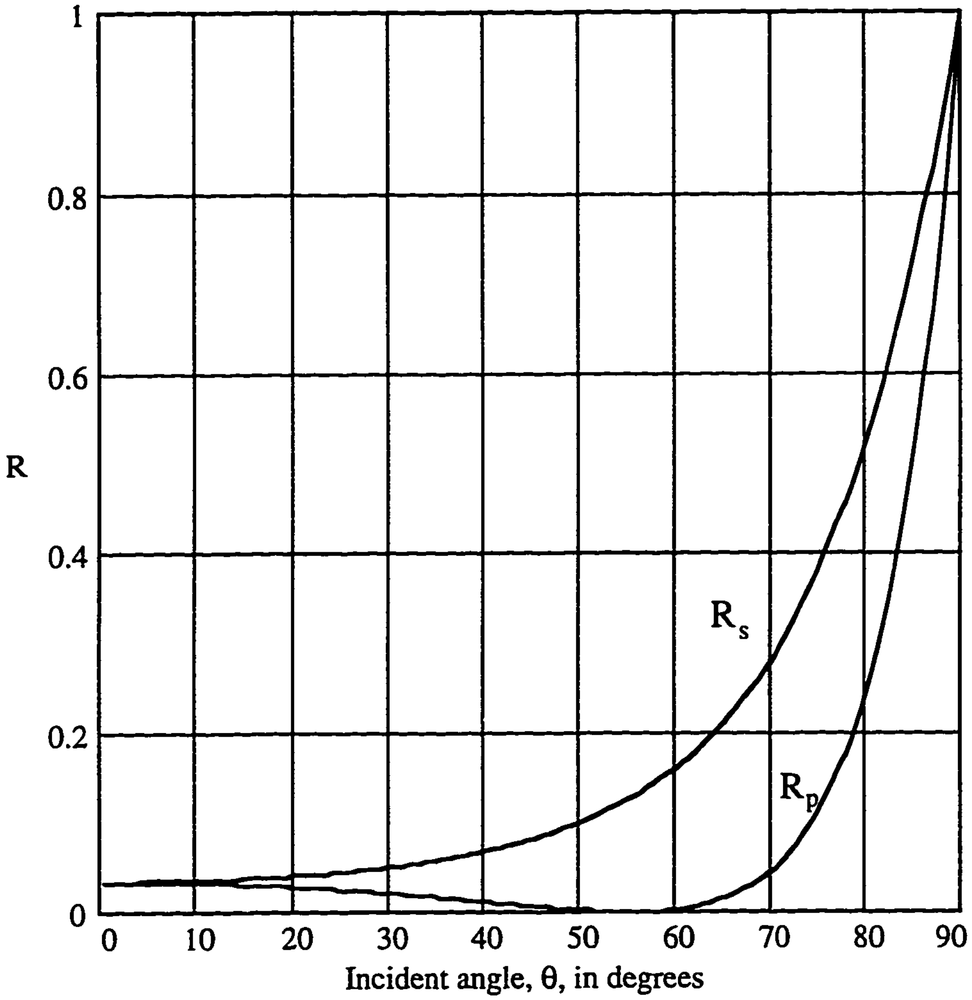

Figure 5.3 Fresnel polarization dependent reflection coefficients, R, for fused silica/air interface as a function of angle of incidence.

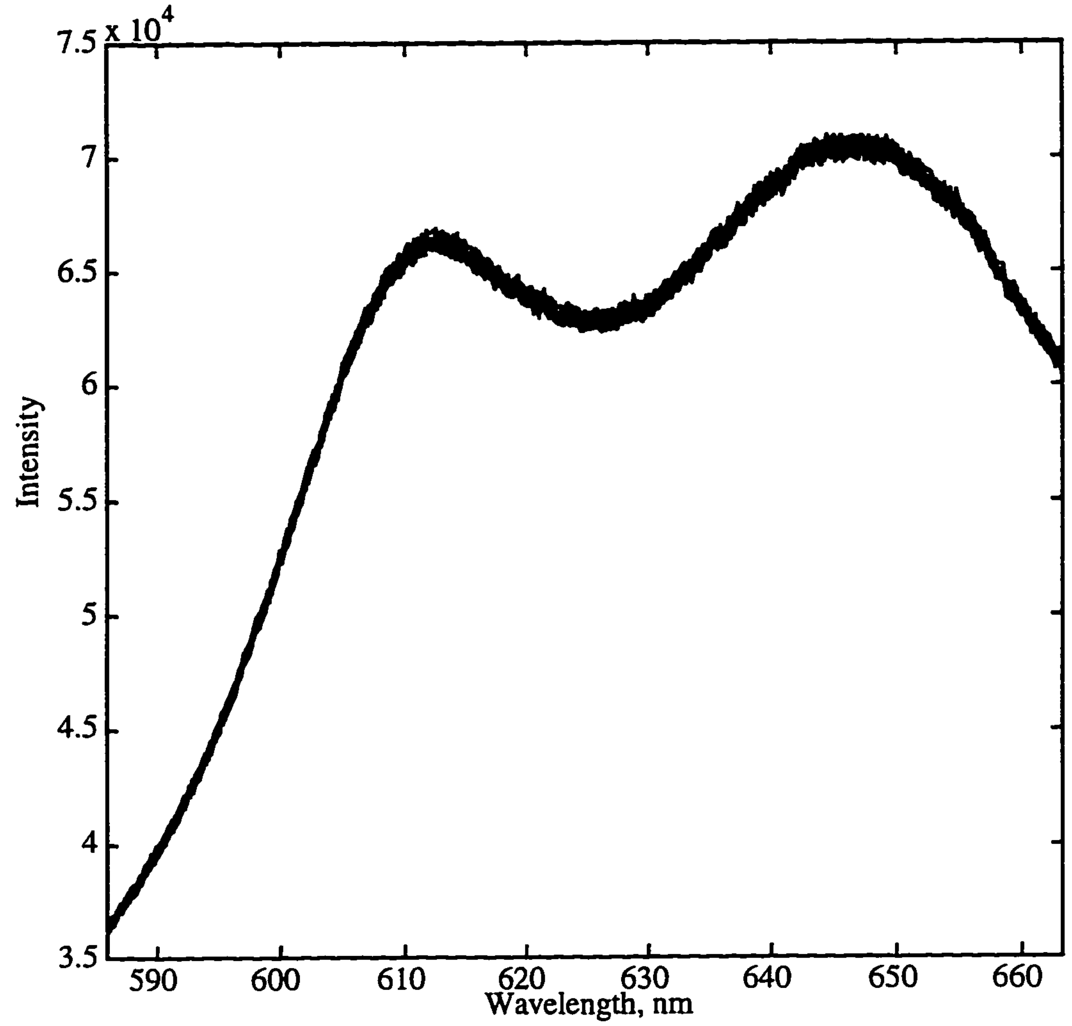

Figure 5.4 Reference channel intensities for 11 20-scan averages corresponding in time to the acquisition of the polarization variation zeroth order reflected intensities. These are representative of the time variance in source intensity over the course of a typical experiment.

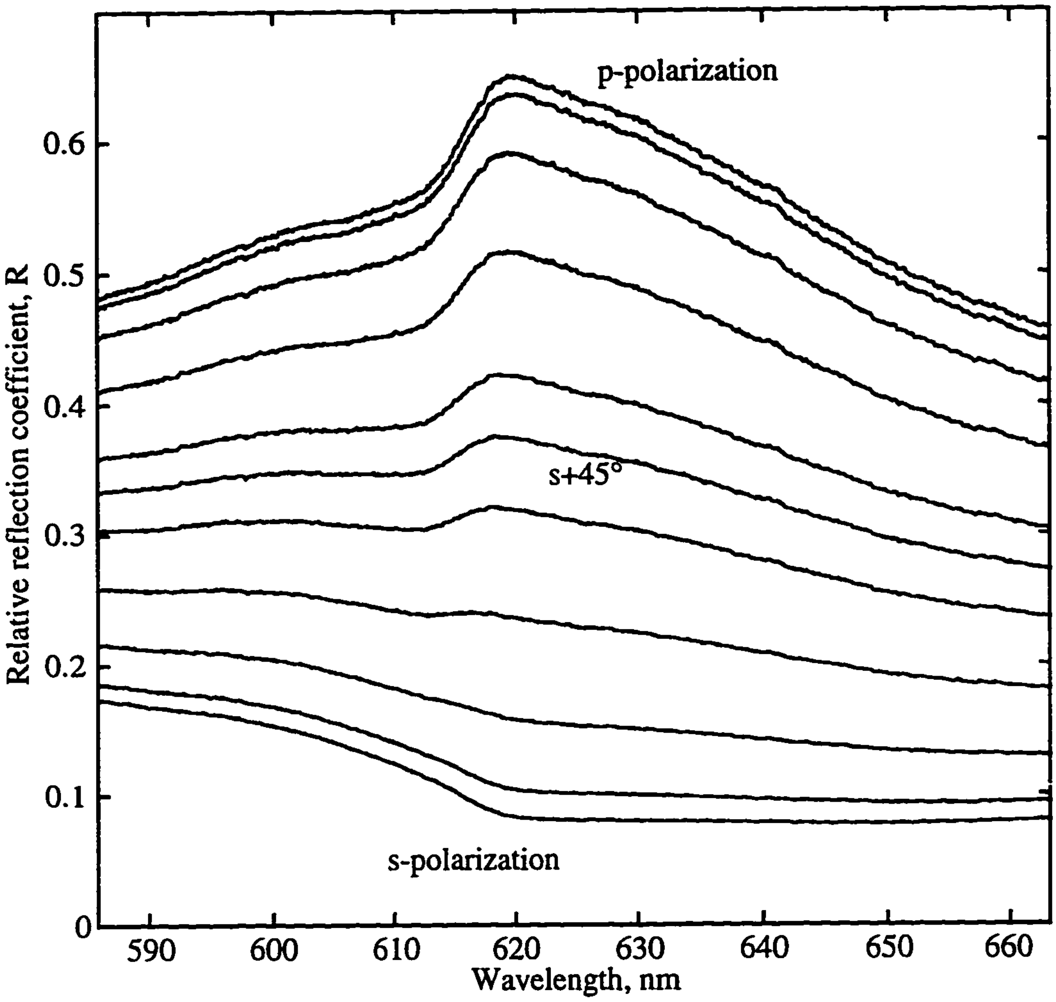

Figure 5.5 GLRS Relative reflection coefficient as a function of polarization angle.

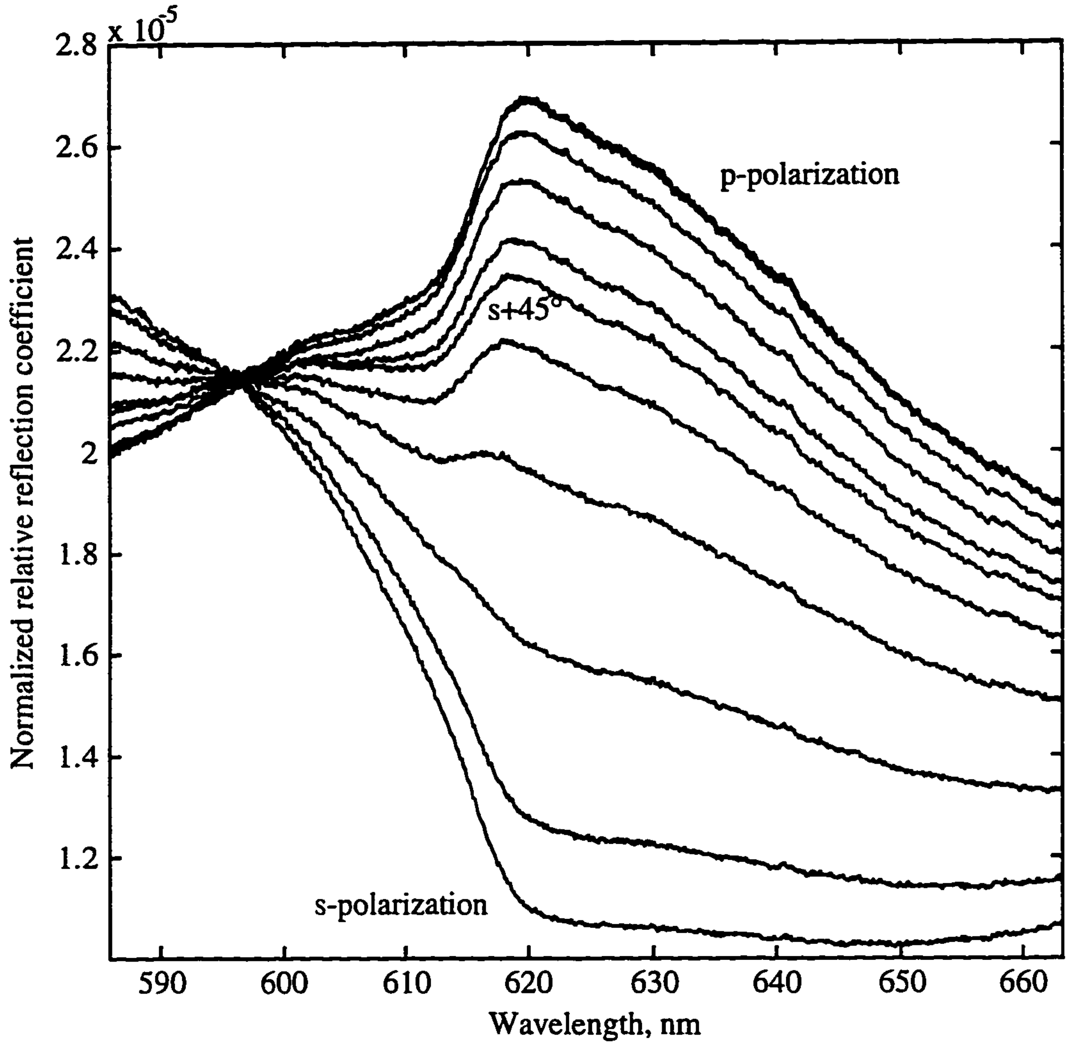

Figure 5.6 Normalized GLRS relative reflection coefficient as a function of polarization angle.

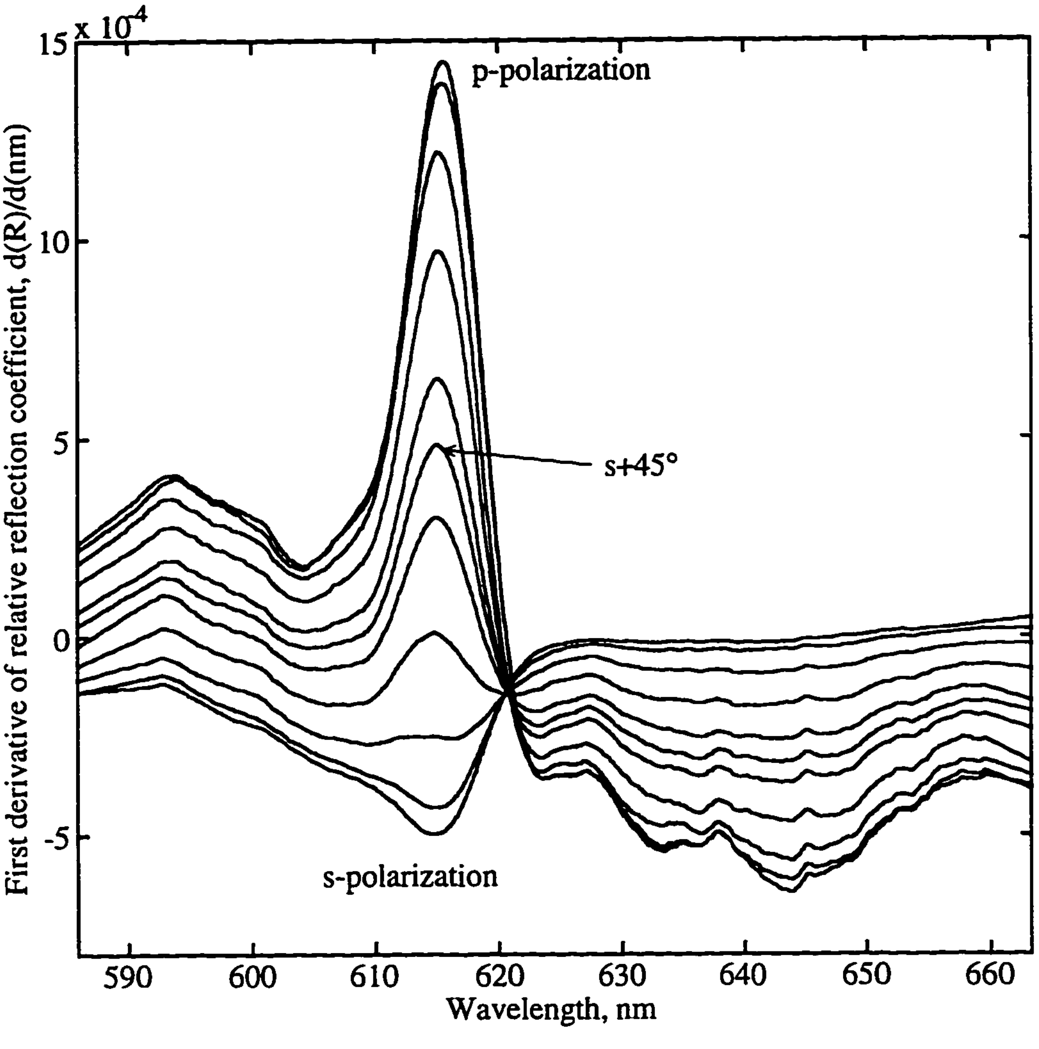

Figure 5.7 GLRS relative reflection coefficient derivative as a function of polarization angle

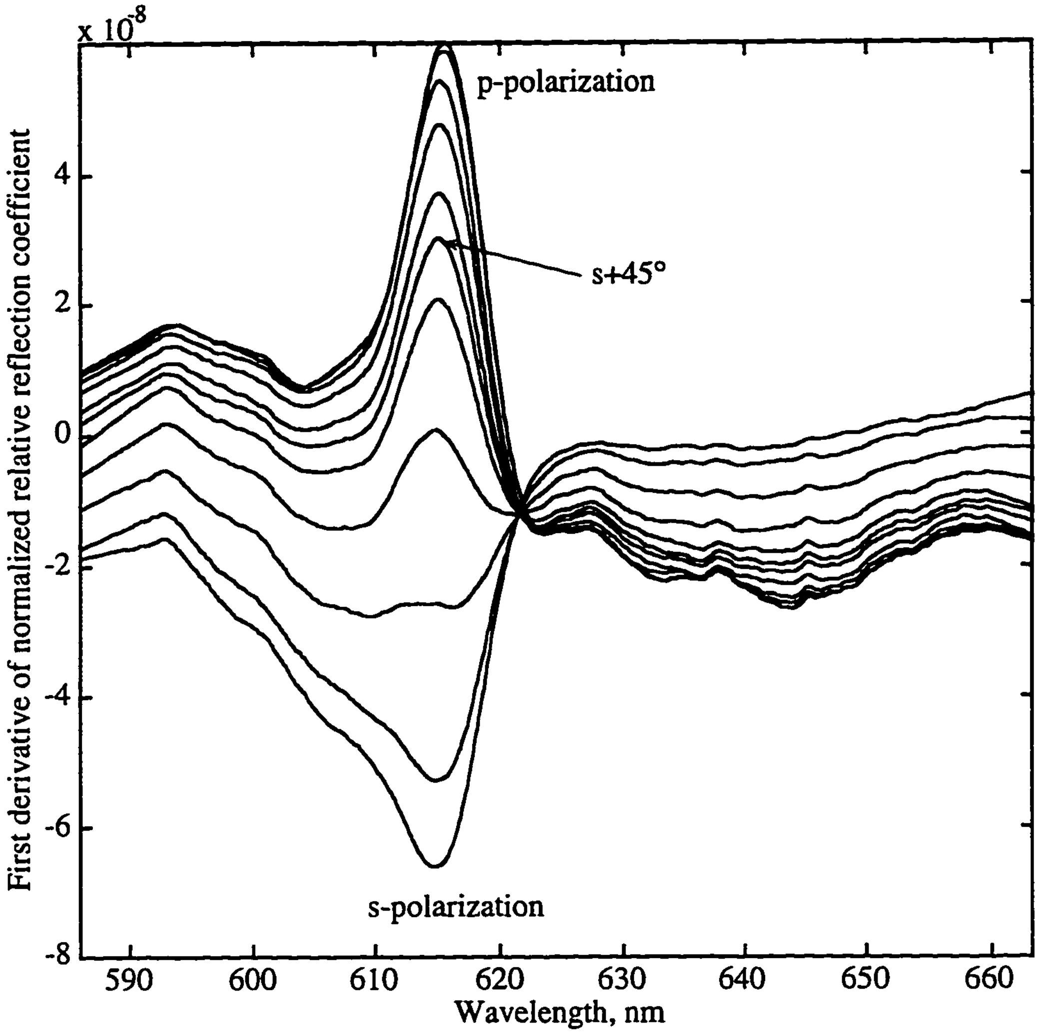

Figure 5.8 GLRS normalized relative reflection coefficient derivative as a function of polarization angle.

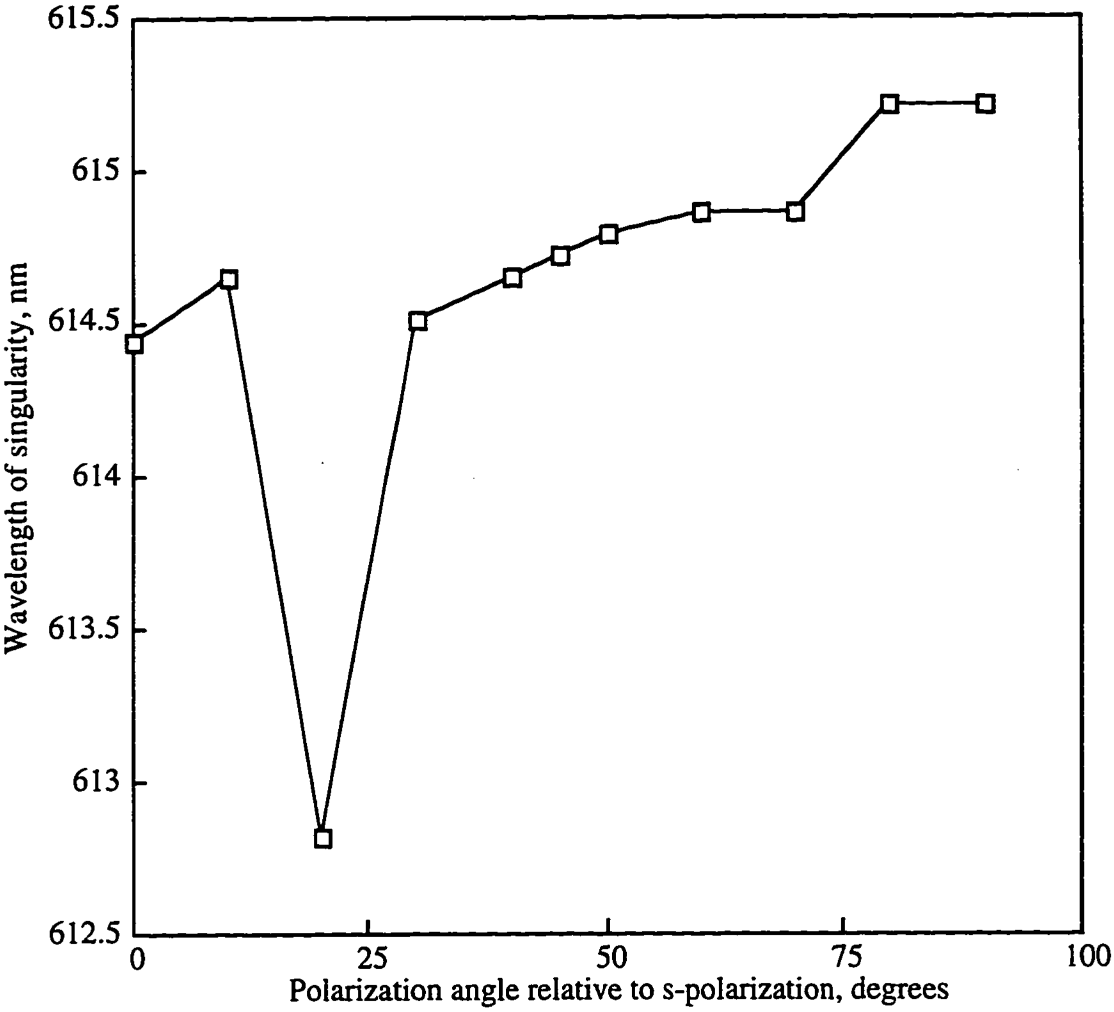

Figure 5.9 Position of GLRS threshold as a function of polarization angle.

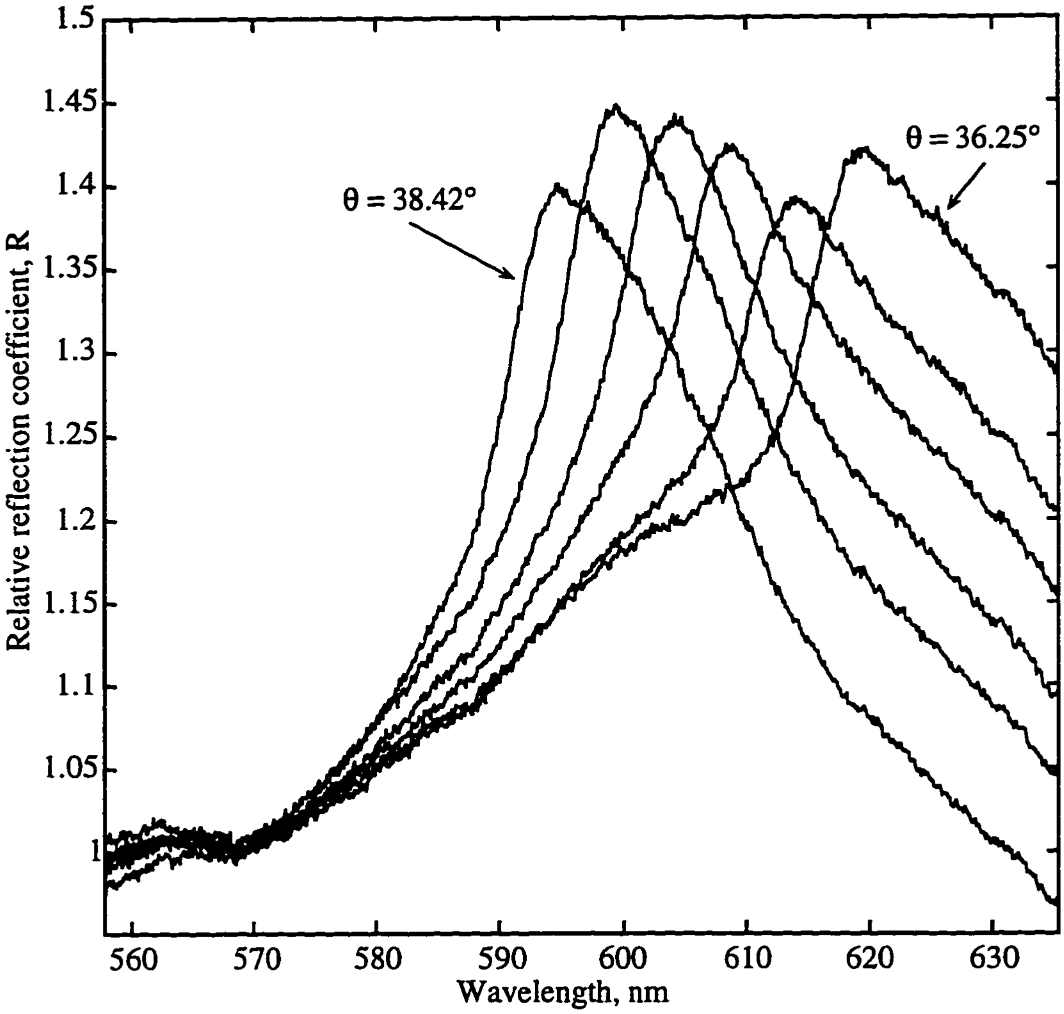

Figure 5.10a GLRS reflection coefficient as a function of incident angle in the range of 36.25° to 38.42°: water in the sample cell.

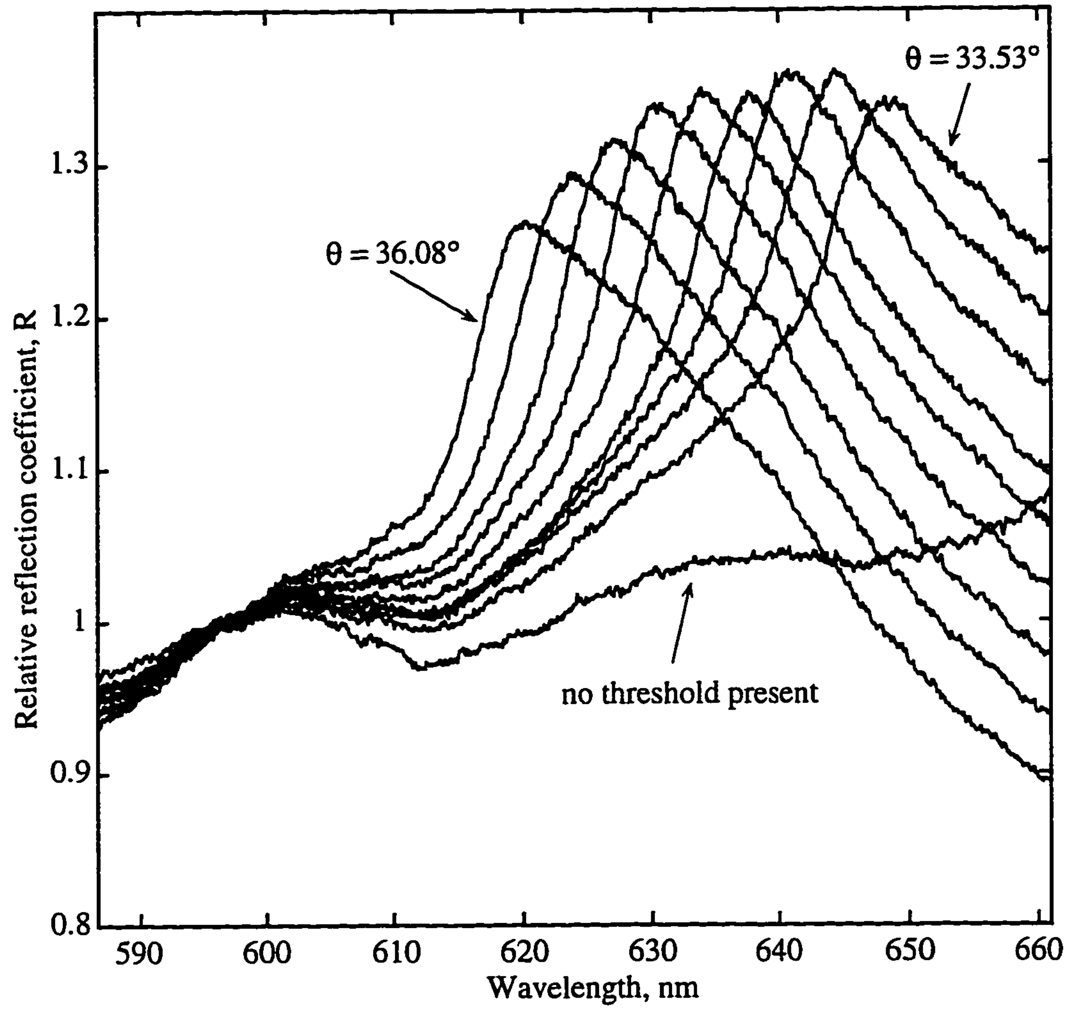

Figure 5.10b GLRS reflection coefficient as a function of incident angle in the range of 33.53° to 36.08°: water in the sample cell.

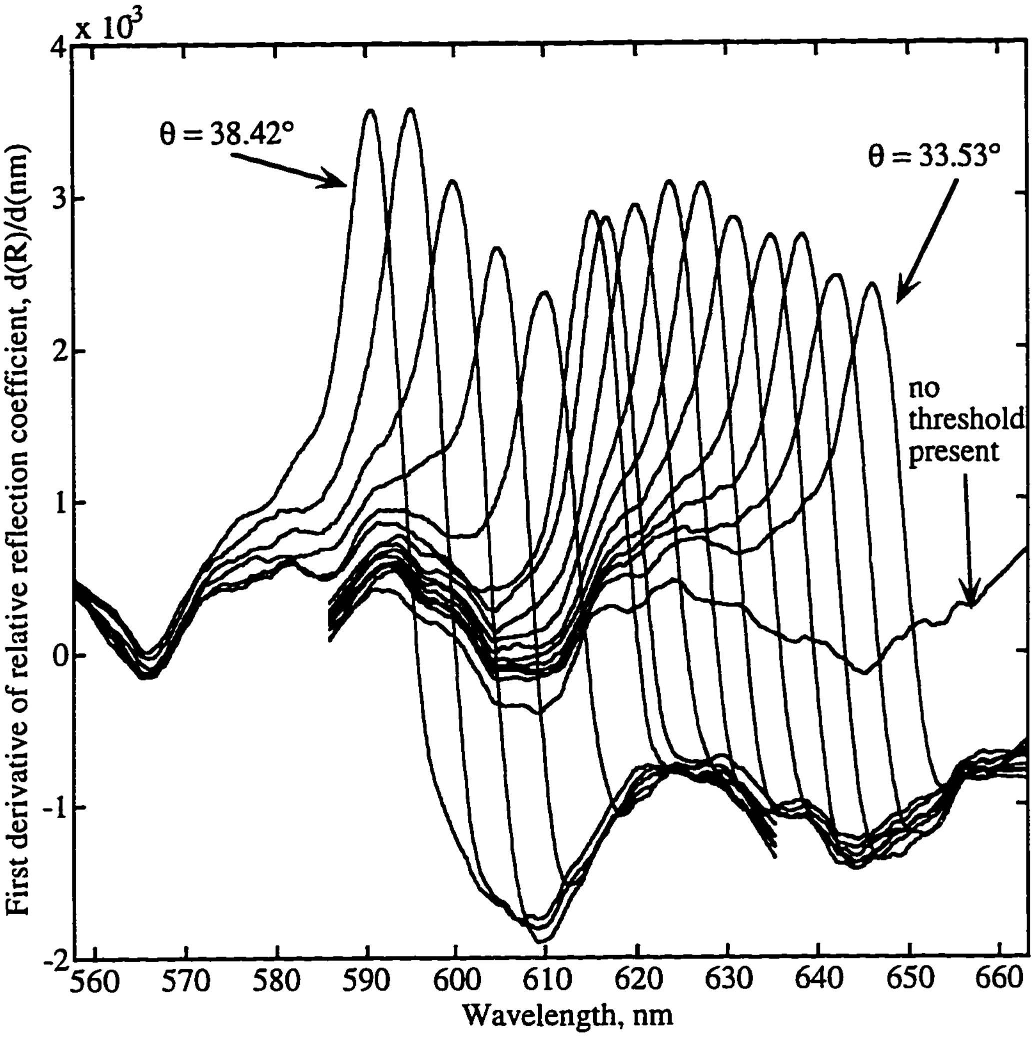

Figure 5.11 GLRS relative reflection coefficient derivative as a function of incident angle: water in the cell.

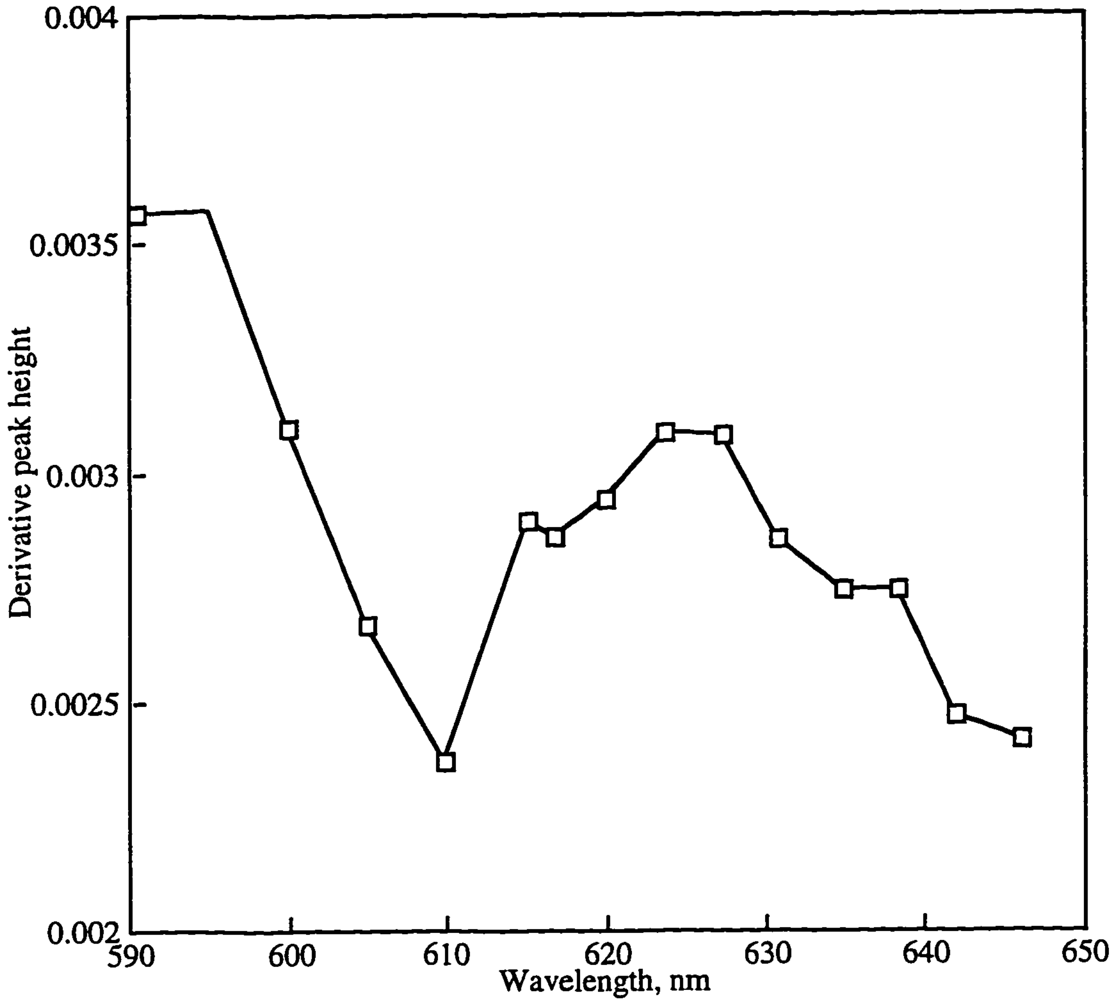

Figure 5.12 Derivative peak height versus wavelength of singularity for water in the cell, angle variation.

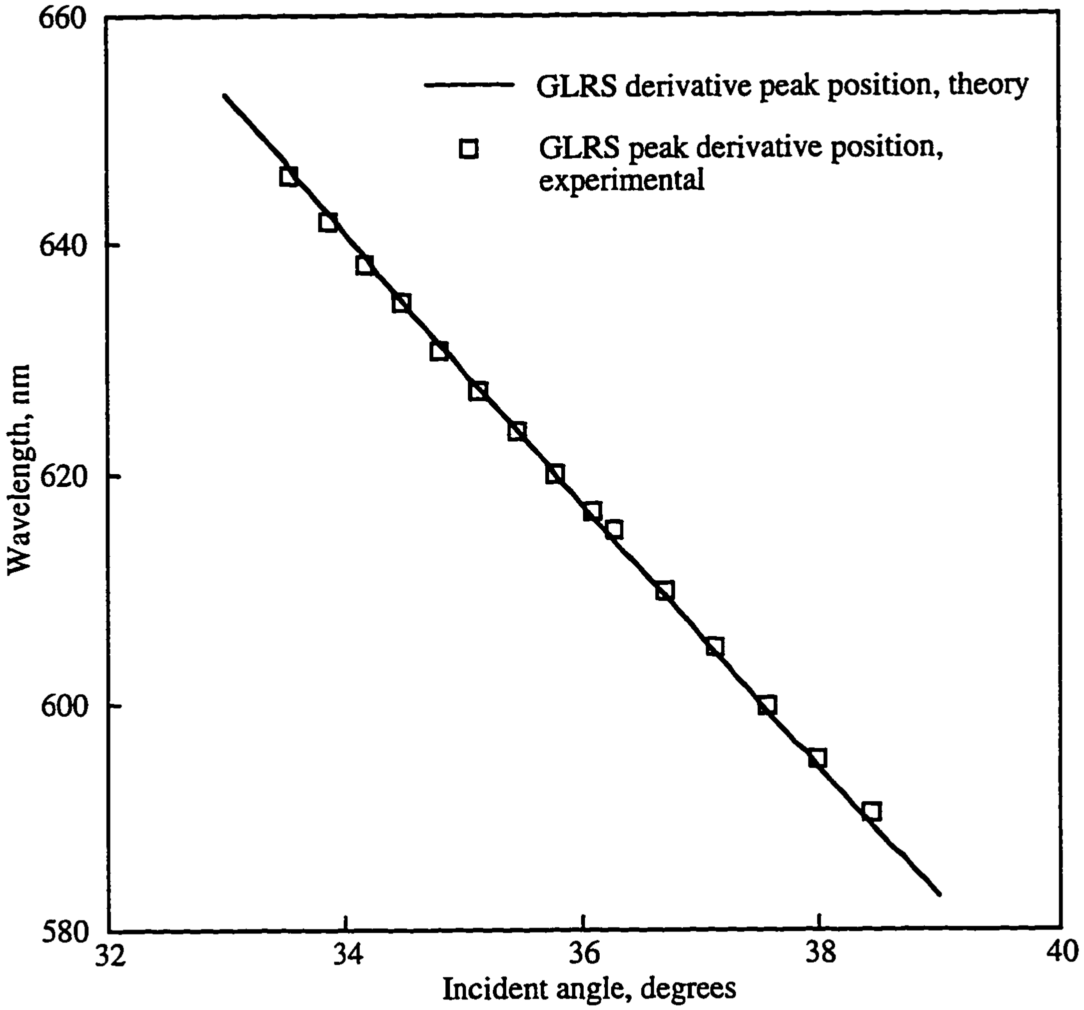

Figure 5.13 Comparison of the predicted versus the experimental threshold positions for the angle variation experiments.

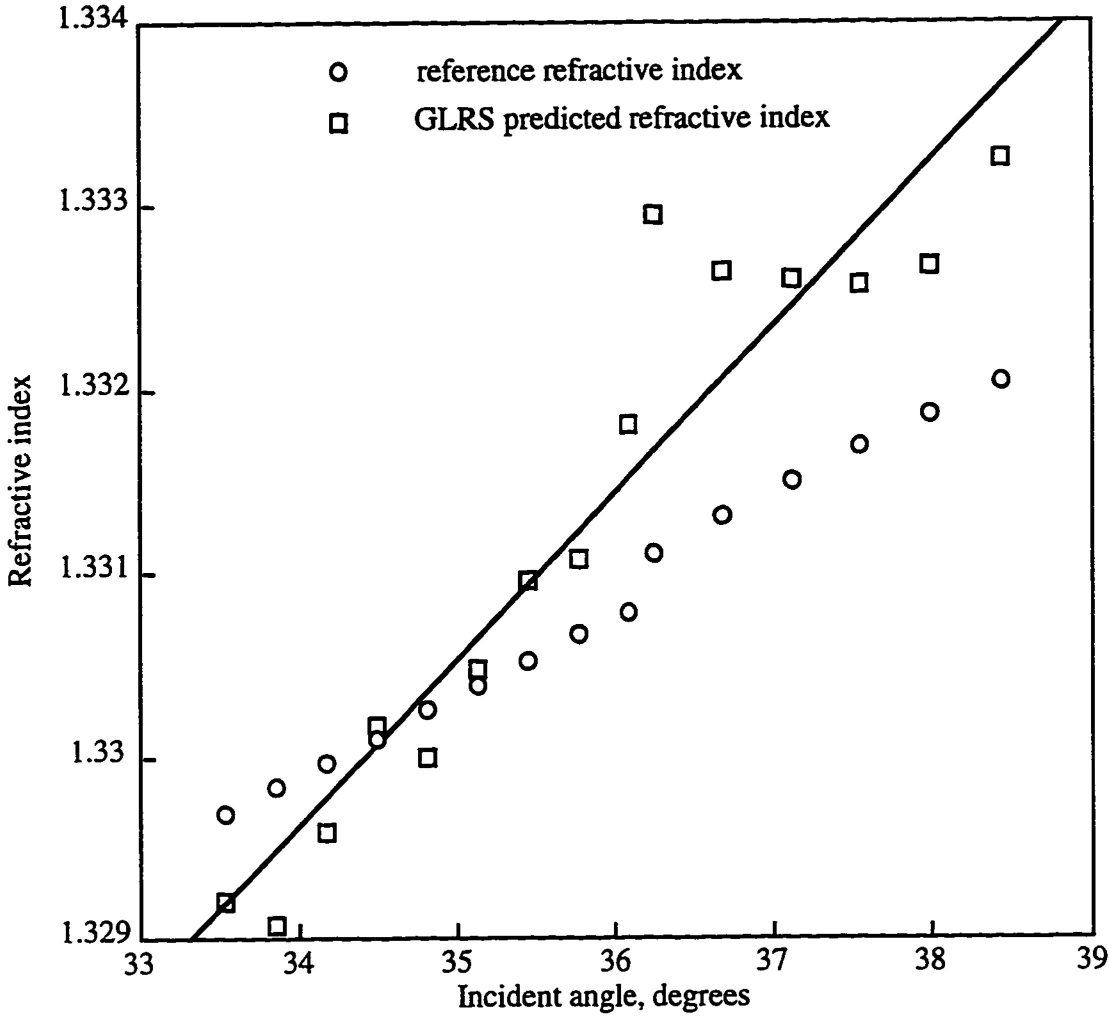

Figure 5.14 GLRS predicted dispersion for water compared to reference Abbe refractometer measurements of dispersion. The regression for the GLRS predicted refractive index with incident angle is y = 1.2987 + 0.0009*x with a correlation coefficient of 0.898.

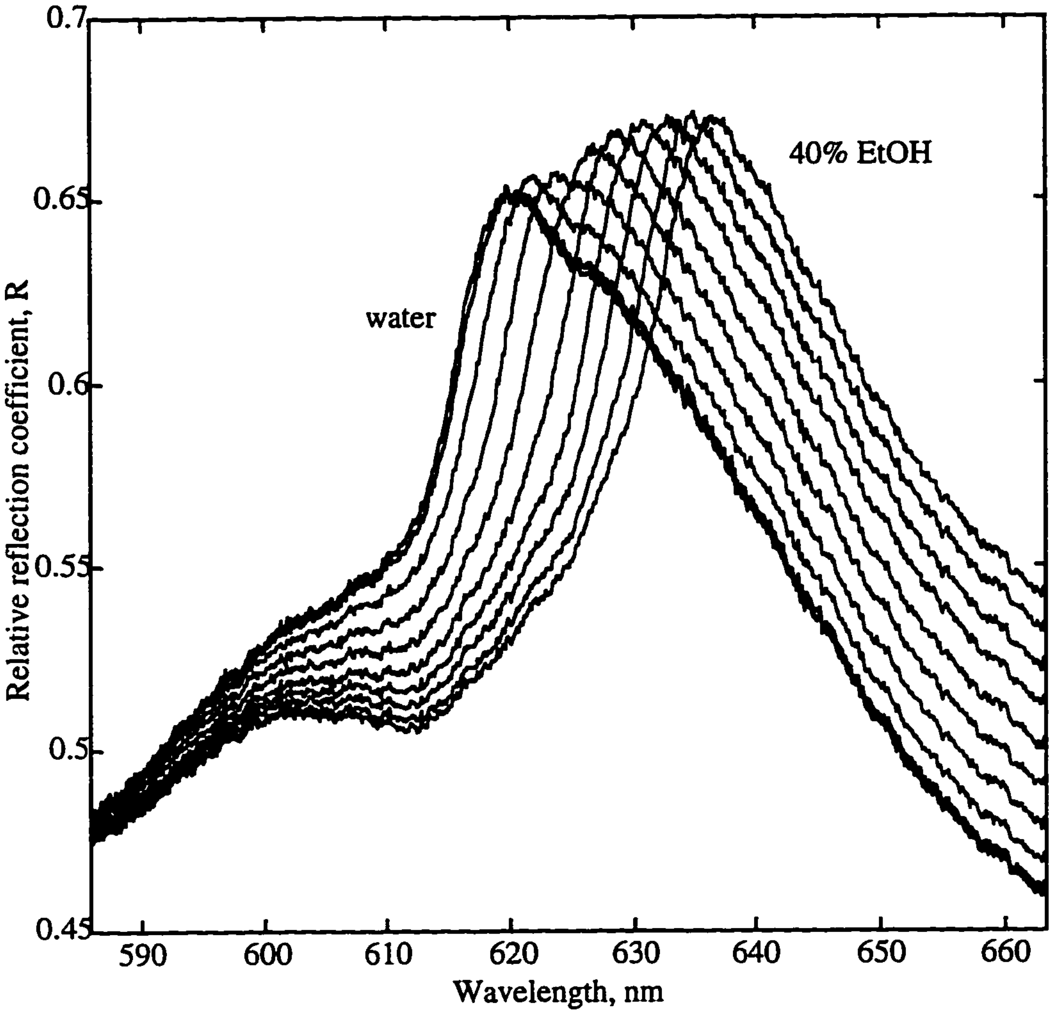

Figure 5.15 GLRS relative reflection coefficient as a function of ethanol concentration, p-polarization.

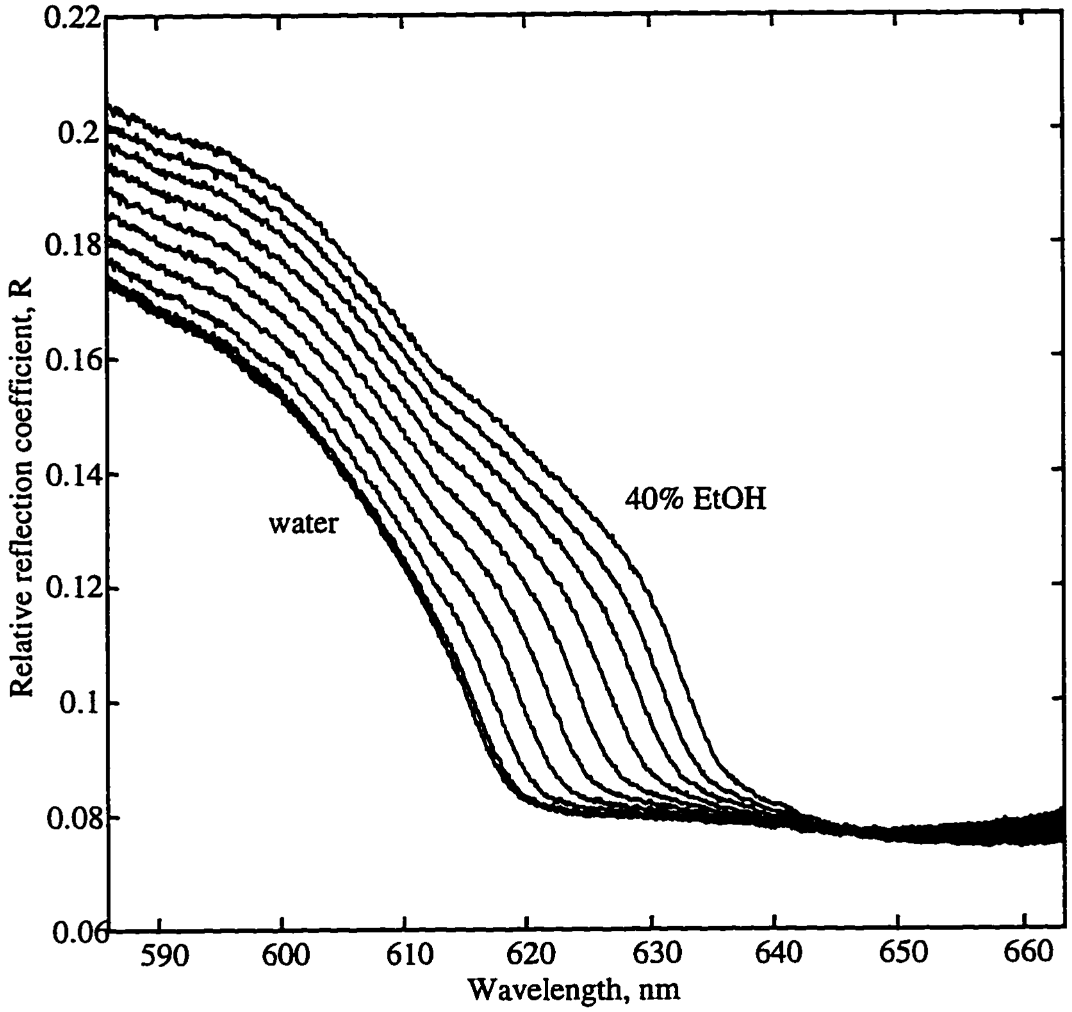

Figure 5.16 GLRS relative reflection coefficient as a function of ethanol concentration, s-polarization.

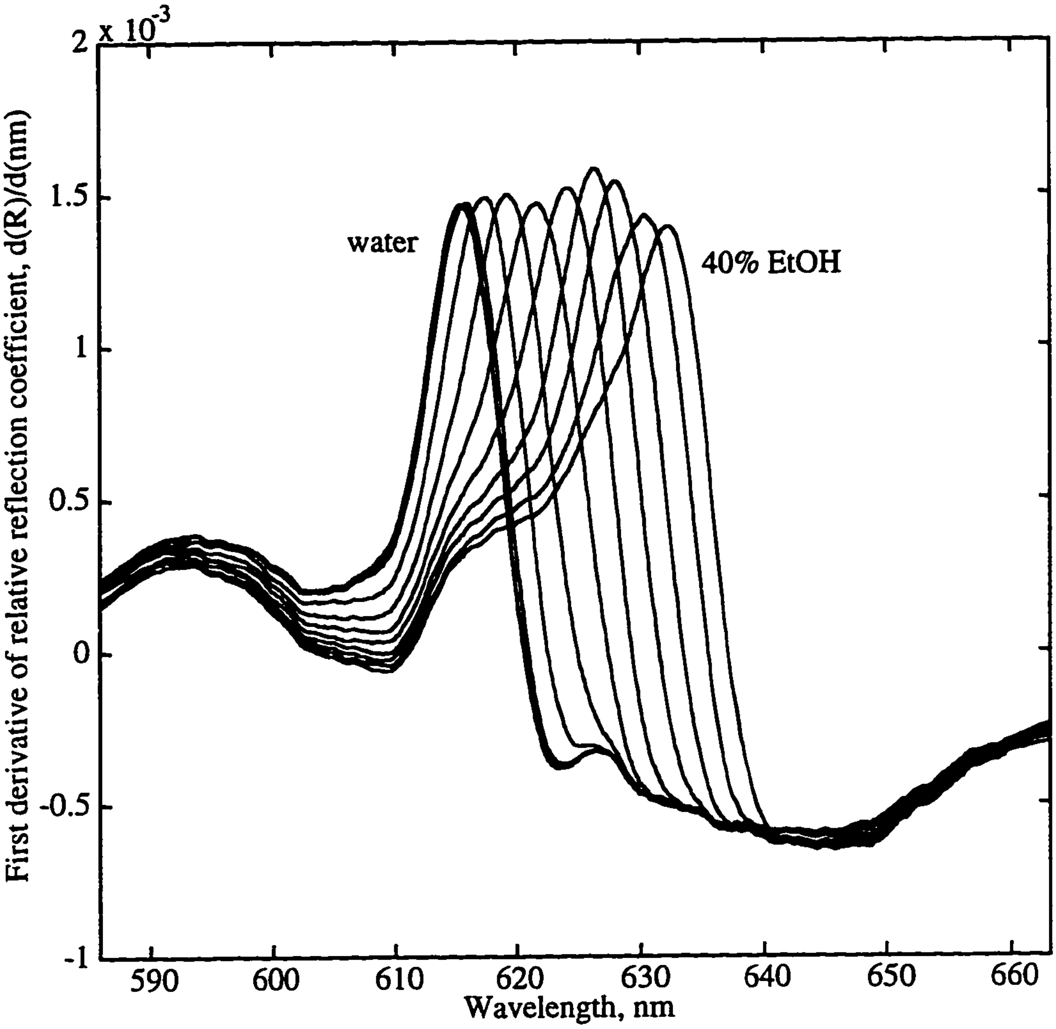

Figure 5.17 GLRS relative reflection coefficient derivative as a function of ethanol concentration, p-polarization.

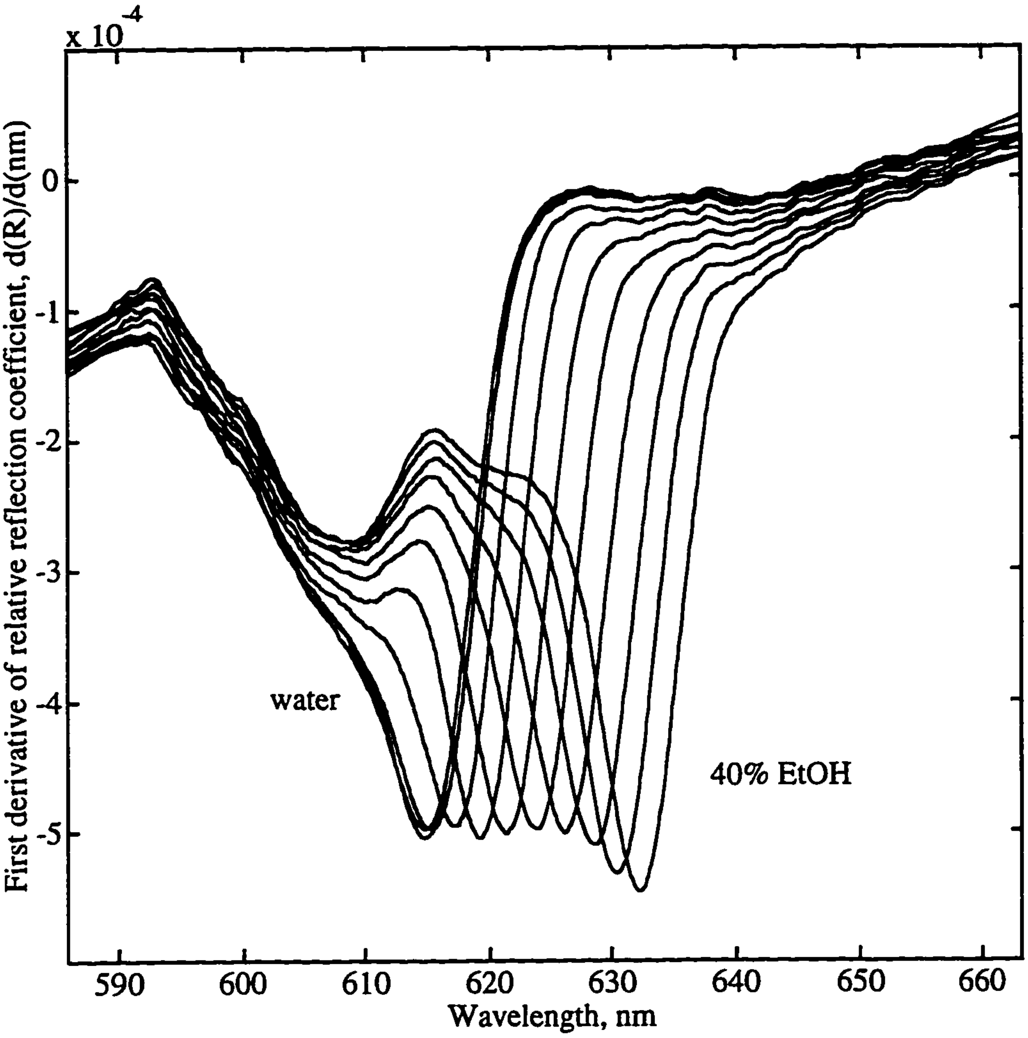

Figure 5.18 GLRS relative reflection coefficient derivative as a function of ethanol concentration, s-polarization.

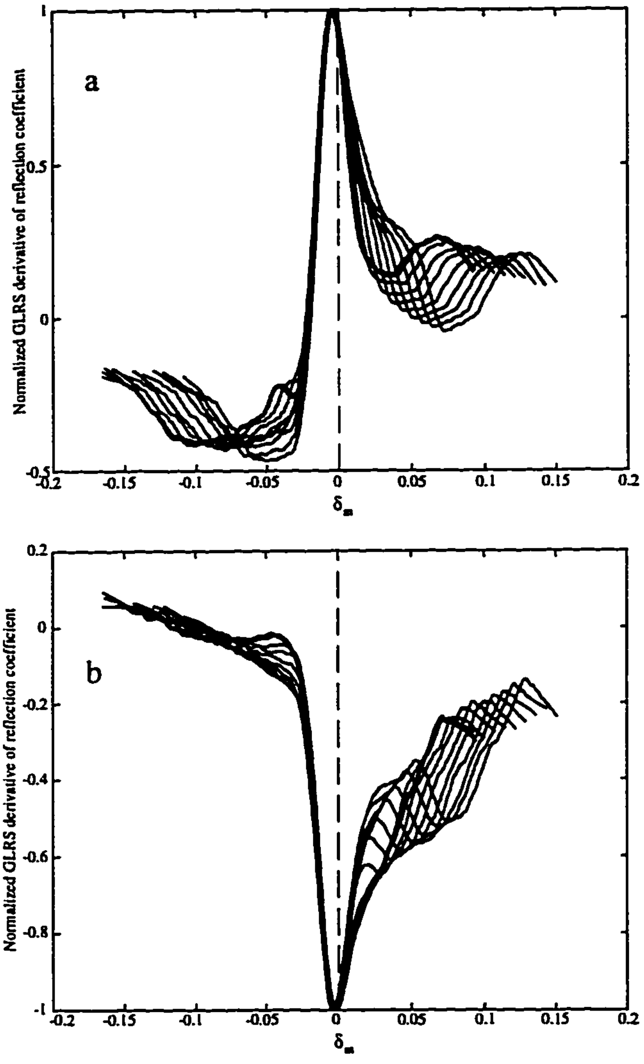

Figure 5.19 GLRS normalized relative reflection coefficient derivatives plotted versus δ_m calculated from ethanol:water refractive indices, GLRS incident angle, grating period, and wavelength for a) p-polarization and b) s-polarization. The dashed line correpsonds to the theoretical zero crossing of δ_m.

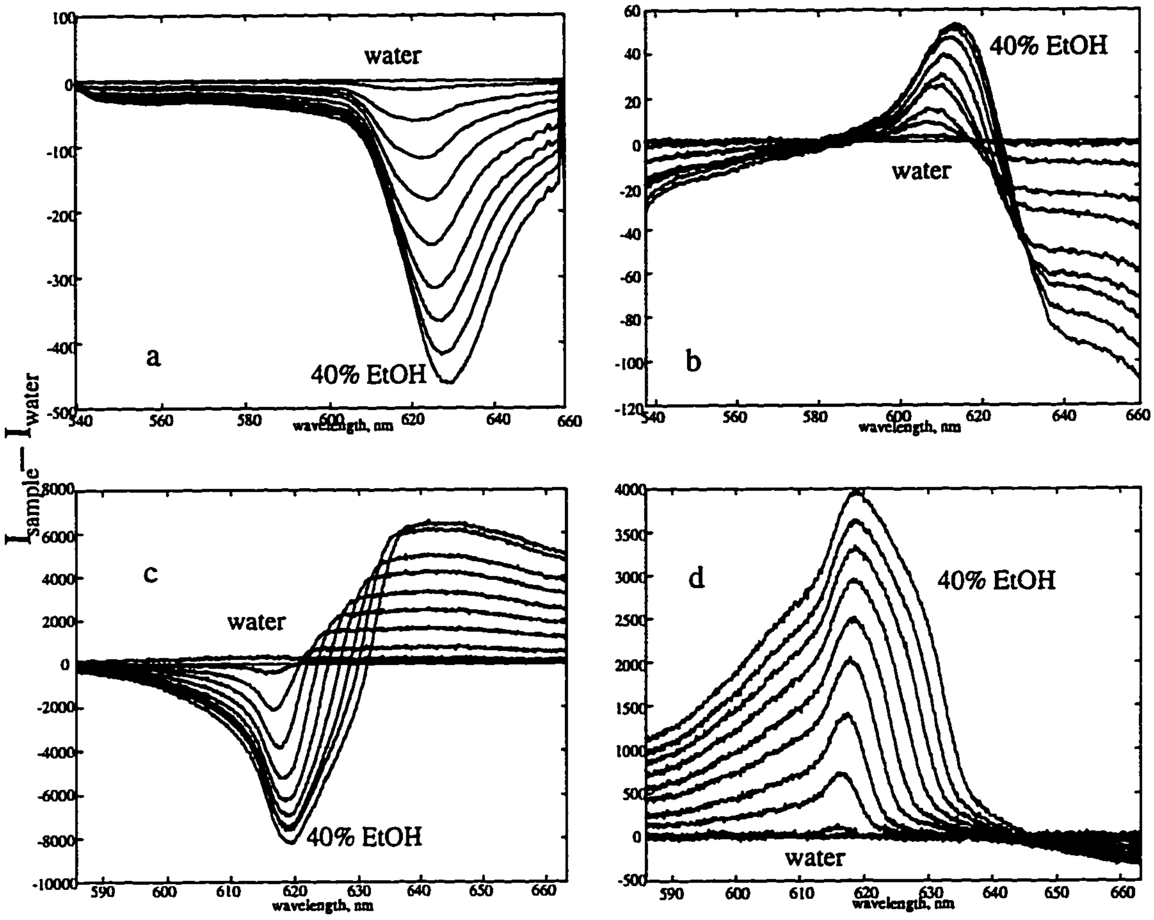

Figure 5.20 Reflected intensity response to ethanol:water solutions, difference with water reflected intensity, for monitored a) first order s-polarization, b) first order p-polarization, c) zeroth order p-polarization, d) zeroth order s-polarization. The peaks here do not correspond to the thresholds but are regions of greatest difference with the water reference reflected intensity.

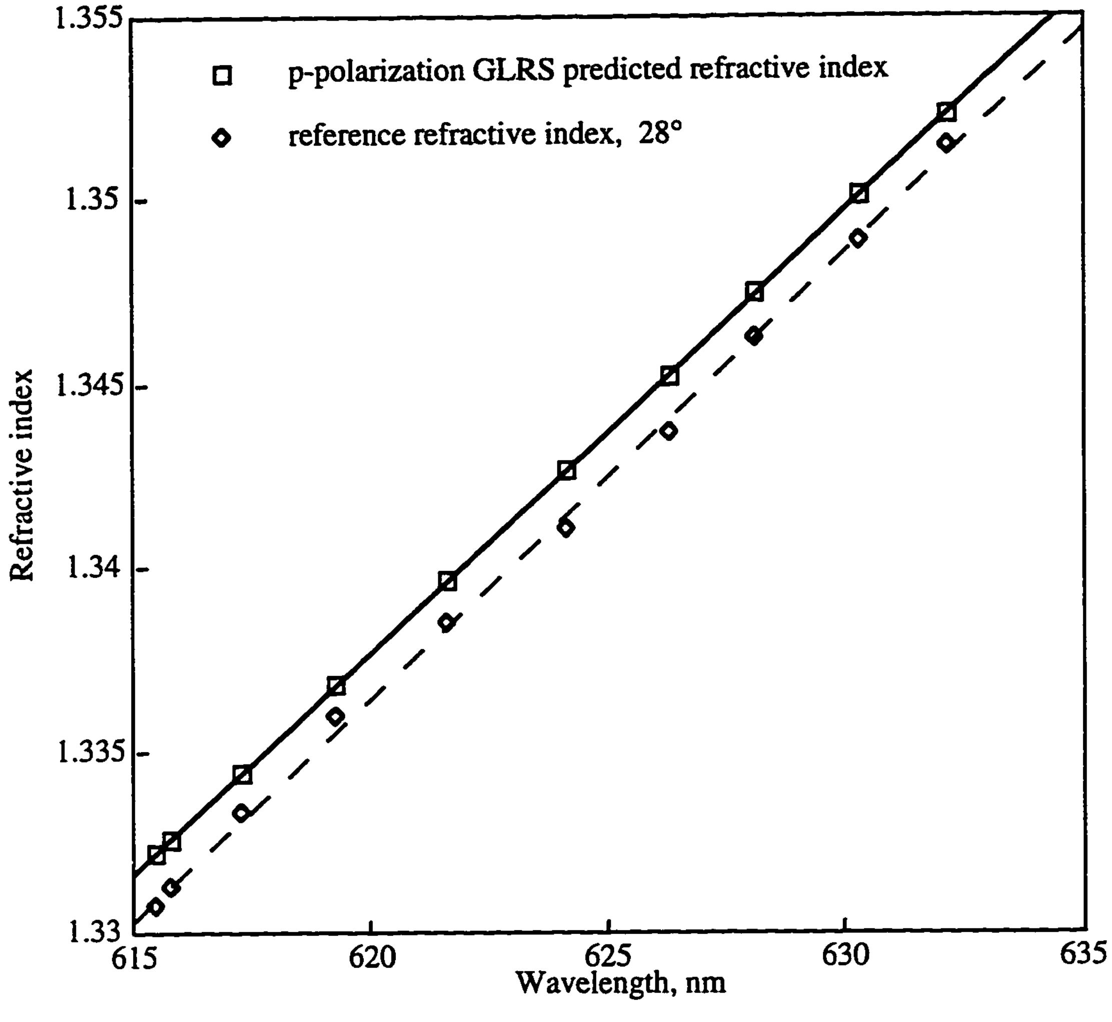

Figure 5.21 Comparison of refractive indices of ethanol:water solutions predicted using GLRS derivative peak positions with reference values, p-polarization. The regression for the GLRS predicted index with wavelength is y = 0.001205*x + 0.5903 with a correlation coefficient of 0.999998. The regression for the reference values with wavelength is y = 0.001215*x + 0.5829 with a correlation coefficient of .998.

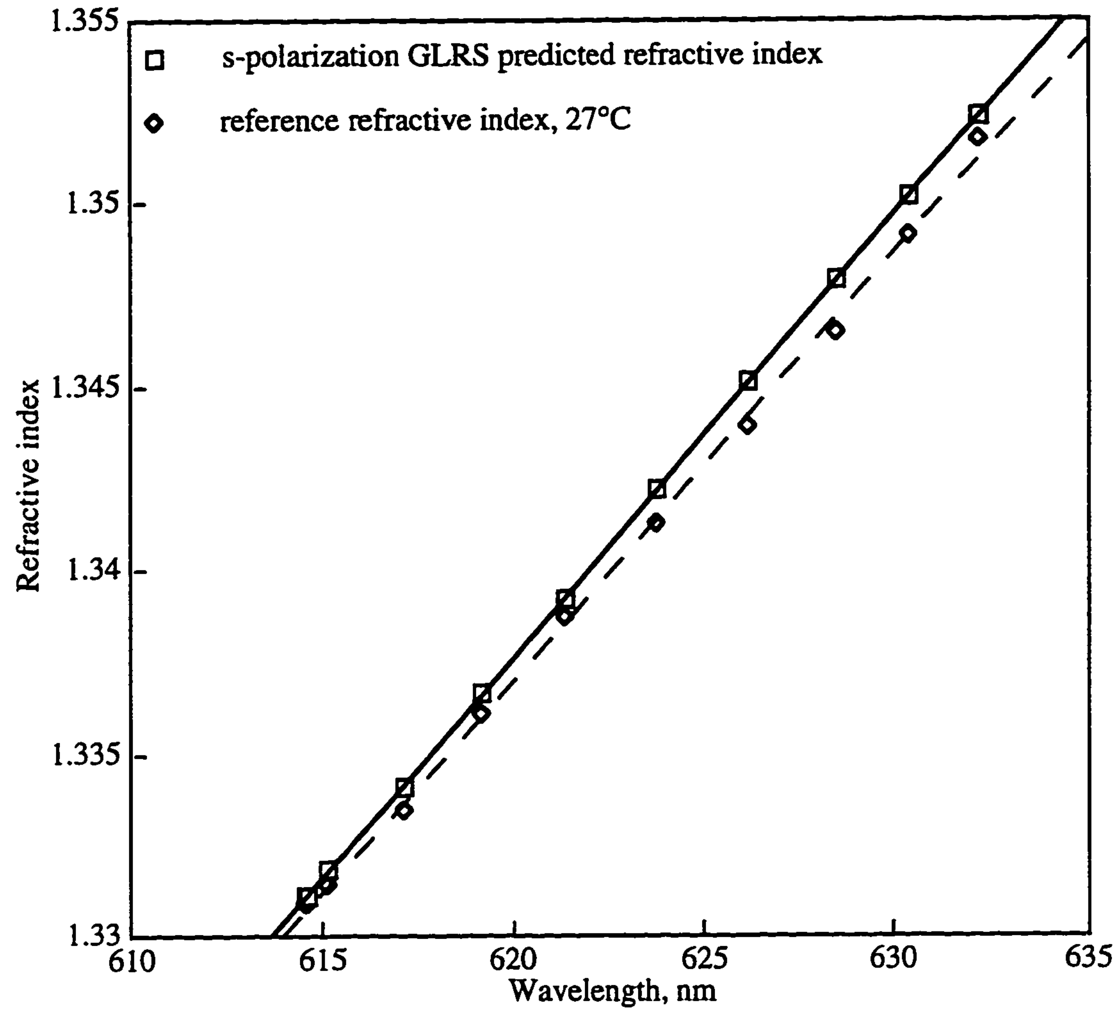

Figure 5.22 Comparison of refractive indices of ethanol:water solutions predicted using GLRS derivative peak positions with reference values, s-polarization. The regression for the GLRS predicted index with wavelength is y = 0.001206*x + 0.5897 with a correlation coefficient of 0.999998. The regression for the reference values with wavelength is y = 0.001162*x + 0.6162 with a correlation coefficient of .998.

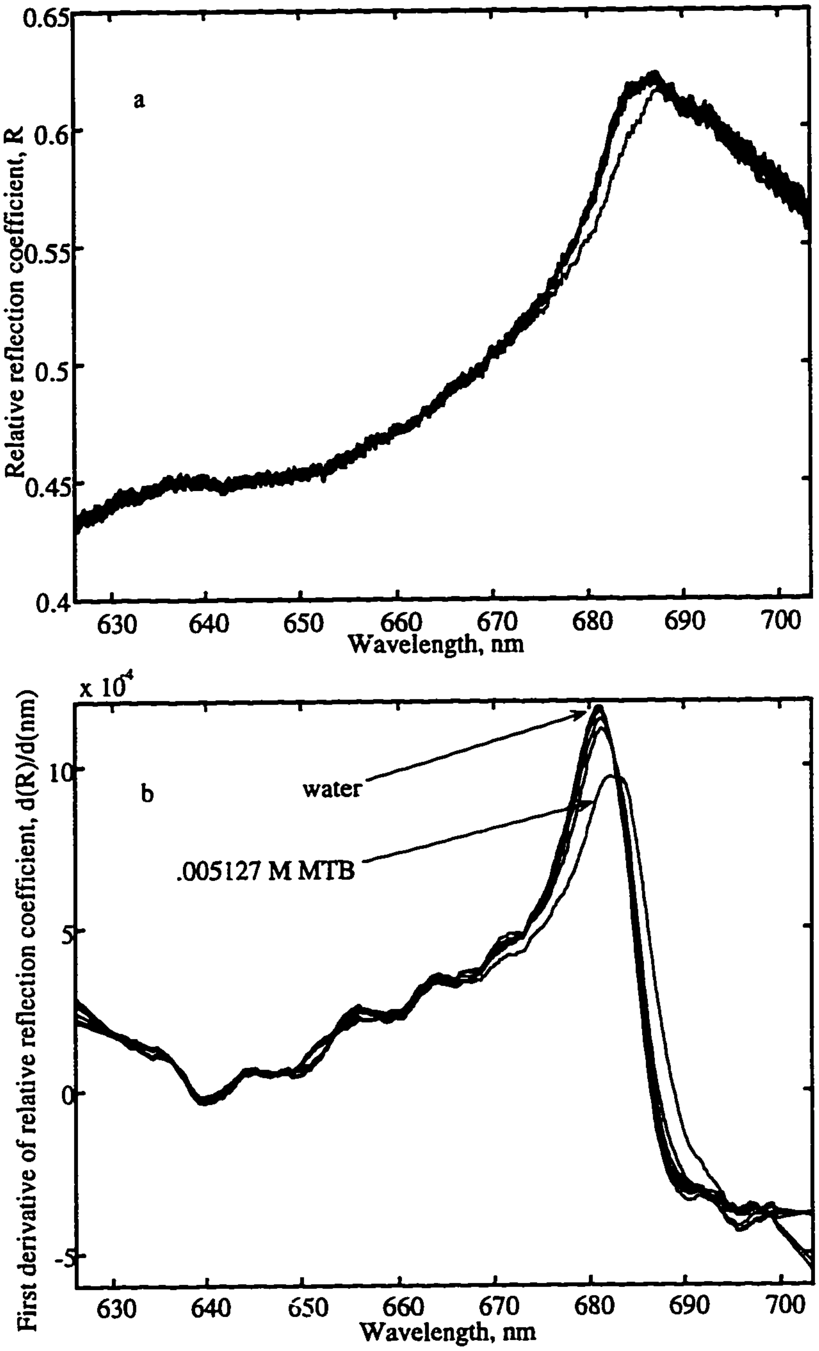

Figure 5.23 GLRS relative reflection coefficient (a) and derivative (b) response to methylene blue sample set, 30.62° incident angle.

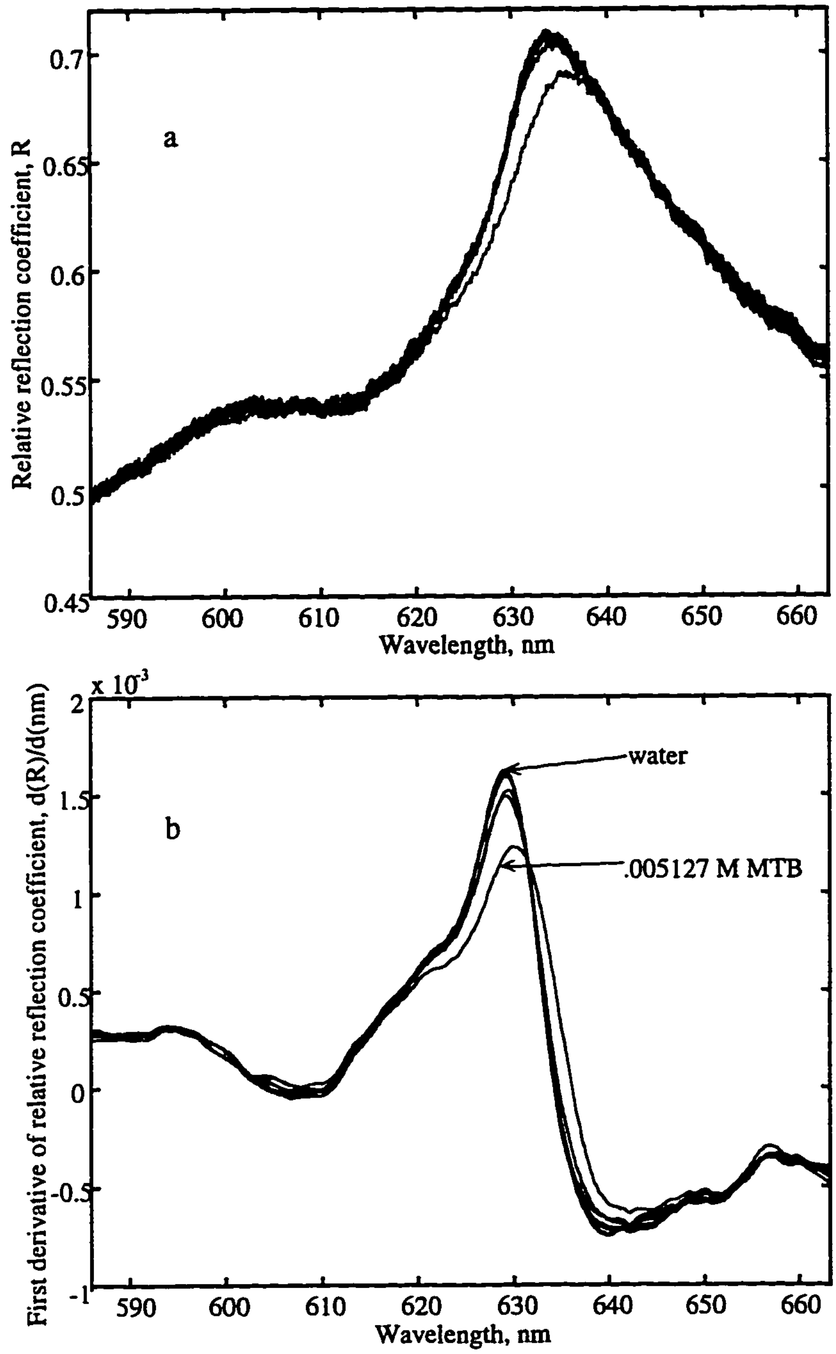

Figure 5.24 GLRS relative reflection coefficient (a) and derivative (b) response to methylene blue sample set, 34.98° incident angle.

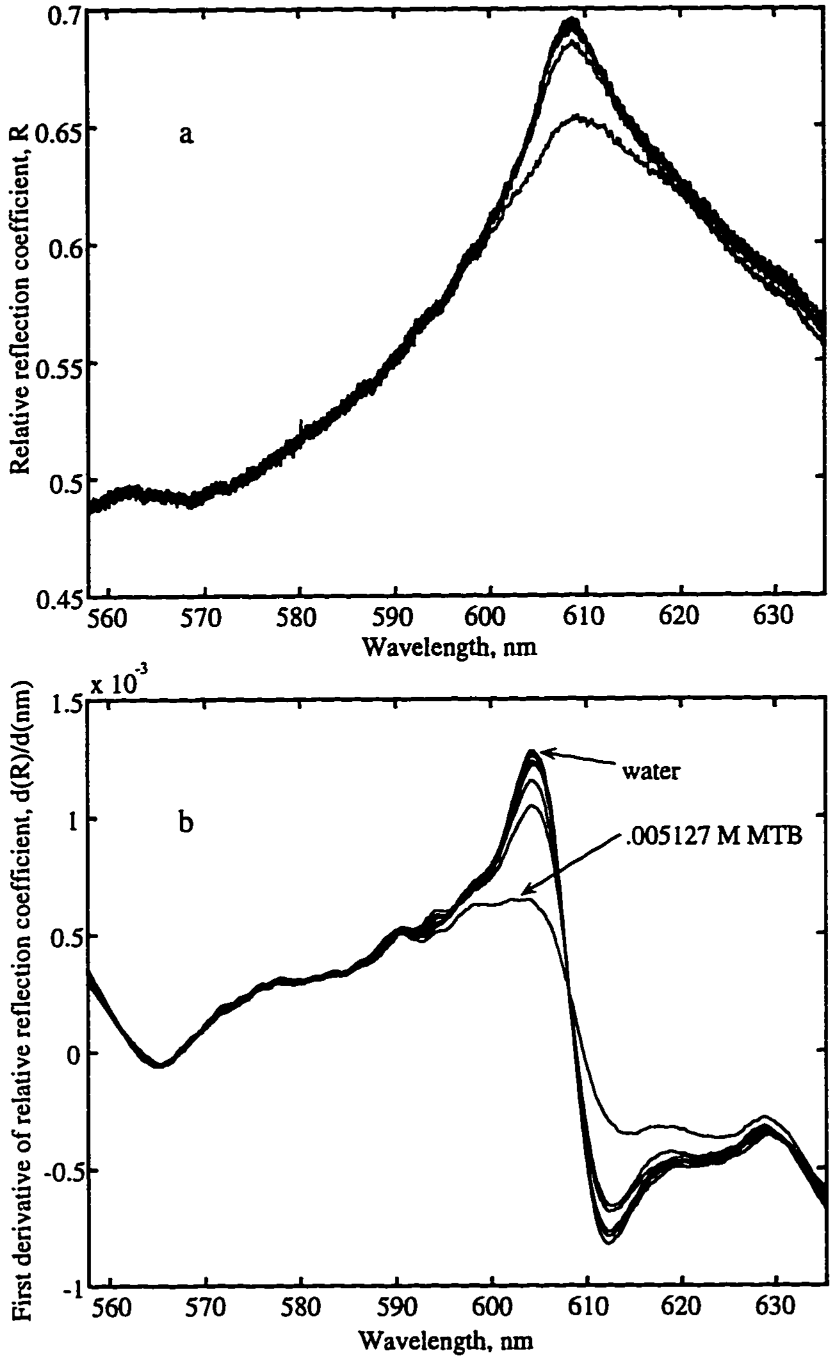

Figure 5.25 GLRS relative reflection coefficient (a) and derivative (b) response to methylene blue sample set, 37.71° incident angle.

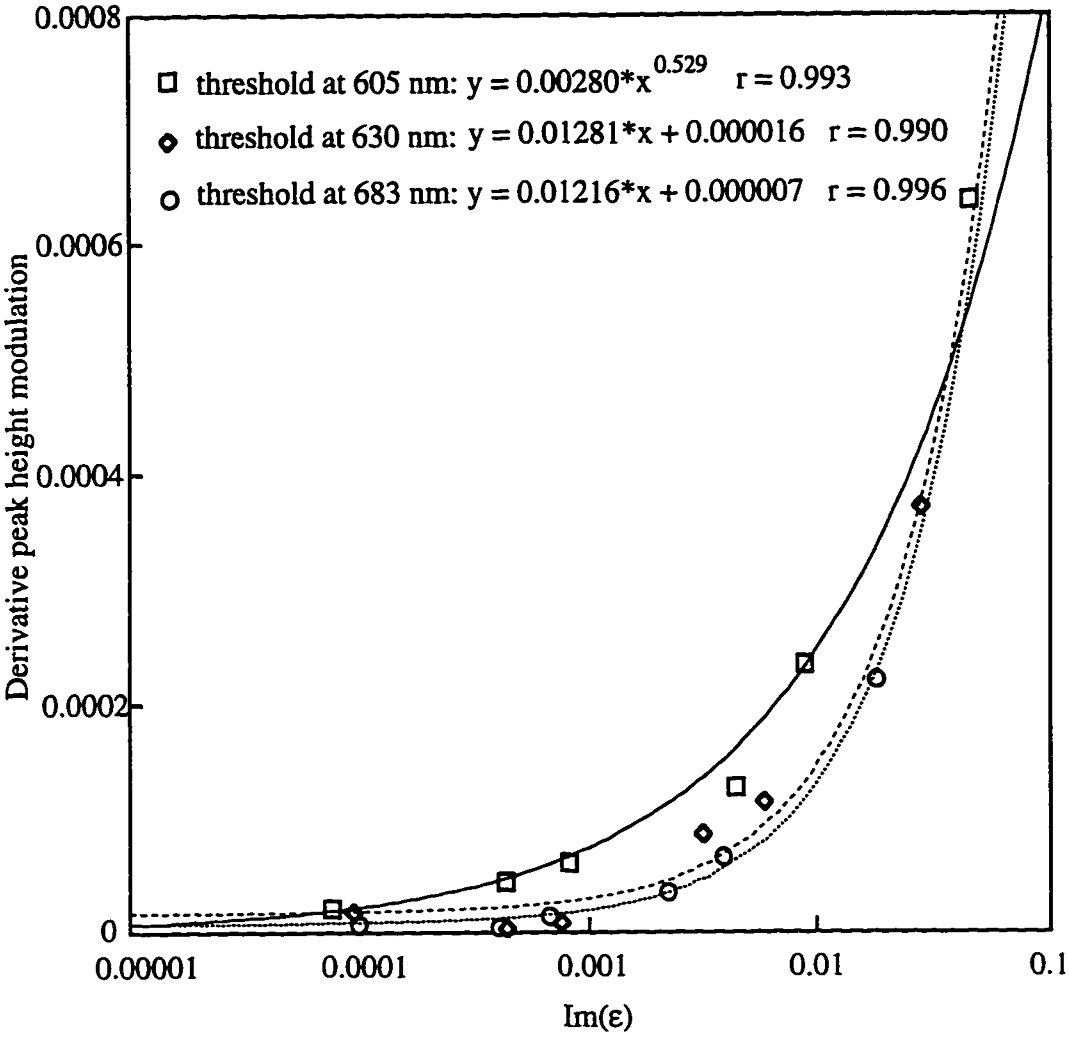

Figure 5.26 GLRS derivative peak height dependence on the imaginary dielectric values of the methylene blue samples for three angles of incidence. Peak height modulation is calculated as a difference from a water reference height.

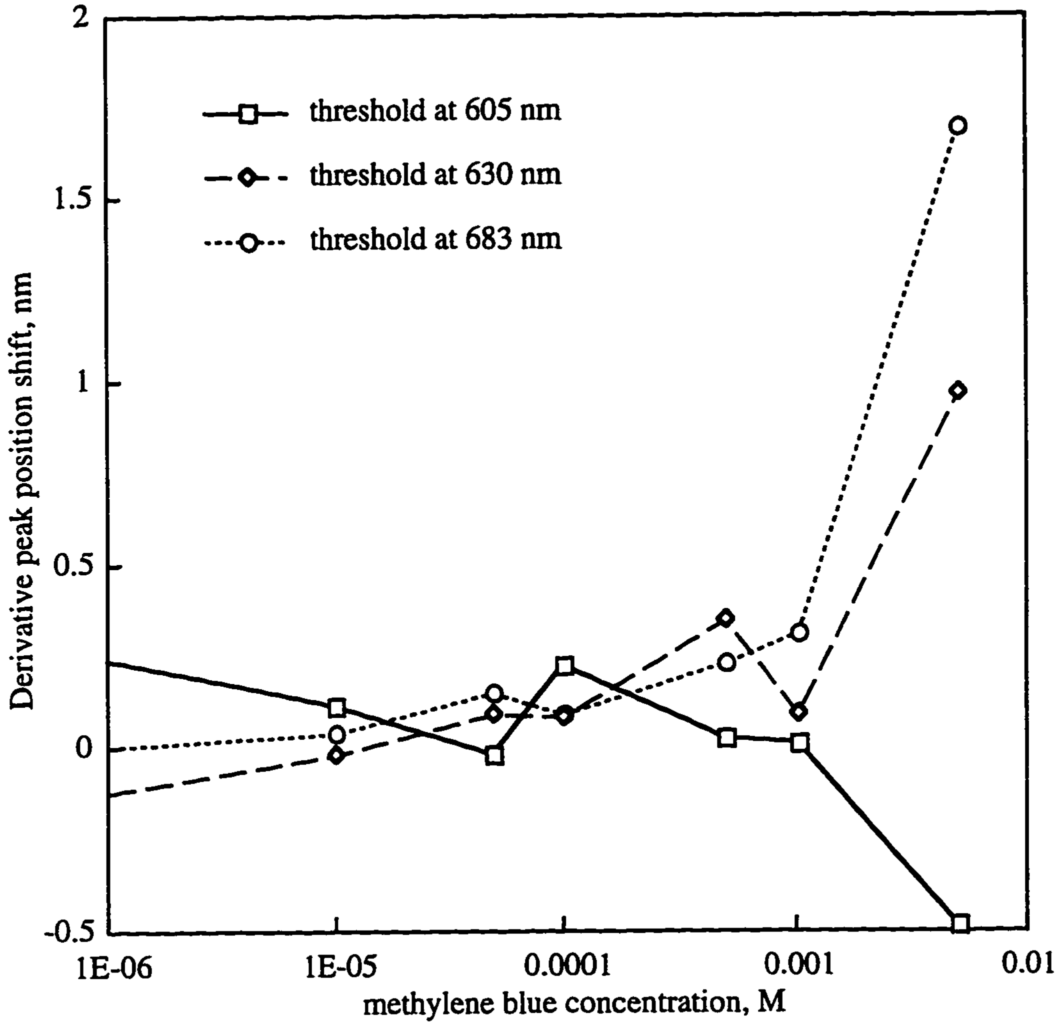

Figure 5.27 GLRS derivative peak position dependence on methylene blue concentration for three angles of incidence. Peak position shifts are relative to the water peak position. Note that the x-axis is logarithmic.

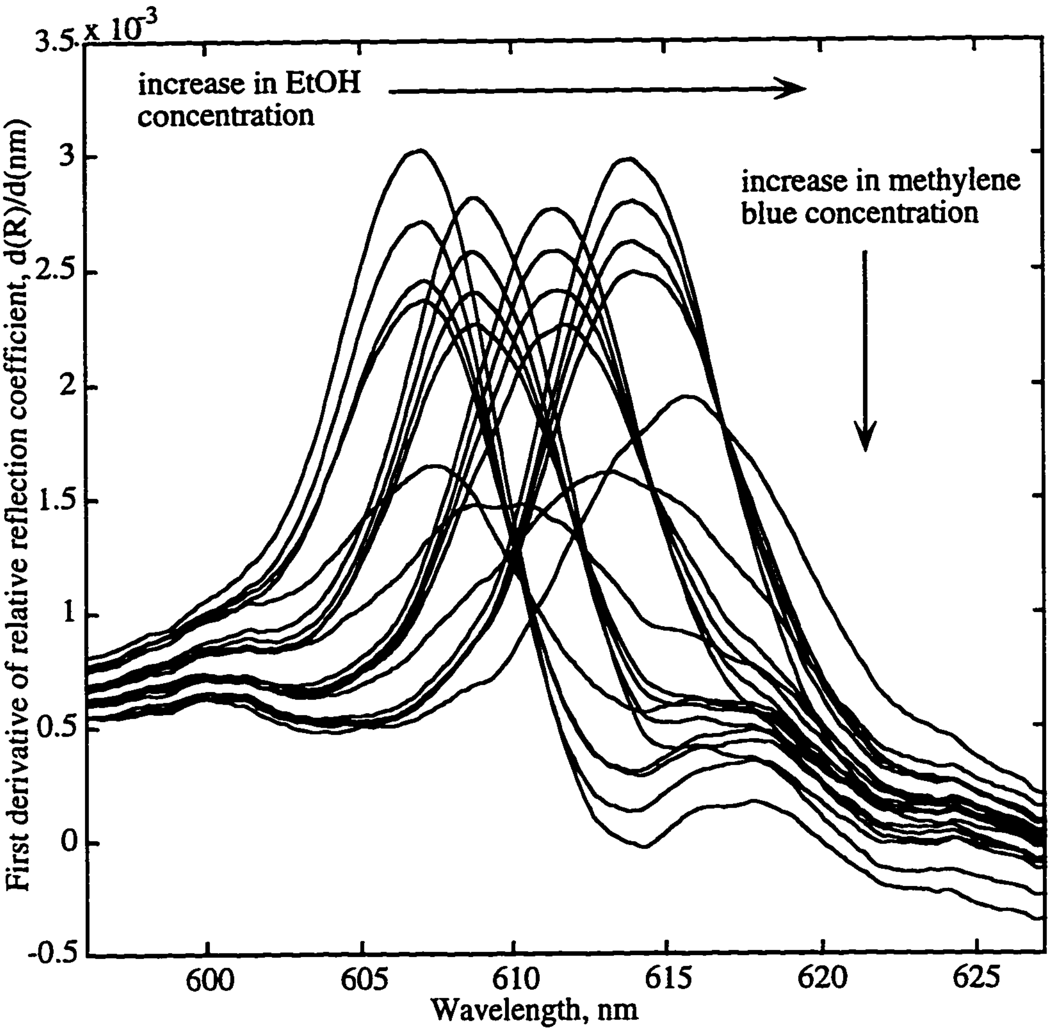

Figure 5.28 GLRS relative reflection coefficient derivative response to ethanol:methylene blue mixtures.

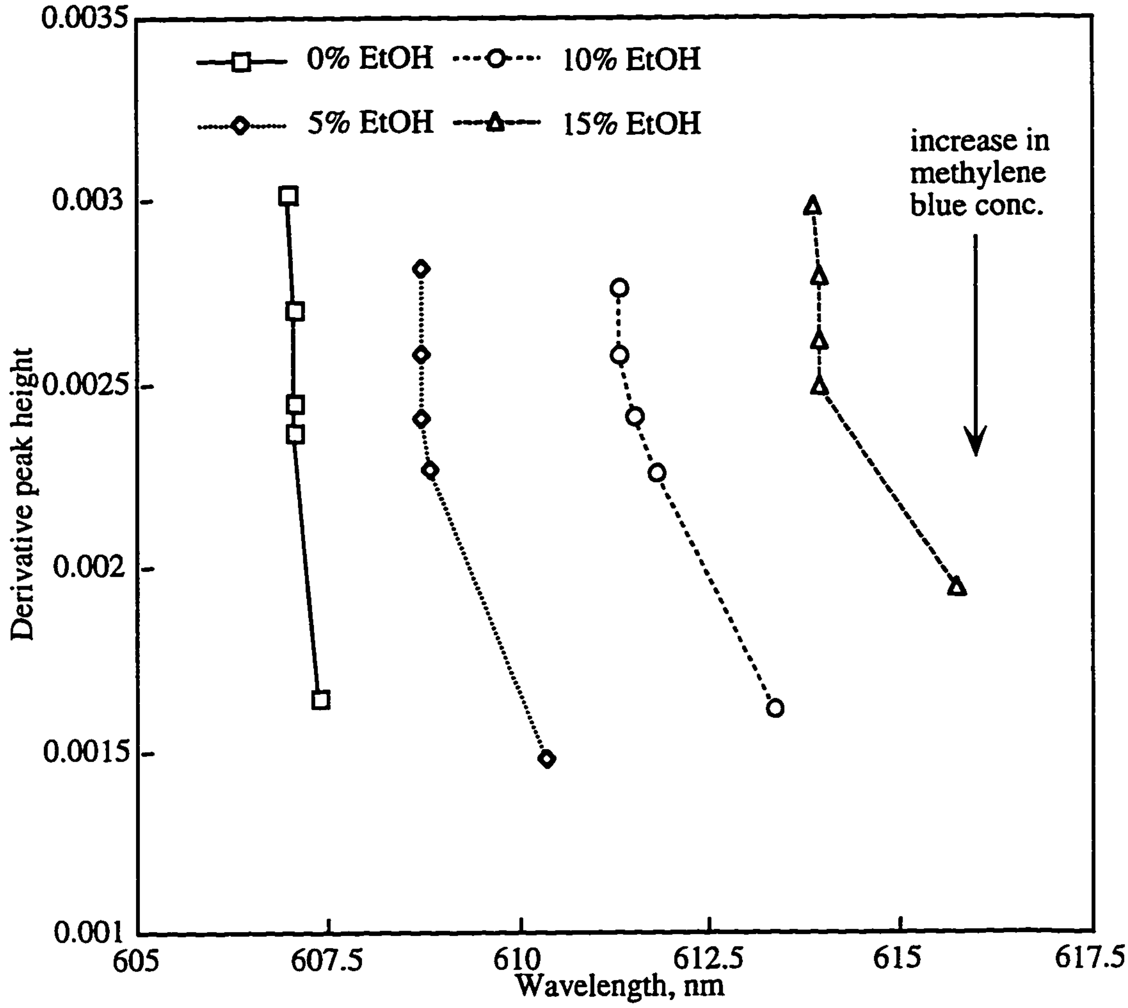

Figure 5.29 GLRS relative reflection coefficient derivative peak height plotted against peak position for the ethanol:methylene blue sample set.

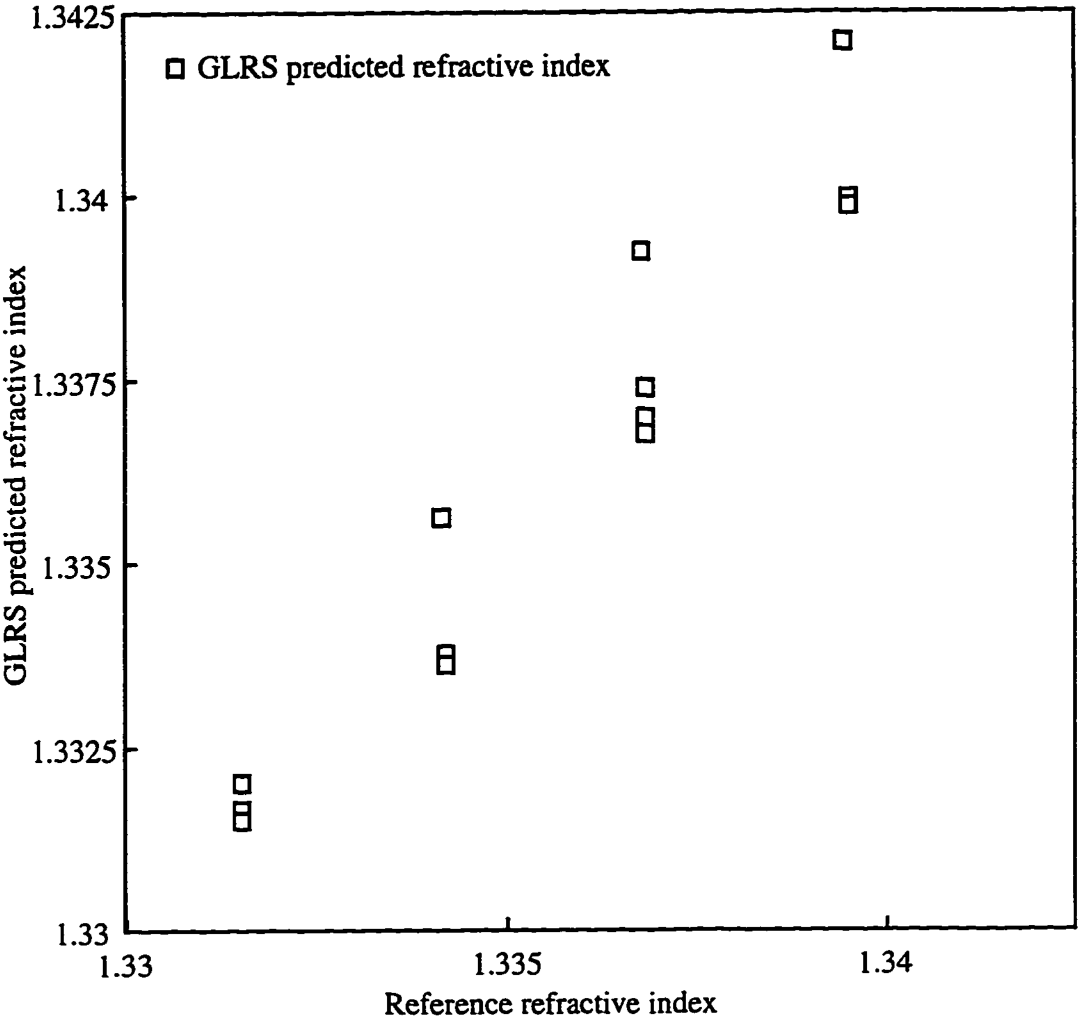

Figure 5.30 GLRS predicted refractive index plotted against the reference refractive indices at the threshold wavelengths for the ethanol:methylene blue sample set.

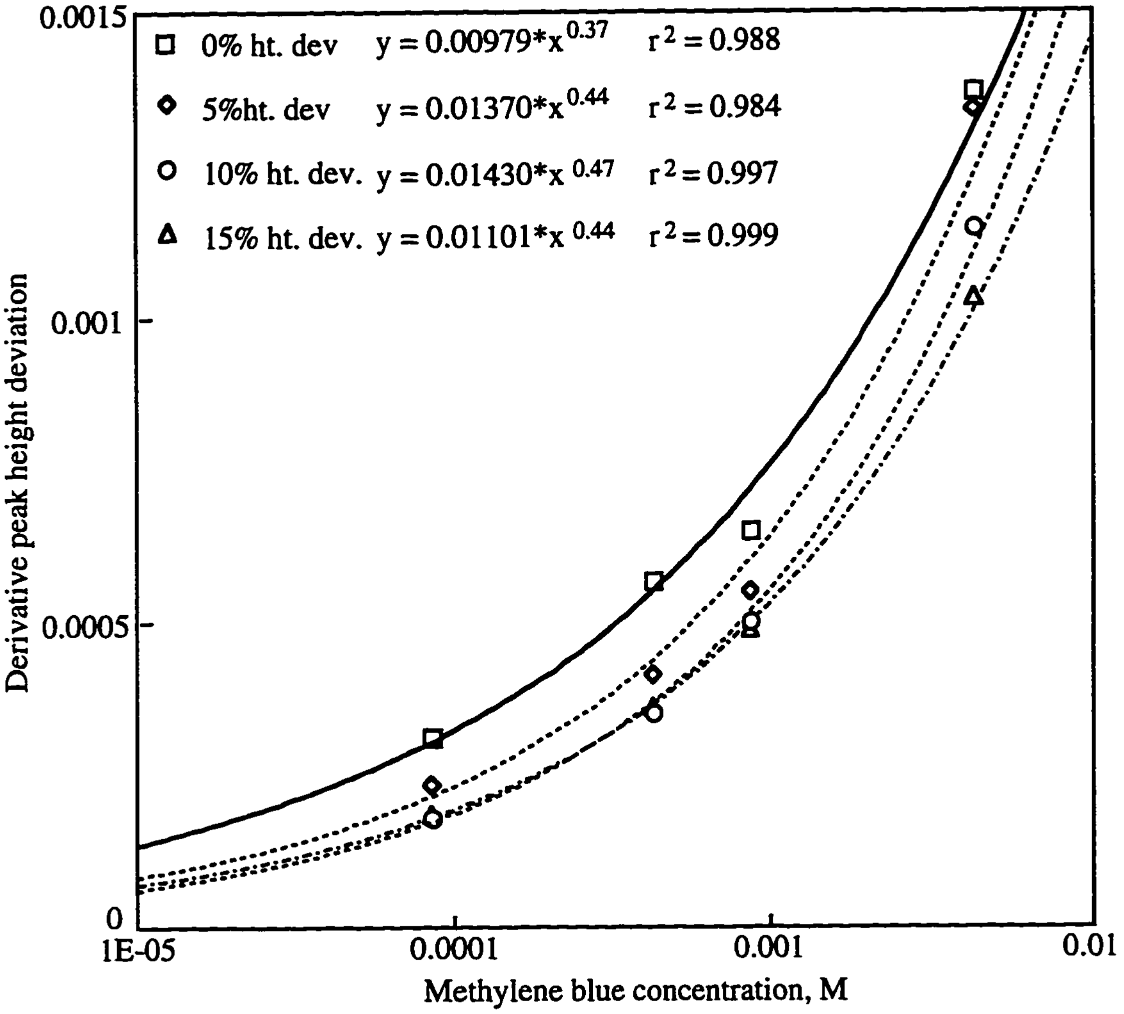

Figure 5.31 GLRS derivative peak height dependence on the concentration of methylene blue samples for ethanol:methylene blue sample set. Peak height modulation is calculated as a difference from a water reference height.

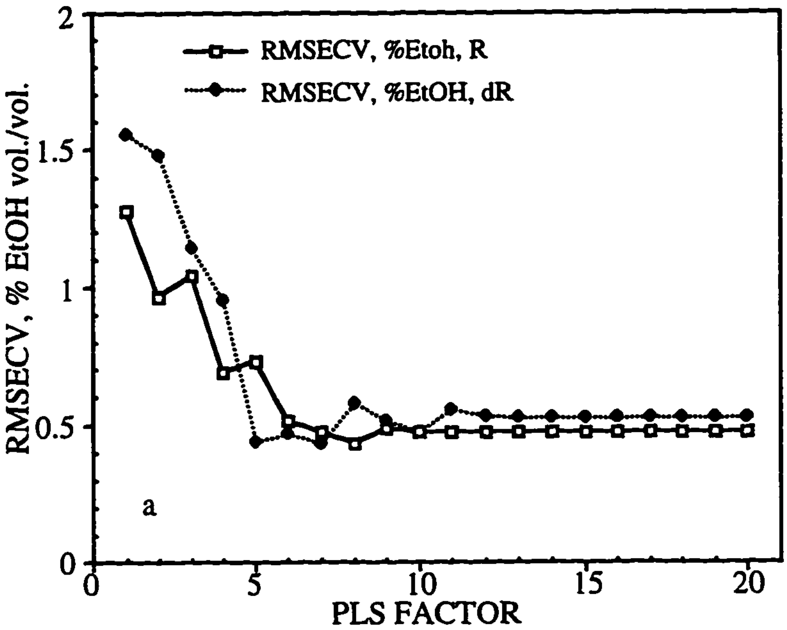

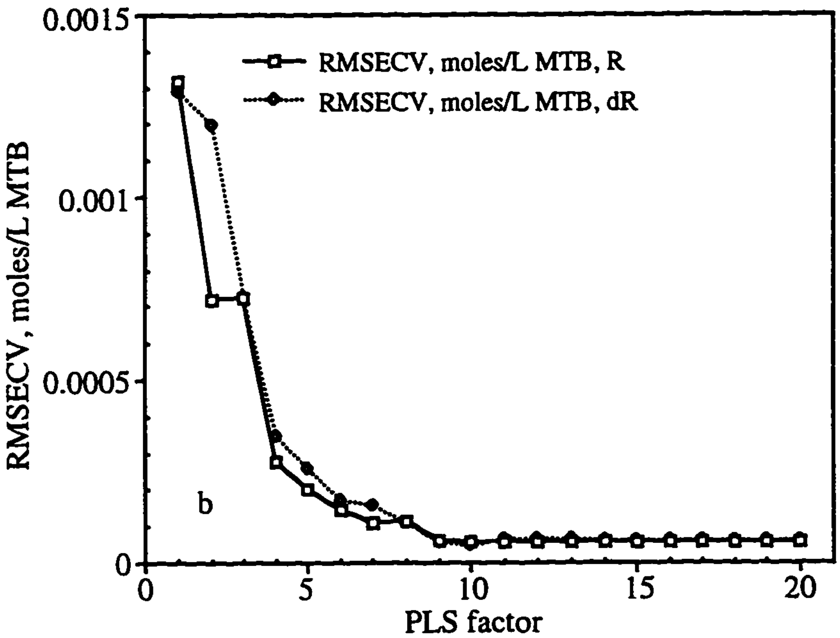

Figure 5.32 RMSECV values for PLS prediction of ethanol concentration (a) and methylene blue concentration (b) in mixture samples. Relative reflection coefficient (R) and derivative (dR) input as response matrices for comparison.

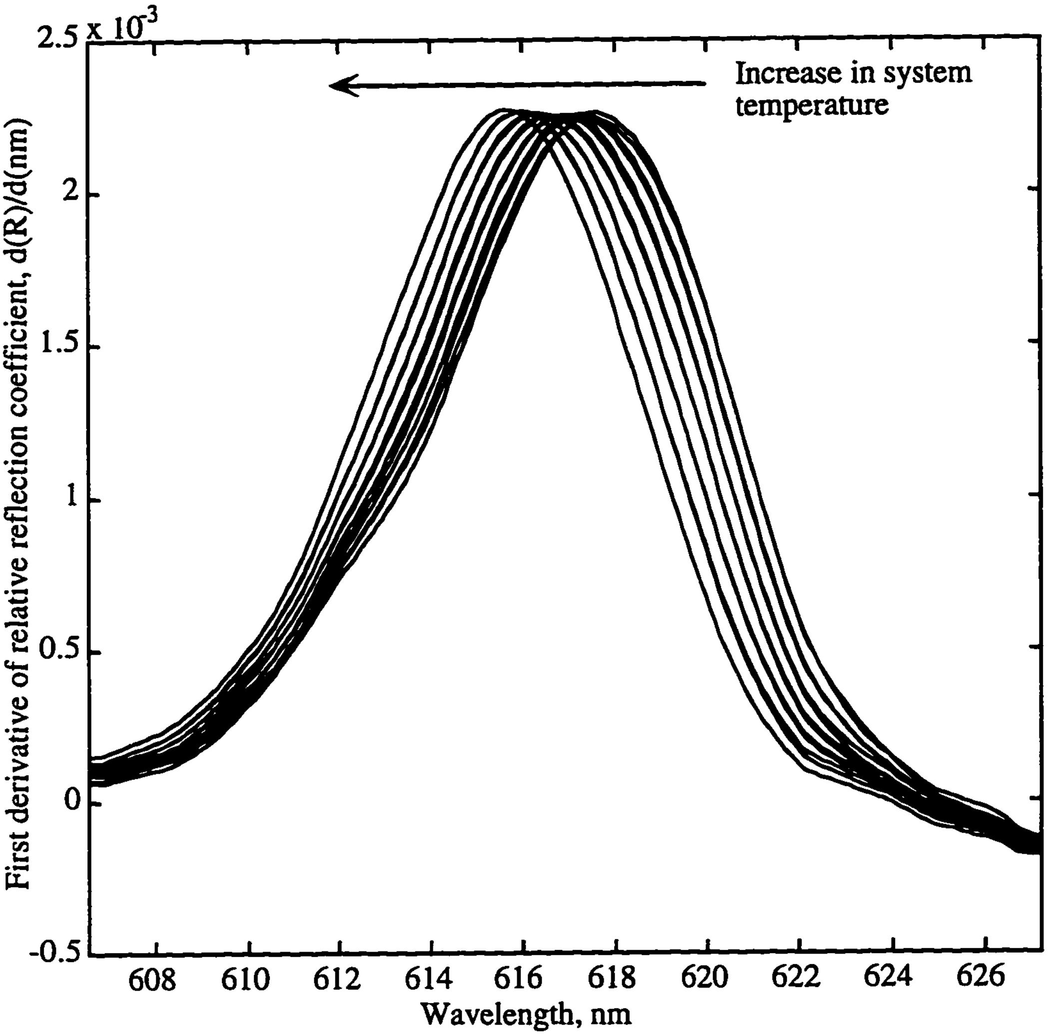

Figure 5.33 GLRS reflection coefficient derivative response to changes in sample/substrate temperature, water in the stopped in the flow cell. Sample was heated through the substrate.

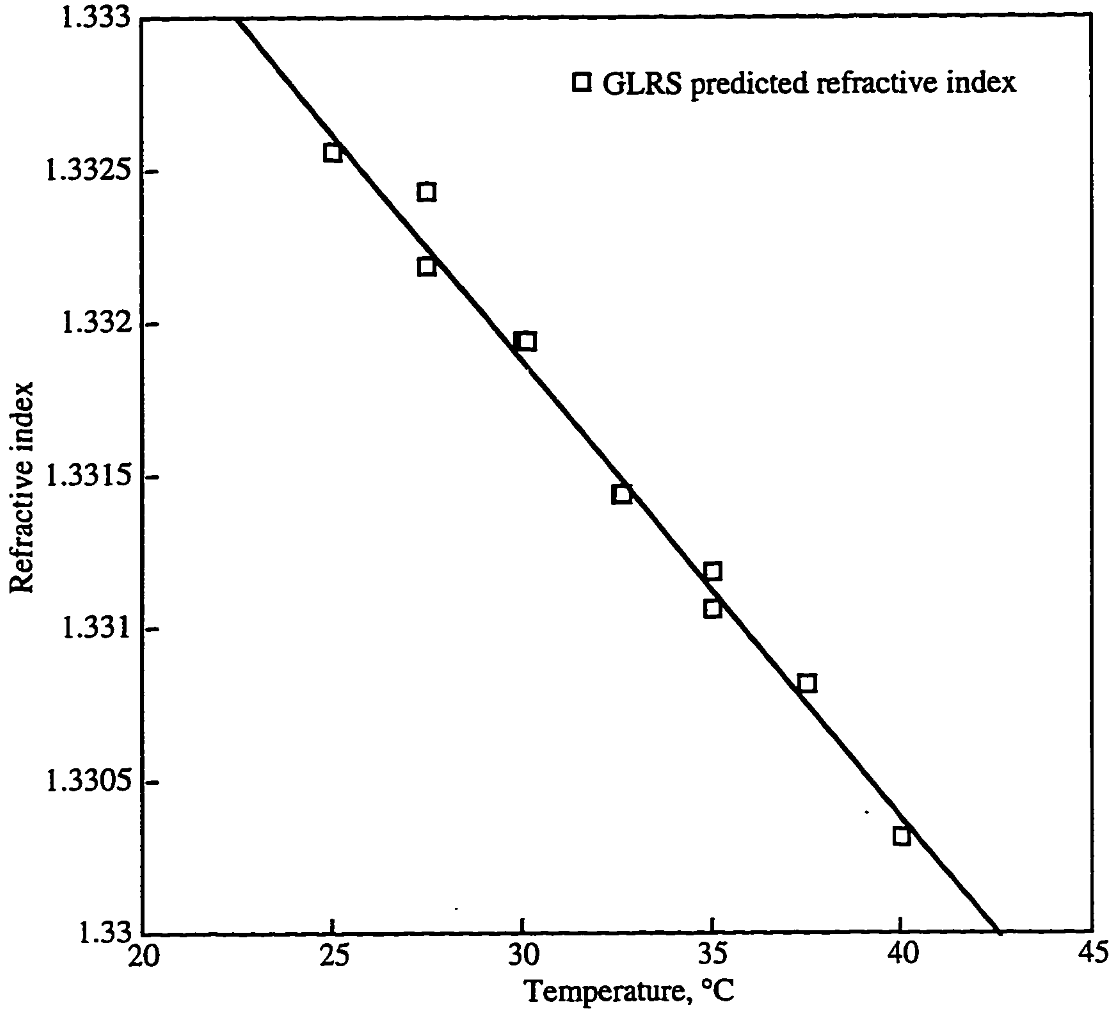

Figure 5.34 GLRS predicted refractive index plotted against system temperature. The slope of the regression between refractive index and temperature yields the temperature dependent dispersion of water: y = -0.000149*x + 1.3363 with a correlation coefficient of .987.

Chapter 6

GLRS Response to Process Relevant Samples

6.1 Introduction

Process analysis refers to the discipline of chemical analysis where the sample is the result of or in transit during a chemical process and analyzed *in situ* and/or in real time. The analysis of such samples, as alluded to in the first chapter, is a demanding and challenging task. The GLRS experimental results presented in Chapter 5 point to the utility of GLRS in process analysis. The ability of GLRS to analyze neat laboratory samples represents a proof of principle of the GLRS phenomenon. However, the real ability of a new technique is tested in systems that preclude the use of existing or competing technologies. Thus, a sample set was devised to help in the understanding of the power of GLRS as it relates to difficult sample matrices.

The first part of this chapter deals with the GLRS response to a simulated fouling layer. Fouling of optical surfaces in process analyzers is a ubiquitous problem in industry. GLRS response to bulk refractive index is predicted to be relatively insensitive to surface fouling and it is important to characterize the surface insensitivity and accurately gauge the "depth of penetration" of the GLRS sensor mechanism. The qualitative theory of this response was presented in Chapter 2 and the discussion presented here will establish trends in reflectivity as a function of layer thickness as well as identify what is described as a transition region from a surface fouling layer to a bulk layer.

The second portion of this chapter will describe the GLRS response to scattering matrices. A plethora of technologies exist that have application in particle size analysis, but most rely on transmission through the process and dilution of the sample stream. Application of GLRS in particle size analysis begins with understanding the nature of the optical interaction of the diffracted beams in the presence of optical heterogeneity on the macro scale. Thus, the GLRS sensor was exposed to a series of mono-and polymodal particle size distribution systems in order to characterize the dominant scattering regime for each system as well as the effect of scattering on the dielectric function of the sample. As changes to the GLRS signal due to scattering particles are the result of changes in the effective dielectric due to forward scattering, theory presented in this chapter will focus on the expressions that describe the effective dielectric of the sample. The GLRS scattering results are presented for comparison with theory for monomodal dispersions. Qualitative results regarding the polymodal systems will be presented as well.

6.2 Surface Fouling

6.2.1 Experimental Procedure

6.2.1.1 Materials

The characterization of the GLRS sensor response to surface fouling represents an experimental challenge in that a suitable fouling layer material must be chosen. A number of different systems were considered as test layers and included polystyrene thin films (applied by spraying a fine mist of dilute solution onto the substrate) and spin-coating of dilute polymer solutions. A difficulty in the application of these materials lies in the optical characterization of the thin film after curing and the contamination of the films by moisture and air-borne solvents that would tend to swell the layer after curing. In addition, the presence of the threshold was to be determined for a bulk water sample in contact with the fouling layer, and any layer would need to be impervious to water in liquid form in order to prevent lift off or delamination of the layer. Thus, a sputtered dielectric (non-conducting) oxide layer was chosen as a material in order to provide mechanical durability and reproducible optical characteristics for each successive layer application.

Another factor affecting the selection of a dielectric layer was the ability to reproducibly apply a layer of known thickness to an accuracy of ~1 nm. The GLRS response is expected to change as a function layer thickness over a range of thicknesses from 0 nm to approximately 1-2 microns. In order to obtain a reasonable data depth, small increments in layer thickness needed to be used. Thus, the layer thickness increment of 50 nm was chosen which allows for gross characterization of the penetration depth with some degree of accuracy. In light of these considerations, the tantalum pentoxide system (Ta_2O_5) was chosen as the dielectric material due to the ease with which it may be deposited via a DC-planar magnetron vacuum sputter coating system. In addition, the mechanical durability of Ta_2O_5 films is such that water will not swell the layer or cause it to delaminate.

6.2.1.2 Thin Film Coating Procedure

The sputter coater system used in these experiments was a Denton Vacuum DC planar magnetron sputterer with a quartz crystal microbalance installed for sputtered thickness measurements (see figure 6.1). A dielectric thin film is deposited underneath a target as a result of reactive sputtering of the target material in the presence of an oxidizing agent. Specifically, argon ions are generated in a DC electric field and accelerated to the target material. The collisions of the argon ions with the target release target material atoms which then undergo an oxidation reaction as they fall to the substrate surface. In this way reproducible uniform layers are produced with sub-nanometer thicknesses attainable. A tantalum target was installed for sputtering the oxide and sputtering parameters for oxygen and argon pressures as well as voltage and current levels were calculated based on literature reports of fast, stoichiometric oxide sputtering[1,2]. The experimental parameters used in the sputtering of the thin films are summarized in table 6.1.

Reference samples were prepared on silicon wafer substrates in order to calibrate the QCM sensor, which was placed approximately 2 cm. off-axis of the target center. Layers were sputtered on three different silicon substrates to approximately 50 nm thicknesses as read on the QCM, which is internally corrected for film density and impedance. The samples were then measured on an AUTOEL[2] (Rudolf Research) ellipsometer that simultaneously calculates film thickness and refractive index. The measured refractive indices and thicknesses are tabulated in table 6.2. The average refractive index of the sample films of 2.3127 ($\lambda_0 = 632.9$ nm) agrees well with the literature values for similarly sputtered films having refractive indices of ~2.1 ($\lambda_0 = 500$ nm)[1]. The *in situ* QCM measured film thicknesses corresponded to ~85% of the true thickness and the correction factor was applied to the target thickness values for the GLRS experiments. This deviation was due to the difference in substrate position relative to the QCM under the target.

6.2.1.3 GLRS Data Collection

The cleaned substrate (#2, period = 829.2 ± 1.4 nm) was mounted in a modified sample holder as shown in figure 6.2. The substrate was held in place via an o-ring and a

---

[1] Heller, J.*Thin Solid Films*, **1973**,*17*, 163-176.

Teflon spacer on either side and each face of the cell was counterbored to minimize shadow effects during sputtering. On the backside of the holder was affixed an aluminum fluid cell that was removed during deposition and reattached for GLRS data collection. The target thickness for the measurements was 50 nm. The QCM target reading was 42.5 nm, and this was reached to within ± 1 nm for all sample runs for a sputter rate of 2.0 -2.5 angstroms/second. Before each subsequent deposition, the substrate was scrubbed with ethanol and a cotton swab and then rinsed in deionized water and dried in a clean nitrogen stream. This ensured that the film surface was clean before subsequent depositions. The experiments consisted of 20 individual deposition steps to arrive at a final thickness of approximately one micron. Therefore, the experiments were performed over two days due to the time required to pump the sputter coater vacuum chamber to high vacuum (2.0×10^{-6} torr) prior to each deposition.

After each layer deposition, the fluid cell was attached to the substrate holder and the entire assembly fixed to the staging described in chapter 4. The incident angle was set to 34.83°, p-polarization, which corresponds to a threshold position of 630 nm for water in the cell. Spectral data were collected using the Princeton Instruments LN/CCD as described in chapter 4 with twenty scans collected at one second integration times for simultaneous collection of reference and sample beams. For each simulated fouling layer thickness run, data were collected following rinsing and filling of the cell with deionized water.

Relative reflection coefficients were calculated for each run using the reference beam as before. First derivatives were calculated using a 51-point Savitsky-Golay filter as the number of data points was reduced to 575 due to the change in detector relative to the initial characterization experiments. Second derivatives were calculated using a 101-point derivative filter on the reflection coefficient data. In addition, the reflection coefficient spectra were integrated to obtain overall reflectivity data that could be compared with thin-film reflectivity theoretical data.

6.2.2 Fouling Simulation Results and Discussion

6.2.2.1 GLRS Fouling Response: Forms of the Reflection Coefficients

The rationale behind the selection of this particular experimental design lies in the desire to look for a transition region where the response abruptly changes form. The

---

[2] Shiller, S.; Heisig, U.; Steinfelder, K.; Strumpfel, J.*Thin Solid Films*, **1979**, *63*, 369-375.

presence of a threshold for water would indicate that water is the bulk medium, and as the fouling layer increases in thickness, it is expected that the water peak in the derivative will give way to a form that is indicative of the film acting as the bulk. The overall reflectivity of the fused silica:grating:water system is expected to change as a function of film thickness based on the presence of a multilayer dielectric stack. Therefore, the results may be compared with a simple model of the reflectivity of a stack consisting of a fused silica bulk layer, a thin film of Ta_2O_5, and a bulk layer of water.

Clues to the validity of this comparison lie in the forms of the reflection coefficients, which change shape and intensity on a periodic basis. It was apparent from the preliminary data analysis that the forms and reflectivities of the reflection coefficients followed a periodicity of approximately 150 nm in layer thickness. Figures 6.3-6.5 display the reflection coefficients as a function of thin film thickness in 150 nm increments. Data are displayed in this format in order to compare reflection coefficient forms without normalization as the periodic response yielded reflectivities on the same order of magnitude for each grouping of curves. It is clear that for the first set of curves in figure 6.3 that the predominate form of the reflection coefficient resembles that for the p-polarization reflection coefficients presented in the previous chapter. However, there is a transition in form between the curves corresponding to 450 and 600 nm layer thicknesses. The change in form most likely corresponds to the GLRS optical transition from bulk water response to bulk Ta_2O_5 response. In addition, as the layer thickness increases past 600 nm to 950 nm, a feature marches across the wavelength space that indicative of an etalon peak or some sort of waveguiding phenomenon in the tantalum oxide layer, which would be expected for film thicknesses greater than the wavelength of incident light.

Figure 6.4 displays the reflection coefficients for the second grouping of 150 nm increments in layer thickness. Again, the forms and intensities change as a function of layer thickness but the forms for what correspond to the water responses are quite different than either the s- or p-polarization responses. The forms correspond to what is represented in Figure 2.5, curve c. This may be explained by the fact that the coefficients in (2.8) are polarization state dependent as well as dependent upon the reflectivity of the entire interface system due to Fresnel reflections. Thus, it is expected that the forms will change to intermediate states for a constant incident polarization state. However, a transition region is again seen between 500 nm and 650 nm in layer thickness between bulk water response and bulk Ta_2O_5 response. Likewise, a similar feature for the larger thicknesses is seen as a peak in the reflectivity due to etalon or waveguiding effects.

Similarly, figure 6.5 displays features in the curves that indicate bulk transition effects as well as reflectivity effects associated with the three-layer system. The forms of the curves are similar to what is given in Figure 2.5 (b). Once again, a transition region is seen between 550 nm and 700 nm where the tantalum oxide layer transits from a surface layer to a bulk layer. The dominant feature in the curves for the larger thicknesses of oxide is a peak that again may correspond to waveguiding or an etalon effect.

As has been seen qualitatively, similarities exist in all three groupings of reflection coefficient curves that are dependent upon fouling layer thickness. The periodicity associated with the overall reflectivity may be modeled based on Fresnel reflection coefficients for a multilayer stack[3]. The p-polarization reflectivity of a three layer stack (see figure 6.6) of dielectric materials is given by:

$$R=\frac{r_{12}{}^2+r_{23}{}^2+r_{12}r_{23}\cos(2\beta(h))}{1+r_{12}{}^2r_{23}{}^2+r_{12}r_{23}\cos(2\beta(h))} \qquad (6.1)$$

where the Fresnel reflection coefficients r_{ij} for p-polarization are given by

$$r_{ij}=\frac{\frac{1}{n_j}\cos(\theta_i)-\frac{1}{n_i}\cos(\theta_j)}{\frac{1}{n_j}\cos(\theta_i)+\frac{1}{n_i}\cos(\theta_j)} \qquad (6.2)$$

and the argument $\beta(h)$ is

$$\beta(h)=\frac{2\pi}{\lambda_0}n_2h\cos(\theta_2). \qquad (6.3)$$

The i and j subscripts correspond to the incident and transmission media respectively where the media are designated 1, 2, and 3 for fused silica, tantalum oxide, and water, respectively. The physical film thickness is given by the parameter h where the optical film

---

[3] Born, M.; and Wolf, E. *Principles of Optics*, 5th ed., Pergamon Press, Oxford, 1975, 59-60.

thickness may be calculated by taking n_2h. The incident and transmitted angles θ_i or θ_j are related by Snell's law across the reflection boundary.

These expressions were used to calculate the reflectivity of the three layer system without the grating present for a wavelength of 630 nm, fused silica index of 1.4572, Ta_2O_5 film index of 2.3127, water index of 1.33206, and an incident angle in air of 34.83°. The reflectivity calculations neglected dispersion in the materials for simplicity. Figure 6.7 shows the dependence of the reflectivity at 630 nm as a function of physical film thickness. The periodicity of the reflectivity may be calculated by taking $2\pi/\beta(h)$ independent of h. This yields a periodicity of 140 nm for the three layer stack without a grating present. For comparison, the similarities in reflectivities and forms of the GLRS reflection coefficients exhibited periodicities on the order of 150 nm mainly due to the 50 nm increment in layer thickness application. Likewise, the overall GLRS reflectivity may be calculated across the bandpass of the instrument by integrating the reflection coefficients. The integrated values are plotted vs. film thickness in figure 6.8. The solid line in the plot is interpolated between values and clearly shows the periodicity of the overall reflectivity of the grating/sample interface in the presence of a building fouling layer. It is clear that the periodicity of this function approximates that calculated for the three layer system with no grating present. In addition, as seen in the reflection coefficient curves, a transition region exists at around 500 nm to 600 nm layer thickness that seems to point to the appearance of tantalum oxide as the bulk medium that generates the GLRS response. Thus, this analysis points to a superposition of effects at the grating surface where the GLRS response is convoluted with the reflectivity due to the presence of a dielectric thin film. The analysis of the derivatives of the reflection coefficients will give further insight into the GLRS response to bulk water in the presence of a fouling layer.

6.2.2.2 GLRS Fouling Response: Reflection Coefficient Derivatives

As demonstrated in the previous chapter, insight into the positions of singularities in the reflection coefficients may be gained by analyzing the positions of peaks in the derivative plots. Figures 6.9, 6.10, and 6.12 display the first derivatives of the reflection coefficients shown in figures 6.3-6.5 using the similar groupings based on the aforementioned periodicity. Figure 6.9 shows that peaks in the derivative are present for the first four curves that correspond the position expected for a threshold due to water. At

600 nm thickness, the derivatives begin to transition to forms associated with the fouling layer bulk GLRS response. Small shifts in the position are most likely due to realignment of the optics before each run as the heating and cooling of the substrate holder oxide layer during deposition produced small changes in the mounting angle. In addition, changes in the forms of the reflection coefficients do affect the position of the thresholds as seen in derivative plots due to the nature of the Savitsky-Golay smoothing.

Figure 6.10 displays derivatives for the second grouping that resulted in quite different forms for the reflection coefficients as compared with the p-polarization response for water. As expected from the forms of the reflection coefficients, there is no peak in the derivative plot that corresponds to water, but instead a shoulder that occurs at 630 nm for curves corresponding to layer thicknesses below 650 nm. Thus, it is expected that a second derivative will yield peaks that correspond to positions of thresholds, and this is borne out in figure 6.11, which displays the second derivatives that correspond to the curves in figure 6.4. Notice that peaks are observed for the four curves corresponding to thicknesses below 650 nm. The presence of peaks at 630 nm indicate that the form of the reflection coefficient corresponding to this grouping requires a second derivative in order to locate the GLRS threshold position. However, at a film thickness of around 650 nm, the transition occurs that is indicative of a shift from water bulk to tantalum oxide bulk.

Finally, figure 6.12 displays the first derivatives for the last grouping of reflection coefficients. Notice that there is a monotonic increase in wavelength position of the peak around 630 nm for an increase in layer thickness up to 700 nm physical thickness. This may be due to shifts in reflection coefficient forms as a function of layer thickness within a periodic group. As the layer thickness increases to 400 nm, the form seems to resemble the first derivative forms in figure 6.11 where second derivatives are required to locate the position of the thresholds. Once again, the transition region around 550 nm -600 nm exists.

In summary, it appears that the GLRS sensor responds to the bulk medium in the presence of fouling layers to a physical depth of approximately 550 nm, which, for this layer material, corresponds to an optical thickness of 1271 nm which is approximately twice the wavelength of light in the bulk medium. As seen in the data, the nature of the fouling determines the changes in the reflection coefficient form, but the presence of the fouling layer doesn't appreciably affect the position of the thresholds due to bulk media, which is directly predicted from theory. This is in contrast to the response of ATR and SPR to fouling layers present at the reflection interface. ATR relies on evanescent phenomena exclusively, and the amount energy that samples the bulk decreases exponentially with distance form the interface. Thus, the majority of the energy is concentrated at the TIR interface, and fouling layers of monolayer dimensions drastically affect the interaction of the incident beam with the interface in such a way as to convolute surface and bulk effects[4].

Likewise SPR is extremely sensitive to small changes in interface dielectric properties. Thin, angstrom scale dielectric layers change the plasmon resonance position in wavelength space, thus changing the effective dielectric measured by SPR. If the presence of fouling is not corrected for in data analysis, bias is introduced in the measurement. Indeed, thin dielectric materials have been used to modulate the dynamic range for refractive index sensitivity in SPR sensors[5]. The fouling results presented in these studies point to the effectiveness of GLRS as a process sensor where ATR and SPR would yield biased or convoluted results for similar fouling materials.

6.3 Scattering Matrices

6.3.1 Theory

6.3.1.1 Effective Dielectric Function

GLRS measurements of scattering media are based on the effect of light scattering by particles in a liquid matrix, where scattering events that change the properties of evanescent waves near the threshold leads to the change of threshold characteristics. These changes occur as a result of the appearance of an imaginary component in the effective dielectric constant due to coherence distortion even if the particles do not absorb light in the exploited frequency interval. A schematic of the sensing mechanism with particles present is given in figure 6.13. The measurement of particle characteristics by GLRS experimental technique bears some analogous relationship to the "frustrated total internal reflection" method used previously for the measurement of static and dynamic properties of colloid particles in electrolyte solutions[6].

---

[4] Kuhn, K. J.; Burgess, L. W. *Analytical Chemistry*, **1993**, *65* (10), 1390-1398.

[5] Jorgenson, R. *Surface Plasmon Resonance Based Bulk Optic and Fiber Optic Sensors*, **1993**, Ph.D. Dissertation, University of Washington.

[6] Prieve, D.; Bike, S.; Frej, N. *Faraday Discuss. Chem. Soc.*, **1990**, *90*, 209-222 and literature therein.

Light scattering in random media, a very complex phenomenon, is a function of different light scattering events by non-uniformities which include coherence changes and absorption of incident light. The analytical theory of such scattering in random media is fully developed only for the limiting cases of dilute systems or systems where the wavelength of light is larger than the characteristic distance of density variations, where it is possible to use the quasi-classical approximation[7]. In the case of GLRS the theoretical interpretation is substantially simplified by the fact that only the fraction of light scattered by particles which travels in the forward direction and which remains coherent with the incident light is probed by GLRS. Since the diffraction patterns of GLRS are dominated by the interference of the scattered beams with the incident beam, the observed diffraction peaks correspond to the directions of constructive interference. The fraction of the scattered energy departing from its original propagation direction (but still at the same frequency since only elastic scattering is considered here) becomes incoherent and effectively lost for constructive interference. The possibility of a certain part of the incoherent wave energy being returned to the coherent state may be disregarded here since to be coherent means that propagation is not only in the original direction but also with the same phase, and these combined requirements make the return probability essentially zero.

Thus, the sample optical properties as they relate to GLRS measurements may be described by the following effective dielectric constant:

$$\begin{aligned}\varepsilon_{\text{eff}}^{(2)} &\equiv \left[\sqrt{\varepsilon^{(2)}} + 2\pi \frac{c^2}{\omega^2\sqrt{\varepsilon^{(2)}}} \sum_{\alpha} N_\alpha A_\alpha(0)\right]^2 \\ &\cong \varepsilon^{(2)} + 4\pi \frac{c^2}{\omega^2} \sum_{\alpha} N_\alpha A_\alpha(0)\end{aligned} \tag{6.4}$$

where $\varepsilon^{(2)} \equiv \varepsilon^{(2)}(\omega)$ is the dielectric function of the medium without particles present, ω is the frequency of incident light, N_α and $A_\alpha(0)$ are, respectively, the number of particles of type α per unit volume and the scattering amplitude in the forward direction for those particles. The sum over α in (6.4) is taken over all types of particles. The expression (6.4) is the square of the expression (1.103) in footnote 7 (see also footnote 8) for the effective dielectric function of particles in a vacuum[7,8] with corrections made in order to

---

[7] Newton, R. *Scattering Theory of Waves and Particles*, McGraw-Hill; New York, 1966.

[8] Champion, J.; Meeten, G.; Senior, M. *J. Colloid Interface Science*, **1979**, *72*, 471.

take into account the optical response of the solvent which is described by $\varepsilon^{(2)} \equiv \varepsilon^{(2)}(\omega)$. The applicability of (6.4) is restricted by the following inequality:

$$2\pi \frac{c^2}{\omega^2 \varepsilon^{(2)}} \left| \sum_\alpha N_\alpha A_\alpha(0) \right| < 1 \qquad (6.5)$$

which is fulfilled in dilute solutions. To illustrate the restrictions imposed by (6.5) the case is considered when the particle radius R_α is larger than the wavelength λ. In this case

$$A_\alpha(0) \cong \frac{R_\alpha^2}{\lambda \varepsilon^{(2)}} \qquad (6.6)$$

where the numerical coefficients that are on the order of unity have been omitted. After introduction of (6.6) into (6.5), the condition (6.5) is reduced to

$$\frac{\lambda}{\overline{R}_\alpha} < \frac{d_p \varepsilon^{(2)}}{d_s} \qquad (6.5a)$$

where d_p is the density of the particle material and d_s is the mean weight particle concentration in the solution. The bar over R_α represents an averaging over all particle types.

The amplitudes $A_\alpha(0)$ are in general complex with the imaginary part present, even in the absence of light absorption, due to the coherence loss from scattering. Close enough to the GLRS thresholds the diffracted transmitted waves which transform from traveling to evanescent ones penetrate into the medium to distances

$$L \sim \frac{\lambda}{\operatorname{Im}\left(\varepsilon_{eff}^{(2)}\right)} \qquad (6.7)$$

which are larger than the incident wave's wavelength and the interparticle distances, even in dilute systems, as shown by the surface fouling studies. This property allows for the application of generalized GLRS theory[1] to describe scattering from the grating in contact with colloids and particle suspension solutions by introducing the effective dielectric constants of the type in (6.4) into equation 2.4 from chapter 2:

$$\delta_{m_\alpha} = \operatorname{Re}\left(\varepsilon_{eff}^{(2)}(\omega)\right) - \left(\sin\theta + \frac{m_\alpha \lambda}{a}\right)^2, \qquad \lambda = \frac{2\pi c}{\omega} \qquad (6.8)$$

This expression is essentially unchanged relative to that in (2.4). However, as GLRS is a universal technique that responds to the bulk dielectric, the effective dielectric changes in the sample due to the presence of scattering particles is measurable using this reflection format. Predictions of the effective dielectric using GLRS results are made using (6.8) in the same format that (2.4) was used to predict the refractive indices of neat samples in chapter 5.

6.3.1.2 Scattering Amplitudes

For uniform spherical particles the amplitudes $A_\alpha(0)$ can be calculated exactly using the complicated expressions of Mie theory[7,9]. However, in real systems where there are deviations from perfect spherical shape and constant radial density distributions and thus it is often useful to rely on general limiting approximations corresponding to: Rayleigh scattering, when

$$\lambda = \frac{c}{2\pi\omega} > R\left(\frac{\varepsilon_p - \varepsilon^{(2)}}{\varepsilon^{(2)}}\right), \tag{6.9a}$$

and Fraunhofer diffraction, when

$$\lambda = \frac{c}{2\pi\omega} < R\sqrt{\varepsilon_p}, \tag{6.9b}$$

where R is the characteristic dimension of the particles and ε_p is the dielectric function of the particle material. In the limiting case of (6.9a), the real and imaginary components of the amplitude $A_\alpha(0)$ for all polarizations are equal[3] to:

$$\frac{1}{R_\alpha^2}\operatorname{Re} A_\alpha(0) = \left(\frac{2\pi}{\lambda}\right)^2 \frac{\left(\varepsilon_P - \varepsilon^{(2)}\right)}{\left(\varepsilon_P + 2\varepsilon^{(2)}\right)} R_\alpha \sqrt{\varepsilon^{(2)}}$$

and (6.10a)

$$\frac{1}{R_\alpha^2}\operatorname{Im} A_\alpha(0) = \frac{1}{2}\left(\frac{2\pi}{\lambda}\right)^3 \left(\varepsilon_P - \varepsilon^{(2)}\right) R_\alpha^2$$

for $\operatorname{Im}\varepsilon_P = \operatorname{Im}\varepsilon^{(2)} = 0$. In the case of (6.9b) the scattering amplitude is equal to:

---

[9] The most recent analysis of Mie scattering can be found in Ludlow, I.; Eviert, *J. Physical Review E*, **1996**, *53*, 2909.

$$\frac{1}{R_\alpha^2}\operatorname{Re} A_\alpha(0)=0$$

and (6.10b)

$$\frac{1}{R_\alpha^2}\operatorname{Im} A_\alpha(0)=\frac{1}{4\pi\lambda}$$

Note that (6.10) is correct for non-spherical particles when the condition (6.9a) is fulfilled. It represents the optical analog of the "effective radius approximation" of general wave scattering theory with the parameter R_α representing an averaged (effective) radius. In the transition interval between (6.9a) and (6.9b) the Van De Hulst expression has been taken into account (see footnote 7) for forward the scattering amplitudes which has in the case of scattering by particles in a medium has the following form (see figures 6.16 and 6.17):

$$A(0)=ixR\left[\frac{1}{2}+y^{-1}e^{-y}+y^{-2}\left(e^{-y}-1\right)\right]$$

where

$$y=-2ix\left(\sqrt{\varepsilon_p}-\sqrt{\varepsilon^{(2)}}\right), \qquad (6.11)$$

$$x=\frac{2\pi R}{\lambda}\sqrt{\varepsilon^{(2)}}$$

The approximation (6.11) gives quantitatively correct results for spherical particles in the limits (6.9) if

$$\sqrt{\varepsilon_p}-\sqrt{\varepsilon^{(2)}}<<\sqrt{\varepsilon_p} \qquad (6.12)$$

In general cases the expression (6.12) can serve for the interpretation of the main features of A(0) in transition interval from (6.10a) to (6.10b). In particular, it is important to estimate when the deviations from (6.10a) become substantial.. According to approximation (6.11), which gives reasonable estimations correct up to the numerical coefficients that are on the order of unity, $\operatorname{Re} A_\alpha(0)\frac{1}{R_\alpha^2}$ reaches a maximum and begins to sharply decline at $R_\alpha=R_\alpha^0$:

$$R_\alpha^0\cong\frac{\lambda}{\pi\left(\varepsilon_p-\varepsilon^{(2)}\right)} \qquad (6.13).$$

At approximately the same $R_\alpha = R_\alpha^0$ the dependence of $\mathrm{Im}\,A_\alpha(0)\frac{1}{R_\alpha^2}$ on R_α begins to flatten asymptotically tends to its Fraunhofer value. The decline of $\mathrm{Re}\,A_\alpha(0)\frac{1}{R_\alpha^2}$ and flattening of $\mathrm{Im}\,A_\alpha(0)\frac{1}{R_\alpha^2}$ are generally not monotonic due to the specific interference effects between refracted and diffracted waves. However, the corresponding oscillations are smoothed in most real systems due to the particle surface roughness effects and distribution of particle radii[10].

6.3.2 Experimental Procedure

In order to simplify the comparison of theory and experimental results, polystyrene microsphere dispersions were used in the study. These microspheres were obtained from Polysciences, Inc. and the particle sizes and particle number densities are detailed in table 6.3 for the latex samples as received. Dilutions were prepared by mixing each sample suspension in the cell in a 2:1 sample:water ratio in order to obtain polystyrene concentrations on the order of 1.875% by weight. Mixtures of samples were prepared in the cell as 1:1 mixtures and are detailed in table 6.4. Dilutions and mixtures which were prepared in the sample cell volumetrically using an Eppendorf pipette.

The cleaned GLRS substrate #1 was mounted in the substrate holder with the Teflon sample holder in place. Samples were run in random order with sufficient rinsing of the sample cell between samples. Data were collected as 5 scan averages, 1 second integration time, with sample and source reference spectra obtained simultaneously. Data analysis is similar to that in section 6.1, with the exception that a flat field correction was applied prior to the calculation of the GLRS reflection coefficient derivatives using a 51-point Savitsky-Golay filter. Derivative peak positions and magnitudes were found and used to determine absolute dielectric properties and correlate the experimental data with theory using equations (2.4) and (2.8) to generate prediction statistics and error estimates. In contrast to previously presented results, these will be presented in terms of effective dielectric values, not refractive index and absorption, where direct comparisons with theory

---

[10] A useful discussion about the scattering properties of irregularly shaped particles can be found in Pollack, J.; Cuzzi, J. *Light Scattering by Irregularly Shaped Particles*, (D. Scherman, ed.) Plenum, New York, 1983.

are made. The use of the effective dielectric as a comparison takes into account the real and imaginary parts and will reduce the confusion associated with describing absorbance for a system which doesn't absorb the incident light.

6.3.3 GLRS Scattering Results: Monomode Dispersions

The GLRS response to bulk dielectric fluctuations has been demonstrated by orthogonal responses to the real and imaginary parts of the dielectric in contact with the grating. An increase in effective real part of the dielectric $\mathrm{Re}\varepsilon_{eff}$ should yield a threshold shift to higher wavelengths for constant grating period and incident angle. As shown before, this would appear as a peak in the derivative of the reflection coefficient. Conversely, an increase in the imaginary part of the effective dielectric $\mathrm{Im}\varepsilon_{eff}$ will result in a decrease in the derivative peak amplitude. Figure 6.14 shows the experimental GLRS derivatives for the series of undiluted polystyrene microspheres (wt% 2.5 solids). Figure 6.15 displays the GLRS derivatives for the diluted samples with a nominal concentration of polystyrene of 1.875 wt%. The bulk refractive index for water measured via an Abbe refractometer is 1.3308 at 630 nm and 22° C. For the experimental conditions given in figure 6.15, this bulk refractive index value yields the threshold position at 630 nm predicted using equation (2.4). The GLRS derivative reflection spectra peak maxima and positions for both experiments are tabulated in tables 6.5 and 6.6. The singularity position for water for the dilution experiments yielded a slightly lower index of refraction than water in the previous experiment due to the slightly higher ambient temperature (24°C).

The peak position values were used to predict $\mathrm{Re}\varepsilon_{eff}$ values for all samples using equation (6.8) for comparison with the theoretical real effective dielectric values obtained from the Van de Hulst expression (6.11). In addition, the peak maxima were found, and deviations from the water value were calculated. Theory predicts that the peak height will be inversely proportional to the square root of the imaginary part of the dielectric, and the peak height variations were used to generate normalized $\mathrm{Im}\varepsilon_{eff}$ values for comparison with theory.

The general trend for real dielectric function follows what is expected from theory. As seen in figures 6.14 and 6.15, the real index shift due to Rayleigh scattering is evident for samples having particle radii smaller than the wavelength of incident light. Figures

6.16 and 6.17 show the theoretical values for Reε_{eff} calculated for the system studied: polystyrene bulk dielectric of 2.4869; water as the solvent; and an incident wavelength of 630 nm. Plotted along the x-axes is the ratio of radius to incident wavelength. Also plotted are the GLRS determined Reε_{eff} values to demonstrate the validity of the theory. The low radius wavelength shift is consistent with the expected Reε_{eff} modulation, and the Rayleigh limit Reε_{eff} agrees very well with the GLRS experimentally determined Reε_{eff}.

The small deviations from the theory are demonstrated in the transition region, where the sharpness of the decline is evident in the GLRS values. This is due to the fact that the Van de Hulst expressions are approximate for forward scattering, and in addition, the forward scattering amplitude transition region from Rayleigh to Fraunhofer scattering may be more sharply measured using GLRS in that contribution from Reε_{eff} is deconvoluted from the imaginary part. In addition, the theoretical curve is calculated using a nominal particle concentration of 2.5% by weight, and the actual concentrations of the samples deviate from that nominal value according to table 6.3. However, the transition region occurs in the particle radius range that is predicted from theory, and the theoretical limiting values for Reε_{eff} are consistent with the GLRS measured Reε_{eff}. Thus, the real index shift due to Rayleigh scattering in the limit of small particles is directly measurable using GLRS, even as the contribution from the imaginary part of the dielectric function begins to dominate when the transition region is reached.

The sample containing particles of radius 1.046 microns yields a bulk Reε_{eff} that is lower than either the solvent (water) or the particle material. This is due to the interference effects in forward scattering for spherical, non-absorbing species and further validates the application of GLRS to scattering systems in that the transition region oscillations in Reε_{eff} are directly measurable. In addition, this lends credence to the assertion that a forward scatter mechanism is responsible for the GLRS response based on the relationship between forward scatter amplitude and effective dielectric. This points to the uniqueness of GLRS in that a reflection method is used to interrogate a bulk medium that modulates the reflected light based on changes in the forward scattering properties of the medium.

Figures 6.18 and 6.19 show the calculated theoretical normalized Imε_{eff} values using the Van de Hulst approximation. The normalized experimental values, calculated from the GLRS peak height modulations by taking the square of the height deviation from a water baseline and applying a normalization factor, are also plotted for comparison. It is apparent that the forward scattering approximation agrees very well with the physical phenomena as the monotonic increase in $\mathrm{Im}\varepsilon_{\mathrm{eff}}$ to the peak of the transition region is seen on both the GLRS measured $\mathrm{Im}\varepsilon_{\mathrm{eff}}$ and the theoretical $\mathrm{Im}\varepsilon_{\mathrm{eff}}$. Similarly, the transition region occurs at roughly the same particle radius as the region for the $\mathrm{Re}\varepsilon_{\mathrm{eff}}$ values, and this is where the effective imaginary dielectric begins to dominate and the real part reverts back to the bulk solvent value, as in the case of Fraunhofer scattering. It is interesting to note that the finite $\mathrm{Im}\varepsilon_{\mathrm{eff}}$ expected for larger particles is not evident in the GLRS measurements. This due to the fact that in Chapter 5 it was demonstrated that a threshold of sensitivity to $\mathrm{Im}\varepsilon_{\mathrm{eff}}$ exists for this particular grating/substrate material that is above the $\mathrm{Im}\varepsilon_{\mathrm{eff}}$ values for the dilute polystyrene concentrations used here. Also, as the weight percent polystyrene is essentially constant for each experiment, the number density of scatterers is reduced by a factor of 10^7, and this reduces the number of scattering events close to the grating.

6.3.4 Qualitative GLRS Scattering Results: Polymodal Dispersions

The GLRS scattering response results demonstrate that GLRS can provide information regarding the types of particles in a suspension as well as the distribution for a single mode distribution. Interesting cases arise where the particles in suspension have size ranges that fit bimodal and polymodal distributions. Thus, mixture samples were prepared from the suspensions as received and were used to test the validity of the forward scattering theory in that the response to the bimodal systems should be superpositions of the responses to single mode systems based on the proximity of the distribution to the transition region.

In the figures to follow, the mix## refers to the 1:1 mixtures of samples according to their sample numbers, where a higher sample number corresponds to the larger particle radius. First, samples were run corresponding to nearest neighbor distributions and the first derivatives are shown in figure 6.20. The transition region for these systems is sharp and corresponds well with the region described in the previous discussion for the monomodal systems, occurring at around 0.5 - 1.0 micron particle radius. This is due to the fact that for each sample, all particle size distributions are on the same side of the transition region. As such, the GLRS response is due to a summation of effects, as expected from the Van De Hulst expression. Notice that the effects due to the real part of the effective dielectric are similar to those for the uni-modal systems, where the peak shift is on the order of the 5 nm. As no dilution was made in the preparation of the samples, the weight percent concentration should remain the same when compared to the samples as received. This seems to be the case for these nearest neighbor samples. However, the imaginary dielectric response, as shown in the peak height decline, appears to be the mean of the responses for the single particle size dispersions, and again this is expected from Van de Hulst. Qualitatively, these curves are expected from theory, where the real dielectric response is essentially the response for the single component systems, and the imaginary dielectric effects are summations of the individual responses.

Displayed in figure 6.21 are the reflection coefficient derivatives obtained for the farthest neighbor bimodal mixtures. The GLRS water response is plotted for reference. In each case, the distributions are comprised of particle sizes that correspond to either side of the transition region from Rayleigh to Fraunhofer scattering. The dominant response for these curves is an imaginary dielectric increase. The real dielectric shift is intermediate to that of the pure sample set, and this is due to the summation of real dielectric components due to the combination of large and small particles relative to the transition region. As the particle sizes converge to the transition region, the imaginary component becomes large due to the summation of the imaginary components of the individual particle size classes. As seen above, the imaginary component of the dielectric increases as the transition region is reached form either side, and this is demonstrated succinctly in the response of the farthest neighbor sample set in figure 6.21.

Finally, figure 6.22 displays the derivatives responses of GLRS to systems where the mean particle size traverses the transition region slowly due to the selection of combinations that correspond to samples that differ in sample number by an index of 4. Again, the water response is plotted for reference purposes. It is expected that the GLRS derivative response will be characterized by a large imaginary dielectric component as the mean particle size is close to the transition region for all samples. This is borne out in the curves where the imaginary response goes through a maximum that corresponds to the center of the region. In addition, the real dielectric response is seen as slight shifts that again correspond to a region within the transition region for the system. As seen in the figure, for an increase in mean particle size, the real dielectric shifts closer to the bulk water value without reaching it, indicating that the overall response of the system is due to the proximity to the transition region between Rayleigh and Fraunhofer scattering.

Classically, reflection methods have not been employed in particle size analysis due to the convolution of the forward scattering response with other scattering angles. In addition, the use of ATR for investigation of structured colloids[11], the limiting factor is the application of an appropriate theory to describe the response for particles larger than one micron. In addition, the FT-IR methods employed only take into account the effective imaginary dielectric shifts imparted to the sample by the presence of particles.

In contrast, GLRS represents a quantitative tool for particle size analysis that is used in reflection mode and responds to both real and imaginary components of the effective dielectric of the sample. By optically excluding the effects of other scattering angles, the response of GLRS is more easily described and correlated with existing theory. In addition, the amount of information gathered from the GLRS measurements may be increased if the experiments are performed with varying singularity positions (achieved by incident angle and/or grating period modulation) according to (2.4) which may allow deconvolution of the effects presented for the mixtures.

---

[11] Kemsley, E. K.; Appleton, G. P.; Wilson, R. H. *Spectrochimica Acta*, **1994**, *50A*, 1235-1242.

Table 6.1 Tantalum oxide thin film sputtering parameters using a Denton Vacuum DC planar magnetron sputter coating system.

Initial pump down of chamber	1×10^{-5} torr
Argon partial pressure	4.5 millitorr
Oxygen partial pressure	1.7-2.0 millitorr
Sputter voltage	400 volts
Sputter current	0.3 amperes
Sputter rate on QCM	~3.0 angstroms/second
Target thickness on GLRS substrate	50.0 nanometers

Table 6.2 Ellipsometric measurements of reference tantalum oxide films silicon substrates using a two zone calculation (automated). Target thickness was 50.0 nm on the QCM. Replicate measurements were made at different points on each substrate.

Sample number	Thickness as read on QCM, angstroms	True thickness, angstroms	refractive index at 633.0 nanometers
1	515	617	2.305
1	515	606	2.286
1	515	610	2.294
2	513	592	2.298
2	513	596	2.297
2	513	594	2.301
3	518	598	2.345
3	518	607	2.359
3	518	587	2.329

Mean refractive index of film	2.3127 ± 0.025
Mean correction factor applied to QCM reading	85.8%

Table 6.3 Polystyrene Microsphere samples in water: concentrations and particle radii. Polystyrene refractive index is 1.577 at 589.3 nanometers[12].

Sample	Particle radius, microns	Volume % polystyrene	Particles/mL
1	0.042 ±0.001	2.55	8.08×10^{15}
2	0.101 ±0.005	2.38	5.52×10^{14}
3	0.178 ±0.007	2.51	1.06×10^{14}
4	0.240 ±0.007	2.50	4.31×10^{13}
5	0.349 ±0.006	2.56	1.44×10^{13}
6	0.536 ±0.009	2.44	3.78×10^{12}
7	1.046 ±0.048	2.49	5.19×10^{11}
8	1.418 ±0.068	2.38	1.99×10^{11}
9	5.284 ±0.517	2.38	3.85×10^{9}
10	7.659 ±0.983	2.38	1.27×10^{9}
11	11.006 ±1.515	2.56	4.59×10^{8}

---

[12] Bowman, E. M. , 1992, Ph.D. Dissertation, University of Washington.

Table 6.4 Mixtures of polystyrene microsphere suspensions. 1:1 mixtures were prepared in the sample cell for each run.

Sample	Particle radii, microns, each ~2.5% by weight
mix12	0.043 + 0.101
mix23	0.101 + 0.178
mix34	0.178 + 0.240
mix45	0.240 + 0.349
mix56	0.349 + 0.536
mic67	0.536 + 1.046
mix78	1.046 + 1.418
mix18	0.0425 + 1.418
mix27	0.101 + 1.046
mix36	0.178 + 0.536
mix15	0.043 + 0.349
mix26	0.101 + 0.536
mix37	0.178 + 1.046
mix48	0.240 + 1.418

Table 6.5 GLRS derivative peak positions and amplitude differences (from a water baseline) and corresponding real dielectric functions predicted from the peak positions: nominal 2.5% by weight concentration of polystyrene.

Sample number	Position of GLRS singularity, in nanometers	Predicted $\text{Re}\,\varepsilon_{\text{eff}}$ from GLRS	Peak magnitude deviation from water
water	630.1	1.7709	0.000000
1	635.1	1.7869	0.000141
2	635.1	1.7869	0.001596
3	635.1	1.7869	0.003632
4	634.5	1.7850	0.003328
5	633.9	1.7831	0.004377
6	634.3	1.7844	0.004502
7	628.7	1.7662	0.001919
8	630.1	1.7709	0.000039
9	630.1	1.7709	0.000358
10	630.2	1.7712	0.001371
11	630.1	1.7712	0.000206

Table 6.6 GLRS derivative peak positions and amplitude differences (from a water baseline), and corresponding real dielectric functions predicted from the peak positions: nominal 1.875% by weight concentration polystyrene.

Sample number	Position of GLRS singularity, in nanometers	Predicted Reε_{eff} from GLRS	Peak magnitude deviation from water
water	629.9	1.7703	0.000000
1	633.9	1.7831	0.000461
2	633.5	1.7818	0.001716
3	633.5	1.7818	0.002703
4	633.4	1.7815	0.003202
5	631.5	1.7754	0.004051
6	633.3	1.7812	0.004713
7	629.1	1.7677	0.001155
8	629.5	1.7690	0.000082
9	629.8	1.7699	-0.000020
10	629.9	1.7702	0.000174
11	629.9	1.7702	-0.000143

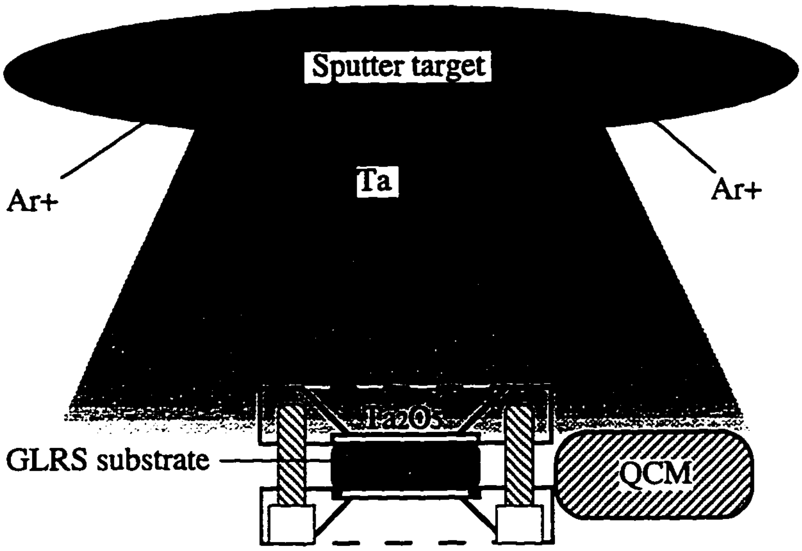

Figure 6.1 Tantalum oxide sputter coating procedure schematic. The QCM is placed in close proximity to the GLRS substrate and calibrated. Oxide films are sputtered onto the grating side of the substrate.

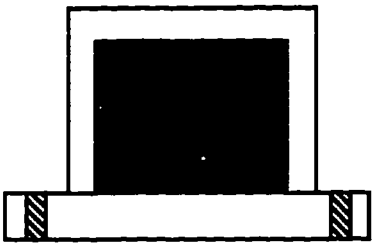

sample cell top view

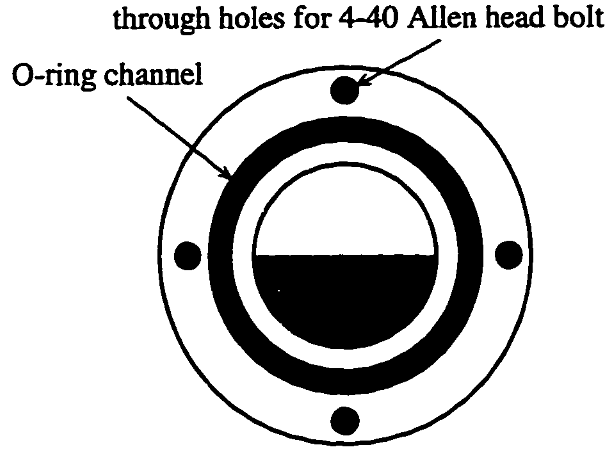

sample cell front view

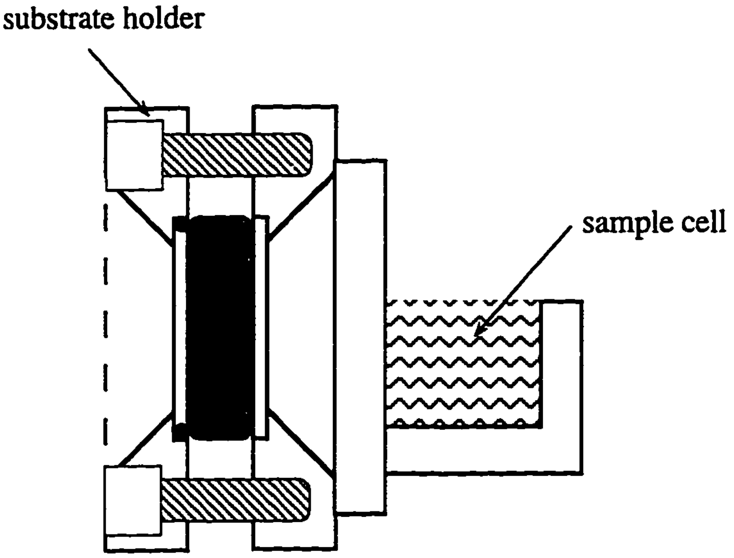

Sample cell mounted to substrate holder, side view

Figure 6.2 Modified substrate/sample holder. Sample cell is removed during film deposition and reattached for data collection.

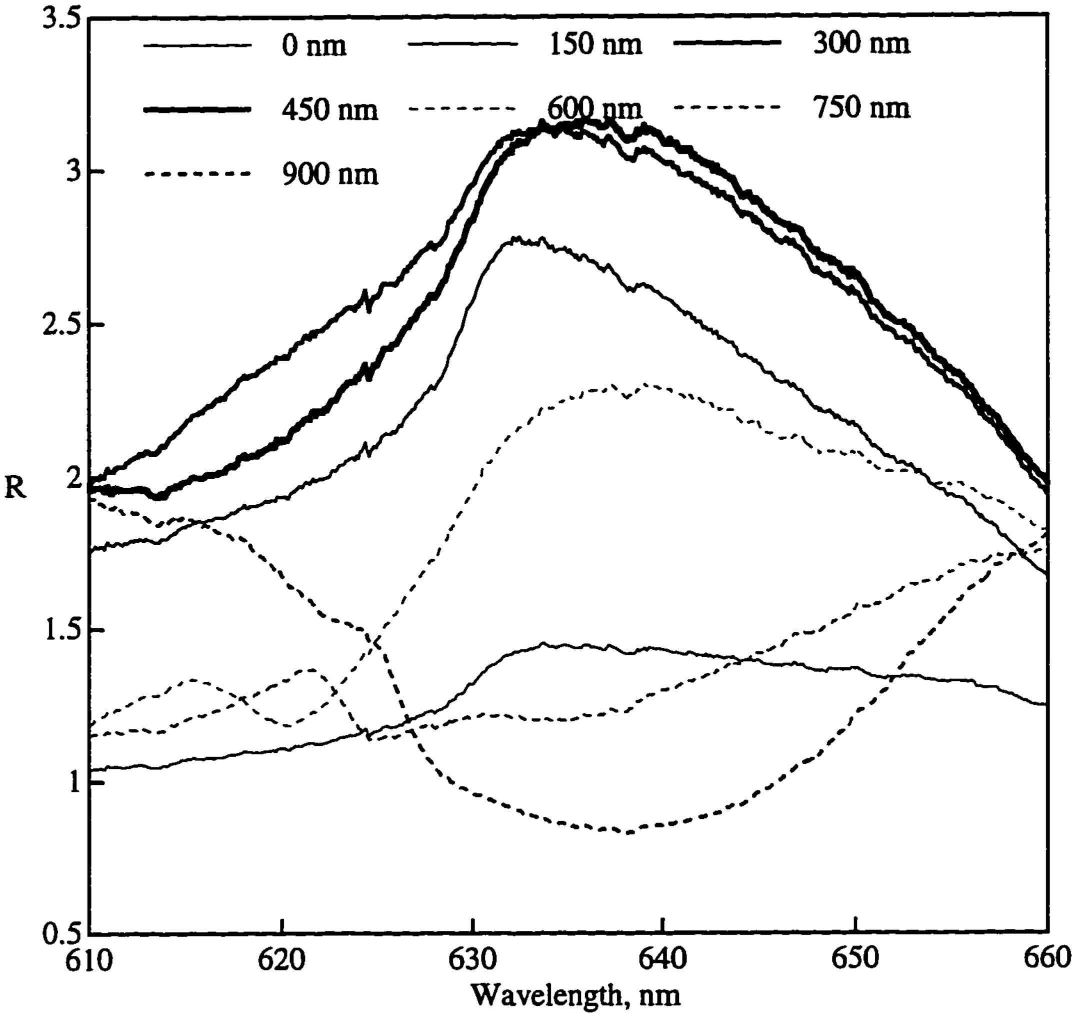

Figure 6.3 GLRS reflection coefficient response to simulated fouling layers. Grouping one, 150 nm increments beginning at 0 nm, p-polarization.

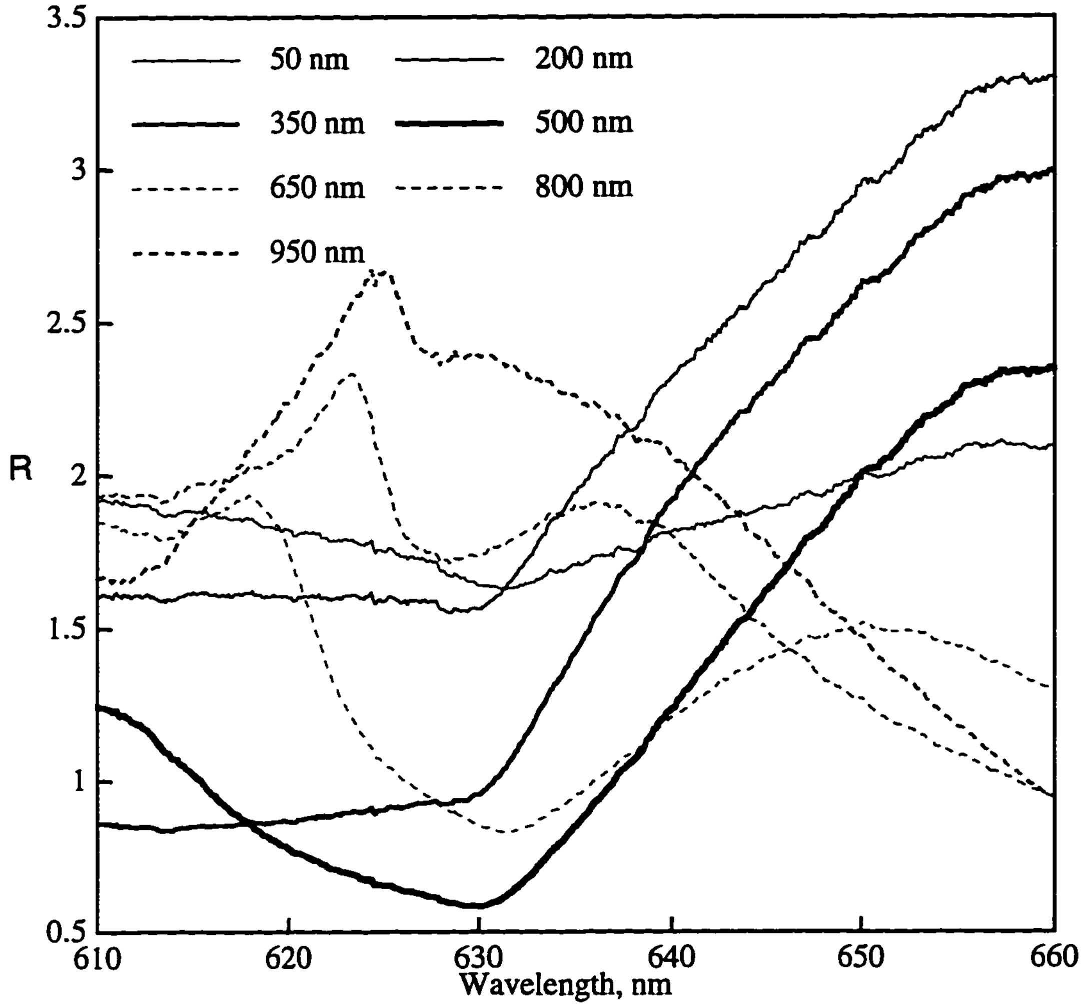

Figure 6.4 GLRS reflection coefficient response to simulated fouling layers. Grouping two, 150 nm increments beginning at 50 nm, p-polarization.

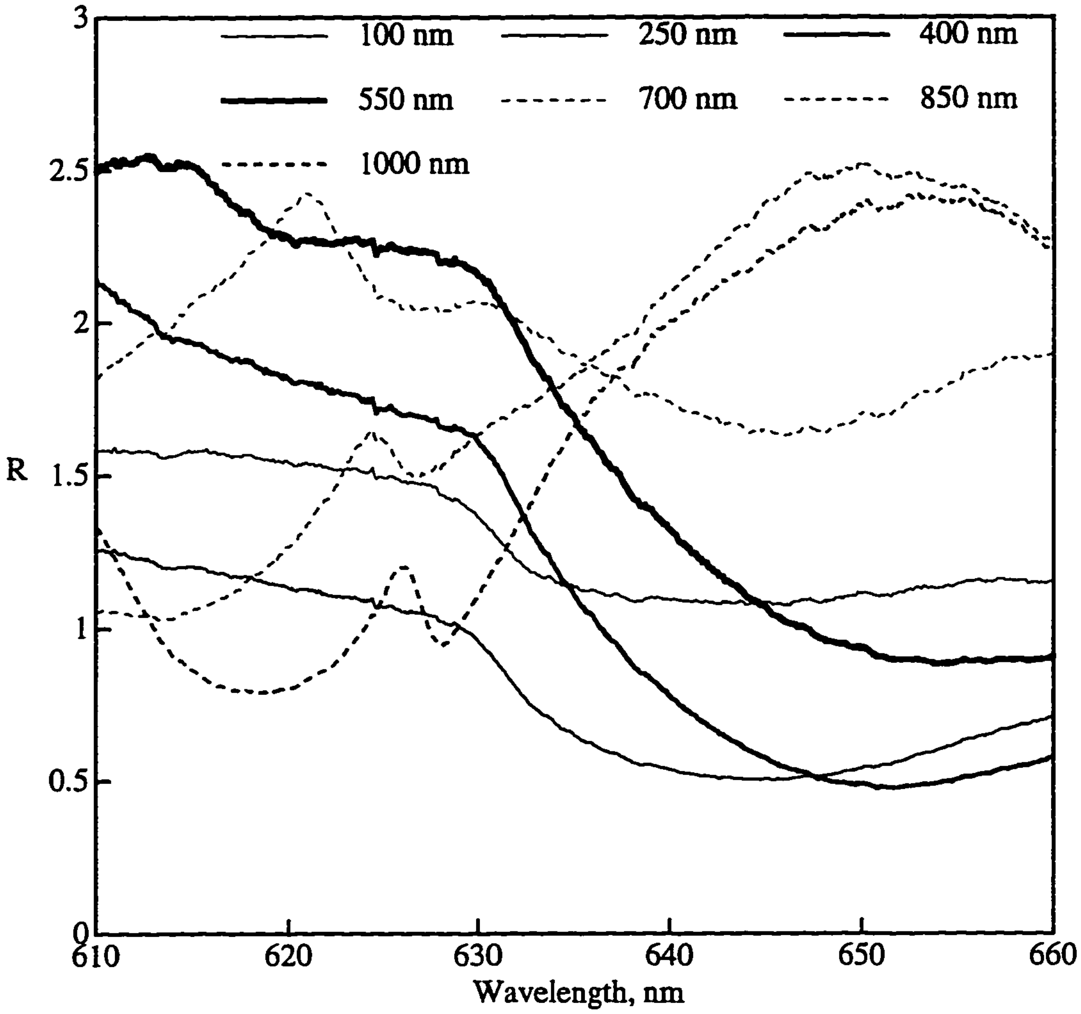

Figure 6.5 GLRS reflection coefficient response to simulated fouling layers. Grouping three, 150 nm increments beginning at 100 nm, p-polarization.

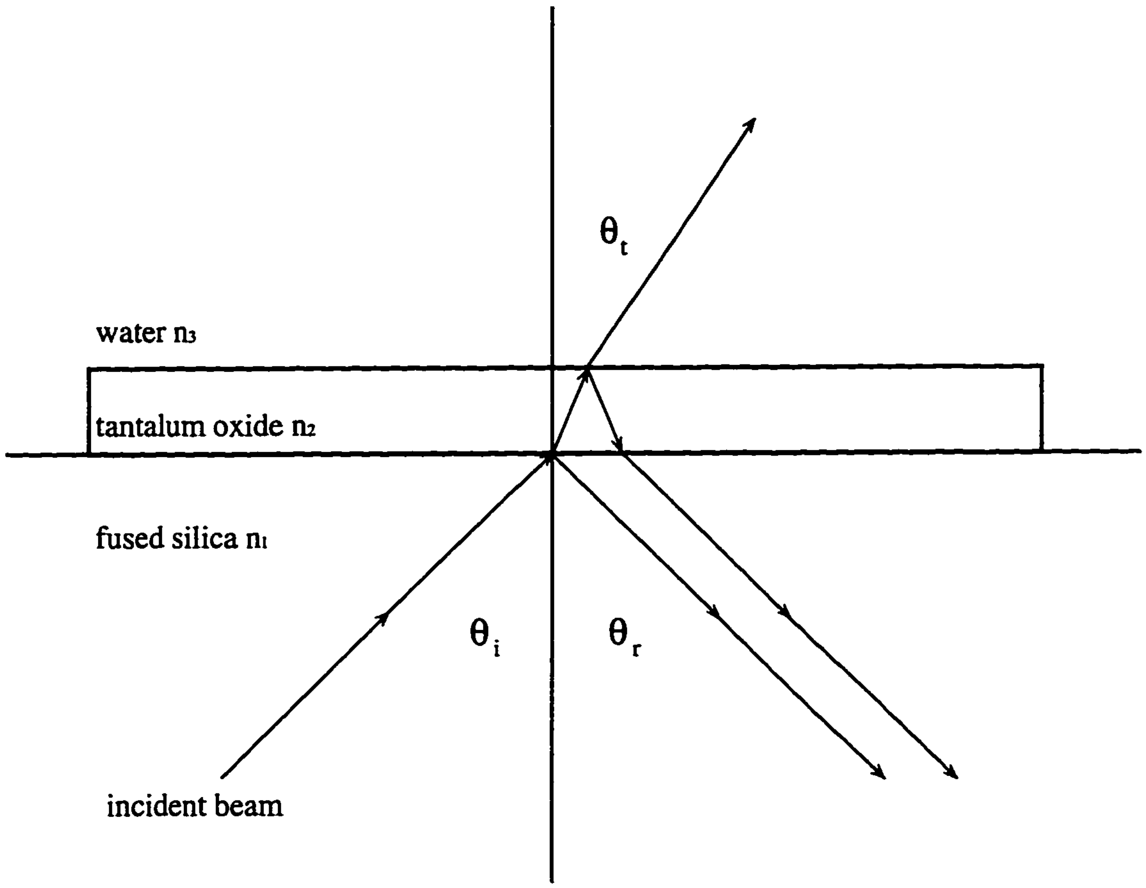

Figure 6.6 Ray trace diagram of reflection from a three layer stack of fused silica, tantalum oxide, and water. Interference effects due to the high refractive index thin film yield drastic, periodic variations in reflectivity with film thickness and wavelength of incident light.

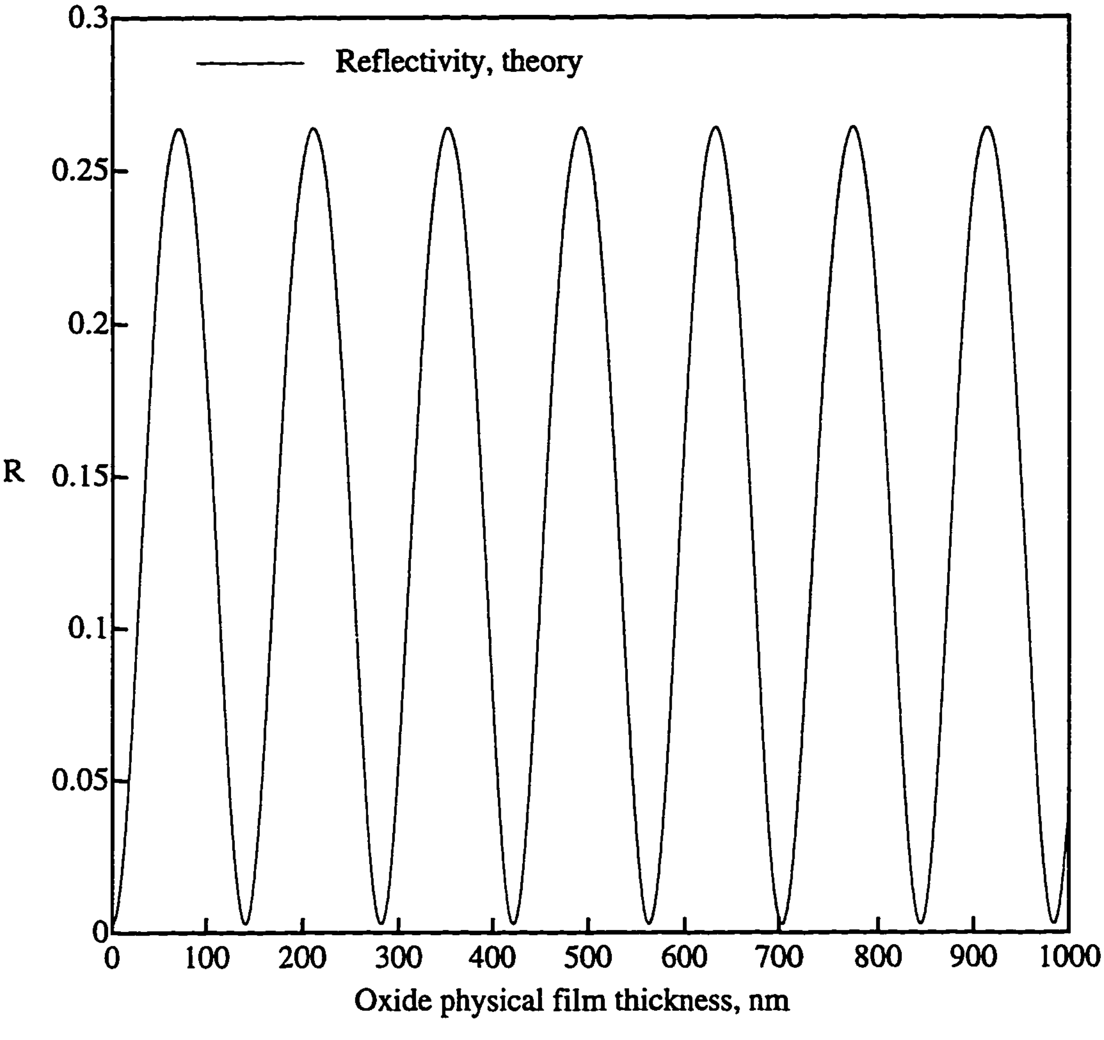

Figure 6.7 Theoretical reflectivity for a fused silica:tantalum oxide:water three layer stack at 630 nm as a function of tantalum oxide thickness.

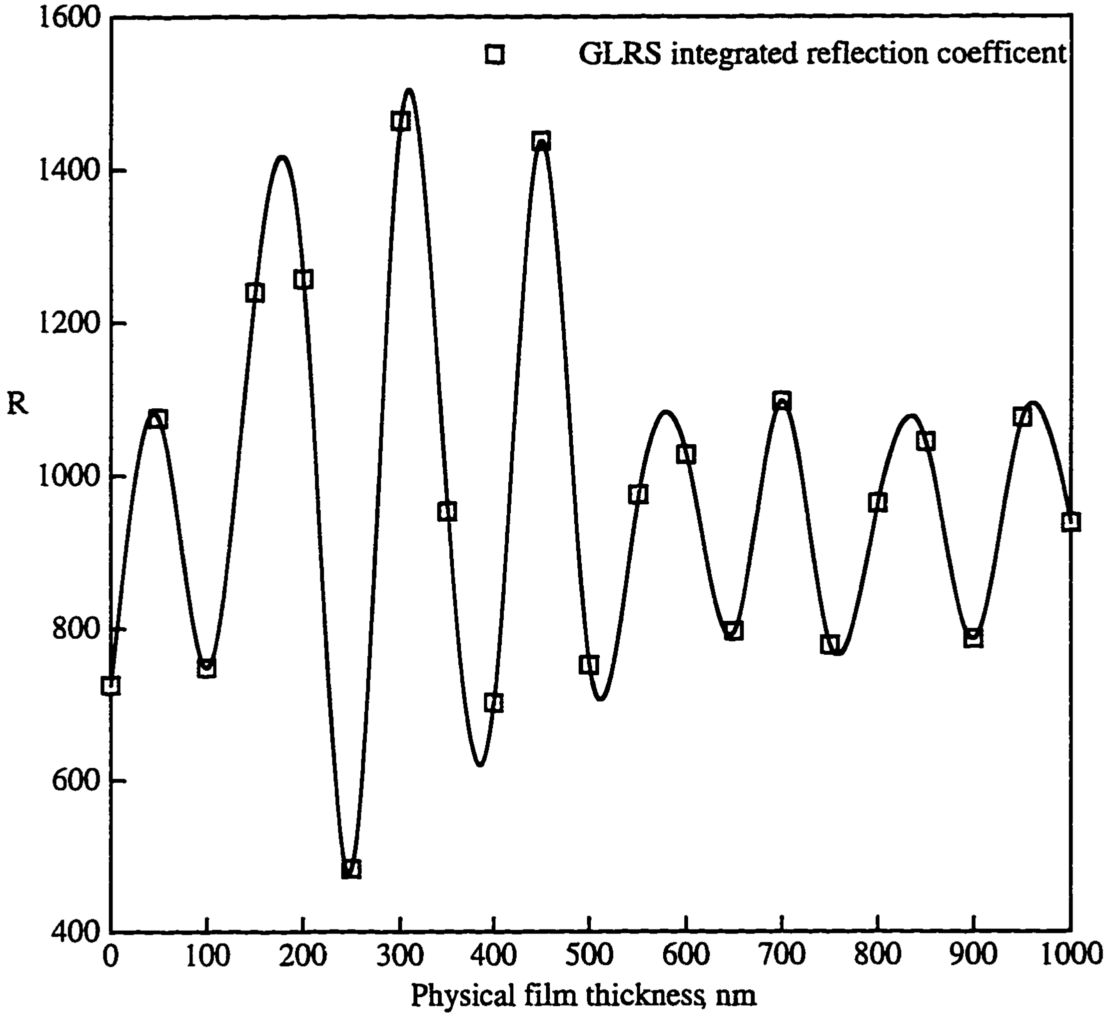

Figure 6.8 Integrated GLRS reflected intensity as a function of oxide film thickness. Lines are interpolated between points to clarify periodicity.

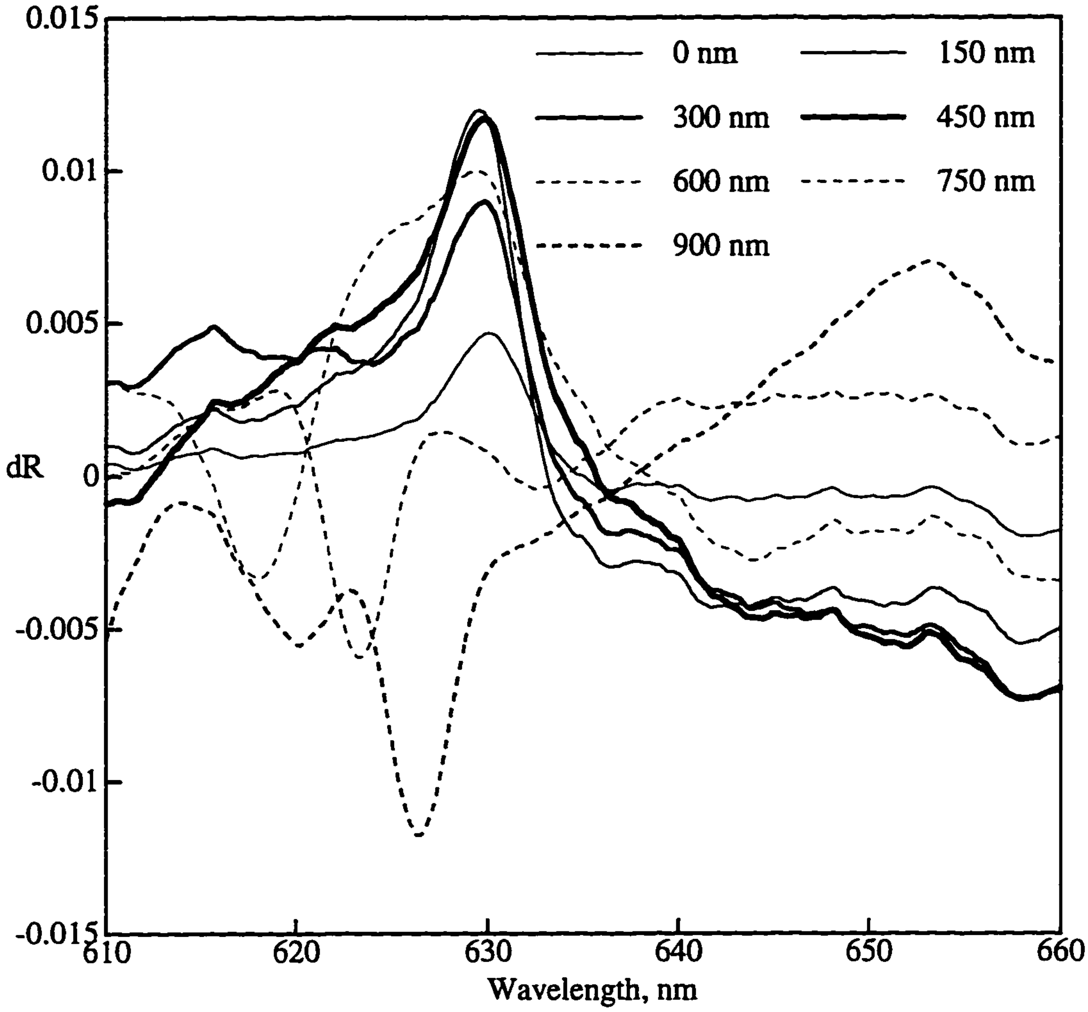

Figure 6.9 GLRS reflection coefficient derivative response to simulated fouling layers. Grouping one, 150 nm increments beginning at 0 nm, p-polarization.

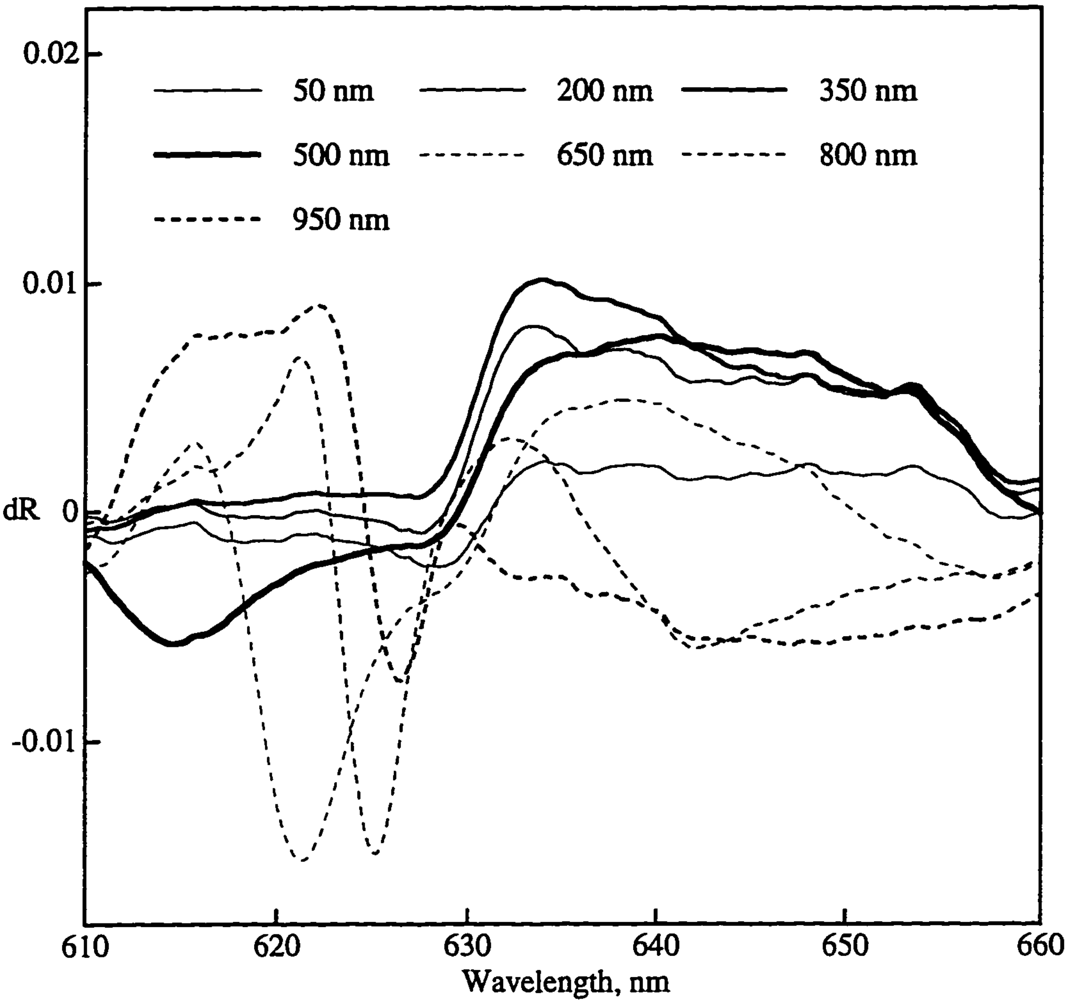

Figure 6.10 GLRS reflection coefficient derivative response to simulated fouling layers. Grouping two, 150 nm increments beginning at 50 nm, p-polarization.

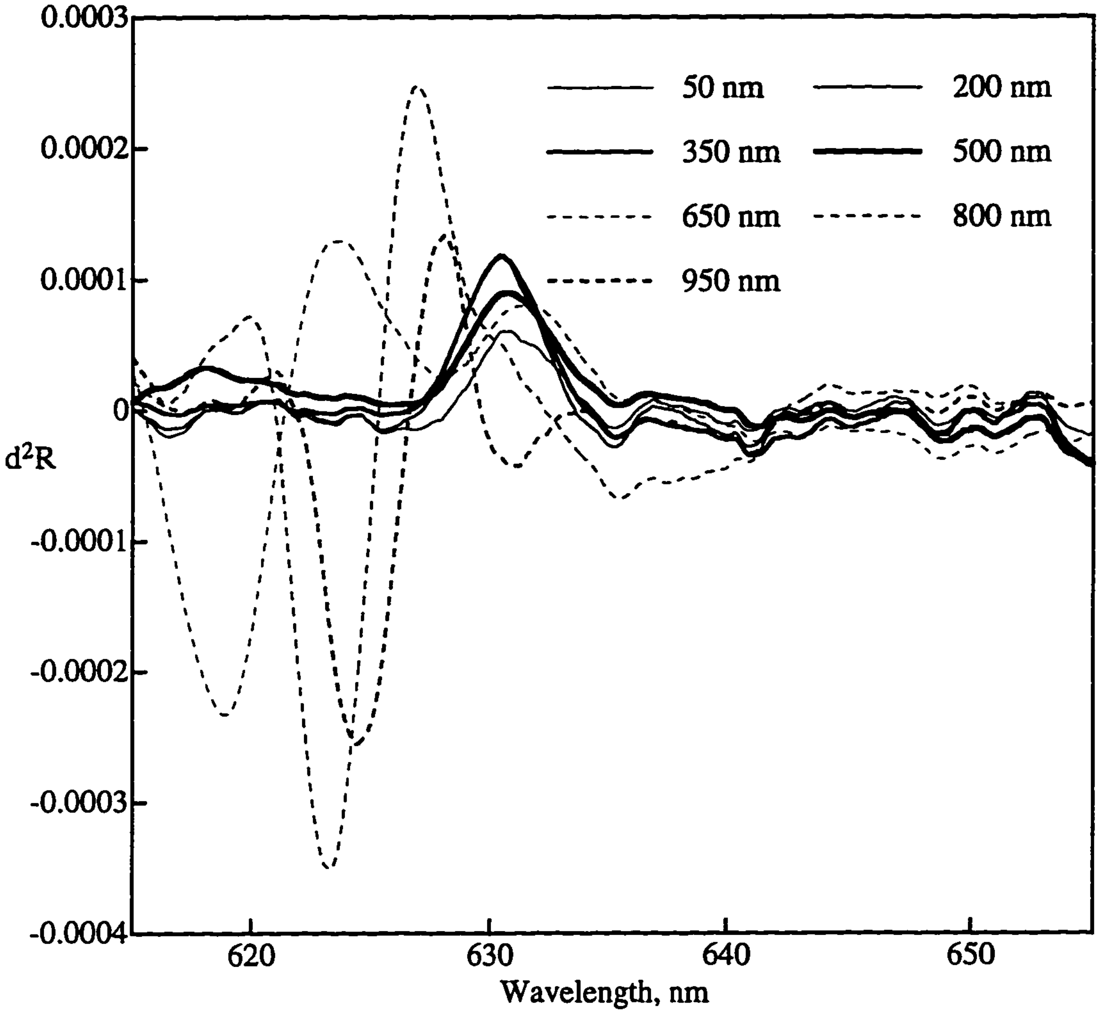

Figure 6.11 GLRS reflection coefficient second derivative response to simulated fouling layers. Grouping two, 150 nm increments beginning at 50 nm, p-polarization.

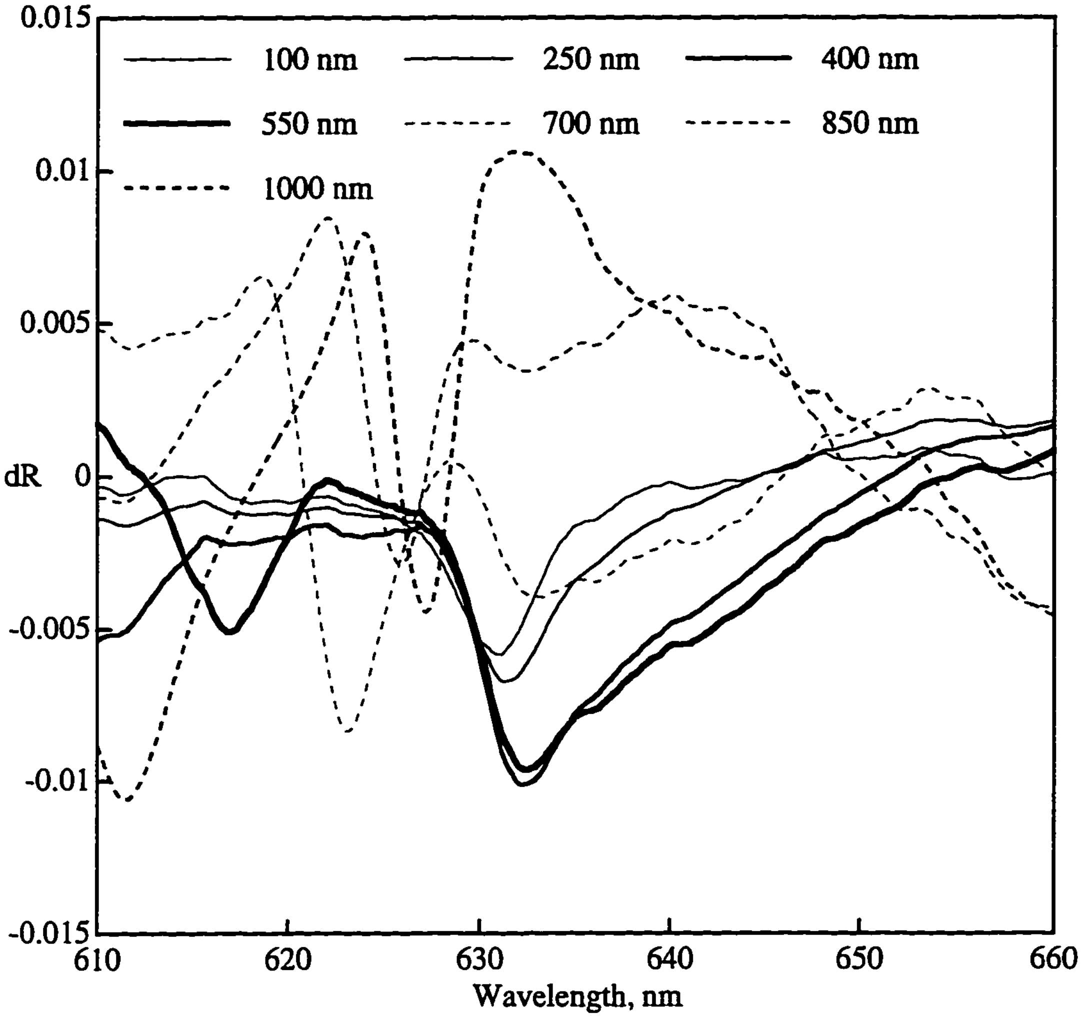

Figure 6.12 GLRS reflection coefficient derivative response to simulated fouling layers. Grouping three, 150 nm increments beginning at 100 nm, p-polarization.

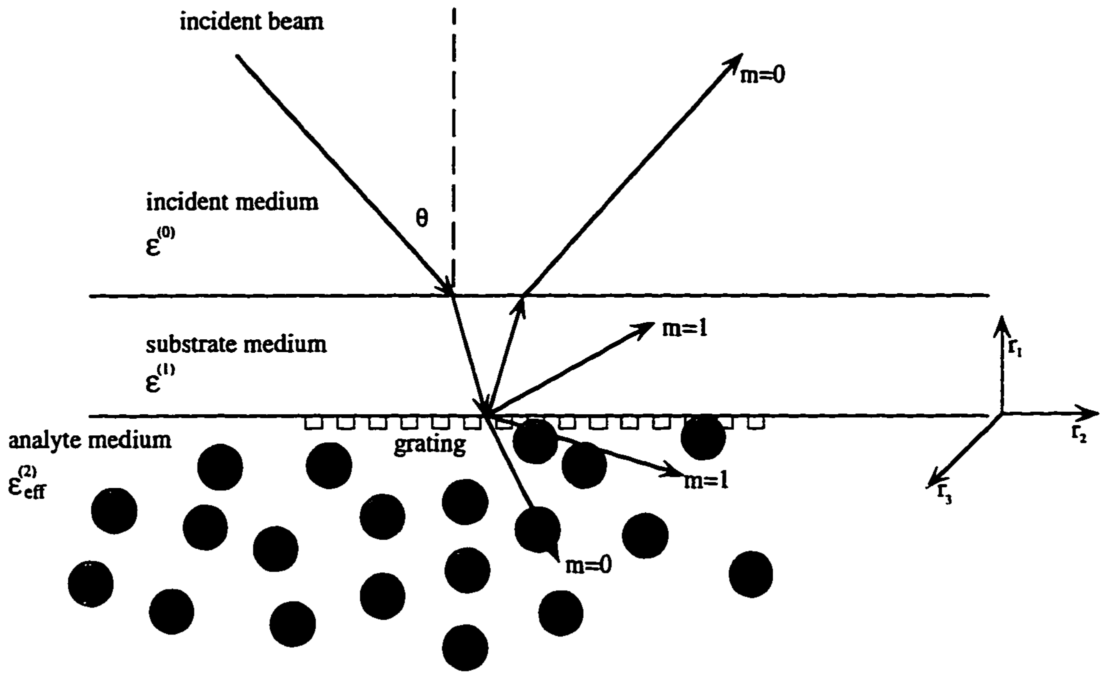

Figure 6.13 GLRS ray-trace diagram illustrating the presence of particles in the sample matrix.

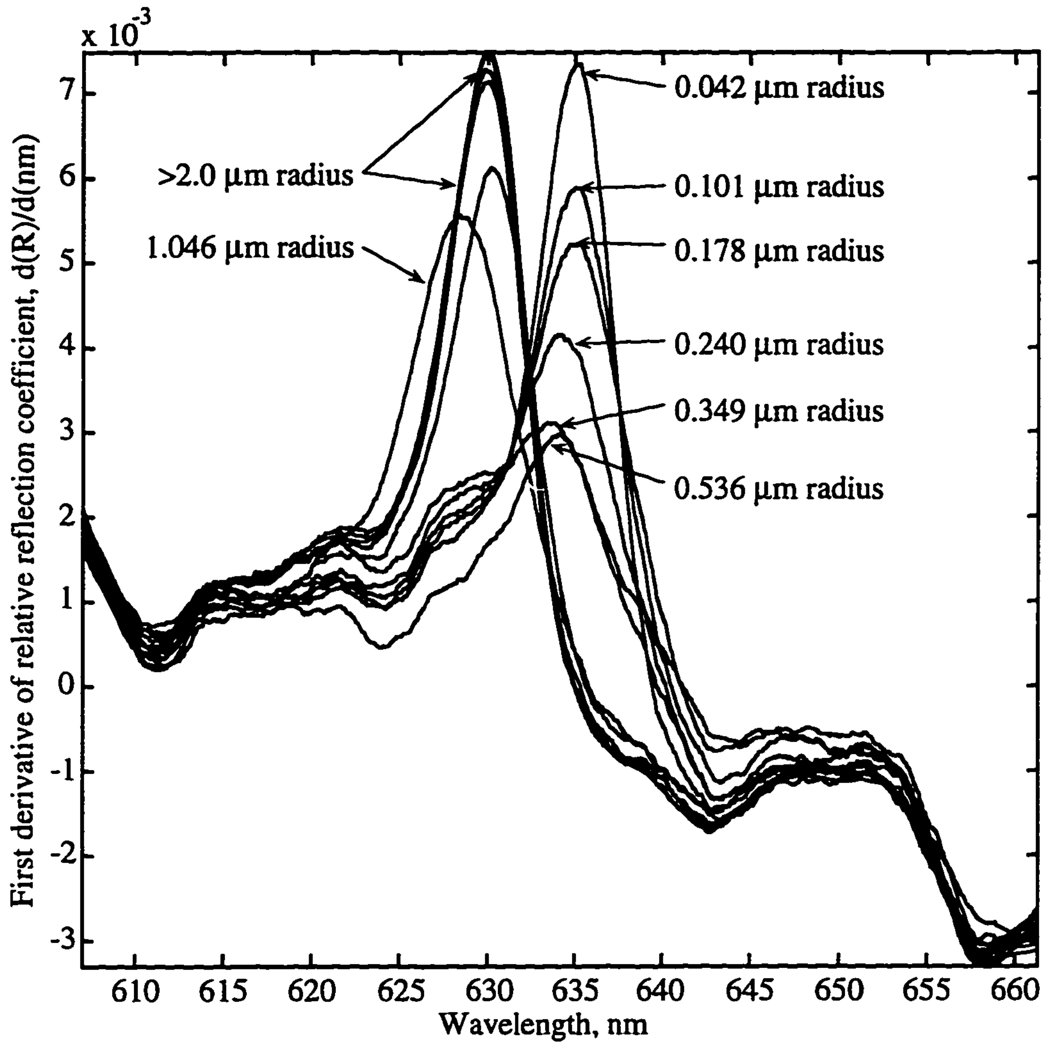

Figure 6.14 GLRS relative reflection coefficient derivative response to polystyrene suspensions, nominal 2.5% solids, p- polarization.

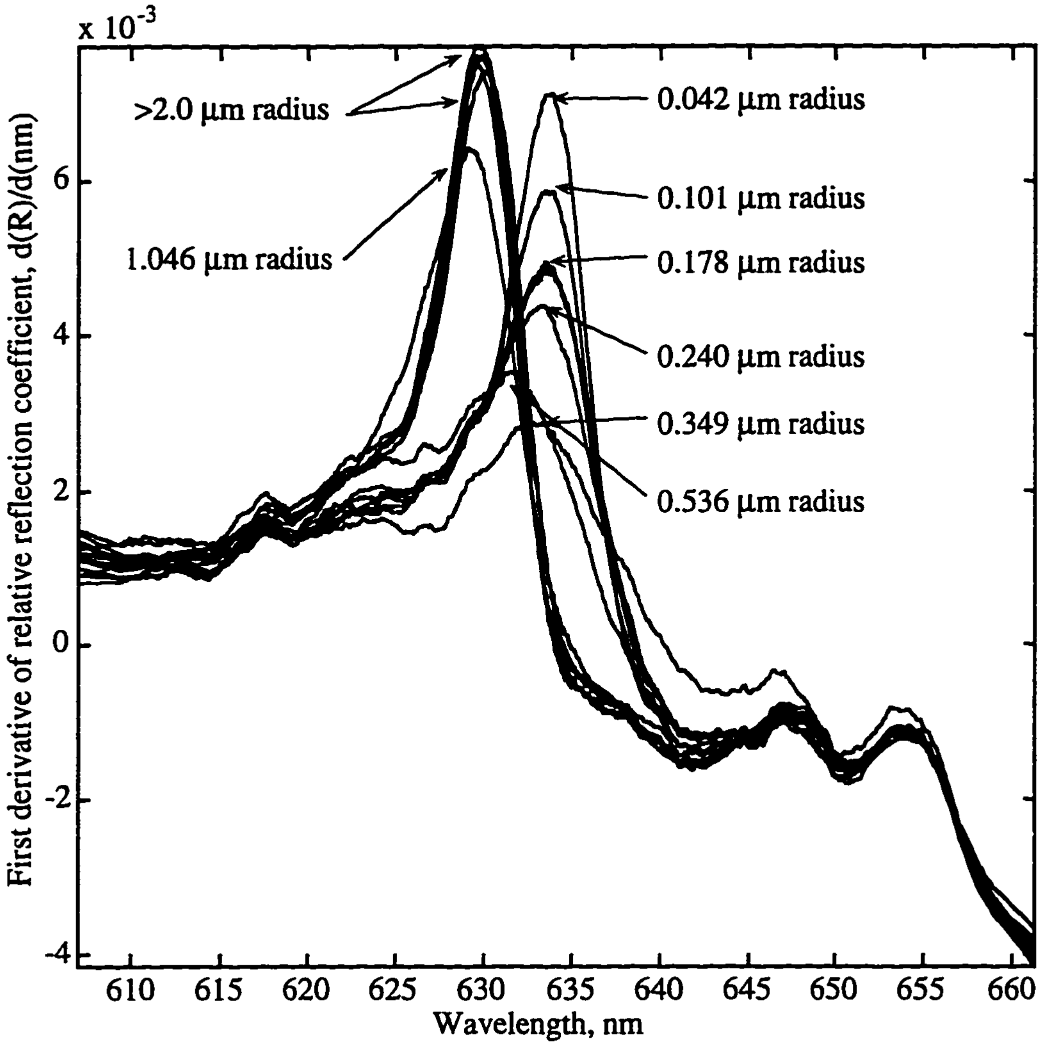

Figure 6.15 GLRS relative reflection coefficient derivative response to polystyrene suspensions, nominal 1.875% solids, p- polarization.

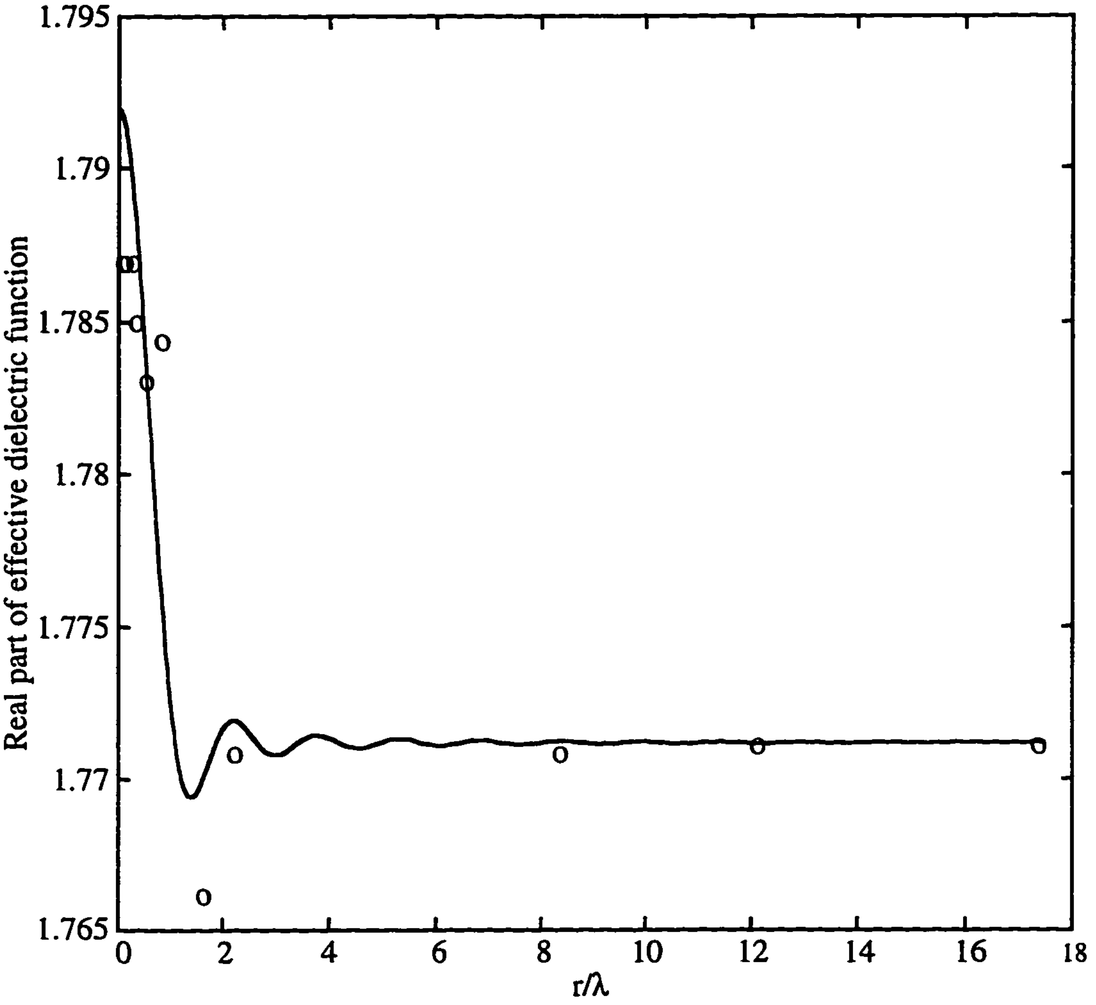

Figure 6.16 Real effective dielectric values predicted from GLRS (o) and calculated from the Van de Hulst expression (-) for the series of ~2.5% solids polystyrene microsphere samples.

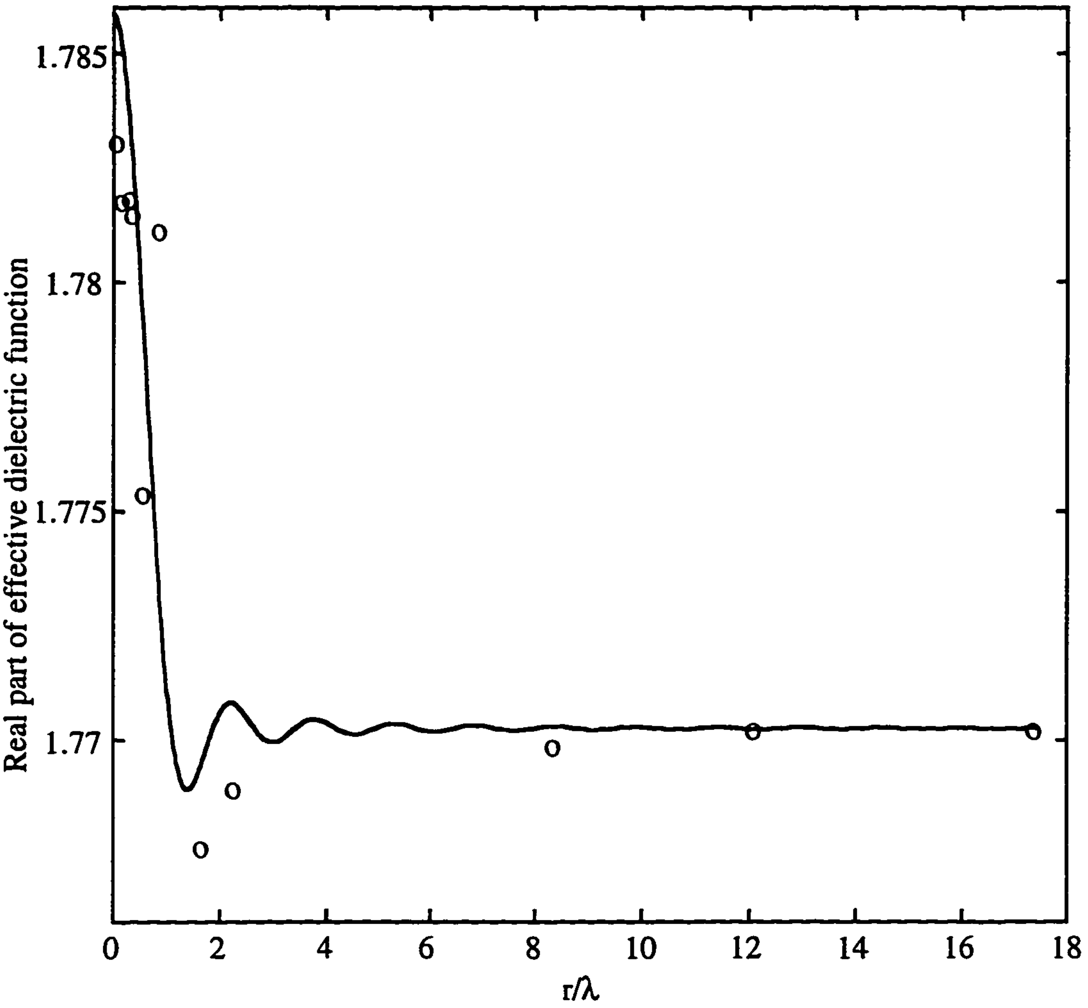

Figure 6.17 Real effective dielectric values predicted from GLRS (o) and calculated from the Van de Hulst expression (-) for the series of ~1.875% solids polystyrene microsphere samples.

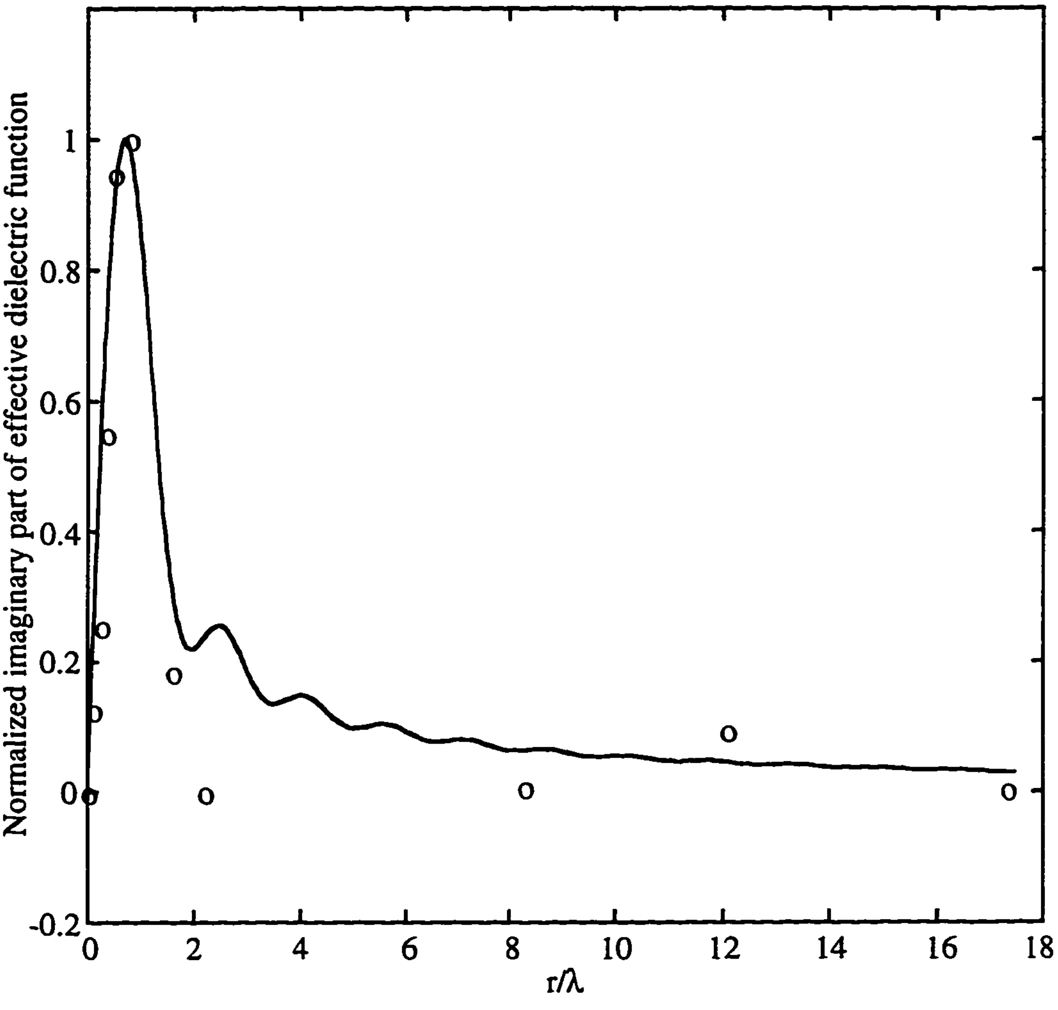

Figure 6.18 Normalized imaginary effective dielectric values predicted from GLRS (o) and calculated from the Van de Hulst expression (-) for the series of ~2.5% solids polystyrene microsphere samples.

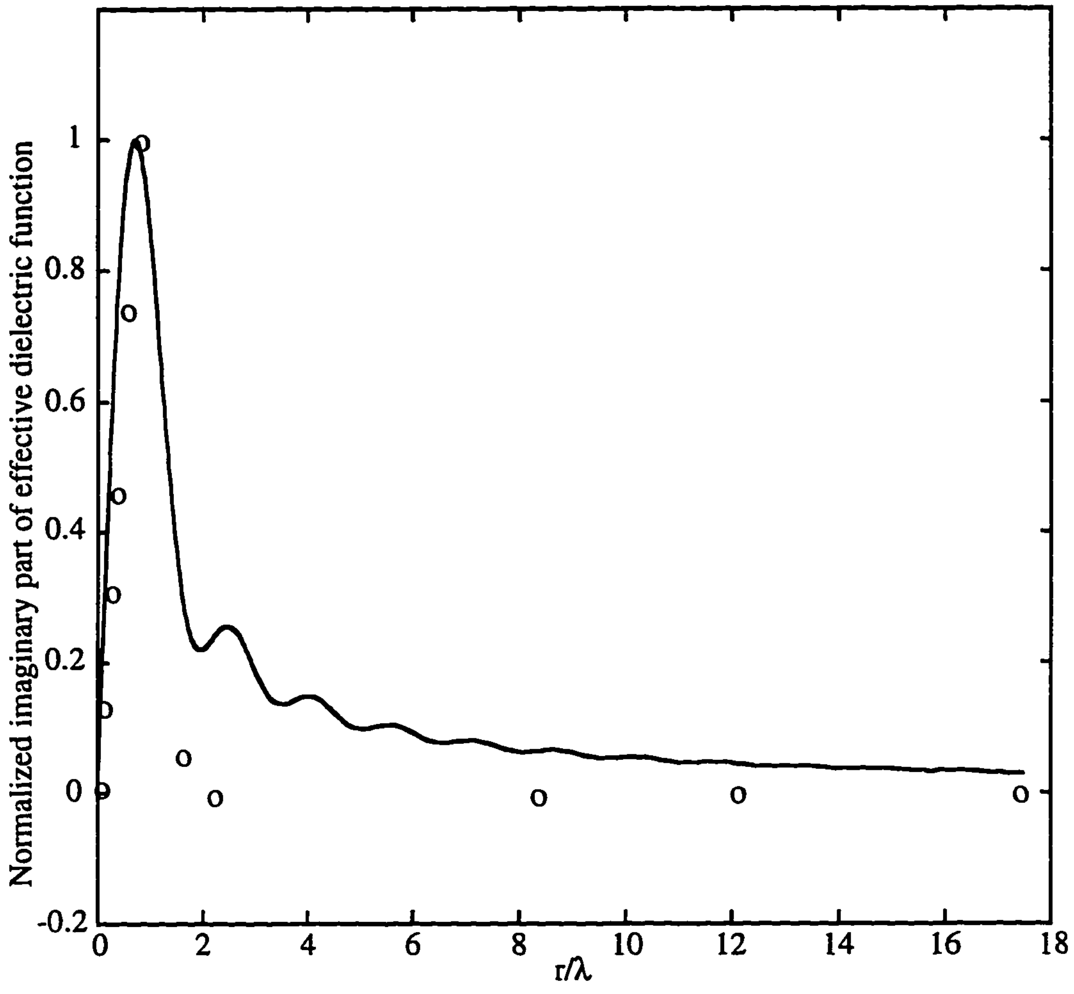

Figure 6.19 Normalized imaginary effective dielectric values predicted from GLRS (o) and calculated from the Van de Hulst expression (-) for the series of ~1.875% solids polystyrene microsphere samples.

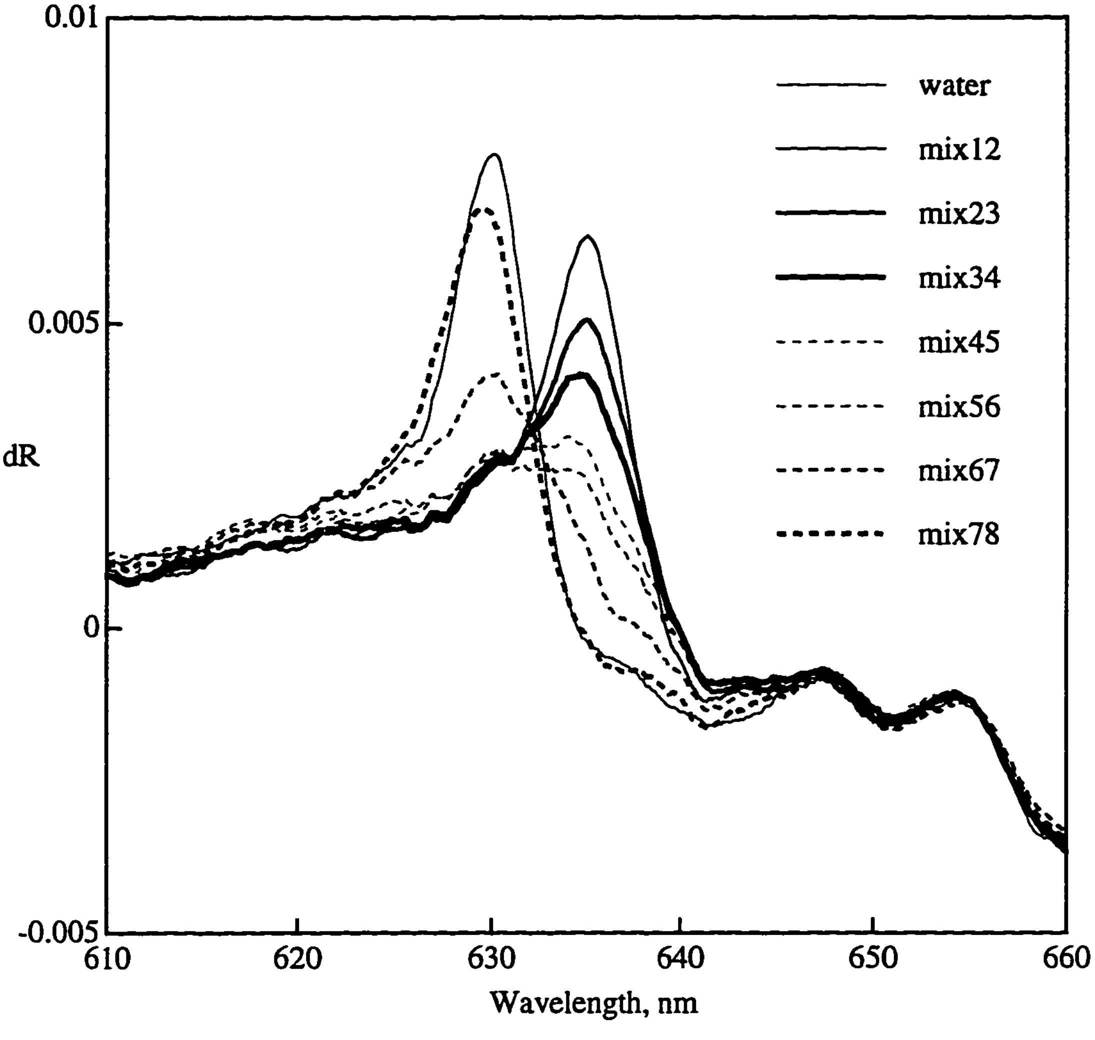

Figure 6.20 GLRS relative reflection coefficient derivative response to mixtures of polystyrene microspheres, ~2.5% solids, bi-modal distributions of nearest neighbor particle sizes (see table 6.4).

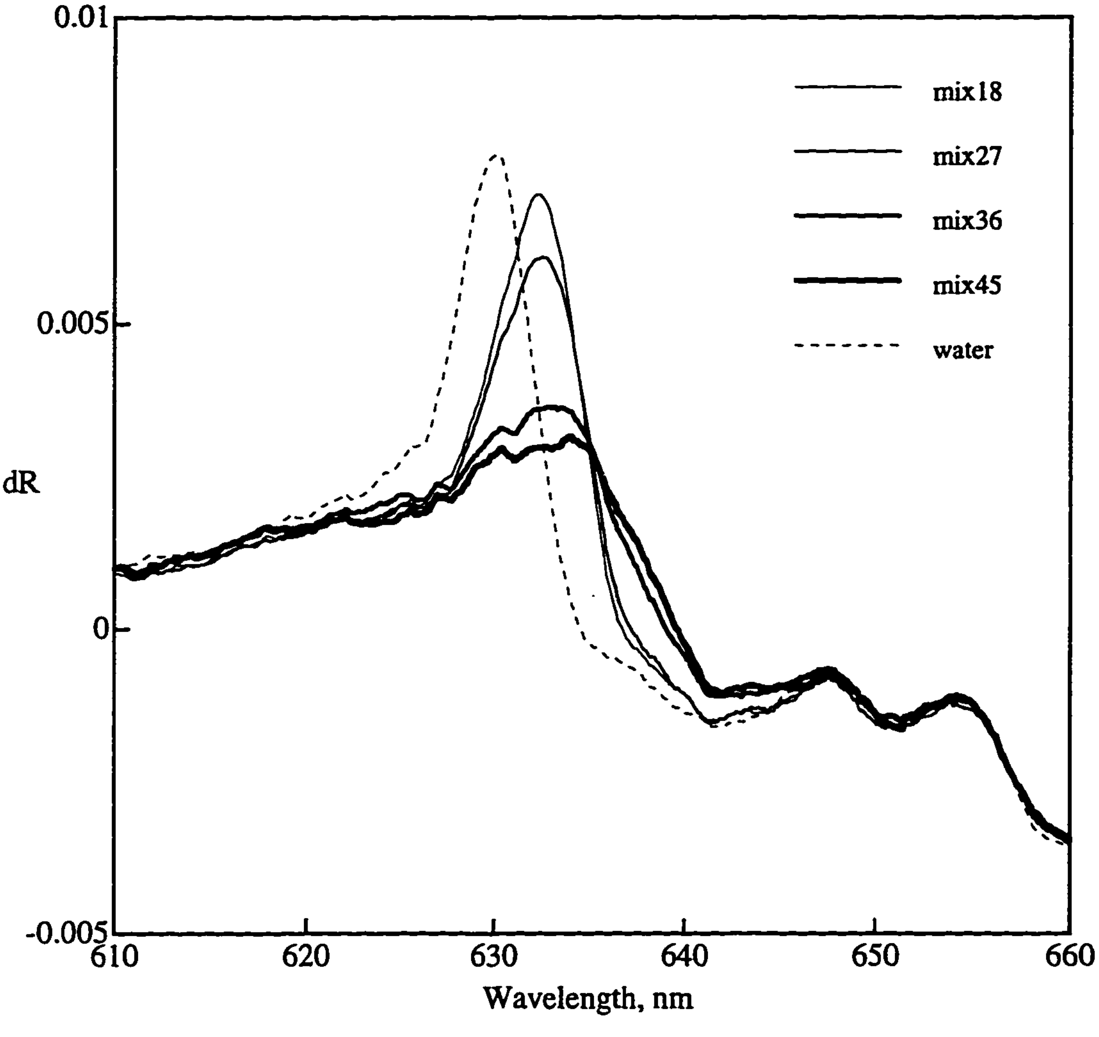

Figure 6.21 GLRS relative reflection coefficient derivative response to mixtures of polystyrene microspheres, ~2.5% solids, bi-modal distributions of farthest neighbor particle sizes (see table 6.4).

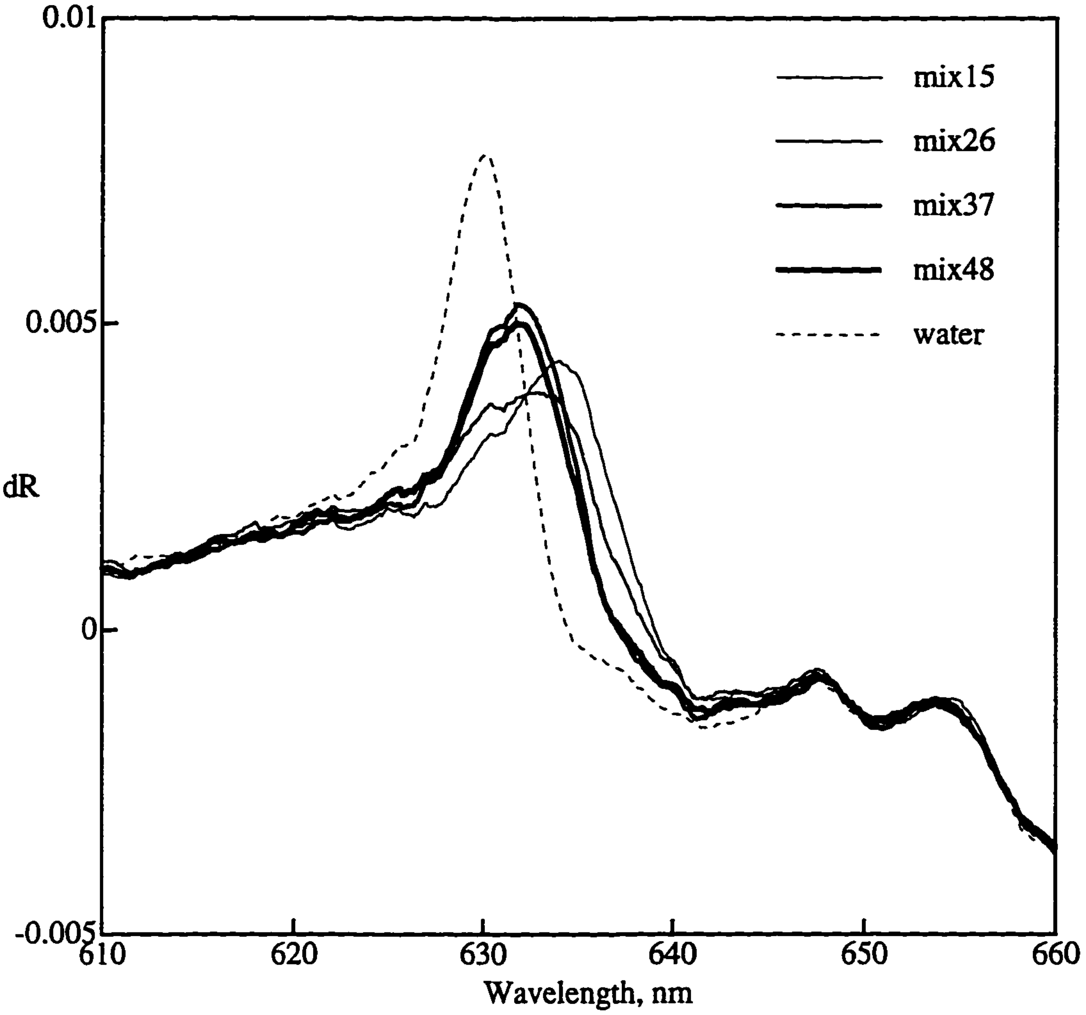

Figure 6.22 GLRS relative reflection coefficient derivative response to mixtures of polystyrene microspheres, ~2.5% solids, bi-modal distributions of particle sizes on either side of scattering regime threshold(see table 6.4).

Chapter 7

Conclusion

7.1 Summary

The theory developed by Dr. Anatol Brodsky in conjunction with the experimental results presented in this dissertation represents a new development in optical theory. It is important to note here that the experiments performed in this dissertation were designed and implemented based on specific predictions made in the interpretation of the theory. In each case, the experiments verified to a high degree the validity of the theory. In light of this, the experiments presented in this dissertation were an attempt to pin down the theoretical predictions on a case by case basis, and in the larger scope of the work it seems that a good experimental underpinning has been developed that will guide future work, both theoretically and experimentally.

7.1.1 GLRS Theory

The relationship between the reflected and transmitted diffraction orders for a transmission grating in contact with a sample matrix has not been previously described in terms of sample properties. In most optical systems, the anomalies associated with the passing off of diffracted orders are not desirable as they present additional effects that need to be corrected for. The development of GLRS has been based on the sensitivity advantages associated with transmission thresholds, and this coupled with the reflection and planar nature of the technique allow for implementation of the theory in direct process applications. The theory presented in this dissertation is a first step in the analysis of the experimental parameters, where threshold positions and peak shape changes are theoretically analyzed for experimental application. The full derivation of the reflection coefficients and scattering matrix elements is a starting point for parameter optimization and are given in the appendix.

7.1.2 Refractive Index and Absorbance Response

Theoretical predictions of refractive index sensitivity, absorbance response, and the deconvolution of the real and imaginary parts of the dielectric provided the motivation for fabrication of transmission gratings with periodicities on the order of the wavelength of light, which are in the submicron range for the visible region of the spectrum. Few reflection technologies exist with the single-reflection sensitivity of GLRS to absorbance and refractive index in neat and mixture systems. For instance, the ability of GLRS to measure absolute refractive index is a departure form other reflection measurements that rely on differential techniques. The sensitivity of GLRS to changes in refractive index demonstrated in this dissertation is limited by the experimental apparatus, not by theory, and enhancements in spectral resolution would yield corresponding enhancements in refractive index sensitivity. Also, demonstrated sensitivity to refractive index is promising in that multivariate statistical calibration models based on GLRS may be constructed that yield sensitivities on the order of transmission based differential laser refractometers. It is predicted from theory that a three order of magnitude increase in sensitivity to refractive index may be achieved by analyzing the phase shift rather than the intensity of reflected light.

The limit of detection for absorbance using GLRS is several orders of magnitude larger than that attainable for transmission measurements, and this is expected. Still, the increase in dynamic range to ~250 A.U. relative to standard 1 cm. transmission measurements indicates that GLRS in its current configuration is uniquely suited to process analysis where samples routinely are not measurable using standard transmission measurements. The sample set chosen for absorbance studies, methylene blue in water, was selected precisely because difficulties had been encountered in the absorbance characterization of GLRS with other dye systems (bromocresol green). However, during the characterization phase of GLRS, the experimental design went through a rigorous optimization of throughput and resolution. This optimization, as well as the large absorbance range associated with the methylene blue system, facilitated the initial absorbance characterization of GLRS. It is clear that further optimization of the grating and experimental conditions will yield wider dynamic ranges and lower limits of detection, making GLRS even more attractive as a process analysis tool as well as a standard sensing platform for a variety of matrices.

7.1.3 Fouling

A key aspect of GLRS that renders it fundamentally different from other reflection based techniques is that the there exists a relative insensitivity of the threshold position to surface fouling. The definition of surface relative to bulk is dependent on the scale of the system and the method used to measure bulk properties. For GLRS, it was important to carefully determine the scale upon which one defines the bulk, and it turned out that the scale is what is predicted by theory, on the order of a few wavelengths of the incident light. As discussed in chapter 6, competing reflection technologies are extremely sensitive to the state of the interface between the sensing element and the sample. GLRS demonstrated similar sensitivity to surface layers in terms of overall reflected intensity, but the key difference is that the effects of the surface loading and the bulk refractive index were deconvoluted. That is, the GLRS threshold modulation occurred at a specific wavelength due to the bulk medium, and surface effects were present in regions away from the threshold modulation. This, again, is explained by the fact that the probing radiation is not a single wave that is propagating through the interface, but is a superposition of reflected and transmitted diffracted waves that are modulated on different scales. The ability of GLRS to sense the presence of a bulk medium in the presence of a different surface medium is again a strong validation of theory and an indication that GLRS is suited to application in process analysis.

7.1.4 Scattering Matrices

The presence of scattering particles in a sample precludes the use of most transmission based measurements for quantitative analysis. This, as stated before, is a ubiquitous problem in industry. Thus, the next logical step in GLRS characterization was the exposure of the sensor to well-characterized scattering samples. The ability of GLRS to characterize samples that transit the region between Fraunhofer and Rayleigh scattering is a promising result. In addition, the nature of the scattering response is orthogonal for opposing scattering regime, i.e. concentration changes for systems in the Rayleigh regime yield position shifts in the threshold and concentration changes in the Fraunhofer regime yield derivative peak height deviations. The theoretical interpretation of GLRS scattering results is simplified in that GLRS responds to forward scattering in the sample. Again, it may be somewhat counterintuitive that a reflection method may be used to quantify forward scatter in a heterogeneous matrix, however, the data supports the assertion that forward scatter phenomena result in the GLRS response to scattering matrices. Thus, GLRS may be utilized for a range of particle sizes that may extend from the nanometer scale to tens or hundreds of microns in particle radius.

7.2 Future Work

The foundation in GLRS experimental understanding established in this dissertation points to the utility of the GLRS sensor in process analysis. As such, the directions in which future research may proceed need to include the application of GLRS and the development of rigorous solutions to the scattering matrix expressions.

The theoretical understanding of the grating specific parameters could be greatly increased by rigorously modeling the reflection coefficients as functions of wavelength and incident angle for a variety of different grating duty cycles and grating/substrate materials combinations. This will undoubtedly lead to better performance in absorbance sensitivity as well as optimization schemes that could be tailored for specific industrial applications. The difficulty in this approach is in the numerical stability associated with digitally modeling a singularity with a reasonable degree of accuracy and limiting assumptions. In addition, theory predicts that a higher sensitivity is achievable when the phase of reflected light is monitored. Thus, coupling the GLRS sensor to a phase sensitive detection system, whether fiber coupled or open path, is the next logical step in verifying further theoretical predictions of GLRS sensitivity. The expectation is that with increased sensitivity that the GLRS phase implementation will find applicability in gas phase sensing. However, with increased sensitivity to sample modulations comes a corresponding decrease in signal to noise ratio, and interferometric systems must be stabilized before reproducible results are achieved. Thus, it is expected that the largest challenge in characterizing the phase response of GLRS will again be in the experimental design and the stability of the apparatus.

An exciting aspect of this research has been the GLRS response to scattering matrices. Mixture samples represent a difficult challenge for GLRS in that for the current static experimental configuration the summation of effects from different particle size distributions leads to convolutions in the data interpretation. Thus, the next stage in GLRS should focus on modulation schemes, where the incident angle is modulated for a given sample. Data collection would yield a matrix of data for each sample, and appropriate data analysis should break the convolutions. In addition, for bi-and multimode distributions, a scanning instrument with a large bandwidth would allow for scattering regime transition regions to be located for each particle size. This would in effect yield a particle size distribution for the sample using a reflection based technique.

The functionalization of the surface of the sensor coupled with modulation techniques may yield a powerful technique for materials characterization. Also, a polymer overlayer could act as a stationary phase for chemical separations and thus an on-column detection system for chromatography could be realized in a reflection format that would respond to the complete dielectric function of the stationary phase. As the sensor responds to scattering systems, the stationary phase would not need to be an optical layer or a homogenous one. Activation of the grating itself would increase the chemical selectivity of the sensor. As the GLRS technique is not constrained to a few metals or by the thickness of the grating material, the metal could be chosen as a catalyst where the catalyzed reaction is monitored by the near field grating. In addition, the grating could be fabricated into an interdigitated microelectrode array. This would yield a hybrid electrochemical optical sensor that would be able to monitor concentration of reactants in the diffusion layer as well as in the bulk material in systems where the diffusion layer is on the order of a micron.

Finally, GLRS is a generalized wave phenomenon and the analysis of the singularities of the wave scattering from grating covered surfaces can be useful, not only in the case of light waves, but also in the cases of other types of waves: acoustic waves, microwaves, and even neutron and atomic de Broglie waves. In the last case, the physical grating may be replaced by a laser standing wave. Thus, for systems that preclude the use of optical transduction, other forms of wave phenomena are available that could take advantage of the GLRS threshold theory. It is clear that a myriad of directions are available for GLRS application and research.

7.3 Outlook

The future of GLRS appears to be very bright. The validity of the theory has been demonstrated to a high degree and the technique itself has been accepted in the scientific literature. The issuance of a United States patent on GLRS points to the uniqueness and utility of the general technique. It is expected that this format will be implemented as a process analysis technology for evaluation within the next two years. The success of GLRS as a process analysis tool will be dependent more on the engineering of the implementation than in the science of the sensing mechanism. In addition, further advances in the theoretical understanding of GLRS will yield more accurate and precise GLRS sensors with wide applicability.

List of References

(1) Anderson, B. B.; Brodsky, A. M.; Burgess, L. W. *Analytical Chemistry*, **1996**, *68* (7), 1081-1088.

(2) Anderson, B. B.; Brodsky, A. M.; Burgess, L. W. *Langmuir*, submitted.

(3) Anderson, B. B.; Brodsky, A. M.; Burgess, L. W. **March 26, 1996**, U.S. Patent Number 5,502,560.

(4) Anderson, B. B.; Brodsky, A. M.; Burgess, L. W. *J. Physical Review E*, **1996**, *54* (1).

(5) Baz', A.; Okun', L. *JETP* (USSR), **1958**, *35*, 757.

(6) Born, M.; and Wolf, E. *Principles of Optics*, 5th ed., Pergamon Press, Oxford, 1975, 59-60.

(7) Born, M.; Wolf, E. *Principles of Optics*, 5th ed., Pergamon Press, Oxford, 1975, 40-41.

(8) Bowman, E. M. , **1992**, Ph.D. Dissertation, University of Washington.

(9) Brandenburg, A.; Gombert, A. *Sensors and Actuators B*, 1993, *17*, 35-40.

(10) Brodsky, A. M.; Urbach, M. Sov. Phys. Uspechi, **1982**, *132*, 413.

(11) Champion, J.; Meeten, G.; Senior, M. *J. Colloid Interface Science*, **1979**, *72*, 471.

(12) Dushkina, N.; Sainov, S. *J. Modern Optics*, **1992**, *39*.(1), 173-187.

(13) Gaylord, T.; *Proceedings of the IEE*, **1985**, *73* (5), 894-937.

(14) Gupta, M. C.; Peng, S. T. *Applied Optics*, **1993**, *32* (16), 2911-2917.

(15) Heller, J.*Thin Solid Films*, **1973**,*17*, 163-176.

(16) Huber, W.; Barner, R.; Fattinger, Ch.; Hubsher, J.; Koller, H.; Muller, F.; Schlatter, D. *Sensors and Actuators B*, **1992**, *6*, 122-126.

(17) Jorgenson, R. *Surface Plasmon Resonance Based Bulk Optic and Fiber Optic Sensors*, **1993**, Ph.D. Dissertation, University of Washington.

(18) Karlsen, S. *Procedure for Fabrication of Diffraction Gratings*, Dept. of Electrical Engineering Class Report, 1992.

(19) Kemsley, E. K.; Appleton, G. P.; Wilson, R. H. *Spectrochimica Acta*, **1994**, *50A*, 1235-1242.

(20) Kuhn, K. J.; Burgess, L. W. *Analytical Chemistry*, **1993**, *65* (10), 1390-1398.

(21) Landau, L.; Lifshitz, E. *Electrodynamics of Continuous Media*, Pergamon, New York, 1985.

(22) Landau, L.; Lifshitz, E. *Quantum Mechanics*, §136, Pergamon, New York, 1984.

(23) Lewis, G. N. et. al *J. American Chemical Society*, **1943**, *65*, 1150.

(24) Lin, J.; Brown, C. W. *Spectroscopy*, **1995**, *10* (5), 48-51.

(25) Ludlow, I.; Eviert, *J. Physical Review E*, **1996**, *53*, 2909.

(26) Lukosz, W. ; Tiefenthaler, K. *Sensors and Actuators*, **1988**, *15*, 273-284.

(27) Lukosz, W. ; Tiefenthaler, K. *Sensors and Actuators*, **1988**, *15*, 285-295.

(28) Lukosz, W.; Nellen, Ph. M.; Stamm, Ch.; Weiss, P. *Sensors and Actuators B*, **1990**, *1*, 585-588.

(29) Mai, X.; Moshrefzadeh, R.; Gibson, U.; Stegeman, G.; Seaton, C. *Applied Optics*, **1995**, *24* (19), 3155-3161.

(30) Nakano, Y.; Tada, K. *Optics Letters*, **1988**, *13* (1), 7-9.

(31) Nellen, Ph. M.; Lukosz, W. *Sensors and Actuators B*, **1990**, *1*, 592-596.

(32) Newton, R. *Scattering Theory of Waves and Particles*, McGraw-Hill; New York, 1966, Chapter 17.

(33) Pankove, J. *Optical Processes in Semiconductors*, Dover, New York, 1971, Chapter 4.

(35) Pollack, J.; Cuzzi, J. *Light Scattering by Irregularly Shaped Particles*, (D. Scherman, ed.) Plenum, New York, 1983.

(36) Prieve, D.; Bike, S.; Frej, N. *Faraday Discuss. Chem. Soc.*, **1990**, *90*, 209-222.

(37) Rabinowitch, E.; Epstein, L. F. *J. American Chemical Society*, **1941**, *63*, 69.

(38) Rytov, S.; Fabelynskii, I. *Zh. Eskp. Teor Fiz., SSSR*, **1950**, *20* , 340.

(39) Sainov, S. *Applied Optics*, **1992**, *31* (31), 6589-6591.

(40) Sainov, S.; Chernov, B.; Dushkina, N. *Optics and Lasers in Engineering*, **1993**, *18*, 293-305.

(41) Sainov, S.; *Sensors and Actuators A*, **1994**, *45*, 1-6.

(42) Sainov, S.; Tontchev, D. *Optics and Lasers in Engineering*, **1989**, *10*, 17-26.

(43) Shiller, S.; Heisig, U.; Steinfelder, K.; Strumpfel, J.*Thin Solid Films*, **1979**, *63*, 369-375.

(44) Spohn, P.K.; Siefert, M. *Sensors and Actuators*, **1988**, *15*, 309-324.

(45) Tiefenthaler, K.; Lukosz, W. J. *Optical Society of America B*, **1989**, 6 (2), 209-220.

(46) Weast, R. C. Ed.*CRC Handbook of Chemistry and Physics*, 70th ed.; CRC Press: Boca Raton, FL, 1989, E-384.

Appendix[1]

Generalized GLRS Threshold Theory

In this appendix the threshold theory of light scattering (reflection and transmission) is considered for a plane interface between substrate and analyte media containing a periodic grating layer with the grating period Λ of the order of the wavelength of incident light. For simplicity the method of calculation is illustrated on an example of the system described by a local dielectric function $\varepsilon_{ij}(\overline{x})$ of the following form:

$$\varepsilon_{ij}(\overline{x}) = \varepsilon_0(x_1,\omega)\delta_{ij} + \delta\varepsilon_{ij}(\overline{x},\omega) \tag{1}$$

where $\varepsilon_0(x_1,\omega)$ describes the dielectric function averaged in the directions parallel to the surface and the interface component $\delta\varepsilon_{ij}(\overline{x},\omega)$ is periodic in the direction parallel to the surface:

$$\begin{gathered}\delta\varepsilon_{ij}(\overline{x},\omega) = \sum_{\substack{n=-\infty \\ n\neq 0}}^{\infty} \delta\tilde{\varepsilon}_{ij}(x_1,n,\omega)e^{in(\overline{q x_\parallel})}; \\ \overline{q} = \frac{2\pi}{\Lambda}\overline{g},\ \ \overline{x}_\parallel = \{x_2, x_3\}\end{gathered} \tag{2}$$

where $\overline{g}$ is the unit two-dimensional vector in the direction of the grating periodicity. It is supposed that the thickness of the substrate/sample interface, ℓ, is much less than the wavelength λ of the scattered light and

$$\delta\varepsilon_{ij}(\overline{x},\omega) = 0 \text{ for } |x_1| > \ell << \frac{c}{\omega} = \frac{\lambda}{2\pi} \tag{3}$$

This inequality will allow us to estimate the coefficients entering into the general threshold approximation with the relative accuracy on the order of

---

[1] Anderson, B. B.; Brodsky, A. M.; Burgess, L. W. *Physical Review E*, **1996**, *54* (1).

$$O\left(\frac{\ell}{\lambda}\right)^2 \tag{4}$$

Beyond the interface interval separating the substrate(1) and sample(2) media the dielectric function is supposed to be equal to frequency dependent bulk values:

$$\varepsilon_0(x_1,\omega)=\begin{cases}\varepsilon^{(1)}(\omega) & \text{for } x_1>\ell \quad \text{for substrate medium}\\ \varepsilon^{(2)}(\omega) & \text{for } x_1<-\ell \quad \text{for sample medium}\end{cases} \tag{5}$$

The distance of the air/substrate interface from the sample in the experimental device is supposed to be much larger than the free space wavelength. This allows us to concentrate on the analysis of the light scattering at the substrate/sample interface. Note that the results of the calculations in the threshold approximation are very general in nature and can be generalized to the more complex cases, i.e. when the dielectric function is nonlocal.

Suppose that the imaginary part of $\varepsilon^{(1)}=\varepsilon^{(1)}(\omega)$ can be neglected and the imaginary part of $\varepsilon^{(2)}=\varepsilon^{(2)}(\omega)$ is relatively small:

$$\begin{aligned}&\operatorname{Im}\varepsilon^{(1)}\cong 0\\ &\operatorname{Im}\varepsilon^{(2)}<<\operatorname{Re}\varepsilon^{(2)}\end{aligned} \tag{6}$$

There exist the following basic sets of solutions (7a) and (7b) to Maxwell's equations with frequency ω in the infinite media with dielectric constants $\varepsilon^{(1)}$ and $\varepsilon^{(2)}$, correspondingly:

$$\overline{E}_1^s(\pm,\overline{k}_\parallel)=\frac{\sqrt{4\pi\omega}}{c}\frac{(\overline{k}_\parallel\times\overline{n}_1)}{\sqrt{\overline{k}_\parallel^{\,2}\cdot k_1^{(1)}}}\cdot e^{i(-\overline{k_\parallel x_\parallel}\mp k_1^{(1)}x_1)}$$

$$\overline{E}_1^p(\pm,\overline{k}_\parallel)=\frac{\sqrt{4\pi\omega}}{c}\frac{((\overline{k}_\parallel\times\overline{n}_1)\times\overline{k}^{(1)})\cdot e^{i(-\overline{k_\parallel x_\parallel}\mp k_1^{(1)}x_1)}}{\sqrt{\frac{\omega^2}{c^2}\varepsilon^{(1)}\cdot\overline{k}_\parallel^{\,2}\cdot k_1^{(1)}}} \tag{7a}$$

$$\overline{E}_2^s(\pm,\overline{k}_\parallel)=\frac{\sqrt{4\pi\omega}}{c}\frac{(\overline{k}_\parallel\times\overline{n}_1)}{\sqrt{\overline{k}_\parallel^{\,2}\cdot k_1^{(2)}}}\cdot e^{i(-\overline{k_\parallel x_\parallel}\pm k_1^{(2)}x_1)} \tag{7b}$$

$$\overline{E}_2^p\left(\pm,\overline{k}_\parallel\right)=\frac{\sqrt{4\pi\omega}}{c}\frac{\left(\left(\overline{k}_\parallel\times\overline{n}_l\right)\times\overline{k}^{(2)}\right)\cdot e^{i\left(-\overline{k_\parallel x_\parallel}\pm k_l^{(2)}x_l\right)}}{\sqrt{\frac{\omega^2}{c^2}\varepsilon^{(2)}\cdot\overline{k}_\parallel{}^2\cdot k_l^{(2)}}}$$

where n_l is the unit vector in the normal direction to the surface and

$$\overline{k}^{1,2}=\left\{k_l^{1,2},\overline{k}_\parallel\right\},$$

$$\overline{k}_\parallel=\left\{k_2,k_3\right\},$$

$$k_l^{(1,2)}=\sqrt{\frac{\omega^2}{c^2}\varepsilon^{(1,2)}-k_\parallel{}^2}\equiv\frac{\omega}{c}\sqrt{\delta^{(1,2)}\left(k_\parallel\right)+i\cdot\operatorname{Im}\varepsilon^{(1,2)}},\qquad(8)$$

$$\delta^{(1,2)}\left(k_\parallel\right)=\operatorname{Re}\left(\varepsilon^{(1,2)}\right)-\frac{k_\parallel{}^2c^2}{\omega^2}$$

The sign index (+,-) in (7) corresponds to the direction of the wave toward and from the interface respectively (incident and outgoing directions). Note the different order of the signs in the exponents in expressions (7a) and (7b). The normalization in (7) is chosen in such a way that the component of Poynting's vector $S_l=\overline{S}\overline{n}_l$ in the direction normal to the interface constructed from the solutions in (7) is equal to unity for real k_l.

The two-dimensional wave vector $\overline{k}_\parallel$ in the discussed scattering problem is always real. According to momentum conservation laws, only the following values of $\overline{k}_\parallel$ in scattered and transmitted waves are possible:

$$\overline{k}_{\parallel,m}=\overline{k}_\parallel^0+m\overline{q},\quad m=0,\pm1,\pm2,\ldots\qquad(9)$$

where $\overline{k}_\parallel^0$ is the value of the tangential component of the wavevector in the incident light.

The normal component of the wave vector $k_l^{(2)}$ always has, according to equation (8), at least a small imaginary component due to the contribution of $\operatorname{Im}\varepsilon^{(2)}$. Large imaginary components of $k_l^{(1,2)}$ correspond to values of $\left(\overline{k}_{\parallel,m}^{(1,2)}\right)^2$ which are larger than $\frac{\omega^2}{c^2}\varepsilon^{(1)}$ or $\frac{\omega^2}{c^2}\varepsilon^{(2)}$, when:

$$\delta_m^{(i)} = \mathrm{Re}\,\varepsilon^{(i)} - \left(k_{\parallel,m}\right)^2 \frac{c^2}{\omega^2} < 0; \text{ for i=1 or 2} \qquad (10).$$

The condition (10) corresponds to the possibility of the formation of evanescent waves in the systems with non-homogeneous interfaces.

In the following the members of the solution set (7) are referred to as channels and designate them, taking into account (9), as $E_\alpha^\pm$ with a combined index subscript α:

$$\begin{aligned} &\alpha = \{i_\alpha, \zeta_\alpha, m_\alpha\} \\ &i_\alpha = 1,2;\ \zeta_\alpha = s,p;\ m_\alpha = 0, \pm 1, \pm 2, \ldots \end{aligned} \qquad (11)$$

and superscript ± corresponding to incident and outgoing directions, respectively.

The full solutions $E_\alpha^{(+)}(\bar{x})$ of the light scattering problem with the incident wave in the α-channel can be represented beyond the interface region in the sample and substrate media in the following form:

$$E_\alpha^{(+)}(\bar{x}) = \bar{E}_\alpha^{+}(\bar{x}) + \sum_{\alpha'} r_{\alpha',\alpha} \bar{E}_{\alpha'}^{-}(\bar{x}) \quad \text{for } x_\mathrm{l}^2 > \ell^2 \qquad (12)$$

where the term with an incident wave is present only at $x_\mathrm{l} > \ell$ or $x_\mathrm{l} < -\ell$ depending on the value of i_α and the set $E_{\alpha'}^{-}(\bar{x})$ includes outgoing and evanescent waves in the medium $i_{\alpha'}$. For simplicity in (12) a contribution under the sum over α' from possible surface and longitudinal bulk waves has been excluded. The generalization corresponding to the introduction of such waves is a straightforward one. The $\hat{r}$-matrix, with the elements $r_{\alpha',\alpha}$, contains all scattering information. These elements $r_{\alpha',\alpha}$ obey the following relations due to time inversion symmetry:

$$r_{\alpha,\alpha'}(\varepsilon) = r_{\alpha',\alpha}^{*}\left(\varepsilon^{*}\right) \qquad (13)$$

In addition to the set of solutions in (12) there is another set of solutions

$$E_\alpha^{(-)}(\bar{x}) = \left(E_\alpha^{(+)}(\bar{x})\right)^{*}\Big|_{\bar{k}_\mathrm{t} \to -\bar{k}_\mathrm{t},\, \varepsilon \to \varepsilon^{*}} \qquad (12a)$$

where the incoming and outgoing waves have been interchanged relative to the set $E_\alpha^{(+)}(\bar{x})$.

According to (8), (9), and (10), there are critical values of $\alpha = \alpha_{cr}$ (threshold singularities) at which one of the transmitted or scattered waves transforms from a traveling wave (with possible attenuation due to absorption) to an evanescent wave. Such values of α are determined by the following condition:

$$\delta_{\alpha_{cr}}=0 \qquad (14)$$

Near the threshold (14) the behavior of the energy fluxes in all channels abruptly changes due to the changing energy distributions and interference patterns. Qualitatively this result follows from energy conservation in the interface layer and the following expression for the Poynting vector, constructed from the solutions in (7):

$$(S_1)_\alpha \sim \mathrm{Re}(k_{1,\alpha}) = |k_{1,\alpha}| \cdot \sqrt{\frac{\sqrt{\delta_\alpha^2+\left(\mathrm{Im}\,\varepsilon^{(i_\alpha)}\right)^2}+\delta_\alpha}{2\sqrt{\delta_\alpha^2+\left(\mathrm{Im}\,\varepsilon^{(i_\alpha)}\right)^2}}}$$

$$=\begin{cases} |k_{1,\alpha}|\cos\frac{\psi_\alpha}{2} & \text{for } \delta_\alpha \geq 0 \\ |k_{1,\alpha}|\sin\frac{\psi_\alpha}{2} & \text{for } \delta_\alpha < 0 \end{cases} \qquad (15)$$

where

$$k_{1,\alpha} = |k_{1,\alpha}| \cdot \begin{cases} e^{i\frac{\psi_\alpha}{2}} & \text{for } \delta_\alpha > 0 \\ ie^{-i\frac{\psi_\alpha}{2}} & \text{for } \delta_\alpha < 0 \end{cases}$$

and

$$\cos\psi_\alpha = \frac{|\delta_\alpha|}{\sqrt{\delta_\alpha^2+\left(\mathrm{Im}\,\varepsilon^{(i_\alpha)}\right)^2}}, \quad 0 \leq \psi_\alpha \leq \pi \qquad (16)$$

Note that $\psi_\alpha \cong \frac{\pi}{2}$ for $|\delta_\alpha| << \mathrm{Im}\,\varepsilon^{(i_\alpha)}$ and $\psi_\alpha \cong 0$ for $\delta_\alpha >> \mathrm{Im}\,\varepsilon^{(i_\alpha)}$.

For the quantitative description of light scattering near the threshold $\delta_{\alpha_{cr}}=0$ it is possible to use, with minor modifications, the threshold theory of multichannel wave scattering[2]. According to this theory:

$$\begin{aligned} r_{\alpha,\alpha_{cr}} &= M_\alpha\sqrt{k_{1,\alpha_{cr}}} \quad \text{for } \alpha \neq \alpha_{cr} \\ r_{\alpha,\alpha'} &= r^0_{\alpha,\alpha'} + a_{\alpha,\alpha'}k_{1,\alpha_{cr}} \quad \text{for } \alpha,\alpha' \neq \alpha_{cr} \end{aligned} \qquad (17)$$

---

[2] Baz', A.; Okun', L. *JETP* (USSR), **1958**, *35*, 757.

$$r_{\alpha_{cr},\alpha_{cr}} = 1;$$

where $k_{1,\alpha_{cr}}$ is equal to: (17'),

$$k_{1,\alpha_{cr}} = \sqrt{\varepsilon^{i_{\alpha_{cr}}} \frac{\omega^2}{c^2} - \left(\bar{k}_{0,\parallel} + \frac{2\pi m_{\alpha_{cr}}}{\Lambda} \bar{g}\right)^2},$$

$r^0_{\alpha,\alpha'}$ are the values of $r_{\alpha,\alpha'}$ at $k_{1,\alpha_{cr}}$=0, and M_α and $a_{\alpha,\alpha'}$ are constants in the threshold approximation (that is up to higher terms in small quantity $\left|k_{1,\alpha_{cr}}\right|$ near the threshold).

The condition of the energy balance on the interface boundaries $x_1 = \pm\ell$ can be written, taking into account (15) and (16), as follows[3]:

$$\sum_{\tilde{\alpha}} r_{\alpha',\tilde{\alpha}} \cdot r^*_{\alpha,\tilde{\alpha}} f(\tilde{\alpha}) = (f(\alpha) - \kappa_\alpha)\delta_{\alpha,\alpha'} \tag{18}$$

where κ_α is the supposedly small (κ_α<<1) fraction of incident light energy absorbed in the thin layer $|x_1| < \ell$ and:

$$f(\alpha) = \begin{cases} \cos\frac{\psi_\alpha}{2} & \text{for } \delta_\alpha \geq 0 \\ \sin\frac{\psi_\alpha}{2} & \text{for } \delta_\alpha < 0 \end{cases} \tag{19}$$

The angles ψ_α are small for all $\alpha \neq \alpha_{cr}$ and correspondingly:

$$f(\alpha) \cong \begin{cases} 1 & \text{for } \delta_\alpha \geq 0 \\ 0 & \text{for } \delta_\alpha < 0 \end{cases} \quad \text{for } \alpha \neq \alpha_{cr} \tag{20}$$

Note that $\psi_{\alpha_{cr}}$ is not small and is equal approximately to $\frac{\pi}{2}$ in the threshold region where $\delta_{\alpha_{cr}} \cong 0$ even if the conditions (6) are fulfilled. It follows from (17)-(20) that the relation (18) near the α_{cr} threshold can be rewritten in the following form:

---

[3] The theory of wave scattering is followed in the stationary picture [ref. 1]. For the interpretation of the described effects in some cases it is more convenient to refer to non-stationary theory [ref. 1] in which, for example, $\int g(\tilde{\omega}) r_{\alpha\alpha'}(\tilde{\omega}) d\tilde{\omega}$ has to be substituted for $r_{\alpha\alpha'}(\omega)$ with the function $g(\tilde{\omega})$ strongly peaked near $\tilde{\omega} = \omega$. In the framework of non-stationary theory it is possible to demonstrate the characteristic threshold increase in the scattering time delay $T = \frac{d(\arg(r_{\alpha\alpha}))}{d\omega} \sim \frac{1}{\sqrt{\delta}}$ for $\delta \to 0$.

$$\sum_{\tilde{\alpha}}\left(r^0_{\alpha,\tilde{\alpha}}+a_{\alpha,\tilde{\alpha}}k_{1,\alpha_{cr}}\right)\left(r^{0^*}_{\alpha',\tilde{\alpha}}+a^*_{\alpha',\tilde{\alpha}}k^*_{1,\alpha_{cr}}\right)+M_\alpha M^*_{\alpha'}\left|k_{1,\alpha_{cr}}\right|f(\alpha_{cr})=\delta_{\alpha,\alpha'}(1-\kappa_\alpha) \tag{21}$$

for $\alpha,\alpha'\neq\alpha_{cr}$

where the sum is taken over all channels $\tilde{\alpha}\neq\tilde{\alpha}_{cr}$ with $\delta_{\tilde{\alpha}}>0$ and the dependence of κ_α on $k_{1,\alpha_{cr}}$ is disregarded. The relation (21) at $\delta_{\alpha_{cr}}<0$, $\delta_{\alpha_{cr}}>0$ and at $k_{1,\alpha_{cr}}=0$, correspondingly takes the following forms:

$$\sum_{\tilde{\alpha}}\left(r^0_{\alpha,\tilde{\alpha}}a^*_{\alpha',\tilde{\alpha}}e^{i\frac{\psi_{\alpha_{cr}}}{2}}-r^{0^*}_{\alpha',\tilde{\alpha}}a_{\alpha,\tilde{\alpha}}e^{-i\frac{\psi_{\alpha_{cr}}}{2}}\right)+M_\alpha M^*_{\alpha'}\sin\frac{\psi_{\alpha_{cr}}}{2}=0,\ \text{for } \delta_{\alpha=\alpha_{cr}}<0$$

$$-i\sum_{\tilde{\alpha}}\left(r^0_{\alpha,\tilde{\alpha}}a^*_{\alpha',\tilde{\alpha}}e^{-i\frac{\psi_{\alpha_{cr}}}{2}}-r^{0^*}_{\alpha',\tilde{\alpha}}a_{\alpha,\tilde{\alpha}}e^{-i\frac{\psi_{\alpha_{cr}}}{2}}\right)+M_\alpha M^*_{\alpha'}\cos\frac{\psi_{\alpha_{cr}}}{2}=0,\ \text{for } \delta_{\alpha=\alpha_{cr}}>0 \tag{22}$$

$$\sum_{\tilde{\alpha}}\left(r^0_{\alpha,\tilde{\alpha}}a^*_{\alpha',\tilde{\alpha}}-r^{0^*}_{\alpha',\tilde{\alpha}}a_{\alpha,\tilde{\alpha}}\right)=0, \text{for } k_{1,\alpha_{cr}}=0$$

The solution of the equations (22) is:

$$a_{\alpha,\alpha'}=-\frac{1}{2}M_\alpha M_{\alpha'}$$

$$M_\alpha=\sum_{\tilde{\alpha}}r^0_{\alpha,\tilde{\alpha}}M^*_{\tilde{\alpha}} \tag{23}$$

The results in (23) are analogous to the those found in the threshold theory of multichannel wave scattering on a localized scatterer[8,9]. The solution (23) together with (16) and (17) allows us to express near the thresholds the reflection coefficients $R_{\alpha,\alpha'}=\left|r_{\alpha,\alpha'}\right|^2$ and phases $\arg\left(r_{\alpha,\alpha'}\right)$ through the coefficients M_α and $r^0_{\alpha,\alpha'}$ as follows:

$$R_{\alpha,\alpha'}=\left|r_{\alpha,\alpha'}\right|^2=\left|r^0_{\alpha,\alpha'}\right|^2-\frac{1}{2}\left[\mathrm{Re}\left(r^0_{\alpha,\alpha'}M^*_\alpha M^*_{\alpha'}\right)\cdot\sqrt{\frac{1}{2}\left(\sqrt{\delta^2_{\alpha_{cr}}+\left(\mathrm{Im}\,\varepsilon^{(i_{\alpha_{cr}})}\right)^2}+\delta_{\alpha_{cr}}\right)}-\right.$$
$$\left.\mathrm{Im}\left(r^0_{\alpha,\alpha'}M^*_\alpha M^*_{\alpha'}\right)\cdot\sqrt{\frac{1}{2}\left(\sqrt{\delta^2_{\alpha_{cr}}+\left(\mathrm{Im}\,\varepsilon^{(i_{\alpha_{cr}})}\right)^2}-\delta_{\alpha_{cr}}\right)}\right]$$

$$\arg\left(r_{\alpha,\alpha'}\right) = \arg\left(r^0_{\alpha,\alpha'}\right) - \mathrm{Re}\left(\frac{M_\alpha M_{\alpha'}}{r^0_{\alpha,\alpha'}}\right)\cdot\sqrt{\frac{1}{2}\left(\sqrt{\delta^2_{\alpha_{cr}} + \left(\mathrm{Im}\,\varepsilon^{\left(i_{\alpha_{cr}}\right)}\right)^2} + \delta_{\alpha_{cr}}\right)} + \tag{24}$$

$$\mathrm{Im}\left(\frac{M_\alpha M_{\alpha'}}{r^0_{\alpha,\alpha'}}\right)\cdot\sqrt{\frac{1}{2}\left(\sqrt{\delta^2_{\alpha_{cr}} + \left(\mathrm{Im}\,\varepsilon^{\left(i_{\alpha_{cr}}\right)}\right)^2} - \delta_{\alpha_{cr}}\right)}$$

$$\text{for } \alpha,\alpha' \neq \alpha_{cr}$$

The result (24) can be summarized as follows. Near the threshold $\delta_{\alpha_{cr}} = 0$ the reflection coefficients and phases of all scattered and transmitted waves have singular behavior of the type depicted in figure 2 with coefficients constructed from the real and imaginary parts of $r^0_{\alpha,\alpha'}$, $M^*_\alpha M^*_{\alpha'}$, and $\frac{M_\alpha M_{\alpha'}}{r^0_{\alpha,\alpha'}}$. The position of the singularity depends only upon the bulk dielectric properties[10].

Until now, all calculations have been made in the framework of the general threshold approximation. In order to estimate the values of the combinations of the constants $r^0_{\alpha,\alpha'}$, M_α, and $M_{\alpha'}$ in (24) the perturbation theory in the parameter $\frac{\ell}{\lambda}$ is used. According to the "golden rule" of perturbation theory in the continuous spectrum[4] the scattering amplitudes $r_{\alpha,\alpha'}$ from unit surface area are equal to[5]:

$$r_{\alpha,\alpha'} \underset{S\to\infty}{=} \frac{\omega}{\left(2\pi\right)^{\frac{1}{2}}}\frac{1}{S}\sum_{i,j=1}^{3}\int\left(E^{F,(-)}_{\alpha,i}\left(\bar{x}\right)\right)^*\delta\varepsilon_{ij}\left(\bar{x},\omega\right)E^{F,(+)}_{\alpha',j}\left(\bar{x}\right)d\bar{x}^3 \text{ for } m_\alpha \neq m_{\alpha'} \tag{25}$$

where S is the surface area and the functions $E^F_{\alpha,\alpha'}(\bar{x})$ are Fresnel's solutions of the unperturbed problem with a stepwise uniform interface which have the form (12) and (14) with coefficients $r^0_{\alpha,\alpha'}$ equal to

---

[4] Landau, L.; Lifshitz, E. *Quantum Mechanics*, §136, Pergamon, New York, 1984.

[5] The expression (25) can also be obtained by the perturbative solution of the regularized integral equations for the light surface scattering (See Brodsky, A. M.; Urbach, M. *Sov. Phys. Uspechi*, **1982**, *132*, 413).

$$r^0_{\alpha,\alpha'} = r^F_\alpha \text{ for } \alpha = \alpha'$$

$$r^0_{\alpha,\alpha'} = \sqrt{\frac{k^{(1)}_\alpha}{k^{(1)}_{\alpha'}}}\left(1 - r^F_\alpha\right)\begin{cases} 1 \text{ for } i_\alpha \neq i_{\alpha'};\ \zeta_\alpha = \zeta_{\alpha'} = s;\ m_\alpha = m_{\alpha'} \\ \sqrt{\dfrac{\varepsilon_\alpha}{\varepsilon_{\alpha'}}} \text{ for } i_\alpha \neq i_{\alpha'};\ \zeta_\alpha = \zeta_{\alpha'} = p;\ m_\alpha = m_{\alpha'} \end{cases} \tag{26}$$

$$r^0_{\alpha,\alpha'} = 0 \text{ for } \zeta_\alpha \neq \zeta_{\alpha'} \text{ and/or } m_\alpha \neq m_{\alpha'}$$

where r^F_α are Fresnel's reflection amplitudes[6]:

$$r^F_\alpha = \frac{\varepsilon^{(\tilde{i}_\alpha)}\left[\frac{\omega^2}{c^2}\varepsilon^{(i_\alpha)} - \left(\bar{k}^0_\parallel + m_\alpha\bar{q}\right)^2\right]^{\frac{1}{2}} - \varepsilon^{(i_\alpha)}\left[\frac{\omega^2}{c^2}\varepsilon^{(\tilde{i}_\alpha)} - \left(\bar{k}^0_\parallel + m_\alpha\bar{q}\right)^2\right]^{\frac{1}{2}}}{\varepsilon^{(\tilde{i}_\alpha)}\left[\frac{\omega^2}{c^2}\varepsilon^{(i_\alpha)} - \left(\bar{k}^0_\parallel + m_\alpha\bar{q}\right)^2\right]^{\frac{1}{2}} + \varepsilon^{(i_\alpha)}\left[\frac{\omega^2}{c^2}\varepsilon^{(\tilde{i}_\alpha)} - \left(\bar{k}^0_\parallel + m_\alpha\bar{q}\right)^2\right]^{\frac{1}{2}}} \text{ for } \zeta_\alpha = p$$

$$\tag{26a}$$

$$r^F_\alpha = \frac{\left[\frac{\omega^2}{c^2}\varepsilon^{(i_\alpha)} - \left(\bar{k}^0_\parallel + m_\alpha\bar{q}\right)^2\right]^{\frac{1}{2}} - \left[\frac{\omega^2}{c^2}\varepsilon^{(\tilde{i}_\alpha)} - \left(\bar{k}^0_\parallel + m_\alpha\bar{q}\right)^2\right]^{\frac{1}{2}}}{\left[\frac{\omega^2}{c^2}\varepsilon^{(i_\alpha)} - \left(\bar{k}^0_\parallel + m_\alpha\bar{q}\right)^2\right]^{\frac{1}{2}} + \left[\frac{\omega^2}{c^2}\varepsilon^{(\tilde{i}_\alpha)} - \left(\bar{k}^0_\parallel + m_\alpha\bar{q}\right)^2\right]^{\frac{1}{2}}} \text{ for } \zeta_\alpha = s$$

$$\left(\tilde{i}_\alpha\right) = \begin{cases} 1 \text{ for } \left(i_\alpha\right) = 2 \\ 2 \text{ for } \left(i_\alpha\right) = 1 \end{cases}$$

The coefficient $\frac{\omega}{(2\pi)^{\frac{1}{2}}}$ in (25) corresponds to the kinematics of scattering by an infinite flat interface and is different from the analogous coefficient in the perturbation theory of wave scattering by a scatterer localized in all dimensions[11].

The Fresnel's solutions of light scattering problems have continuous across the interface components of the field $E^F_\alpha(\bar{x})$ parallel to the interface and a normal to the interface component of the displacement $D^F_{\alpha,1}(\bar{x}) = \varepsilon_0(x_1)E^F_{\alpha,1}(\bar{x})$. Near the interface these continuous field components change on relatively large (in the discussed perturbation theory) distances $\lambda >> \ell$ which allows us to take them out of the integral over dx_1 in (25) at the point x_1=0 on the interval $|x_1| < \ell$ where $\delta\varepsilon_{ij}(\bar{x})$ is concentrated:

---

[6] Landau, L.; Lifshitz, E. *Electrodynamics of Continuous Media*, Pergamon, New York, 1985.

$$r_{\alpha,\alpha'} \underset{S\to\infty}{\cong} \frac{\omega}{S\cdot c}\int_S d^2x_{\parallel}\left\{\left[\left(\overline{E}^{F,-}_{\alpha,\parallel}(\overline{x})\right)^{*}\overline{E}^{F,+}_{\alpha',\parallel}(\overline{x})\right]\Bigg\|_{x_1=0}\int_{-\infty}^{\infty}dx_1\delta\varepsilon(\overline{x},\omega)-\right.$$
$$\left.\left[\left(\overline{E}^{F,-}_{\alpha,1}(\overline{x})\varepsilon^{(i_\alpha)}\right)^{*}\overline{E}^{F,+}_{\alpha',1}(\overline{x})\varepsilon^{(i_{\alpha'})}\right]\Bigg\|_{x_1=0}\int_{-\infty}^{\infty}dx_1\delta\frac{1}{\varepsilon(\overline{x},\omega)}\right\}+O\left(\left(\frac{\ell}{\lambda}\right)^2\right) \qquad (27)$$

It is supposed in (27), for simplicity, that $\delta\varepsilon_{ij}(\overline{x})$ is symmetrical:

$$\delta\varepsilon_{ij}(\overline{x})=\delta_{ij}\delta\varepsilon(\overline{x}) \qquad (28)$$

The function $\delta\frac{1}{\varepsilon(\overline{x},\omega)}$, introduced in (27), which determines the scattering amplitudes of p-polarized light has the following form:

$$\delta\frac{1}{\varepsilon(\overline{x},\omega)}\equiv\frac{-1}{\varepsilon^2(\overline{x},\omega)}\delta\varepsilon(\overline{x},\omega)=\sum_{n=-\infty}^{\infty}\tilde{\delta}\frac{1}{\varepsilon}(x_1,n,\omega)e^{in(\overline{qx_{\parallel}})}$$
$$\cong\frac{1}{\varepsilon(\overline{x},\omega)}-\frac{1}{\varepsilon_0(x_1,\omega)} \qquad (29)$$

The expressions (27) can be transformed further taking into account that

$$\left|E^{F,+}_{\alpha,i}(\overline{x})\right\|_{x_1=0}=\left(1+r^F_\alpha\right)\frac{1}{\sqrt{k_{1,\alpha}}}\frac{\sqrt{4\pi\omega}}{c} \qquad (30)$$

Introducing (30) into (27) it is found with (2), (7), (12), (13a), (14), and (29) that

$$r_{\alpha,\alpha'}=\frac{16\pi\omega^2}{c^2}\frac{\overline{k}_{\parallel,\alpha}\overline{k}_{\parallel,\alpha'}}{\sqrt{\overline{k}^2_{\parallel,\alpha}\overline{k}^2_{\parallel,\alpha'}}}\frac{\sqrt{k^{*}_{1,\alpha}k_{1,\alpha'}}}{\left(k_{1,\alpha'}+k_{1,\bar{\alpha}'}\right)\left(k^{*}_{1,\alpha}+k^{*}_{1,\bar{\alpha}}\right)}\frac{1}{\sqrt{2\pi}}\int_{-\infty}^{\infty}dx_1\delta\tilde{\varepsilon}(x_1,m_\alpha-m_{\alpha'},\omega),$$

for $\zeta_\alpha=\zeta_{\alpha'}=s$

$$r_{\alpha,\alpha'}=\frac{16\pi(m_{\alpha'}-m_\alpha)\left|\overline{k}^0_{\parallel}\times\overline{q}\right|k_{1,\alpha}\frac{\omega}{c}}{\sqrt{\varepsilon^{(i_\alpha)}\left(\overline{k}_{\parallel,\alpha}\right)^2\left(\overline{k}_{\parallel,\alpha'}\right)^2}}\frac{\left(\varepsilon^{(i_\alpha)}\sqrt{k_{1,\alpha}}\right)^{*}\sqrt{k_{1,\alpha'}}}{\left(\varepsilon^{(\bar{i}_\alpha)}k_{1,\alpha}+\varepsilon^{(i_\alpha)}k_{1,\bar{\alpha}}\right)^{*}\left(k_{1,\alpha'}+k_{1,\bar{\alpha}'}\right)}\cdot$$
$$\frac{1}{\sqrt{2\pi}}\int_{-\infty}^{\infty}dx_1\delta\tilde{\varepsilon}(x_1,m_\alpha-m_{\alpha'},\omega), \qquad (31)$$

for $\zeta_\alpha=p,\ \zeta_{\alpha'}=s$

$$r_{\alpha,\alpha'}=\frac{16\pi\cdot\varepsilon^{(\bar{i}_{\alpha'})}\sqrt{\left(\varepsilon^{(i_\alpha)}k_\alpha\right)^*\left(\varepsilon^{(i_{\alpha'})}k_{\alpha'}\right)}}{\sqrt{\bar{k}^2_{\parallel,\alpha'}\cdot\bar{k}^2_{\parallel,\alpha}}}\frac{1}{\left(\varepsilon^{(\bar{i}_\alpha)}k_{1,\alpha}+\varepsilon^{(i_\alpha)}k_{1,\bar{\alpha}}\right)^*}\frac{1}{\left(\varepsilon^{(\bar{i}_{\alpha'})}k_{1,\alpha'}+\varepsilon^{(i_{\alpha'})}k_{1,\bar{\alpha}'}\right)}\cdot$$

$$\left\{\left(\bar{k}_{\parallel,\alpha}\bar{k}_{\parallel,\alpha'}\right)k_{1,\alpha}k_{1,\alpha'}\int_{-\infty}^{\infty}dx_1\delta\tilde{\varepsilon}\left(x_1,m_\alpha-m_{\alpha'},\omega\right)+\bar{k}^2_{\parallel,\alpha}\bar{k}^2_{\parallel,\alpha'}\int_{-\infty}^{\infty}dx_1\delta\frac{\tilde{1}}{\varepsilon}\left(x_1,m_\alpha-m_{\alpha'},\omega\right)\right\}$$

for $\zeta_\alpha=\zeta_{\alpha'}=p$

The expression for the transition amplitudes for $\zeta_\alpha=s$, $\zeta_{\alpha'}=p$ can be found from (31) with the help of (13). It follows from (17) and (31) that in the approximation (4):

$$M_\alpha=\frac{1}{\sqrt{\varepsilon^{\bar{i}_{\alpha_\sigma}}-\varepsilon^{i_{\alpha_\sigma}}}}\frac{1}{\sqrt{2\pi}}\int_{-\infty}^{\infty}dx_1\delta\varepsilon\left(x_1,m_\alpha-m_{\alpha_\sigma},\omega\right)$$

for $\zeta_\alpha=s$,

$$\tag{32}$$

$$M_\alpha=16\pi\sqrt{\frac{\varepsilon^{(i_{\alpha_\sigma})}}{\varepsilon^{(\bar{i}_{\alpha_\sigma})}}}\left.\frac{\sqrt{\left(\bar{k}^2_{\parallel,\alpha}\right)^*\left(\varepsilon^{i_\alpha}k_\alpha\right)^*}}{\left(\varepsilon^{(\bar{i}_\alpha)}k_{1,\alpha}+\varepsilon^{(i_\alpha)}k_{1,\bar{\alpha}}\right)}\right|_{\delta_{\alpha_\sigma}=0}\frac{1}{\sqrt{\varepsilon^{\bar{i}_{\alpha_\sigma}}-\varepsilon^{i_{\alpha_\sigma}}}}\cdot\int_{-\infty}^{\infty}dx_1\delta\frac{\tilde{1}}{\varepsilon}\left(x_1,m_\alpha-m_{\alpha_\sigma},\omega\right)$$

for $\zeta_\alpha=p$,

The expressions (32) indicate that the qualitatively different threshold behavior of the s- and p-polarized light scattering can be expected in the case of metallic gratings on dielectric substrates or vice versa. When the grating and substrate dielectric functions have real parts of different signs for different values of $\bar{x}$ the continuation of the function $\delta\frac{1}{\varepsilon(\bar{x},\omega)}$ into the complex plane of x_1 becomes infinite at some point $x_1-x_1^0$ with the distance from the real axis $\operatorname{Im}x_1^0$ proportional to the value of the imaginary component of $\delta\varepsilon\left(\bar{x},\omega\right)$. This effect can be interpreted as a result of the formation of local surface plasmon resonances. The corresponding enhancement of the imaginary component of the integral

$$\int_{-\infty}^{\infty}dx_1\delta\frac{\tilde{1}}{\varepsilon}\left(x_1,m_\alpha-m_{\alpha'},\omega\right)\tag{33}$$

leads to the complex values of M_α with comparable real and imaginary parts even if the imaginary part of $\widetilde{\delta\varepsilon}$ is substantially smaller than the real part. It follows from (24), (27), and the structure of (33) that in particular in the expressions for the specular p-wave scattering, the coefficients in terms in (24) proportional to $\sqrt{\frac{1}{2}\left(\sqrt{\delta_{\alpha_\sigma}^2+\left(\operatorname{Im}\varepsilon^{\left(i_{\alpha_\sigma}\right)}\right)^2}+\delta_{\alpha_\sigma}\right)}$ and $\sqrt{\frac{1}{2}\left(\sqrt{\delta_{\alpha_\sigma}^2+\left(\operatorname{Im}\varepsilon^{\left(i_{\alpha_\sigma}\right)}\right)^2}-\delta_{\alpha_\sigma}\right)}$, respectively, have to be of the same order of magnitude and negative. In the case of the s-wave scattering the corresponding coefficients in the term proportional to $\sqrt{\frac{1}{2}\left(\sqrt{\delta_{\alpha_\sigma}^2+\left(\operatorname{Im}\varepsilon^{\left(i_{\alpha_\sigma}\right)}\right)^2}+\delta_{\alpha_\sigma}\right)}$ must be substantially larger than the coefficients in the second term proportional to $\sqrt{\frac{1}{2}\left(\sqrt{\delta_{\alpha_\sigma}^2+\left(\operatorname{Im}\varepsilon^{\left(i_{\alpha_\sigma}\right)}\right)^2}-\delta_{\alpha_\sigma}\right)}$.

Vita

Brian B. Anderson

Education

Bachelor of Science, Chemistry, Central Washington University, Ellensburg, Washington, 1992.

Doctor of Philosophy, Analytical Chemistry, University of Washington, Seattle, Washington, 1996.

Dissertation Title

Grating Light Reflection Spectroscopy

Publications

Anderson, B. B.; Brodsky, A. M.; Burgess, L. W. "Grating Light Reflection Spectroscopy for Determination of Bulk Refractive Index and Absorbance," *Analytical Chemistry*, **1996**, *68* (7), 1081-1088.

Anderson, B. B.; Brodsky, A. M.; Burgess, L. W. "Threshold Effects in Light Scattering from a Binary Diffraction Grating," *J. Physical Review E*, **1996**, *54* (1).

Anderson, B. B.; Brodsky, A. M.; Burgess, L. W. "Grating Light Reflection Spectroscopy of Colloids and Suspensions," *Langmuir*, **1996**, submitted.

Anderson, B. B.; Brodsky, A. M.; Burgess, L. W. "Application of Grating Light Reflection Spectroscopy in Analytical Sensors," Proceedings of the SPIE, **2293**, 80 (1994).